THE RESPONSE OF ORDERED ALLOYS TO ELECTRON IRRADIATION

A thesis submitted for the degree of
Doctor of Philosophy

by

JULIE FRANCES WAITING
(née ORCHARD)

Department of Metallurgy and Materials Science,
Royal School of Mines,
Imperial College of Science and Technology,
London University.

February, 1983

To

my dear parents,

Frances and Eric Orchard

ABSTRACT

The Response of Ordered Alloys to Electron Irradiation

An investigation has been made of the effects of high energy electron irradiation on the degree of long-range order, S . in the fully ordered alloys Ni_3Al and Ni_3Fe based on the f.c.c structure, NiAl and FeAl based on the b.c.c structure and Mg_3Cd based on the h.c.p structure. The irradiations were carried out at temperatures between 15K and 600K in a high voltage electron microscope operating at a range of accelerating voltages between 200 kV and 1000 kV.

The disordering response of the alloys can be divided into three distinct temperature regimes. At 'high' temperatures disordering is not observed because the irradiation produced and/or thermal point defects are sufficiently mobile to restore the equilibrium degree of order to the alloy. At intermediate temperatures there is a balance set up between radiation induced disordering and reordering which produces a steady-state value of S . Analysis of the results in this temperature regime, by the application of a kinetic model, has shown that in Ni_3Al, Ni_3Fe and Mg_3Cd vacancies are the defect species responsible for reordering under electron irradiation. At 'low' temperatures, below which vacancies can be considered immobile, all the alloys, except NiAl, become fully disordered when irradiated above the threshold displacement energy for disordering and the disordering rate increases with decreasing temperature and increasing accelerating voltage. This result is consistent with disordering by the propagation of replacement collision sequences down mixed atom rows, with the energy of the p.k.o. defining the length of the sequence and the temperature dependence arising from an attenuation of the sequence length due to lattice vibrations. NiAl is more resistant to disordering than the other alloys investigated being only partially disordered after extended irradiation with a damage rate of 10^{-3} dpa.sec^{-1} at 15K. This behaviour is interpreted in terms of the defect structure of the non-stoichiometric Al-rich NiAl alloy. The concentration of nickel vacancies together with the high ordering energy of this alloy promotes correlated 'athermal' recombination.

TABLE OF CONTENTS

Page

Abstract. 2

Table of contents. 3

List of common symbols. 6

Chapter 1. Introduction. 8

Chapter 2. Order and Disorder.

- 2.1. Theoretical background information. 11
  - 2.1.1. The long-range order parameter, S. 11
  - 2.1.2. Superlattice structures. 12
  - 2.1.3. Thermodynamic considerations. 13
  - 2.1.4. The kinetics of order-disorder transformations. 19
  - 2.1.5. Diffusion in ordered alloys. 21
  - 2.1.6. Domains and antiphase domain boundaries. 23
  - 2.1.7. Antiphase domain coalescence. 24
- 2.2. The ordered alloys investigated in the present work. 25
  - 2.2.1. Crystal structure. 25
  - 2.2.2. Physical properties. 26

Chapter 3. Radiation Effects.

- 3.1. The fundamental aspects of electron irradiation damage in ordered alloys. 29
  - 3.1.1. The atomic displacement process. 29
  - 3.1.2. Threshold displacement energy determination. 34
  - 3.1.3. Orientation dependence of E_d. 35
  - 3.1.4. Temperature dependence of E_d. 35
  - 3.1.5. Focusing effects. 38
  - 3.1.6. Radiation enhanced diffusion. 49
- 3.2. The effects of electron irradiation on ordered alloys. 58
  - 3.2.1. Ordering under electron irradiation. 58
  - 3.2.2. Disordering under electron irradiation. 66

Chapter 4. Experimental Procedure. 76

- 4.1. Alloy preparation. 76
- 4.2. Electron irradiation. 76
  - 4.2.1. Characteristics of the electron beam and its interaction with the specimen. 76
- 4.3. Measurement of changes in S during electron irradiation using electron diffraction. 80

Page

4.3.1. Electron diffraction in the kinematical condition. 80

4.3.2. Electron diffraction in a crystalline specimen containing a high density of defect loops. 81

4.3.3. The anisotropy of superlattice reflection intensity change. 86

4.3.4. Photography and measurement of the diffracted electron intensity. 91

4.4. Electron microscopy specimen preparation. 95

4.5. Evaluation of the vacancy migration energy in Mg_3Cd. 95

4.5.1. X-ray diffraction study of ordering in Mg_3Cd. 95

4.5.2. Determination of the activation energy for domain coarsening from the kinetics of antiphase domain growth. 96

Chapter 5. Experimental Results. 100

5.1. The response of fully ordered Mg_3Cd (DO_{19}) structure to electron irradiation. 101

5.1.1. Effect of temperature and accelerating voltage. 101

5.1.2. Effect of orientation. 105

5.2. Evaluation of the activation energy for vacancy migration in Mg_3Cd. 109

5.2.1. X-ray diffraction study of ordering. 109

5.2.2. Determination of the activation energy for domain coarsening from a study of the kinetics of antiphase domain growth. 115

5.2.3. A study of point defect loop growth in Mg_3Cd under 1000 kV electron irradiation. 119

5.3. The response of fully ordered Ni_3Al and Ni_3Fe (Ll_2 structure) to electron irradiation. 123

5.3.1. Effect of temperature and accelerating voltage. 123

5.3.2. Effect of orientation. 143

5.4. The response of fully ordered NiAl and FeAl (B2 structure) to electron irradiation. 144

5.4.1. NiAl. 144

5.4.2. FeAl. 150

Page

Chapter 6. Discussion.

6.1. Temperature dependence of the disordering cross-section. 152

6.1.1. Threshold displacement energy assumptions. 155

6.1.2. $L1_2$ alloys. 157

6.1.3. Summary. 162

6.1.4. Effect of temperature on replacement collision sequence length. 162

6.1.5. Effect of accelerating voltage on R.C.S. length. 166

6.1.6. Effect of Debye temperature on R.C.S. length. 171

6.1.7. Mg_3Cd. 171

6.1.8. B2 alloys. 175

6.1.9. Orientation effects. 176

6.1.10. Recombination volume effects. 176

6.1.11. Previous investigations. 177

6.2. Analysis of the results where a balance exists between disordering and reordering under electron irradiation. 179

6.2.1. Ni_3Al. 179

6.2.2. Ni_3Fe. 185

6.2.3. Mg_3Cd. 186

6.2.4. NiAl. 189

Chapter 7. Summary, Conclusions and Proposals for Future Work. 198

7.1. Measurement of changes in S during electron irradiation using electron diffraction. 198

7.2. The response of ordered alloys to electron irradiation. 198

7.2.1. Temperature dependence of the disordering cross-section. 198

7.2.2. Temperature regime where there is a balance between disordering and reordering. 199

7.3. Proposals for future work. 200

Acknowledgements. 202

References. 203

Appendix I. 210

Appendix II. 211

Appendix III. 213

List of Common Symbols

The following symbols have been used throughout the text. Others have appeared in specific instances and are defined only where they occur.

A_i	interstitial entropy factor (= $\exp^{s_i^M/k_b}$, where s_i^M is interstitial migration entropy.
A_v	vacancy entropy factor (= $\exp\ {s_v^M/k_b}$, where s_v^M is vacancy migration entropy.
D	Antiphase domain size.
E_d	Threshold displacement energy.
E_F	Critical focusing energy.
E_i^F	Interstitial formation energy.
E_i^M	Interstitial migration energy.
E_s	Energy transferred in a secondary atom-atom collision.
E_T	Energy transferred in an electron-atom collision.
E_v^F	vacancy formation energy.
E_v^M	vacancy migration energy.
f_A	atomic electron scattering factor of A.
F_{hkl}	structure factor.
i	concentration of irradiation-produced interstitials.
I_F	Fundamental reflection intensity.
I_S	Superlattice reflection intensity.
K	atomic displacement rate.
k_b	Boltzmann's constant.
S	The long-range order parameter.
T	Absolute temperature.
T_c	Critical temperature.
V	Ordering energy.
v	Concentration of irradiation produced vacancies.
v_o	Concentration of thermal vacancies.
z	Co-ordination number.
Z	Recombination volume.
α_i	Interstitial sink density.
α_v	Vacancy sink density.
ε	Ratio of the number of atomic replacements to atomic displacements.
σ_d	Total atomic displacement cross-section.

λ	Atomic jump distance.
ν_i	Interstitial jump frequency.
ν_v	Vacancy jump frequency.
ν_o	Natural atomic vibration frequency.

CHAPTER 1

Introduction

The current interest in the response of ordered alloys to irradiation arises from their use as nuclear engineering materials. They are often employed to provide dispersion strengthening and also have a potential application as 'dosimeters' to monitor damage or recovery processes, via quantitative changes in the degree of long-range order, S. Furthermore, the irradiation behaviour of ordered alloys is of considerable fundamental interest as their response is a powerful tool in the study of radiation damage events.

It has been well established experimentally that irradiation of an ordered alloy above its threshold displacement energy can lead to changes in S. (For a recent review see Schulson (1979).) In a fully ordered alloy each atom displaced produces a decrease in the state of order in the crystal which can only be restored if mutual recombination of an interstitial and a vacancy of the 'right' type occurs. In simple theories of disordering (Aronin (1954), Venables and Lye (1969) and Polenok (1973)), where reordering is neglected, it is assumed that

$$S = S_o \exp(-\varepsilon\sigma_d\phi t) \qquad \text{(i)}$$

where S_o is the initial degree of long-range order, ε is a multiplication factor which depends on the assumptions of the particular model, σ_d is the displacement cross-section, ϕ is the irradiation flux and t is the irradiation time. At temperatures where the irradiation-produced and/or thermal defects are mobile enough to restore order to the lattice disordering is resisted. Theories which assume a balance between disordering and ordering under irradiation have been developed (Butler (1979) and Liou and Wilkes (1979)) and predict:

(i) At low temperatures complete disordering is favoured as the defect mobility is insufficient to resist disordering,

(ii) At elevated temperatures the mobility and concentration of irradiation produced and thermal defects is high and so ordering is favoured, and

(iii) At some intermediate temperature the disordering and ordering rates have approximately the same magnitude and these become equal at some pseudo-equilibrium, steady-state value of S.

The available experimental evidence for a range of ordered alloys under cascade and non-cascade producing irradiation supports the exponential dependence of S on dose, (ϕt), (Aronin (1954), Sweedler and Cox (1975), Butler and Swann (1977), Carpenter and Schulson (1978), Liu et al (1980) and Kinoshita et al (1982)) and the above theoretical predictions with respect to temperature (Howe and Rainville (1977), Butler (1978) and Carpenter and Schulson (1981)).

The present work is concerned with the effects of electron irradiation on the mechanisms of disordering. Disordering mechanisms specific to high energy electrons which are important enough to lead to significant disordering can be identified as:

(i) uncorrelated interstitial-vacancy recombination: interstitials escaping from the recombination volume following displacement recombine with vacancies of the 'wrong' type.
(ii) replacement followed by uncorrelated recombination within the recombination volume: the primary displaced atom has sufficient energy to displace its unlike neighbour which then recombines athermally with the 'original' 'wrong' vacancy,
(iii) replacement collision sequences down mixed atom rows: each displaced atom starts a knock-on chain creating a ribbon of disorder the length of the replacement sequence.
(iv) replacement collision sequences down rows of like atoms: equivalent to (i) if the sequence culminates in an interstitial ejected outside the recombination volume.

If mechanism (iii) is the dominant disordering mechanism then ε will be greater than unity as the effect of one displaced atom is multiplied by the number of replacements in the collision chain. If mechanisms (i), (ii) and (iv) are dominant then ε will be less than unity as not every displacement combines uncorrelatedly. Recent investigations have indicated (Butler and Swann (1977), Carpenter and Schulson (1978), (1981), Liu et al (1980) and Kinoshita et al (1982)) that disordering by mechanisms based on both uncorrelated recombination and replacement collision sequences can occur under electron irradiation. However, the mechanisms have not been studied systematically and there are many details which require clarification. Notable in this respect are the effects of temperature, orientation and accelerating voltage.

The present work was undertaken with two main objectives:

(i) To establish the mechanisms of disordering under electron irradiation, and

(ii) To identify the defect species responsible for reordering under electron irradiation.

With regard to these objectives five ordered alloy systems were chosen so that in addition to the effect of temperature, accelerating voltage and orientation, the effect of crystal structure, ordering energy, and defect mobility on the disordering response could also be investigated.

The ordered alloys investigated in the present work are Ni_3Al and Ni_3Fe which have an $L1_2$ superlattice based on the fcc structure, NiAl and FeAl which have a B2 superlattice based on the bcc structure and Mg_3Cd which has a DO_{19} superlattice based on the hcp structure. Ni_3Al, NiAl and FeAl are considered to be fully ordered up to their melting points (> 1500K) and have high vacancy migration energies (> 1.5 eV). In the absence of irradiation Ni_3Fe disorders readily above 786K and Mg_3Cd disorders readily above 426K, these alloys have vacancy migration energies of $\sim$1 eV and 0.5 eV respectively.

All the electron irradiations were carried out in a high voltage electron microscope equipped with heating and cooling stages. Electron diffraction was used to monitor changes in S.

CHAPTER 2

ORDER AND DISORDER

2.1. Theoretical Background Information

2.1.1. The Long-range Order Parameter, S.

In a substitutional solid solution the atoms will, in general, be arranged randomly amongst the lattice sites and the alloy is said to be disordered. If the interaction energy between unlike atoms, V_{AB}, is less than the average interaction energy between like atoms, V_{AA} and V_{BB}, then this provides the driving force for ordering to occur, i.e. the ordering energy V must be negative, where

$$V = V_{AB} - 1/2(V_{AA} - V_{BB}) \qquad (1)$$

In this condition the different atoms will become arranged in a particular distribution pattern amongst the lattice sites in which the number of A-B bonds is maximised and the alloy is said to exhibit long range order. An alloy exists in the ordered state at low temperatures because the atomic arrangement lowers the internal energy of the system and the entropy contribution to the overall free energy is small. However, on increasing the temperature the entropy contribution becomes more important and any process which increases the entropy and thus lowers the free energy will be more favoured. Since disordering is accompanied by an increase in configurational entropy, there is, for many ordered alloys, a critical temperature, T_c, above which long range order is destroyed. However, some alloys have an ordered structure which is stable up to the melting point, e.g. NiAl and FeAl which is indicative of a high ordering energy.

Bragg and Williams (1934) introduced a long-range order parameter, S, for a binary AB alloy in terms of the probability of finding a particular atom occupying a particular lattice site. They defined S such that

$$S = \frac{P_A^{\alpha} - X_A}{1 - X_A} = \frac{P_B^{\beta} - X_B}{1 - X_B} \qquad (2)$$

P_A^{α} and P_B^{β} are the probabilities of an A atom residing on an α 'ordered' site and a B atom residing on a β ordered site respectively.

X_A and X_B are the atomic fractions of the different species. Thus S is unity for perfect order and zero when the alloy is completely disordered.

2.1.2. Superlattice Structures

The structures of long-range ordered alloys can be conveniently described in terms of the sublattices of their parent disordered phases. For example, the long-range ordered structure of the B2 AB alloy develops when the atoms cease to be randomly distributed amongst the sites of the parent b.c.c. phase and occupy only one of the two simple cubic lattices. Thus, the ordered structure has a lower symmetry resulting in a change in the Bravais lattice. The diffraction patterns of ordered alloys exhibit extra diffraction maxima known as superlattice reflections to distinguish them from the fundamental reflections that are present even when the alloy is disordered. The nature of the changes in the diffraction pattern can be determined by calculation of the structure factor, F_{hkl} for the ordered and disordered atomic arrangements with the intensity of a diffracted beam, (h, k, l) being directly proportional to $|F_{hkl}|^2$. The structure factor equation adds together the amplitudes of the waves scattered by all the individual atoms in the unit cell, taking due account of their phase, it is of the form

$$F_{hkl} = \sum_{1}^{n} f_n \, e^{2\pi i \, (hu_n + kv_n + lw_n)} \qquad (3)$$

where $u_1 \, v_1 \, w_1, u_2 \, v_2 \, w_2 \ldots \; u_n \, v_n \, w_n$ are the co-ordinates of the atoms in the unit cell and $f_1, f_2 \ldots f_n$ are the atomic scattering factors.

Structure Factor Calculation for an AB B2 Alloy

Consider an AB alloy with a bcc structure whose atoms are arranged randomly, see Figure 2.1. There are two atoms in the unit cell at (0,0,0) and $(\frac{1}{2},\frac{1}{2},\frac{1}{2})$ each having an atomic scattering factor of $\frac{1}{2}(f_A + f_B)$. The structure factor is therefore equal to:

$$F_{hkl} = \tfrac{1}{2}(f_A + f_B) \, [1 + e^{\pi i (h + k + l)}]$$

when (h + k + l) = 2n, where n is an integer

$$F_{hkl} = f_A + f_B$$

when (h + k + l) = 2n + 1

$$F_{hkl} = 0$$

i.e. there are no reflections when (h + k + l) = 2n + 1.

On ordering the A atoms occupy the cube corners and the B atoms the cube centres, see Figure 2.2. The structure factor is now equal to

$$F_{hkl} = f_A + f_B\, e^{\pi i(h + k + l)}$$

when (h + k + l) = 2n

$$F_{hkl} = f_A + f_B$$

when (h + k + l) = 2n + 1

$$F_{hkl} = f_A - f_B$$

Thus direct evidence that ordering has taken place is the presence of superlattice reflections which occur in the diffraction pattern when (h + k + l) = 2n + 1. The superlattice reflections are weaker than the fundamental reflections because their intensity is proportional to the difference in the atomic scattering factors rather than the sum. It follows that as the degree of order is decreased the scattering factors of the atomic sites become more equal so that the intensity of the superlattice reflections diminishes. It is shown in Appendix I that the structure factors of a partially ordered AB, B2 alloy are equal to

$$F_{fund.} = f_A + f_B$$

$$F_{super.} = S(f_A - f_B)$$

Similar reasoning leads to the same result for ordered alloys based on the fcc and hcp structures. Thus the intensities of superlattice reflections are directly proportional to S^2.

2.1.3. Thermodynamic Considerations

The theoretical derivation of the variation of the long-range order parameter, S, with temperature has received a great deal of attention (For reviews see Muto and Takagi (1955), and Krivoglaz and Smirnov (1964)). However, the various thermodynamic and statistical models of Bragg and Williams (1934), Bethe (1935) and Peierls (1936) yield approximately equivalent solutions and so mainly the straightforward pioneering work of Bragg and Williams will be examined here.

The basic concept of the Bragg-Williams theory is that of long-range order. They calculated the relative probability of an atom being on a 'right' ordered site as compared to a 'wrong' one, by

Figure 2.1.

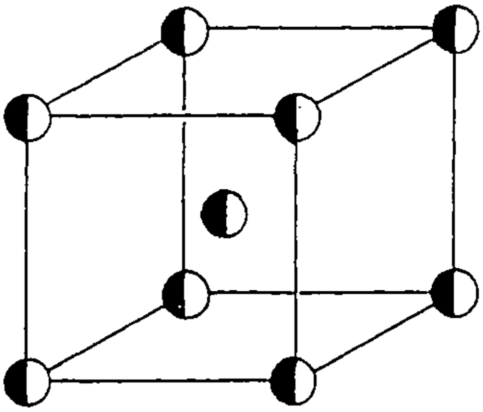

Arrangement of atoms in a disordered AB alloy with a b.c.c. structure.

Figure 2.2.

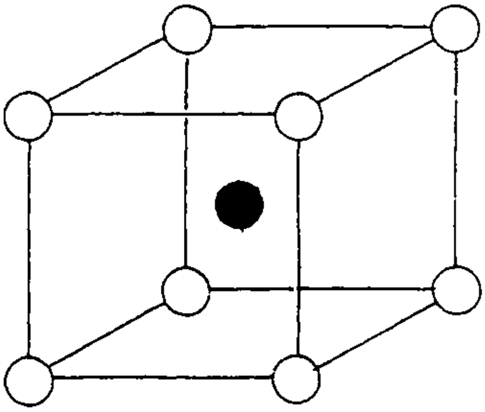

Arrangement of atoms in an ordered AB alloy with a B2 structure.

Figure 2.3.

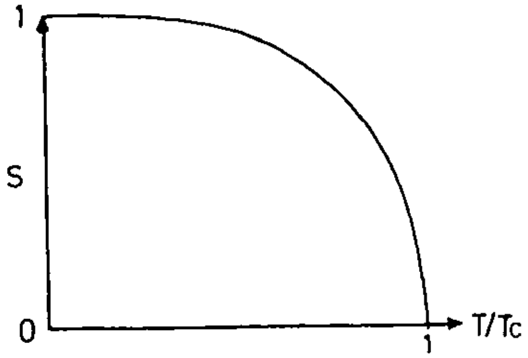

Figure 2.4.

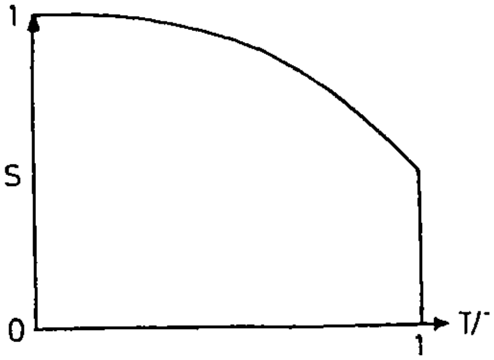

Variation of S with temperature as a function of T/T_c for an AB alloy (Figure 2.3.) and an AB_3 alloy (Figure 2.4.) as derived by Bragg and Williams (1934).

weighting the wrong site occupancy by the Boltzmann factor $\exp^{-V}/k_bT$. V was defined such that it is equal to the increase in the potential energy of the system when an atom is moved from an ordered to a disordered site. V is a function of S because when the alloy is fully ordered the creation of a wrong atom requires a definite amount of energy V_o. However as the alloy becomes disordered the amount of energy required to effect such an interchange becomes less until at S equal to zero, V must equal zero. Bragg and Williams assumed the simplest linear relationship between V and S, such that

$$V = V_oS \qquad (4)$$

For the simplest case of an AB alloy the temperature dependence of S is described by the relationship

$$S = \tanh V/4\,k_bT \qquad (5)$$

where k_b is Boltzmann's constant and T is the temperature. The solution of this equation as a function of T/T_c is shown in Figure 2.3. and gives a general idea of the way in which S varies with temperature. The degree of order is unity at low temperatures and decreases slowly as the temperature is raised. As the number of atoms occupying the wrong sites increases, disordering of the remainder becomes easier, and so S decreases more rapidly until all the long-range order is lost at T_c. This is a typical feature of a co-operative phenomenon. The theory predicts that for an AB alloy the ordering energy will be related to the critical temperature by the relationship

$$V_o = 4k_bT_c \qquad (6)$$

The results of the Bragg and Williams approximation for the variation of S with temperature in an AB_3 alloy are shown in Figure 2.4. In contrast to the AB alloy, S drops discontinuously at T_c to zero. The relationship between V_o and T_c is found to be

$$V_o = 4.9k_bT_c \qquad (7)$$

2.1.3. (i) Short Range Order

A weakness of the Bragg and Williams approach is that the ordering energy acting on any particular atom is assumed to be dependent on all the other atoms in the crystal. However, quantum theory shows that the forces between atoms decrease rather rapidly as the distance between them increases. Bethe (1935) was the first to consider the order-disorder transformation in terms of the potential energy between nearest neighbours in the ordered and disordered states. A short-range order parameter, σ, was introduced to define the atomic configuration in the immediate vicinity of an atom, i.e. the extent of local order is given by

$$\sigma = \frac{q - q_v}{q_m - q_v} \qquad (8)$$

where q is the fraction of unlike nearest neighbours, q_m is the fraction of unlike nearest neighbours in the fully ordered condition and q_v is the fraction of unlike nearest neighbours in the random (disordered) state. σ is defined in a similar manner to S, i.e. it varies from between zero and unity. However, it is possible to have no long-range order present in the alloy and yet still have a high degree of short range order, as the number of unlike nearest neighbour pairs remains larger than would be found in a random distribution. Evidence of short-range ordering occurs in the form of low intensity broad maxima which are superimposed on the diffraction pattern at the same angular position as the sharp superlattice maxima. However, these effects are very weak and can be easily masked by other forms of diffuse scattering, e.g. Compton scattering and temperature effects. Bethe's analysis has been used to determine the variation of S with temperature by assuming a group of atoms to be typical of the entire lattice. The result is approximately equivalent to that of Bragg and Williams for an AB alloy, as is the relationship between V_o and T_c which is equal to

$$V_o = \ln (z/z\text{-}2)\ k_b T_c \qquad (9)$$

where z is the number of nearest neighbours.

2.1.3.(ii) The Degree of Order-Disorder Transformations

The theoretical treatments discussed in the previous sections predict that the order-disorder transformation can occur with a discontinuous change in S at $T = T_c$ or with a continuous change in S through T_c, i.e. the transformation can be of the first or second order respectively. The order of a transformation is classified by the order of the lowest derivative of the free energy to show a discontinuity.

The first derivatives of the free energy, G, with respect to temperature and pressure are

$$\left(\frac{dG}{dT}\right)_P = -S \quad \text{and} \quad \left(\frac{dG}{dP}\right)_T = V \qquad (10)$$

In a transition of the first degree the entropies and volumes of the two phases differ so there are abrupt changes in these parameters at the transformation temperature. The transformation occurs between two well defined phases which can co-exist in equilibrium and a two phase region occurs on the phase diagram (see Figure 2.5.) In a transition of the second degree S and V are continuous through T_c and a discontinuity occurs in the second derivative of the free energy, viz;

$$\left(\frac{d^2G}{dT^2}\right)_P = -\left(\frac{dS}{dT}\right)_P = -\frac{C_P}{T} \qquad (11a)$$

$$\left(\frac{d^2G}{dP^2}\right)_T = \left(\frac{dV}{dP}\right)_T = -\beta V \qquad (11b)$$

That is, the values of the heat capacity at constant pressure C_p and of the isothermal compressibility β may differ in the two phases at equilibrium. In a second order phase transformation the two phases never co-exist and only one is present depending on whether the temperature is above or below the transition temperature. This is marked by a single line on the equilibrium diagram (Figure 2.6.)

Several first degree order transitions have been established experimentally. Studies on Cu_3Au (Rhines and Newkirk (1953)), Mg_3Cd (Davies and Stoloff (1964)), NiPt (Greenholz et al (1972)) and Ni_3Fe (Drijver and Van der Woude (1975)) have demonstrated the co-existence of ordered and disordered phases in equilibrium or a discontinuous change in S at $T = T_c$. However, it is much more difficult to establish that a transition is of the second order but there is experimental evidence to support the view that the A2 (bcc) to B2 transition in CuZn (Chipman and Warren (1950)) and FeCo (Normanton et al (1975)) are of this type. Guttman (1956) concluded from the available experimental results that transitions from B2 or DO_3 structures to disordered A2 may be second order and all others first order. He suggested that the reason for the differentiation is that in the B2 and DO_3 structures the nearest neighbours of any one atom are not nearest neighbours of each other and it is the greater degree of atomic interconnection in the f.c.c and h.c.p type structures which promotes a more abrupt first order transition.

2.1.4. The Kinetics of Order-Disorder Transformations

The simplest kinetic theory of homogeneous ordering was derived by Dienes (1955) using chemical rate theory. The theory was constructed entirely in terms of the long-range parameter, S, and is equivalent to that of Bragg and Williams at equilibrium. Dienes considered the order-disorder transformation in a binary stoichiometric alloy as a simple direct interchange reaction in the solid state. In this approach the rate of change of S with time was determined by considering the forward and backward movements between right (ordered) and wrong (disordered) lattice sites as a chemical reaction, i.e.

$$A^{\alpha} + B^{\beta} \underset{K_O}{\overset{K_D}{\rightleftharpoons}} A^{\beta} + B^{\alpha} \qquad (12)$$

where A^{α} and B^{β} represent A and B atoms respectively on ordered sites and A^{β} and B^{α} represent A and B atoms respectively on disordered sites. K_O and K_D are the rate constants for the ordering and disordering transformations respectively. In addition to the energy difference term, V, between the ordered and the disordered states, as defined by Bragg and Williams, Dienes introduced a term, E, which is equal to the activation barrier in going from the disordered to the ordered state. Thus the rate constants are equal to

$$K_D = \nu_1 \exp(-(E + V)/k_bT) \qquad (13)$$

$$K_O = \nu_2 \exp(-E/k_bT) \qquad (14)$$

where ν_1 and ν_2 are the vibrational frequencies of the atoms in the ordered and disordered states respectively. Assuming $\nu_1 = \nu_2$, the equilibrium constant of the reaction is equal to

$$K_e = K_D/K_O = \exp(-V/k_bT) \qquad (15)$$

By defining the number of right and wrong atoms in terms of S, Dienes produced the following equation for the rate of ordering

$$dS/dt = \nu \exp^{-E/k_bT}[X_AX_B(1-S)^2 - \exp(-V/k_bT)[S+X_AX_B(1-S)^2]] \qquad (16)$$

where X_A and X_B are the atomic fraction of A and B atoms respectively and ν is the average vibrational frequency. This differs from an ordinary second order chemical equation because V depends on S, thus the rate of the reaction depends on the amount of reaction that has already taken place. To produce a more dramatic fall in S as T_c is approached, the Bragg and Williams expression for the ordering energy (equation (4)) was modified such that

$$V = V_o(S + S^3/3) \tag{17}$$

Dienes solved the rate equations numerically as a function of S. The results for the AB and AB_3 alloy systems are shown in Figure 2.7. For the AB alloy the theory predicts that for any temperature below T_c, ds/dt is always positive, i.e. any fluctuations towards order will be accompanied by a lowering of the free energy of the system. Thus no nucleation event would be necessary for order to develop homogeneously from the disordered solid solution. For the AB_3 alloy, at temperatures below T_c but greater than T_i, ds/dt is negative when S is close to zero. This corresponds to a virtual disordering rate, the implication being that large fluctuations in S are required to produce a degree of order which is stable, i.e. only nuclei with a substantial degree of order will become stable. For $T < T_i$ the system becomes unstable to infinitesimal fluctuations in S and a homogeneous transformation becomes possible. Thus although the model is based on chemical rate theory it predicts two different mechanisms for the creation of an ordered superlattice:

i) a homogeneous transformation where order develops by repeated atomic interchange which occurs simultaneously in all parts of the crystal,

ii) a nucleation and growth mechanism where the formation of the superlattice begins at discrete centres and continues outwards until all the disordered regions are consumed.

Factors such as strain energy, anisotropy, volume changes and surface energy are not taken into account in the theory, so that whilst homogeneous transformations are predicted nucleation and growth may be the preferred mechanism. Both types of mechanism are observed experimentally in real systems. It has been proposed that in NiPt (Greenholz et al (1972)) and Ni2V (Tanner (1972)) the ordering mechanism changes from nucleation and growth to homogeneous as the temperature is lowered.

Vineyard (1956) investigated homogeneous ordering kinetics by considering the motion of the atoms between the 'wrong' and 'right' lattice sites. For the energetically favourable vacancy interchange mechanism, an expression for the kinetics of ordering in an AB alloy can be written as: (Penisson and Bourret (1975))

$$\frac{ds}{dt} = 2C_V \nu_V [\sinh(\frac{T_c}{T})\ S - \cosh(\frac{T_c}{T})\ S] \qquad (18)$$

where C_V is the vacancy concentration and is proportional to $\exp(-E_V^F/k_bT)$ and ν_V is the vacancy jump frequency and is proportional to $\exp(E_V^M/k_bT)$. E_V^F and E_V^M are the vacancy formation and migration energies respectively. The solutions of the rate equations of Vineyard are qualitatively similar to those of Dienes. From the models which define equations (16) and (18) it can be seen that two factors determine the kinetics of ordering:- the thermally activated diffusion processes concerned with the atomic redistribution which define a "rate constant" and the difference in the free energies which define a "driving force" term. Assuming the activation energies for vacancy formation and migration are independent of S then Vineyard's model predicts a symmetrical variation of ds/dt with S, resulting in a sigmoidal S versus time curve at constant temperature (Figure 2.8.). However, in the model of Dienes the ordering energy V is inextricably linked with S which causes an asymmetrical variation of ds/dt with S. This implies a more parabolic relationship of S with time, at constant temperature (Figure 2.9.)

2.1.5. Diffusion in Ordered Alloys

It is generally found experimentally (Smithells (1976)) that diffussivities measured in alloys in the ordered state are lower than in the disordered state, i.e. $(E_V^F + E_V^M)_{ORD.} > (E_V^F + E_V^M)_{DIS.}$ (where E_V^F and E_V^M are the vacancy formation and migration energies respectively). A possible explanation for this is that the diffusion mechanism is more complex than nearest neighbour vacancy interchange because in an ordered alloy this usually produces disordering. Successive jumps of a vacancy away from its initial site will increase the amount of disorder, and hence the configurational energy will induce the vacancy to retrace its steps to its original site, resulting in no long range diffusion. Therefore, it has been suggested (Elcock (1959)) that the diffusion mechanism in ordered alloys involves a correlated jump cycle and although there is disordering during the cycle there is no net disorder after the cycle has been completed. Girifalco (1964) related the vacancy formation and migration energies to the degree of long-range order, S, and found that

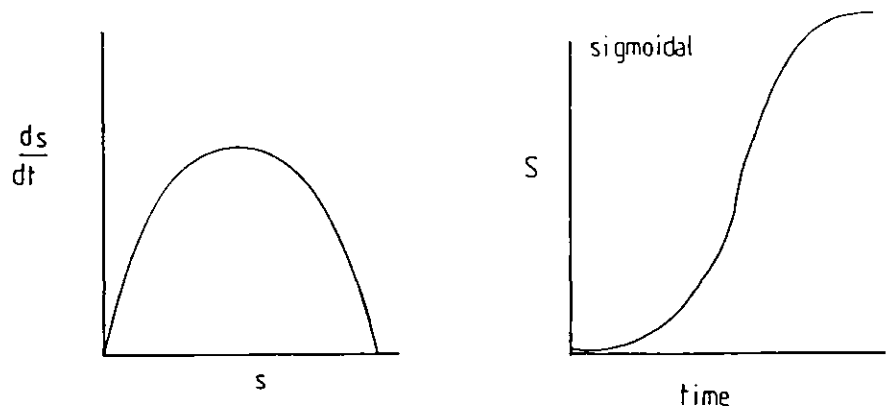

Figure 2.8. Symmetrical variation of ds/dt with S resulting in a sigmoidal S versus time curve at constant temperature.

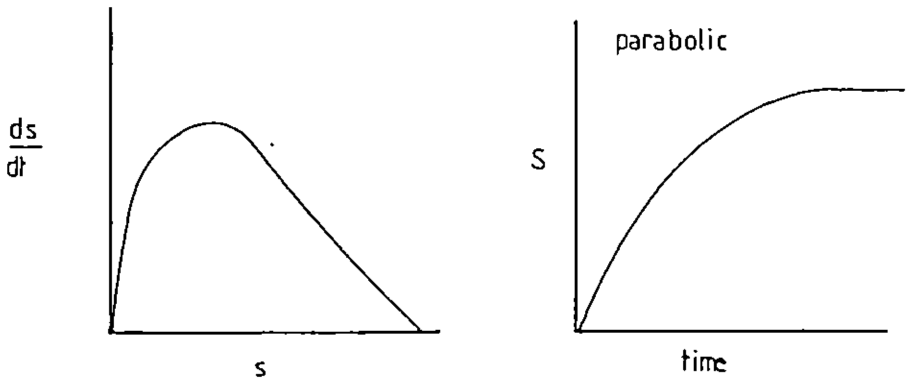

Figure 2.9. Asymmetrical variation of ds/dt with S resulting in a parabolic S versus time curve at constant temperature.

the greatest increase on ordering took place in the vacancy migration energy. The relationship is of the form

$$E_v^M = E_{vd}^M (1 + C S^2) \qquad (19)$$

where E_{vd}^M is the activation energy for vacancy migration in the disordered state and C is a constant.

2.1.6. Domains and Antiphase Domain Boundaries

An ordered alloy is defined such that each atom species is assigned to a particular sublattice of the disordered alloy. However, in general a given atomic species will not occupy the same sublattice throughout a grain. The volume over which the sublattice is constant, is an antiphase domain (APD). Where two domains meet and there is a change in sublattice occupancy and an antiphase domain boundary (APB) is produced. This may occur as the result of growth and impingement of different domains, or as the result of certain dislocation movements. An APB is defined by the plane in which it lies, and its antiphase vector $\underline{R}$. $\underline{R}$ is the displacement through which the ordered crystal on one side of the APB must be moved to bring it into coincidence with the ordered crystal on the other side of the APB. The creation of an APB involves the formation of wrong neighbours and so the potential energy of the boundary is higher than that of the atoms within the domains. The energy per unit area is calculated by the summation of the energies of the extra wrong bonds created at the APB. Considering only nearest neighbour interactions and assuming complete long-range order, this may be written as

$$E_{APB} = \left(\frac{\text{energy}}{\text{area}}\right) = \left(\frac{\text{atoms}}{\text{area}}\right)\left(\frac{\text{wrong bonds}}{\text{atom}}\right)\left(\frac{\text{energy}}{\text{wrong bond}}\right) \qquad (20)$$

B2 Superlattice

For the simplest case of a B2 superlattice only two domains exist and these are related by the lattice vector ½<111>. Cupschalk and Brown (1968) calculated the APB energy as a function of orientation and found that there are no orientations of zero energy and additionally there are only minor variations from plane to plane, i.e. the APB energy is isotropic. Non-crystalline boundaries have been observed experimentally in CuZn (Cupschalk and Brown (1968)), FeCo (Buckley and Rajkovic (1979)) and VMn (Sakauchi et al (1979)).

$L1_2$ Superlattice

In an AB_3 alloy with an $L1_2$ superlattice, the A atoms occupy the corner sites and the B atoms the face centred sites. Three other equivalent unit cells can be formed by allowing the A atoms to occupy opposite face centred sites and the B atoms the remainder. The four types of domain are related by the displacement of ½<110>. Flinn (1960) calculated the APB energy as a function of orientation and found that since there are no wrong nearest neighbours when the APB lies in the (001) plane, boundaries with this configuration will have a very low energy. Although second nearest neighbour interactions cause the energy to be non-zero, it is predicted that the APB energy of $L1_2$ alloys will be strongly anisotropic. This prediction has been verified by transmission electron microscopy for Cu_3Au and Ni_3Mn which shows that the domains exhibit a (001) texture (Marcinkowski (1963)).

2.1.7. Antiphase Domain Coalescence

A mosaic structure of antiphase domains is formed when the disordered material is completely consumed by the initially separated ordering domains. During prolonged annealing the larger domains grow at the expense of the smaller ones to minimise the antiphase boundary area. English (1966) has demonstrated the similarity between domain coarsening and classical grain growth and has shown that

$$\frac{dD^n}{dt} = k\ M\ \sigma = \text{constant} \qquad (21)$$

where D is the domain size after time t, M is a temperature dependent mobility, σ is the free energy of the antiphase boundary, k is a constant and n is an exponent which is equal to two. Integration of the above equation gives

$$D^2 - D^2_o = k't \qquad (22)$$

where D_o is the domain size at t = o. Such a relationship with n = 2 has been observed experimentally in a number of systems, e.g. FeCo-2V (English (1966), Rogers et al (1975)), Cu_3Au (Poquette and Mikkola (1969)), Ni_3Fe (Calvayrac and Fayard (1973), Morris et al (1976)) and VMn (Sakauchi et al (1979)). However, it has been suggested (Mikkola and Rundman (1972)) that the exponent is only equal to two when the equilibrium degree of order (S_{eq}) has been achieved in the structure. There is experimental evidence to support this and n has been found to be both greater and less than two when $S < S_{eq}$ in the above experimental systems. A rapid period of domain growth ($n < 2$) has been attributed to the system ordering by the rapid growth of the domains in the disordered matrix. Whereas a reduced rate of domain growth ($n > 2$) has been attributed to the system attaining the equilibrium degree of order by local fluctuations in composition (in a manner similar to spinodal decomposition), and thus domain growth during this time is reduced. As in grain growth (Gordon and El-Bassyouni (1965)) another factor which can alter the value of n is the presence of impurities which can modify the APB energy and mobility.

2.2. The Ordered Alloys Investigated in the Present Work

2.2.1. Crystal Structure

2.2.1.(i) Mg_3Cd

Mg_3Cd transforms from a disordered hexagonal structure to an ordered DO_{19} structure below the critical temperature, T_c, of ∿153°C. (Welber et al (1953), Davies and Stoloff (1964)). The DO_{19} structure is composed of four interpenetrating sublattices of the close packed hexagonal structure and the unit cell is composed of Cd atoms at (0,0,0) and (1/3,2/3,1/2) and Mg atoms at (1/2,0,0), (0,1/2,0) (1/2,1/2,0), (1/3,1/6,1/2), (5/6,1/6,1/2) and (5/6,2/3,1/2), see Figure 2.10. It has been established that the order-disorder transformation is of the first order by the observation of a two phase (ordered and disordered) region below T_c using X-ray diffraction (Davies and Stoloff (1964)).

2.2.1.(ii) Ni_3Al and Ni_3Fe

Ni_3Al and Ni_3Fe have an ordered $L1_2$ structure which is composed of four interpenetrating simple cubic lattices. Within this structure, based on the composition A_3B, A atoms occupy face centre sites and B atoms occupy corner sites (Figure 2.11.) Thus the unit cell is made up of A atoms at (1/2,1/2,0), (1/2,0,1/2), (0,1/2,1/2) and a B atom at (0,0,0).

It has been shown using high temperature X-ray diffraction that Ni_3Al is still ordered up to 1320°C. (Stoeckinger and Neumann (1970)). This suggests that if disordering occurs it does so within 65°C of the melting point.

Calvayrac and Fayard (1972) found that a hysteresis exists around the order-disorder transition temperature in Ni_3Fe, such that order develops in an initially disordered alloy below 503°C but the transition temperature for the reverse process is 10K higher. It has been established using Mössbauer spectroscopy (Drijver and Woude (1975)) that the phase transition is of the first order.

2.2.1.(iii) NiAl and FeAl

NiAl and FeAl have an ordered B2 structure which is composed of two interpenetrating simple cubic lattices. Within this structure, based on the composition AB, A atoms occupy corner sites and B atoms occupy body centre sites (Figure 2.12). Thus the unit cell is made up of an A atom at (0,0,0) and a B atom at (1/2,1/2,1/2).

The fully ordered nature of stoichiometric NiAl near room temperature is well documented and has been verified by X-ray measurements (Cooper (1963a)) and nuclear magnetic resonance (West (1964)). It is generally accepted that the alloy is fully ordered up to its melting point of 1638°C. Evidence for this is its highly ordered nature at lower temperatures due to a degree of covalent bonding (Cooper (1963b)) and that no significant changes have been found in S dependent physical properties with temperature. The physical properties measured include, elastic constants up to 800°C (Wasilewski (1966)) and diffusion coefficients in the range 1050-1350°C (Berkowitz et al (1954)) and 977-1393°C (Hancock and McDonnell (1971a)).

Taylor and Jones (1958) have shown using high temperature X-ray diffraction that FeAl is fully ordered up to 1250°C which is just below (∿ 5°C) the solidus temperature.

2.2.2. Physical Properties

Table 2.1. lists certain physical properties of each of the ordered alloys investigated in the present work.

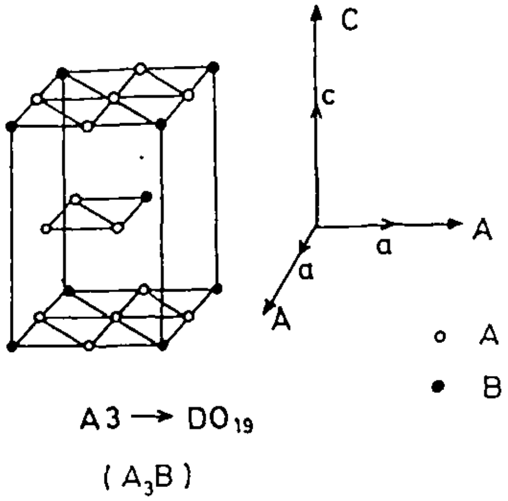

Figure 2.10. DO_{19} Superlattice

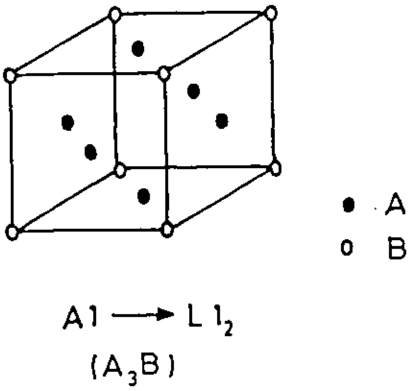

Figure 2.11. $L1_2$ Superlattice

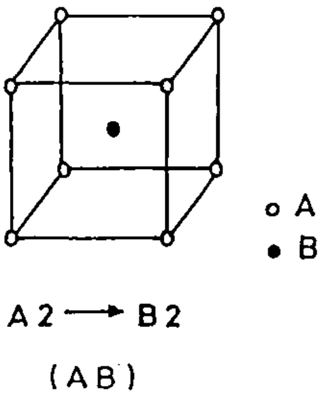

Figure 2.12. B2 Superlattice

Table 2.1.

Physical Property	Mg_3Cd	Ni_3Al	Ni_3Fe	NiAl	FeAl
Disordered Structure	h.c.p	f.c.c	f.c.c	b.c.c	b.c.c
Ordered Structure	DO_{19}	$L1_2$	$L1_2$	B2	B2
Critical Temperature (K)	426	~1658	776	~1911	~1528
Melting Point (K)	763	1658	1728	1911	1528
Lattice Parameter (Å)	a = 6.3 c = 5.08	3.56	3.55	2.89	2.89
Activation Energy (eV)					
Self diffusion	DIS. 0.56 ORD. 0.71 (Smithells 1976)	ORD. 3.15	DIS. 1.99 ORD. 2.06 (Suzuki et al 1959)	ORD. 3.19	ORD. 2.52
Vacancy migration		1.65		1.87	1.61
Vacancy formation		1.49 (Hancock et al 1971b)		1.39 (Hancock et al 1971a)	0.91 (Riviere et al 1975)
Interstitial migration				0.1 (Liu et al 1981)	1.36 (Riviere et al 1974)
Debye Temperature K		390 (Stoeckinger et al 1970)	380 (Tomokiyo et al 1980)		
Ordering Energy (eV) Calculated using equations (6) and (7)	0.18	0.69	0.33	0.66	0.53
APB energy (S=1) (mJm^{-2})		$\frac{1}{2}\langle 110\rangle\{111\}$ 250-350 (Taunt et al 1974) $\frac{1}{2}\langle 110\rangle\{100\}$ 47-64 (Rand et al 1973)	$\frac{1}{2}\langle 110\rangle\{111\}$ 54 ± 5 (Koneva et al 1973)	$\frac{1}{2}\langle 111\rangle\{110\}$ 200 ± 40 (Campany et al 1972)	

CHAPTER 3

The following chapter is divided into two distinct sections; in the first the fundamental aspects of electron irradiation damage in metals are discussed and the basic physical principles involved are introduced. In the second a review is made of the literature concerning the effects of electron irradiation on ordered alloys.

3.1. The Fundamental Aspects of Electron Irradiation Damage in Ordered Alloys

3.1.1. The Atomic Displacement Process

The Transferred Energy E_T:

The inelastic scattering of an electron beam incident on a crystalline solid is due to electron-electron interactions and electron-atom interactions. The former can be neglected in metals as the resulting perturbations in electronic charge are quickly removed by the free electrons in the conduction band. The electron-atom collision can be considered as a coulombic interaction between the electron and the atom nucleus. The energy transferred to the target atom can be calculated using the laws of conservation of energy and momentum treating the electron relativistically, since it has a velocity close to that of light.

Seitz (1956) has shown that the energy transferred is equal to

$$E_T = \frac{2E(E + 2mc^2)\ \sin^2\psi/2}{Mc^2} \qquad (23)$$

where E and m are the electron energy and rest mass respectively, c is the velocity of light, M is the mass of the target atom and ψ is the angle through which the electron is scattered. The maximum value of E_T (known as E_{Tmax}) clearly occurs when $\psi = \pi$. The recoil angle of the atom is equal to

$$\theta = \pi/2 - \psi/2 \qquad (24)$$

Therefore the following relationship holds between the energy transferred to an atom and its scattering angle:

$$E_T = E_{Tmax}\cos^2\theta \qquad (25)$$

Threshold Displacement Energy E_d

The simplest treatment of displacement damage assumes that the probability for displacement, $P(E_T)$, is a simple step function of the kinetic energy transferred to the atom, E_T. This is shown in Figure 3.1.

Figure 3.1

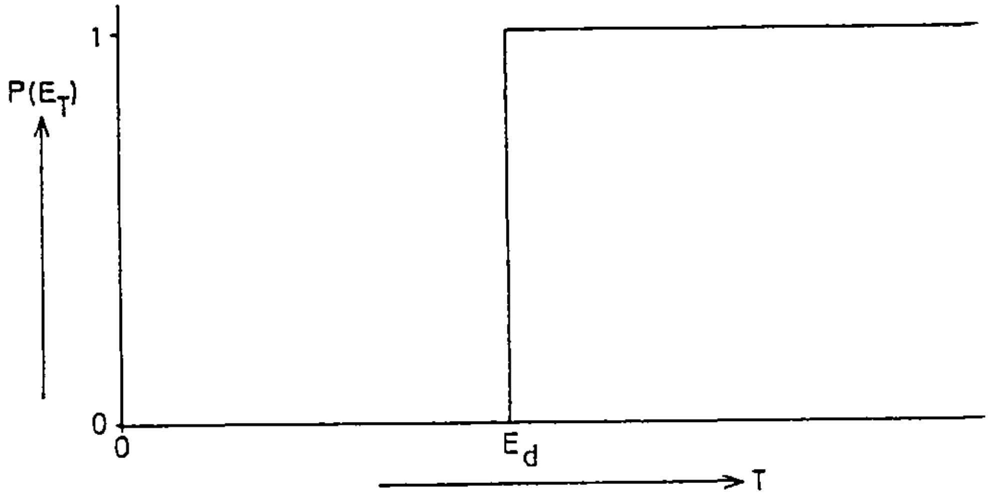

E_d is the threshold displacement energy and is equal to the minimum energy required to displace an atom from its lattice site. The minimum observed displacement energies in metals are between ∿10 - 30 eV (Gittus (1978)). These energies are significantly higher than the bonding energies (which in metals are between ∿1 - 3 eV) because in order to displace an atom in a close packed crystalline lattice several bonds must be broken and others seriously perturbed around the normally unoccupied interstitial site. It is clear that E_d will be orientation dependent since it will be more easy to move the displaced atom in directions where the lattice potential is at a minimum, i.e. between neighbouring atoms rather than directly at the centre of a neighbouring atom. This situation is shown schematically in Figure 3.2.

The Number of Displaced Atoms

The number of primary displacements is given by

$$K_p = \phi t \sigma_p \qquad (26)$$

where ϕ is the incident flux, t is the duration of the irradiation and σ_p is the primary displacement cross-section. The 'cross-section' gives the probability of an interaction occurring.

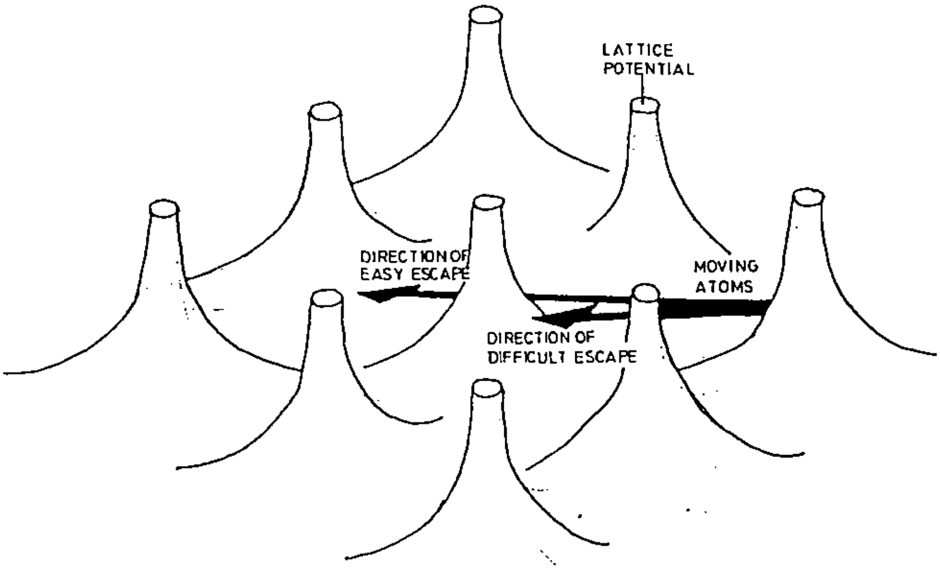

Figure 3.2. Escape of a lattice atom from its potential well (Schematic).

It is defined as the average number of individual processes occurring per target atom per incident particle.

$$\therefore \ \sigma_p = \frac{\text{number of p.k.o/unit volume}}{\text{number of atoms/unit volume x number electrons/area}}$$

The units of the displacement cross-section are those of area, the practical unit is the barn which is equal to $10^{-28}m^2$. Calculation of σ_p requires the use of scattering theory based on relativistic quantum mechanics and integration of all the possible recoil directions of the struck atom. The probability that an atom is recoiled into the direction $\underline{n}_r$ is given by the differential recoil cross-section $d\sigma_r/dw$, where w is the solid angle defined by the scattering angle Θ.
For light elements (up to $Z = 28$) $d\sigma_r/dw$ is given with sufficient accuracy by the analytical formula of McKinley and Feshbach (1948). For the scope of the present work it is sufficient to refer to the following two properties of $d\sigma_r/dw$:

(i) $d\sigma_r/dw$ has its minimum in the forward direction, $\Theta = 0$, and increases rapidly with increasing Θ. For $\Theta \rightarrow \pi/2$ (which is the maximum recoil angle) $d\sigma_r/dw$ diverges as $\cos^{-3}\Theta$.

(ii) The increase in the recoil cross-section for increasing Θ becomes more pronounced at larger electron energies.

To illustrate these properties consider a nickel lattice with a uniform displacement threshold of 22 eV. This corresponds to a minimum incident electron energy of 420 keV. When $E_T > E_d$ the maximum angle, Θ_M, that a displaced atom can recoil through can be determined from equation (25). The probability of an atom recoiling at an angle Θ_M to the forward direction is given by the ratio $d\sigma_r/dw(\Theta = \Theta_M)/d\sigma_r/dw(\Theta = 0)$ which is calculated using the McKinley-Feshbach formula. The results of these calculations for three electron energies are shown in Table 3.1.

It can be seen that for E significantly above E_d the main contribution to σ_d stems from large angle recoil events with Θ close to Θ_M. Even at energies not very much above E_d recoils are not favoured in the forward direction.

Table 3.1.

Electron energy keV	E	500	700	1000
Maximum Energy transferred eV	E_T	28	44	74
Maximum Recoil Angle $\theta°$	θ_M	27	45	57
Probability of recoil at θ_M to forward direction	$\frac{d\sigma_r/dw(\theta = \theta_M)}{d\sigma_r/dw(\theta = 0)}$	2.8	11	48

Secondary Displacements

In a simple model of the crystal lattice the atoms are represented by hard spheres sitting at their lattice sites. A primary knock-on is represented by a similar hard sphere moving through the lattice in a particular direction. Using classical mechanics, the maximum energy which can be transferred in a secondary 'head-on' collision, $E_s$max, is equal to

$$E_s\text{max} = \frac{4M_1M_2}{(M_1 + M_2)^2} E_1 \qquad (27)$$

where M_1 and E_1 are the mass and energy of the primary knock-on respectively and M_2 is the mass of the struck atom. Thus when the energy transferred to the primary knock-on is greater than E_d it is possible for one electron-atom collision to result in more than one displacement. Kinchin and Pease (1955) used the above result to estimate the number of secondary displacements, n_d, due to a primary recoil of energy E. The basic result is

$n_d = 1$ when $E_d \leqslant E \leqslant 2E_d$

$n_d = E/2E_d$ when $E > 2E_d$

Thus the total number of atomic displacements, K, is equal to

$$K = \phi t \, \sigma_p \, n_d \qquad (28)$$

$\sigma_p n_d$ is equal to the total displacement cross-section, σ_d, this has been evaluated by Oen (1973) using numerical integration techniques for a range of elements. For example, under 1 MeV irradiation the primary displacement cross-section of aluminium is increased by a factor of 1.3 due to secondary displacements.

3.1.2. Threshold Displacement Energy Determination

The threshold displacement energy is generally measured by electron irradiation using one of two methods (Vajda (1977)):

(i) by monitoring changes in electrical resistivity in an electron accelerator.

(ii) by directly observing visible displacement damage (point defect clusters) in the high voltage electron microscope (HVEM). Measurements are made as a function of accelerating voltage, the threshold voltage is determined by extrapolation to zero damage rate and E_d is then calculated from equation (23).

The first method is the classical technique for E_d determination; irradiations are generally carried out at liquid helium temperature (∿4K) to preserve the defect configuration that exists immediately after the damage event. The effect of orientation is investigated using single crystal specimens. The specimen preparation is the main disadvantage of this technique. Resistivity measurements of the damaged specimens after annealing at different temperatures are useful in determining the activation energies of various recovery processes.

The main advantage of the second method is that it is relatively easy to study the effect of orientation, using electron diffraction to orientate the specimen. However, the sample thickness can have an important influence on the results of such experiments. This is because the surfaces of the specimen act as sinks for the displaced atoms, creating a denuded layer at each surface where no loops are formed. Makin (1970) has derived an equation for the width of a defect-free zone, x, which is of the form

$$x = 0.66\lambda \left(\frac{\nu_i}{\sigma_d Z \phi}\right)^{1/4} \qquad (29)$$

where λ is the jump distance, ν_i the interstitial jump frequency, Z the recombination volume and ϕ the electron flux. Assuming a true threshold of 395 kV for Cu the effect of foil thickness on the apparent threshold voltage required to produce defect loops is shown in Figure 3.3.

The effect of temperature must also be considered. In most experiments irradiation is carried out at ambient temperatures and the results are interpreted in terms of the thermally activated migration of free interstitials. However, cluster formation has also been observed in Cu and Ni (Urban (1973)) at liquid helium temperatures when thermally activated migration of defects is not possible. Such observations have been attributed to radiation-induced diffusion (Urban and Seeger (1974)).

There are two other factors which can lead to erroneus results. Light impurity atoms which when present in the metal can lead to a determination of a threshold energy which is lower than the true displacement threshold (Bauer and Sosin (1964)). Also displacements may occur at an angle Θ to the incident electron beam where the threshold energy may be significantly lower. This is known as the "$\cos^2$" effect since the amount of energy transferred is reduced by the factor $\cos^2\Theta$ (equation (25)). Therefore only the lowest measured threshold is likely to be the true threshold for a specific direction in the crystal.

More recently a novel technique of E_d determination has been developed which incorporates the advantages of the other methods. Specimens are irradiated in the HVEM and changes in electrical resistivity are monitored at liquid helium temperatures in-situ (King et al (1980)).

3.1.3. Orientation Dependence of E_d

The experimentally determined threshold displacement energies of the constituent elements of the alloys used in this investigation are presented in Table 3.2. It can be seen that E_d varies up to a factor of approximately 2, and exhibits a minimum in the close packed directions close to <110>, <100> and <11$\bar{2}$0> in the f.c.c, b.c.c and h.c.p metals respectively.

3.1.4. Temperature Dependence of E_d

Experimental evidence for the temperature dependence of the threshold displacement energy, E_d, is relatively limited, with most of the work having been carried out on <110> Cu. The results of recent investigations (Drosd et al (1978), Yoshida and Urban (1980)) are shown in Figure 3.4. The experimental evidence indicates that E_d decreases as the temperature is increased. With respect to the explanation of such a temperature dependence two conceptually separate processes must be considered:

(i) the probability that the displaced atom escapes correlated recombination,

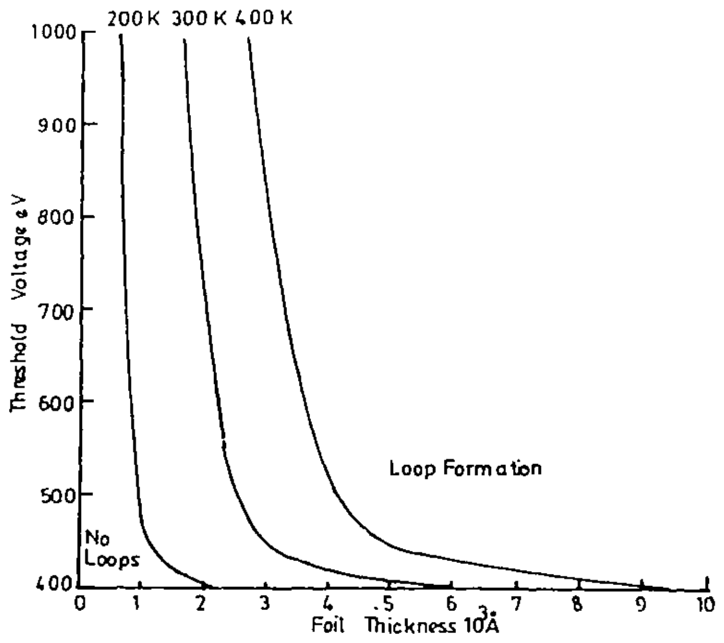

Figure 3.3. The predicted variation in apparent threshold voltage required to produce clusters in copper as a function of foil thickness, assuming that the true threshold is 395 kV. (Makin 1971b).

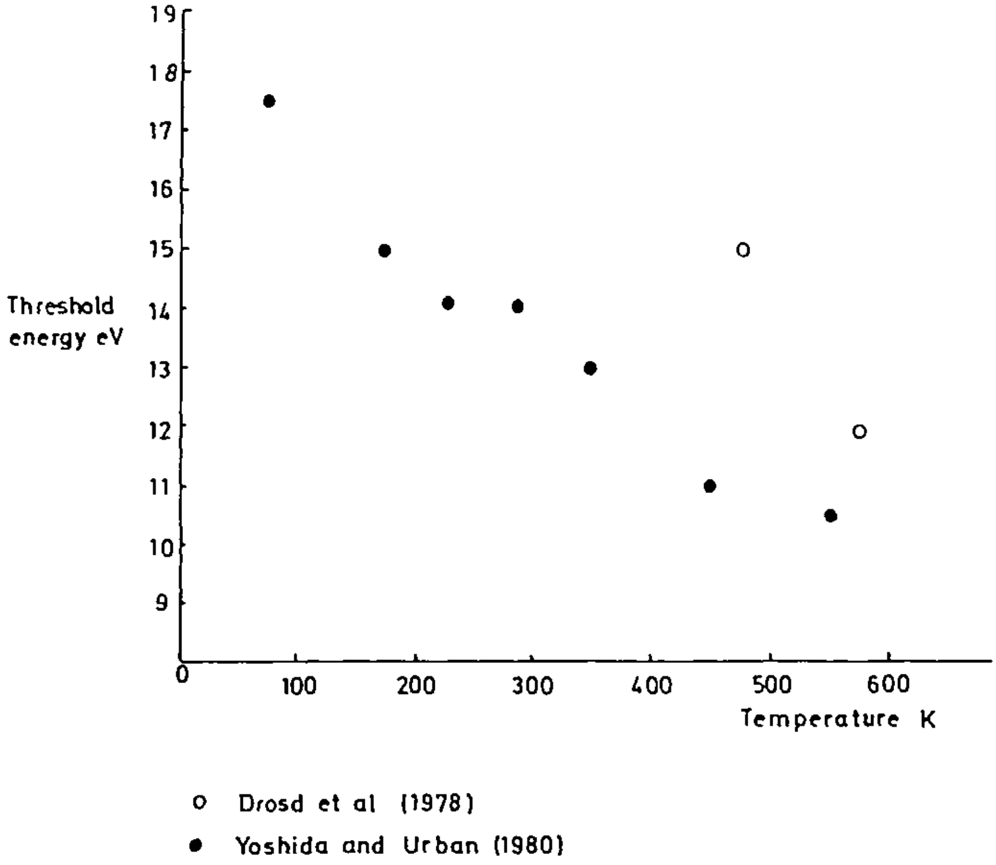

Figure 3.4. Experimentally observed variation in the threshold displacement energy of <110> orientated copper with temperature.

Table 3.2. Orientation Dependence of Threshold Displacement Energy

Metal	Structure	Orientation	E_d (eV)	Technique	Reference
Ni	f.c.c	<110>	23	)HVEM	Bourret
		<111>	28	)	(1971)
		<100>	31	)	
Al	f.c.c		16	Accelerator	Iseler et al (1967)
			17	HVEM	Wolfenden (1972)
Fe	b.c.c	<100>	20	)Accelerator	Lomer and
		<110>	30	)	Pepper (1967)
		<111>	30	)	
		<100>	17	)Accelerator	Maury et al
		<110>	30-35	)	(1976)
		<111>	20	)	
Mg	h.c.p	<0001>	14	)HVEM	Hossain and
		<10$\bar{1}$0>	11	)	Brown (1977a)
		<1$\bar{2}$10>	9	)	
		<0001>	13	)HVEM	Karim et al
		<10$\bar{1}$0>	10	)	(1978)
		<11$\bar{2}$0>	<10	)	
Cd	h.c.p	<0001>	11	)HVEM	Karim et al
		<10$\bar{1}$0>	9	)	(1978)
		<11$\bar{2}$0>	8	)	

(ii) the actual displacement event itself.

There is experimental evidence (Becker et al (1972)) which indicates that in high purity Cu the probability of interstitial vacancy recombination increases with decreasing temperature. This effect would support an explanation based on the first process. There has been little discussion concerning the effect of temperature on the displacement event itself. However, in a recent computer simulation of low energy damage events in Cu, using the molecular dynamics technique, Tenenbaum (1978) has shown that there is a decrease in the threshold displacement energy with increasing temperature. Although both these observations can explain the experimental results it is clear that the situation is complex and requires more investigation.

3.1.5. Focusing Effects

Another process which can have important consequences in radiation damage studies is the mechanism by which displaced atoms can travel large distances, without thermal activation, by focused collision sequences. When the energy of a primary knock-on becomes small enough the lattice is able to impose rigid conditions upon the possible modes of momentum transfer. There are two types of sequence:

(i) 'Silsbee' (1957) or momentum focusing, where momentum is focused from the collision by the correlated motion of atoms in a particular direction.

(ii) Replacement collision sequences (R.C.S's) where the momentum focusing results in mass transport and each atom in the collision range is replaced by its predecessor.

In Silsbee focusing momentum is transferred down the atom chain until either all the energy is dissipated or the chain strikes a discontinuity such as a surface. In so far as the damage structure is concerned, the former process will dissipate energy without defect formation whereas the latter will create a Frenkel defect at a discontinuity. Replacement collision sequences, on the other hand, will increase the distance between an interstitial and its vacancy. Although this will have no further effect in monatomic solids, in ordered alloys a line of disorder can be introduced.

3.1.5. (i) Theoretical Considerations of Focusing

The mechanism of momentum focusing was first treated analytically by Silsbee (1957) who considered focusing in a close packed direction as a series of elastic collisions between hard spheres of radius R. The effect is shown schematically in Figure 3.5. The initial separation of the spheres is denoted by D. If the first atom receives a momentum vector along the direction AP making an angle Θ_1 with the line of centres AB then a hard sphere collision occurs when the centre of atom 1 reaches the point P. The second atom moves off along PB which makes an angle Θ_2 with the line AB. For small angles it can be shown that;

$$(D - 2R)\Theta_1 = -2R\ \Theta_2$$

and a focusing parameter f can be defined such that:

$$\frac{\Theta_2}{\Theta_1} = (-f)$$

then:

$$f = \frac{D}{2R} - 1$$

If $D/R < 4$ and $f < 1$, the angles between successive collisions will converge to zero and then momentum transfer will occur with 100% efficiency. However, if $D/R > 4$ and $f > 1$, the angles between successive collisions will increase and the atoms will cease to collide. Considering the rows of atoms in a crystal, f will be least for the closely packed rows which have the smallest value of D_{hkl}. There will therefore be a tendency for focusing to occur along these directions.

In the hard sphere model the sphere radius is defined as a function of the collision energy, since the penetration between two atoms is greater at higher energies than at lower energies (Liebfried (1959)). The relationship is of the form

$$R = 1/2b\ \log_e\ (2A/E) \qquad (30)$$

where A and b are Born-Mayer constants of the lattice potential (Born and Mayer (1932)) and E is the collision energy. Thus the critical focusing energy, E_F^{hkl}, below which R is large enough for focusing to occur in the <hkl> direction can be defined when $D_{hkl} = 4R$, i.e.

$$E_F = 2A\ \exp(-\ D_{hkl}/2b) \qquad (31)$$

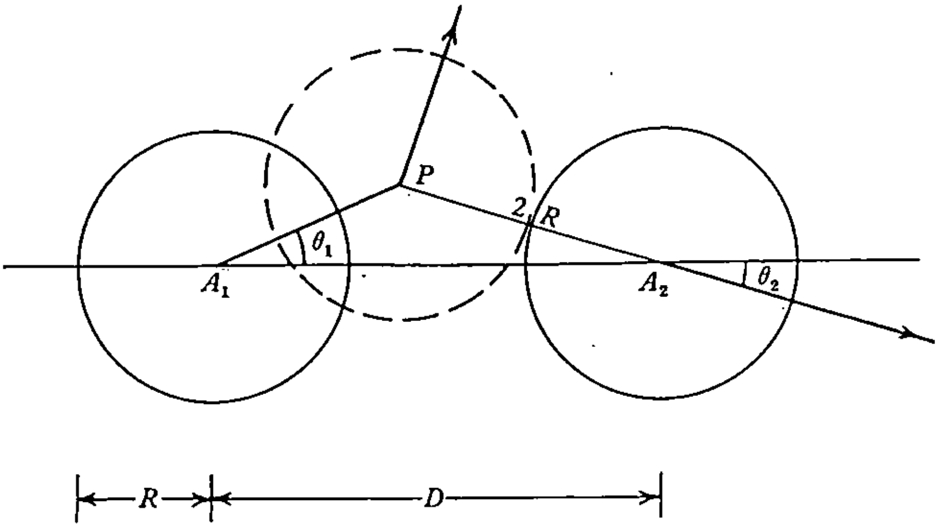

Figure 3.5. The simple focusing process.

The calculated values of the <110> focusing energy for certain f.c.c crystals, listed in Table 3.3. were evaluated using Brinkmans empirical equations to calculate the Born-Mayer constants (see Appendix II).

Table 3.3.

Element	Calculated values of E_F^{110}(eV)
Ni	35
Cu	40
Ag	87
Au	620

It can be seen that for elements of medium atomic weight, focusing is important at relatively low energies (< 100 eV).

Thompson (1969) has discussed the mechanisms of atomic collisions developing the ideas of Silsbee to allow for the transport of mass in a similar manner to momentum, whereby atoms in a collision sequence are replaced by their predecessor. The atomic collisions were considered to be 'soft' in nature, i.e. there is interaction between the lattice potentials. An important result to come from this work is the determination of a critical replacement energy, E_R^{hkl}, below which replacement collision sequences cannot occur. This is defined as

$$E_R^{hkl} = 1/2A \exp(-D_{hkl}/2b) \qquad (32)$$

where $E_R^{hkl} = 0.25\ E_F^{hkl}$. Thus if a primary displacement has an energy which lies in the interval $E_R^{hkl} < E < E_F^{hkl}$, it can generate a replacement collision sequence.

3.1.5. (ii) Attenuation of Focused Collision Sequences

The attentuation of focused collision sequences has been discussed by Nelson et al (1962) and Sanders and Fluit (1964). Three important ways in which a collision sequence can lose energy have been identified:

(i) Energy lost directly to the rings of atoms surrounding the focusing axis; this effect may be enhanced by thermal vibration of the lattice ($= \Delta E_1$).

(ii) Scattering of energy out of the focusing line by misalignment of the atoms caused by lattice vibration ($= \Delta E_2$).

(iii) In crystals containing atoms of differing mass, energy transfer from one atom to the next is inefficient.

Lattice Vibration Effects

Nelson et al (1962) derived analytical energy loss equations for the first two mechanisms of energy loss. The Debye-Waller factor (see for example Klug and Alexander (1954)) was used to calculate the mean squared displacement of an atom from its equilibrium position parallel to a given axis, this is equal to

$$\overline{x^2}_n = \frac{3h^2}{4\pi^2 M k_b \Theta_D}\left[\frac{T^2}{\Theta_D^2}\int_0^{\Theta_D/T}\frac{x\,dx}{\exp(x)-1}+\frac{1}{4}\right] \qquad (33)$$

where h is Plancks constant, M is the atomic mass, k_b is Boltzmanns constant, Θ_D is the Debye temperature and T is the temperature. Evaluation of the energy loss equations which are listed in Appendix II shows that for energies just above the replacement energy, the energy loss mechanism ΔE_1 dominates. However as the energy of the atom increases ΔE_2 dominates. The model predicts that lattice vibrations can significantly reduce the replacement collision sequence length. At any particular temperature the displacement amplitude of the atoms is related to the Debye temperature of the material thus replacement collision sequences are more easily propagated in materials with high values of Θ_D. The predictions of this model concerning the effect of temperature on the replacement collision sequence length are discussed more fully in Chapter 6.2.3. where the energy loss equations are evaluated as a function of temperature for a <110> focusing sequence in nickel.

Mass Difference Effects

According to the principles of the conservation of momentum and energy, the maximum energy that can be transferred in a head on collision between atoms of differing mass is given by equation (27). In ordered alloys, where there is a significant difference in the masses of constituent atoms, it is expected that this energy loss mechanism will have a drastic effect on the replacement collision sequence length. For example, in a CuAu alloy the energy lost per collision of unlike atoms is 25% of the incident atom energy and so long chain replacement collision sequences down mixed atom rows are not predicted. However, this approach to the collision process has been shown to be an oversimplification by Vineyard and Erginsoy (1962) who used computer techniques to simulate collision sequences down mixed atom rows in Cu_3Au. They showed that in a collision sequence between Cu and Au atoms, the energy transferred between two unlike atoms does not occur in one discrete collision but in a series of collisions. For example, if a Au atom moves off with energy E its Cu neighbour will receive 0.75E and move off rapidly because of its small mass to collide with the second Au atom. From this it will rebound and have a second collision with the first atom which is still moving forward. This process is repeated several times, with the Cu atom effectively 'ferrying' energy between the two Au atoms. Thus, the energy transfer is more efficient than predicted by equation (27).

3.1.5. (iii) Computer Simulation of Low Energy Cascades

Computer simulation techniques have also been successfully applied to simulate the energy losses in a crystal after atomic displacement, so that the complex trajectories of many atoms in the lattice may be examined. The molecular dynamics computer modeling approach is based on the work of Vineyard (see Gibson et al (1961)). The model consists of a finite region of crystal in which the atoms interact with forces that correspond to a lattice potential. A constant pressure force balances the repulsion of the surface atoms by the inner neighbours, so that the crystal is in a state of static equilibrium. To simulate damage one atom is initially endowed with an arbitrary kinetic energy and direction of motion as though it had been struck by an incoming particle. The computer integrates the classical equations of motion for a set of atoms showing how the primary knock-on transfers energy to the neighbouring atoms.

The results of these simulations in simple f.c.c and b.c.c static lattices with a primary knock-on energy of less than 100 eV, (Vineyard (1963), Erginsoy et al (1964)) show that the key mechanism of energy transport is the formation of replacement collision sequences in the close-packed atom directions. The main drawback of this type of model is that it fails to take into account the effect of thermal vibrations in the lattice. The static lattice assumption is only really valid when the energy of the primary knock is much higher than the bond energy of the atoms, i.e. at the beginning of a cascade when the time interval between successive collisions is much shorter than the period of atomic vibration and so the lattice appears to be frozen relative to the collision process. However, in a low energy collision sequence, where the time between collisions is comparable to the period of atomic vibration, thermal vibrations can affect the way in which the collision energy is distributed (Nelson et al (1962)). For this reason the molecular dynamics model has been extended to take into account the effect of thermal vibrations on low energy collision sequences (Beeler and Beeler (1975), Tenenbaum (1978) and Kirsanov (1980)). The crystal is placed into thermal equilibrium at the chosen temperature using the Debye-Waller formula (equation (33)) to determine the displacement from the focusing axis. The results of these calculations show that thermal vibrations can significantly influence the cascade structure at low energies. Figure 3.6, from the work of Kirsanov, shows two cascades in Cu starting with a primary knock on atom of 100 eV at 10° to the <110> direction at 0K and 300K. Replacement collision sequences are propagated in the <110> direction at both temperatures but at the higher temperature the length of the replacement collision sequence is reduced and the cascade is more localised.

A more detailed study of these effects has been carried out by Tenenbaum who measured the range of a replacement collision sequence in Cu as a function of energy, temperature and orientation. The results are depicted in Figure 3.7. The range of focusing along <110> shows a maximum between 40 and 50 eV and a regular descent for the higher energies. Along <100> the increase of collision length with energy is slower and there is a broad maximum around 80 eV. For both directions the éffect of increasing temperature is to reduce the length of the collision sequence. Tenenbaum and Doan (1977) further showed that in Cu focused collision sequences along close packed directions may also be initiated by primary knock-ons that make an angle of up to 30° with a <110> direction and up to 20° with a <100> direction, even when thermal vibrations are present. A 30° cone round the twelve <110> directions that originate at a lattice site and a 20° cone around the six <100> directions originating at the same site cover a solid angle of 4π. Thus a knock-on having an arbitrary direction is likely to be 'absorbed' along a close packed direction, so long as the energy is below E_F.

Experimental Evidence

The earliest experimental evidence for focused collision sequences was obtained from back-sputtering experiments. Wehner (1956) bombarded various bcc and fcc single crystal metals with ∿100 eV Ze^+ ions and Nelson and Thompson (1962) bombarded Au with Ar^+ ions in the KeV energy

Figure 3.6.

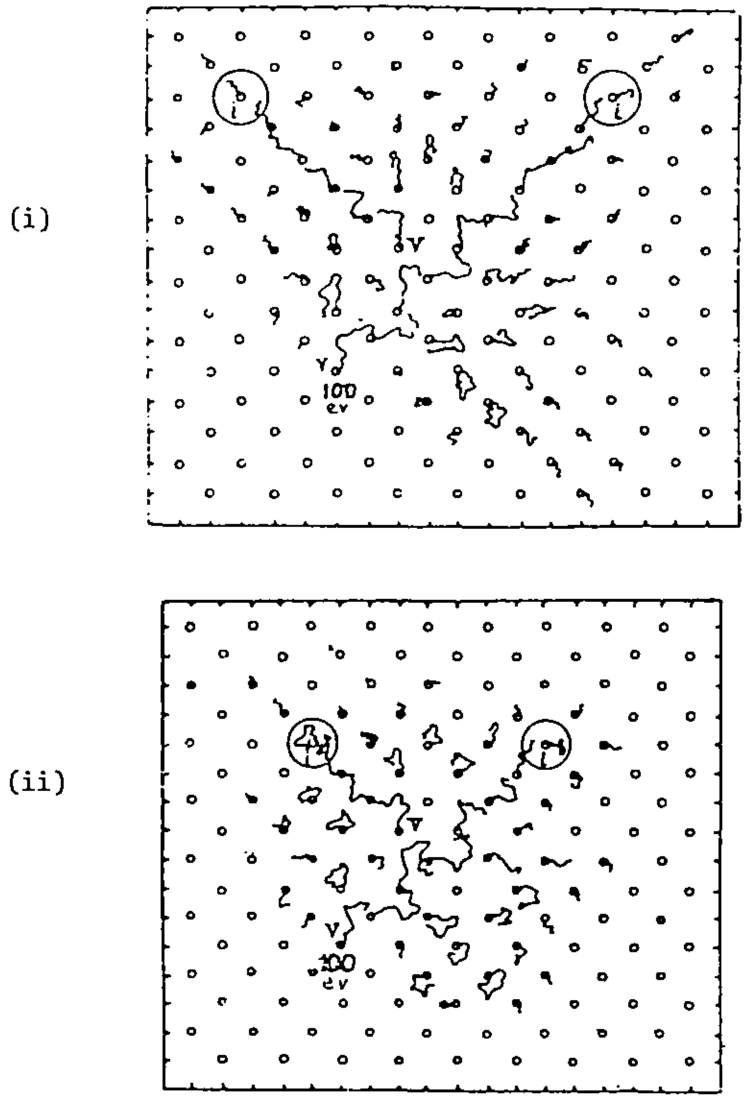

The cascade structure from a 100 eV primary knock-on in the (100) plane at 10° to the <011> direction (i) at OK, (ii) 300K. (Kirsanov 1980).

Figure 3.7.

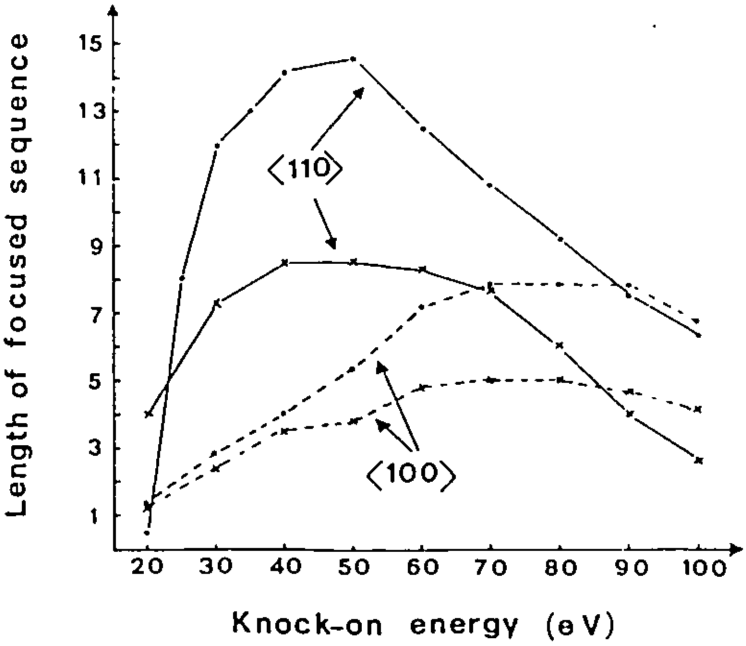

Average length of focused sequences as a function of primary knock-on energy in copper. The units are interatomic spacings. ● = OK x = 293K. Tenenbaum (1978).

range. The results, which showed that the ions were ejected in preferred crystal orientations, were interpreted in as evidence for the formation of focused collision sequences. However, Lehmann and Sigmund (1966) concluded that even a cascade that contains no long range focused sequences will have an anisotropic distribution of ejected ions because there will always be a tendency for the atoms to move off in a cone of directions around the near neighbour axes of the crystal, where ejection requires a minimum of energy. More recent investigations (Nelson and Von Jan (1968), Elich and Roosendaal (1970) and Ecker (1974)) have not resolved the controversy and much stronger evidence for focused replacement collision sequences has been provided by 'interstitial ejection' experiments, 'field ion emission' studies and disordering experiments.

In the interstitial ejection experiments the surface of a target atom is bombarded with ions to induce focusing events. The specimens are thicker than the collision range and so the effects are studied in the interior of the sample using transmission electron microscopy. The first experiments of this type were performed by Hertel et al (1974) who bombarded Cu, Au and Nb with 5 MeV Ar^+ ions and observed interstitial agglomerates at depths of up to several hundred angstroms in the specimens. The results for Cu are shown in Figure 3.8 and illustrate the distribution of defects as a function of depth for {100}, {110} , {112} and {120} surface orientations. For the {100} surface orientation the defect distribution shows a single maximum at 150Å. In foils with a {110} surface orientation the distribution shows two clearly separated maxima at 140Å and 240Å. The larger one contains $\sim$75% of all agglomerates. For the {112} and {120} surface orientations there are indications of three maxima, although they are not so clearly defined as in the {110} foil. The results have been interpreted in terms of replacement collision sequences occurring in the <110> directions. The most convincing feature being the presence of the two maxima in the {110} surface orientation; this occurs because only four of the five <110> directions available for focusing are coincident.

Thomas and Venables (1973) studied the disappearance of vacancy tetrahedra in Au irradiated by 300 eV Xe^+ ions at temperatures from 25K to 300K. They explicitly assumed focusing of the order of 100Å combined with interstitial migration to explain the disappearance or change in structure of the tetrahedra. They concluded however that very long range collisions (i.e. > 1000Å) were unlikely.

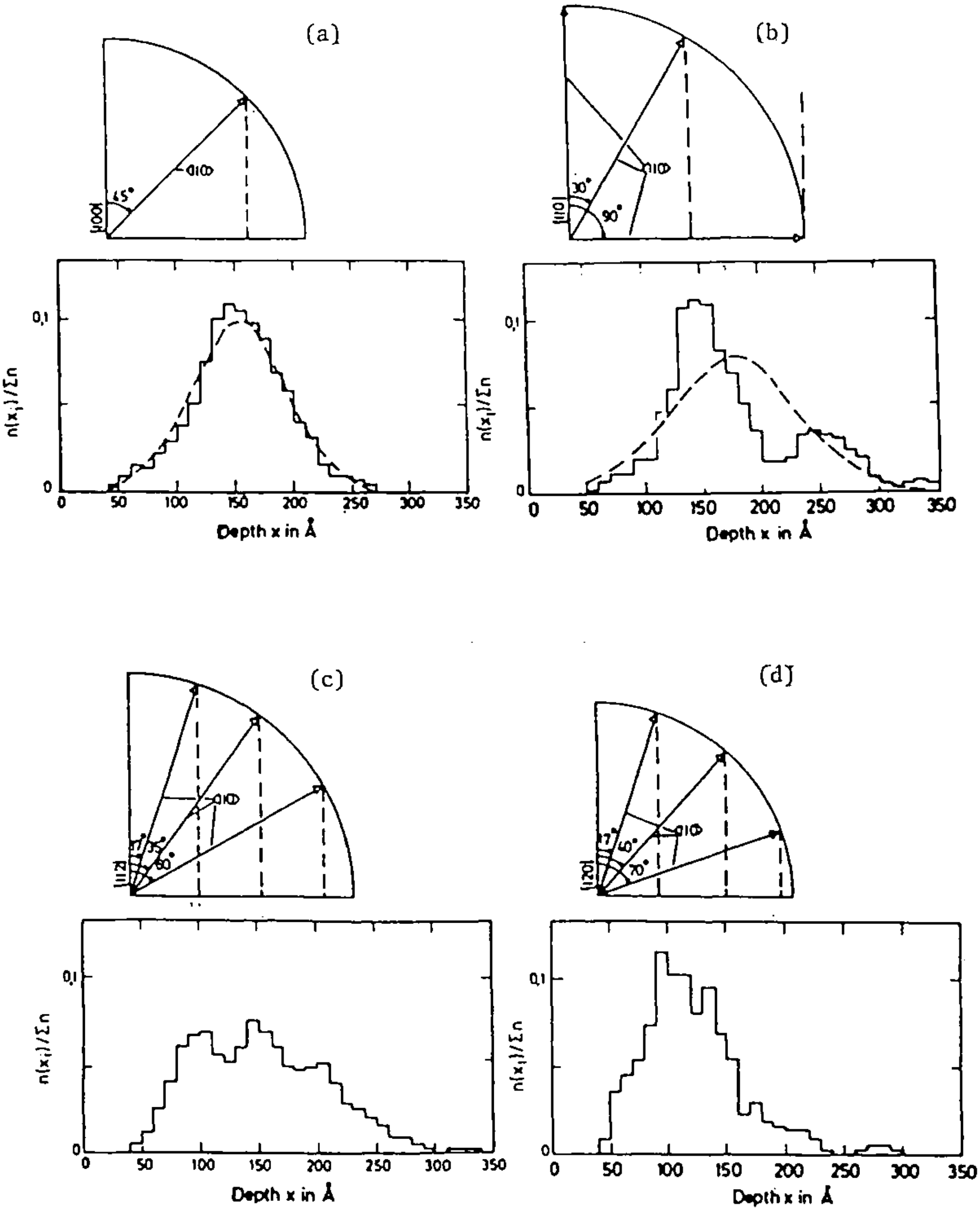

Figure 3.8. Depth distributions of interstitial agglomerates in Cu irradiated with 5 keV Argon ions up to a dose of 10^{15} Ar^+/cm^2, together with angles between the surface and all the {110} directions. Surface orientations:- (a) {100}, (b) {110}, (c) {112}, (d) {120}. $n(\chi_i)/\Sigma_n$ is the normalised number of measurements at a depth x_i.

The field ion microscope with its atomic resolution has been used to study the spatial distribution of point defects within and around the depleted zone created by a displacement cascade. Beavan et al (1971) bombarded a tungsten crystal with 20 keV W^+ ions at 18K. The surface of the specimen was stripped atom layer by atom layer, so that vacancies and interstitials associated with a single cascade could be located. For a cascade of 160 atoms, the vacancies were found in a localized region (depleted zone) with 17 interstitials in the vicinity of the vacancy region. 25 interstitial atoms were found in the peripheral region of the depleted zone at an average distance of 65Å, and it was postulated that these atoms were transported by means of <110> and <111> replacement collision sequences. The remaining 118 interstitial atoms could not be located. They either travelled through the crystal (several hundred Å) or were not detected by the field ion microscope technique.

The use of ordered alloys is one of the most powerful ways of studying replacement collision sequences as the propagation of a replacement collision sequence can leave behind a ribbon of disorder in the crystal. In a definitive experiment Kirk et al (1977) studied the effect of thermal neutron bombardment on the saturation magnetisation, M_S, as a function of the degree of long-range order. The results were interpreted in terms of the Marcinkowski and Poliak (1963) model of magnetic interactions, where a Mn atom aligns ferromagnetically when surrounded by less than three nearest neighbour (nn) Mn atoms, but aligns anti-ferromagnetically when surrounded by three or more Mn atoms. Under thermal neutron bombardment which leads to 450 eV $(n_1\gamma)$ recoils, dM_S/dt decreased with increasing S. Such behaviour was explained by the creation of <110> replacement collision sequences which do not create antiferromagnetically aligned Mn atoms along the chain in a perfectly ordered alloy; i.e. before the <110> R.C.S., Mn has twelve nn Ni atoms whereas after the R.C.S. has propagated it has ten nn Ni atoms and two nn Mn atoms. Hence the Mn atoms remain in the ferromagnetic state. However as the degree of order decreases, the number of Mn atoms with a Mn nn increase and a R.C.S. in the vicinity of a Mn atom pair may result in a Mn atom having three nearest neighbours with a consequent shift to the antiferromagnetic state. It was deduced that 132 ± 10 atoms were replaced per neutron capture event. It was not clear however from the experiments how the replacements were distributed amongst the displaced atoms. If it is assumed, using a Kinchin and Pease (1955) argument, that the primary recoil produces 4 to 8 Frenkel defects and that 20% to 30% of these are formed by <110> R.C.S.'s, then each sequence would average between 66 and 132 replacements.

Despite the difficulties in investigating focusing effects, there does seem to be experimental evidence to support the existence of focused replacement collision sequences.

3.1.6. Radiation Enhanced Diffusion

A consequence of high flux irradiation above the threshold displacement energy is the production of point defects at very high rates; these can strongly influence defect dependent solid state reactions with the result that reaction kinetics can be substantially altered. The magnitude of the increase in the point defect concentrations above their equilibrium values depends upon flux and temperature; the latter affects the mechanism of annealing. At low temperatures mutual recombination is the dominant mechanism whereas at higher temperatures migration to fixed sinks becomes dominant. These opposing processes (production and anihilation) can result in a steady state concentration of point defects being formed in excess of the thermodynamic concentration for which an enhanced diffusion coefficient can be calculated.

3.1.6. (i) Simple Theory

The simplest situation occurs when: (i) the point defect creation rate is constant, (ii) the sinks for the defects are neutral and (iii) there is no defect clustering. The following general equations describe the situation (Sharp 1969).

$$\frac{dv}{dt} = K - K_v v - \nu_i Z(v + v_o)i \qquad (34)$$

$$\frac{di}{dt} = K - K_i i - \nu_i Z(v + v_o)i \qquad (35)$$

K is the point defect creation rate. The terms $K_v v$ and $K_i i$ represent the loss of vacancies and interstitials respectively to sinks. The term $\nu_i Z\ (v + v_o)i$ represents loss of defects through mutual recombination, where v and i respectively are the vacancy and interstitial concentrations produced by the irradiation and v_o is the thermal equilibrium concentration of vacancies. Z is the number of sites around a defect from which recombination can spontaneously occur. ν_v and ν_i are the effective jump frequencies for vacancies and interstitials respectively, and these are equal to

$$\nu_v = A_v \nu_o \exp{}^{-E_v^M/k_bT} \quad (36)$$

and

$$\nu_i = A_i \nu_o \exp{}^{-E_i^M/k_bT} \quad (37)$$

where ν_o is the natural atomic vibrational frequency. A_v and A_i are entropy terms equal to exp S_v^M/k_b and exp S_i^M/k respectively and S_v^M and S_i^M are the entropies of vacancy and interstitial migration respectively. E_v^M is the vacancy migration energy and E_i^M the interstitial migration energy.

K_v and K_i are the proportionality constants for the loss of defects to sinks and are equal to

$$K_v = \alpha_v \nu_v \lambda^2 \quad (38)$$

and

$$K_i = \alpha_i \nu_i \lambda^2 \quad (39)$$

α_v and α_i are measures of the sink densities for the vacancies and interstitials respectively and λ is the atom jump distance.

The recombination volume, Z, is defined as that from which a self interstitial cannot escape recombination with the vacancy. This effect arises from the attraction due to the strain fields around the two defect species, they recombine, even at the lowest temperatures, if the relative distance apart is smaller than a certain critical value. Radiation annealing data indicates that Z is ∿ 100 in copper and nickel at low temperatures (Lück and Sizmann (1964)).

In order to solve equations (34) and (35) it is necessary to assume the system has reached a steady state condition, i.e.

$$\frac{d_v}{dt} = \frac{d_i}{dt} = 0$$

In this state two particular solutions can be identified:

(i) when mutual recombination is the dominant defect loss mechanism, assuming $v \gg v_o$ and $\alpha_v = \alpha_i$

$$v \rightarrow \left(\frac{K}{Z\nu_v}\right)^{1/2} \quad (40)$$

and

$$i \to \frac{1}{\nu_i}\left(\frac{K\nu_v}{Z}\right)^{1/2} \qquad (41)$$

(ii) When losses to sinks is the dominant annealing mechanism

$$v \to \frac{K}{\alpha_v \nu_v \lambda^2} = \frac{K}{K_v} \qquad (42)$$

$$i \to \frac{K}{\alpha_i \nu_i \lambda^2} = \frac{K}{K_i} \qquad (43)$$

Sharp (1969) determined the transition temperature, T_t, at which the number of defects lost by mutual recombination is approximately equal to those anihilated at sinks. This is equal to

$$T_t = \frac{E_v^M}{k_b \ln(\alpha_i \alpha_v \lambda^4 A_v \nu_o / KZ)} \qquad (44)$$

If the defect concentrations are calculated for temperatures $\leqslant T_t$ using equations (40) and (41) and for $T \geqslant T_t$ using equations (42) and (43), the maximum error is a factor of ~ 2 which is negligible.

Using equations (40) and (42) the concentration of vacancies built up under irradiation has been calculated for Ni_3Al and Mg_3Cd. The results and assumed parameters are shown in Figures 3.9 and 3.10 respectively. It can be seen that there is a large increase in the vacancy concentration due to irradiation at the lower temperatures.

However, care should be taken when applying equations (40) → (43) as the assumptions made in their deduction may not always be reasonable. For example, when mutual recombination is the dominant annealing mechanism, the build up time required to reach a steady-state situation is equal to

$$\tau = \frac{1}{2\alpha_v \nu_v \lambda^2} \qquad (45)$$

For nickel at 300K, assuming a vacancy migration energy of 1.2 eV, a sink density of 10^{11} cm^{-2}, a jump distance of 10^{-8}cm, and a vibrational frequency of 10^{15} s^{-1}, the build up time is greater than 10^8 seconds, hence the steady state will never be reached. In this state the vacancy concentration is continually rising and the interstitials take up a quasi steady state concentration, i.e. $di/dt \ll dv/dt$. The concentrations are thus time dependent and it can be shown that (Sharp (1969))

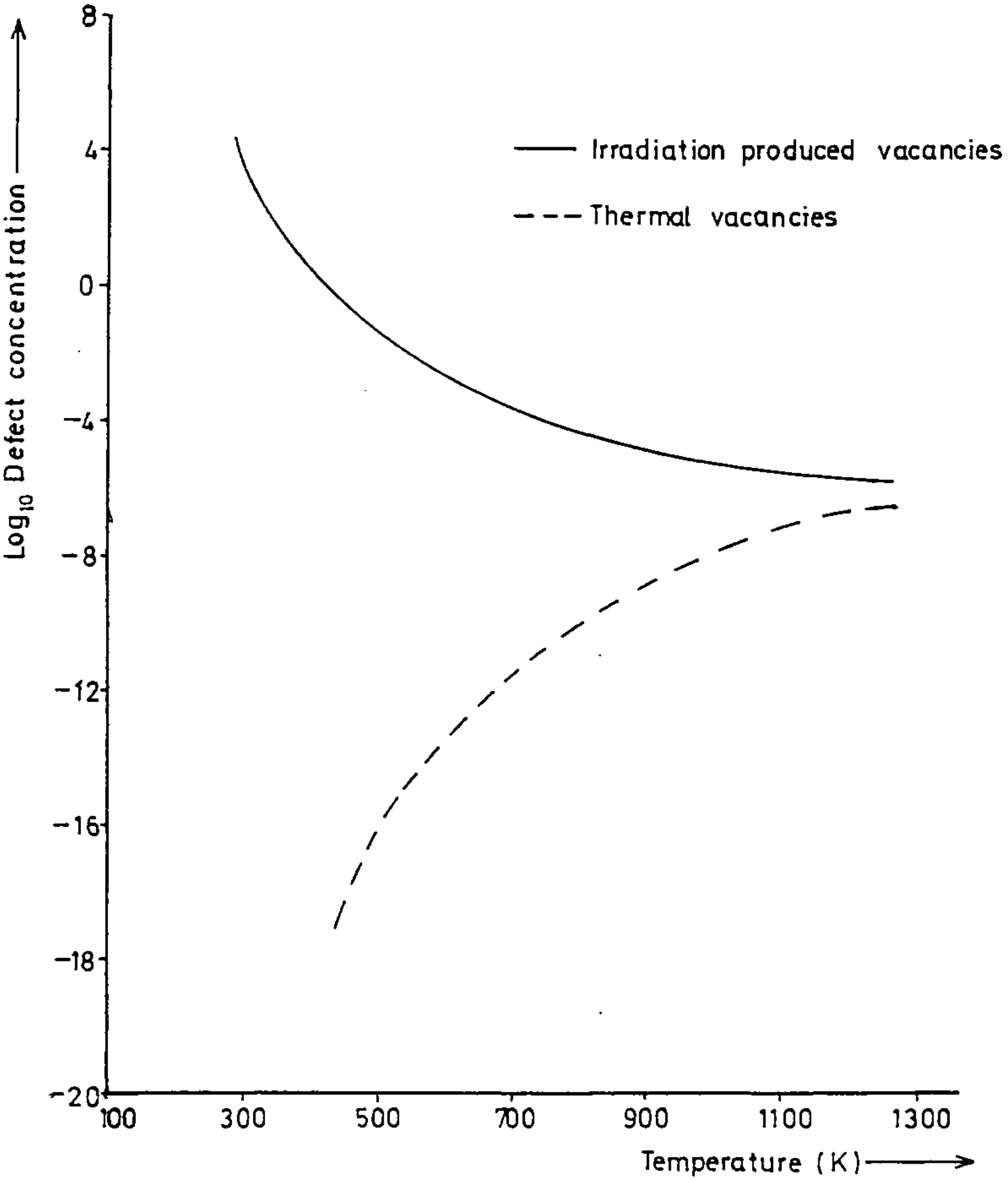

Figure 3.9. Vacancy concentrations in Ni_3Al calculated using equations (40) and (42) for a displacement rate of 10^{-3}d.p.a.s^{-1}, $E_v^M = 1.5$ eV $E_v^F = 1.65$ eV, $\alpha_v = \alpha_i = 10^{11}cm^{-2}$, $\lambda^2 = 10^{15}cm^2$ $\nu_o = 10^{13}s^{-1}$ and Z = 100.

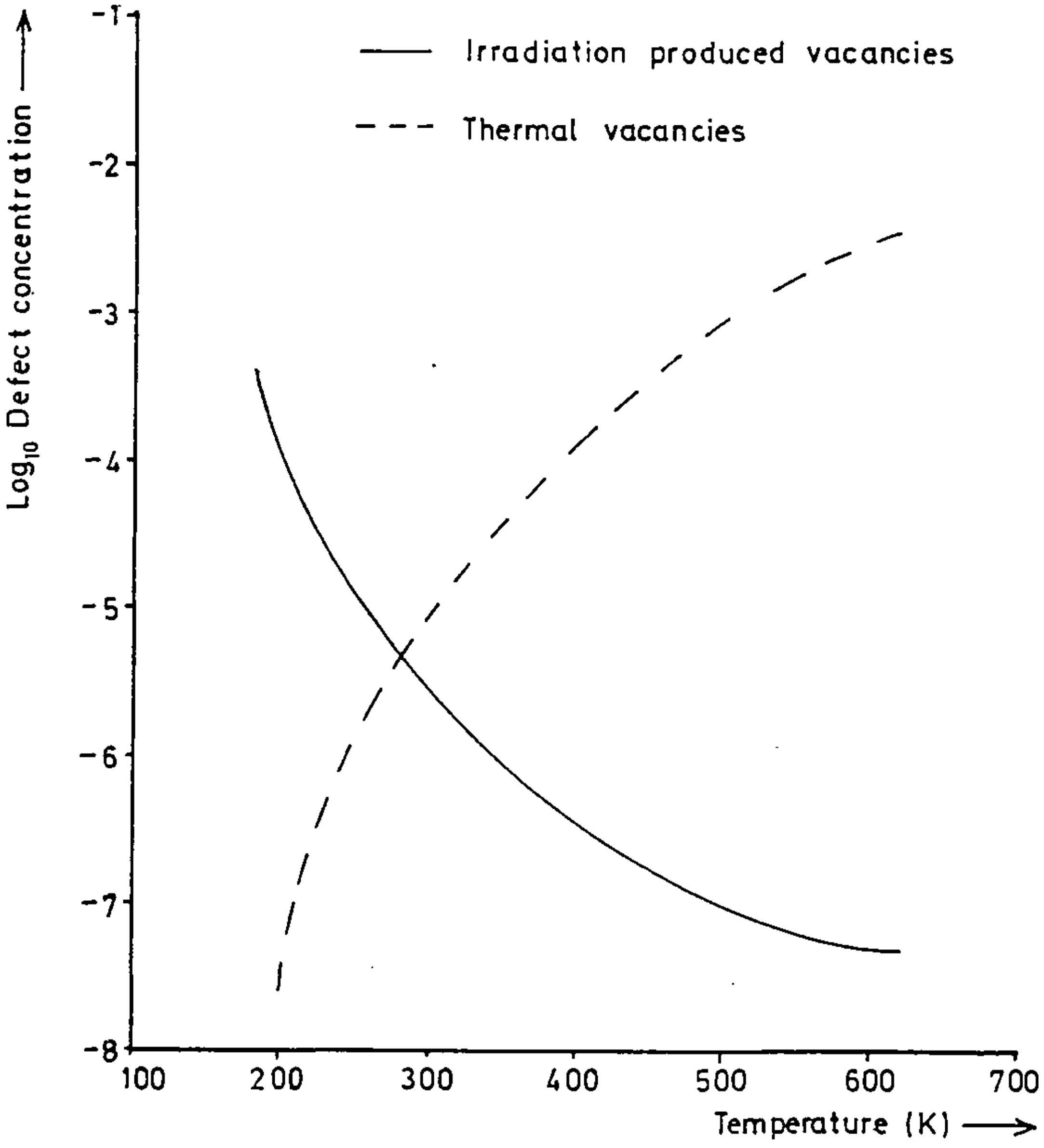

Figure 3.10. Vacancy concentrations in Mg_3Cd calculated using equations (40) and (42) for a displacement rate of 10^{-3}d.p.a.s^{-1}, $E_v^M = 0.5$ eV, $E_v^F = 0.3$ eV, $\alpha_v = \alpha_i = 10^{11}cm^{-2}$, $\lambda^2 = 10^{15}cm^2$, $\nu_o = 10^{13}s^{-1}$ and Z = 100.

$$v = \left(\frac{2K\alpha_i \lambda^2}{Z}\right)^{1/2} t^{1/2} \qquad (46)$$

and

$$i = \frac{1}{\nu_i}\left(\frac{K}{2Z\alpha_i \lambda^2}\right)^{1/2} t^{-1/2} \qquad (47)$$

3.1.6. (ii) Point Defect Clustering

Although the simple theory of the previous section did not consider point defect clustering, it is well established that this can occur when a crystalline solid is irradiated above the threshold displacement energy. Makin (1968a)was the first to observe interstitial cluster formation in Cu and Al irradiated with up to 750 keV electrons at ambient temperatures. Subsequent workers have shown similar forms of visible damage in many other metals and the phenomenon is used for threshold energy determination (see Section 3.1.2.). The probability of loop formation, the loop density and growth rate depend upon the particular irradiation conditions. The most important of these is temperature which controls the thermally activated migration of vacancies and interstitials.

Vacancies Immobile

The situation that was first considered theoretically is that where vacancies can be considered immobile. Makin (1970) used a homogeneous model and Brown et al (1969) used one based on chemical rate theory to describe the observed experimental results. These models are based on the assumption that the interstitial atoms can migrate freely throughout the specimen until one of the following processes occurs:

(i) annihilation with a vacancy,

(ii) trapping by another interstitial atom forming the stable nucleus for a loop, and

(iii) annihilation at the edge of an interstitial loop, causing it to grow.

At the beginning of irradiation, processes (i) and (ii) predominate, whereas at the end of irradiation when there are large numbers of sinks (both vacancies and loops) for interstitials, the interstitial concentration falls and processes (i) and (iii) predominate. Thus, the rate of cluster nucleation decreases rapidly with increasing time and continued irradiation results in the growth of existing loops. The loop growth rate decreases as the irradiation time, t, increases and the vacancy concentration increases. Both models predict a growth rate proportional to $t^{1/3}$ and a saturation cluster density, N, proportional to

$$N \; \alpha \left(\frac{K \exp^{E_i^M / k_b T}}{Z} \right)^{1/2} \qquad (48)$$

where t is the irradiation time and the other parameters have already been defined. Thus as the temperature decreases the interstitial cluster density increases.

Brown et al (1969) considered the heterogeneous nucleation of interstitial loops at impurity atoms. The impurity atoms reduce the migration rate of interstitials and so the cluster density increases. The loop density equation is now proportional to:

$$N \; \alpha \; \left(\frac{K}{Z}\right)^{1/2} \left[\exp^{E_i^M / k_b T} + n \exp\left(\frac{E_i^M + E_b}{k_b T}\right)\right]^{1/2} \qquad (49)$$

where E_b is the binding energy between a self interstitial atom and an impurity atom and n is the impurity concentration. The variation in loop density with temperature and sample purity has been shown in many systems and the results have been used to estimate interstitial migration energies. (For example see Hossain and Brown (1977a) and (1977b) and Shimomura (1977)).

Vacancies Mobile

When vacancies are mobile and there is a steady-state defect concentration, the diffusion coefficients of the irradiation-produced vacancies and interstitials become equal, i.e. $v\nu_v = i\nu_i$. A direct consequence of this is that the number of interstitials condensing on only sink is equal to the number of vacancies condensing; therefore, the simple theory would predict that no loops would nucleate and any loops that are nucleated in the build up time to the steady state (i.e. $i\nu_i > v\nu_v$) would stop growing. Experimentally, however, it is observed that interstitial loops continue to grow even in the steady state.

For cluster growth to occur there must be an asymmetry in the behaviour of the vacancies and interstitials, when both defects are mobile; this must be due to the sinks. It is found that dislocations and existing loops act as biased sinks for the interstitial atoms because of the high strain energy associated with a free interstitial and the resulting relief of the dislocation strain field (Stobbs (1973)). Surfaces and grain boundaries act as neutral sinks and absorb both vacancies and interstitials and so the interstitial loop growth rate is found to be proportional to the rate at which vacancies diffuse to the sinks, i.e. the vacancy mobility. Models which describe these effects have been developed by Urban and Wilkens (1971) and Kiritani et al (1975) and predict a linear loop growth rate with time, i.e. $l \propto t^n$, where l is the loop diameter, t is the irradiation time and n is equal to unity. The rate of linear loop growth as a function of temperature has been used to determine vacancy migration energies. However, there are certain complicating factors in the measurement of such defect parameters by this technique. Yoo and Stiegler (1977) analysed the growth kinetics of interstitial loops in nickel at 450°C under 650 keV electron irradiation and found a range of loop growth rates with n varying from 0.6 to 0.9. The loops situated near the top and bottom surfaces of the foil were larger than those in the middle and this depth dependence became more pronounced the longer the irradiation time. Although the conclusion of the simple models that the interstitial loop growth rate is dictated by the migration of vacancies to sinks is correct, the proximity of the loop to the foil surface is very important, since this is the principal vacancy sink. At the foil surface no interstitial loops are formed because the sink concentration is high. At the centre of the foil the vacancies have the greatest distance to diffuse to the surface sinks and so here the rate of loop growth is reduced. Between these two states the maximum rate of loop growth occurs. Therefore at vacancy mobile temperatures one would expect a range of interstitial loop growth rates. The constant growth rates reported by Urban and Wilkens and Kiritani were obtained from the measurements of a few isolated loops. Yoo and Stiegler modified the general rate theory model to take into account the spatial dependence of the loops and evaluated the activation energy for vacancy migration by fitting to the experimental data reasonable values of various point defect parameters.

From the preceding considerations it can be seen that if there is a local enrichment of vacancies and a depletion of interstitials, i.e. $v\nu_v > i\nu_i$, then vacancy cluster formation can occur. Vacancy cluster formation has been observed to occur in very thin foils of Cu and Ag irradiated at 300K (Urban (1975)) which was attributed to a direct loss of interstitials to the surface, triggered by long-range replacement collision sequences.

3.2. The Effects of Electron Irradiation on Ordered Alloys

The behaviour of an ordered alloy under irradiation is complicated by the possibility of displacement damage altering the distribution of atoms between the 'right' and 'wrong' sites thus changing the degree of order. The particular response of an ordered alloy depends strongly upon the irradiation temperature and the degree of order before irradiation. Evidence for and against the mechanisms of such irradiation induced order $\rightleftarrows$ disorder transformations are introduced in the following sections. For a recent review see Schulson (1979).

3.2.1. Ordering Under Electron Irradiation

Ordering under electron irradiation has been observed directly using the transmission electron microscope (TEM) by recording the formation or increase in the intensity of superlattice reflections. Measurements of changes in the electrical resistivity, (r), have also been made and these provide an indirect determination of changes in the degree of order, since at any particular temperature the resistivity decreases on ordering (Krivoglaz and Smirnov (1964)).

Experimental evidence for ordering under electron irradiation is listed in Table 3.4.

3.2.1. (i) Mechanisms of Ordering Under Electron Irradiation

Physically ordering corresponds to an increase in the probability that an A atom occupies an α site and a B atom a β site. This change in atomic siting requires the thermally activated migration of point defects. Under irradiation vacancies and interstitials can be formed in excess of the normal thermal equilibrium concentration and so only the migration energy need be provided thermally for diffusion to occur. Thus under irradiation a lower thermal energy is required for ordering.

In order to determine whether both the vacancies and interstitials or just one of the defect species is responsible for ordering, experiments have been carried out to try and isolate the effects of one of the defects. Brinkman et al (1954) carried out resistivity measurements on quenched specimens of Cu_3Au. It was observed that ordering occurs at 423K which is approximately the same temperature that ordering is observed under 1 MV electron irradiation (Adam et al (1952)). Furthermore, it was shown that the initial rate of ordering at 423K increases with the quench temperature. Thus, it was concluded that

Table 3.4. Experimental Evidence of the Ordering of Alloys under Electron Irradiation

Alloy	Structure	Technique	Electron Energy MeV	Total dose d.p.a.	Initial S	Observation	Reference
Cu_3Au	$L1_2$	r	1	$\sim 10^{-5}$	S → 1	After irradiation at 315K and subsequent annealing at 373K r falls, a response which does not occur in the absence of irradiation	Adam et al (1952)
CuZn	B2	r	1.5	$\sim 10^{-5}$	S → 1	After irradiation at 20K and subsequent annealing (∿ 180K) r falls to a level below the pre-irradiated value	Koczak et al (1971)
NiFe	B2	TEM	1	4	S → 0	The rate of ordering which is observed during irradiation in the temperature range 373K - 573K is much greater than is observed in the absence of irradiation. Ordering is not observed under irradiation at 293K	Penisson and Bourret (1975)
Au_4Mn	*	TEM	1	5	SRO	At 473K and 593K long-range ordering is observed within 300 seconds of irradiation with a dose rate of $1.5 \times 10^{19} e.cm^{-2} sec^{-1}$. This is much faster than is observed on thermal annealing in the same temperature range	Van Tendeloo et al (1979)

*centred tetragonal superstructure of f.c.c. lattice both observations strongly support the view that vacancies are the dominant species responsible for ordering under electron irradiation. In support of this it was also argued that one might expect a gold interstitial to have a higher formation energy than a copper interstitial, because of its larger size. Thus it would be energetically favourable for a gold interstitial to replace a copper interstitial but not the reverse. Hence interstitial migration would mostly occur on the copper sublattice which would not lead to ordering. Additional experimental evidence which supports a vacancy mechanism has been reported by Gilbert et al (1973) who irradiated Cu_3Au with 1 MV and 1.5 MV electrons at liquid helium temperatures and then carried out isochronal annealing. Ordering was not observed during the stage I annealing where interstitials are mobile.

Koczak et al (1971) also carried out quenching experiments on CuZn and characterised the results of both these experiments and electron irradiation experiments (see Table 3.4.) in terms of vacancy migration with an activation energy of $\sim$ 0.4 eV. Electron irradiation at 78K, where vacancies can be considered immobile and interstitials mobile, produced no change in the degree of order. It was concluded therefore that vacancies are the dominant species responsible for ordering under irradiation. Similar 'size factor' arguments to those of Brinkman were advanced to explain the absence of interstitial ordering under irradiation. Penisson and Bourret (1975) successfully analysed their results on the irradiation induced ordering of NiFe also in terms of a model based on vacancy migration as ordering was not observed under 1 MV electron irradiation at 293K. Most of the experimental evidence for irradiation induced ordering supports a vacancy mechanism, since at temperatures where interstitials are mobile and vacancies are immobile ordering is not observed. There is experimental (Ehrhart and Schilling (1973)) and theoretical (Dederichs et al (1978)) evidence to show that interstitials do not sit in isolated sites but form split dumbbells with atoms sitting in the lattice, which minimise the forces extended on neighbouring atoms. The most stable configurations for the f.c.c and b.c.c structures are the <100> and <110> split interstitial dumbbells respectively. These are shown schematically in Figure 3.11.
The migration of the dumbbell occurs by combined rotational and translational jumps. The mechanisms with the lowest activation energies ($\sim$ 0.1 eV in Cu, Ni and Al (Young (1978)) are shown in Figure 3.12.

Figure 3.11.

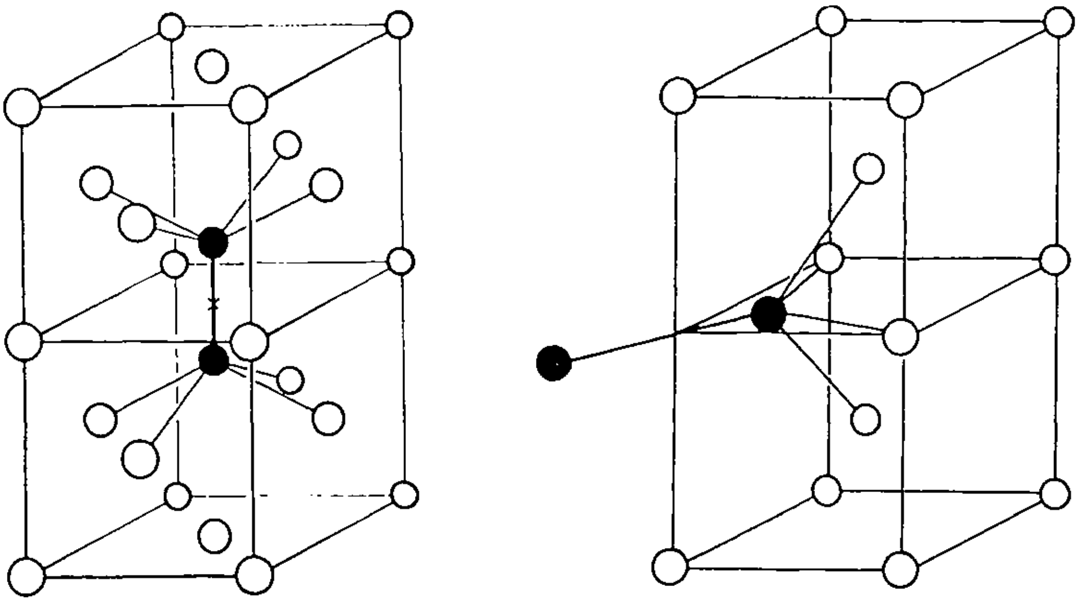

(i) [100] - dumbbell in fcc crystal.

(ii) [110] - dumbbell in bcc crystal.

Figure 3.12.

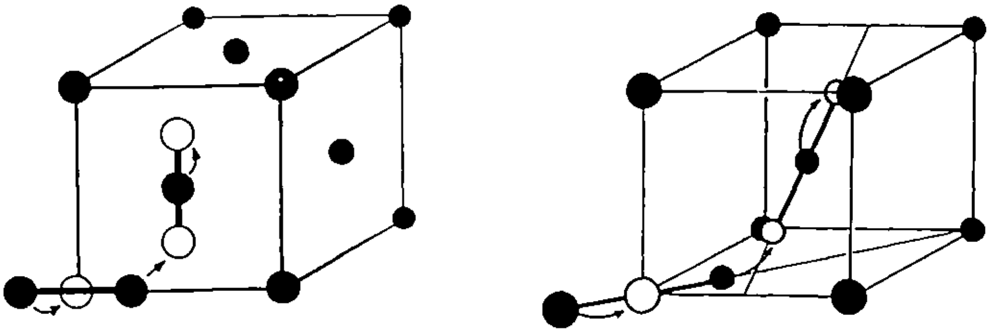

Elementary jumps of the dumbbell interstitials:
• positions before jump; o positions changed by
jump (i) fcc. (ii) bcc.

Migration of interstitials by combined rotational and translational jumps can lead to ordering if the dumbbells which are formed contain both atomic species, thus allowing long-range migration of both types of atom. Figure 3.13 shows the ordering of an AB_3, $L1_2$ alloy by the motion of a <100> mixed dumbbell. The black dots represent the B atoms whose ordered position is at the face centre, and the white dots represent the A atoms whose ordered position is at the face corner. Thus in this example there are two disordered sites in the lattice before the formation and migration of the mixed dumbbell. However, such a situation may not occur in alloys, when there is a large difference between the effective atomic volumes of the alloying elements, and the undersized atoms are preferentially accommodated at the dumbbells. If this occurs only one species will diffuse by this mechanism and the degree of order will be little affected.

There is experimental evidence (Wollenberger (1978)) for the formation of mixed dumbbells in dilute alloys ($\sim$ 0.25 at%) of aluminium and copper with solute atoms which are smaller than the host, e.g. Mn, Zn and Ag in Al and Be in Cu. However, it is observed that the migration energy of the mixed-atom dumbbells becomes greater than that of the like-atom dumbbells of the host interstitial, i.e. the freely migrating interstitials become trapped at the solute atoms. Theoretical calculations support this observation (Dederichs et al (1978)) and predict that the migration energy of a mixed atom dumbbell is greater than that of a like atom dumbbell because long-range migration requires additional energy to dissociate the mixed-atom species. Hence if mixed-atom dumbbells do form, the activation energy for an ordering jump is not necessarily the same as the free interstitial migration energy and so ordering may not be observed at temperatures where only single interstitials are mobile. However, interstitial migration, via mixed-atom dumbbells, could contribute to irradiation induced ordering at higher temperatures.

3.2.1. (ii) Kinetics of Ordering Under Electron Irradiation

The two theoretical models which have recently been proposed (Butler (1979) and Liou and Wilkes (1979)) to describe radiation enhanced ordering treat the effect in an almost identical manner. The ordering rate under irradiation has been evaluated by introducing into thermal ordering rate equations the concentration of irradiation produced defects.

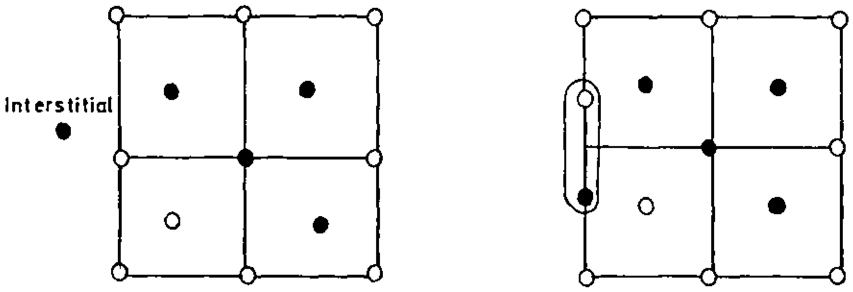

Lattice with two disordered sites

Formation of [100] split interstitial

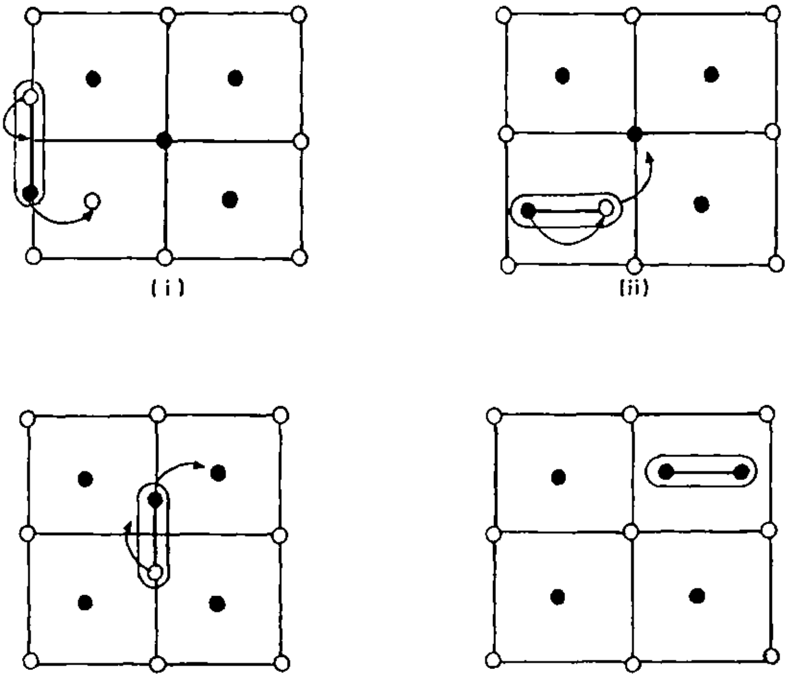
(i)

(ii)

(iii)

(iv)

Motion of interstitial by three successive jumps removes disorder from the lattice.

Figure 3.13. Ordering by interstitial motion in $L1_2$ lattice (after Liou and Wilkes (1979)).

For example, Dienes (1955) produced the following equation for the rate of thermal ordering in a AB alloy (see Chapter 2.1.4. equation (16)).

$$\frac{ds}{dt} = \nu\exp(-E/k_bT)[X_AX_B(1-S)^2-e(-V/k_bT)[S + X_AX_B(1-S)^2]]$$

where E is the activation energy required to change an atom from the disordered to the ordered state.

It is presumed that ordering occurs by the diffusion of point defects and so E in the thermal rate constant can be equated to the sum of the activation energies for vacancy formation and migration. (The thermal interstitial concentration is so small that thermal ordering via interstitial diffusion can be neglected.) Thus under certain irradiation conditions an increase in the point defect concentration can enhance the rate of ordering by removing from the activation energy of the rate constant the defect formation energy. The enhanced ordering rate under irradiation is equal to

$$\frac{ds}{dt} = \nu(v\ \exp(-E_v^M/k_bT) + i\ \exp(-E_i^M/k_bT))[X_AX_B(1-S)^2 - e(-V/k_bT)[S+ X_AX_B(1-S)^2] \qquad (50)$$

where v and i are the irradiation-produced vacancy and interstitial concentrations respectively which can be calculated from the standard radiation enhanced diffusion equations (Section 3.1.6.).

Butler (1979) investigated the effects of irradiation on the kinetics of ordering in a theoretical AB system by evaluating equations (16) and (50). It was assumed that both thermal ordering and irradiation enhanced ordering proceed via a vacancy mechanism. The concentration of irradiation produced vacancies was calculated using equation (40) which is equal to

$$v = (K/Z\nu_v)^{1/2}$$

This equation is valid when mutual recombination is the dominant defect loss mechanism, the defect sinks are neutral and the build-up time to the steady-state concentration is short. The results of these calculations for temperatures below T_c, at S = 0.7, are shown in Figure 3.14, with the assumed parameters. At 400K the radiation enhanced diffusivity are equal but as the temperature is lowered the irradiation-produced vacancy concentration becomes greater than the thermal vacancy concentration and so the kinetics of ordering are greatly enhanced by irradiation.

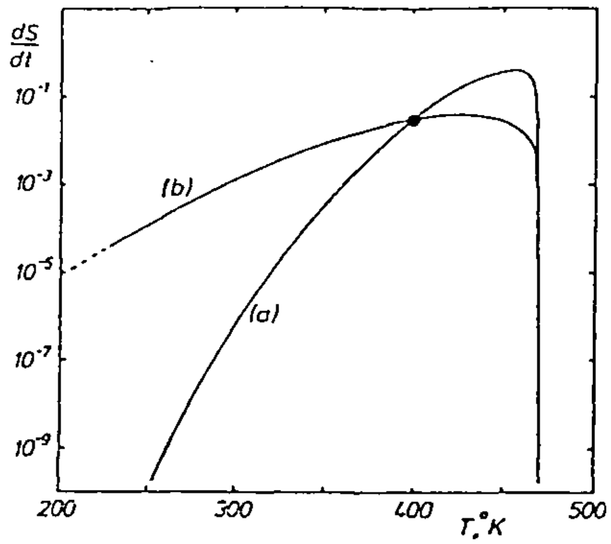

Figure 3.14. The ordering kinetics at $S = 0.7$ as a function of temperature below T_c as controlled by (a) thermally activated diffusion and (b) radiation enhanced diffusion in a theoretical AB system. The assumed parameters are: $E_v^F = 0.44$ eV, $E_v^M = 0.65$ eV, $\nu_0 = 10^{15} s^{-1}$, $T_c = 500K$, $K = 10^{-3}$ dpas^{-1} and $Z = 100$. (from Butler (1979)).

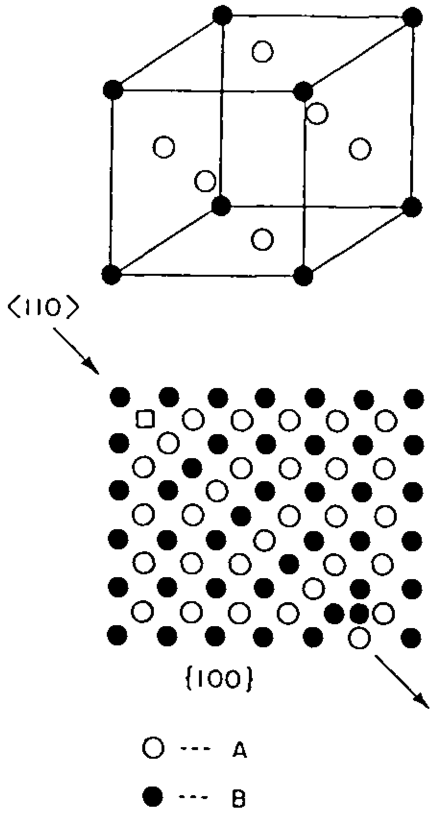

Figure 3.15. Schematic sketch of a <110> replacement in the $L1_2$ superlattice.

3.2.2. Disordering Under Electron Irradiation

Electron irradiation induced disordering has been observed directly in the HVEM by monitoring changes in:

(i) the superdislocation spacing (S.D.S.),
(ii) the thickness fringe spacing (T.F.S.), and
(iii) the superlattice reflection intensity (S.L.I.).

Superdislocation Spacing

In ordered alloys dislocations tend to move in pairs so that the second dislocation can restore the order to the lattice which was destroyed by the movement of the first. Thus the two separate dislocations, known as a superdislocation, have an antiphase boundary between them. It is the surface tension of the APB which balances the mutual repulsive force between the dislocations and determines their equilibrium separation, d. Brown and Herman (1956) have shown that d is related to S by the equation

$$d = \frac{A}{S^2} \qquad (51)$$

where A is a constant. Therefore changes in S during electron irradiation can be directly related to changes in the superdislocation width by the relationship

$$S(t) = S_o\sqrt{\frac{d_o}{d(t)}} \qquad (52)$$

where S_o and d_o are the degree of order and the superdislocation spacing before irradiation respectively and t is the irradiation time.

One problem that can arise with this technique is that the dislocations can act as bias sinks for the interstitial atoms (Stobbs (1973)). This results in the dislocations being pinned in a fixed position so that no changes in width occur as S changes. Hence this method is most useful to monitor changes in S in the early part of the disordering response before pinning occurs.

Thickness Fringe Spacing

Kinoshita et al (1977) have developed a technique for detecting the variation in S under electron irradiation from changes in the spacing of thickness fringes. The extinction distance, εg, is calculated as a function of S, for a perfectly wedge-shaped crystal set at the Bragg position, using the many beam dynamical theory. To determine changes in S, the experimental variation in the thickness fringe spacing is related to that predicted theoretically.

The main limitation of this technique is that the magnitude of the variation of εg with S depends on accelerating voltage. For example, in B2 Fe_3Al it is only practical to use this technique for accelerating voltages above 500 kV, whereas for $L1_2$ Cu_3Au the variation in εg with S is large enough to monitor changes in S at accelerating voltages from 200 kV to 1000 kV. Also the experimental errors involved with this technique can be large if the specimens markedly deviate from wedge-shaped, i.e. have irregular surfaces and/or are locally bent, since a uniform wedge-shaped crystal is assumed in all the εg calculations.

Superlattice Reflection Intensity

Electron diffraction can be used to monitor changes in S during electron irradiation since the intensity of a superlattice reflection is directly proportional to S^2 (see Chapter 2.1.2.). The advantages and limitations of this technique, which has been used in the present investigation, are fully discussed in Chapter 4 on experimental procedures.

Table 3.5. lists the experimental evidence of disordering under electron irradiation in a range of ordered alloys using the above techniques.

3.2.2. (i) Mechanisms of Disordering Under Electron Irradiation

Various models have been proposed to describe simple radiation disordering (Aronin (1954), Venables and Lye (1969) and Polenok (1973)), when reordering can be neglected, these are of the general form

$$S = S_o \exp(-K't) \qquad (53)$$

where S_o is the initial degree of order, t is the irradiation time and K is a parameter which measures the effectiveness with which the incident particle disorders the material. It is equal to

$$K' = \varepsilon \sigma_d \phi \qquad (54)$$

where ϕ is the incident flux, σ_d is the total displacement cross-section and ε is a multiplication factor which depends on the assumptions of the particular model.

Disordering mechanisms specific to high energy electrons and important enough to lead to significant disordering can be identified as:

(i) uncorrelated interstitial-vacancy recombination: interstitials escaping from the recombination volume following displacement recombine with vacancies of the 'wrong' type.

(ii) replacement followed by uncorrelated recombination within the recombination volume: the primary displaced atom has sufficient energy to displace its unlike neighbour which then recombines athermally with the original 'wrong' vacancy.

(iii) replacement collision sequences down mixed atom rows: each displaced atom starts a knock-on chain creating a ribbon of disorder the length of the replacement sequence. (see Figure 3.15).

(iv) replacement collision sequences down rows of like atoms: equivalent to (i) if the sequence culminates in an interstitial ejected outside the recombination volume.

Mechanisms (i), (ii) and (iv) depend on uncorrelated recombination to disorder the alloy. If this is the dominant disordering mechanism, ε will be less than unity as only a proportion of the primary displacements are followed by an uncorrelated event. However, if the propagation of replacement collision sequences down mixed atom rows is the dominant disordering mechanism, then ε will be greater than unity as the disordering effect of the primary displacement is multiplied down the collision chain. Thus ε is equal to the ratio of the number of replacements to displacements.

With reference to Section 3.1.5, the importance of disordering mechanisms involving replacement collision sequences will increase relative to those involving uncorrelated recombination as:

(i) The energy of the primary knock-on increases up to the limit of the critical focusing energy.

(ii) The efficiency of energy transfer is increased, i.e. at low temperatures and in alloys where there is little difference between the atomic masses of the constituent atoms.

Orientation effects are expected if the creation of replacement collision sequences down mixed atom rows is the dominant disordering mechanism. However, such effects may not be particularly pronounced if the primary displacements recoil at some angle to the incident beam. In this situation replacement collision sequences are created down mixed atom rows irrespective of orientation. As was shown in Section 3.1.1., even at energies just above E_d there is a high probability of recoil.

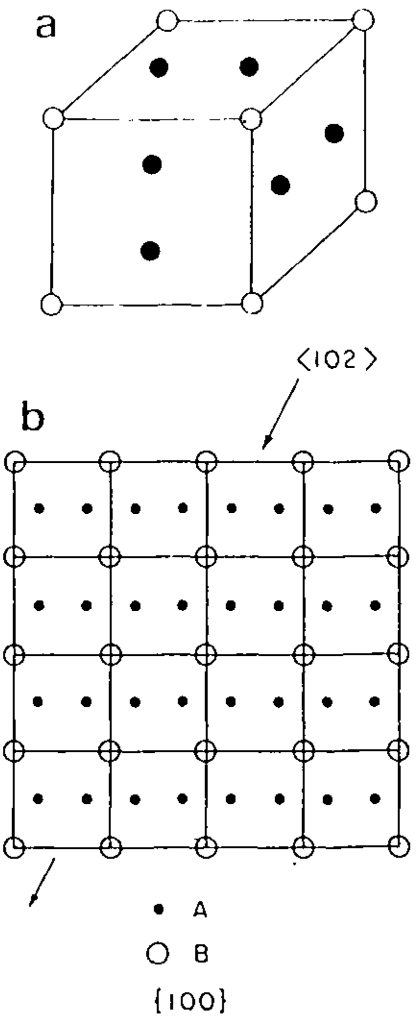

Figure 3.16. (a) The A_3B A-15 superlattice (b) The (100) plane of the A-15 superlattice showing the <102> mixed-atom direction.

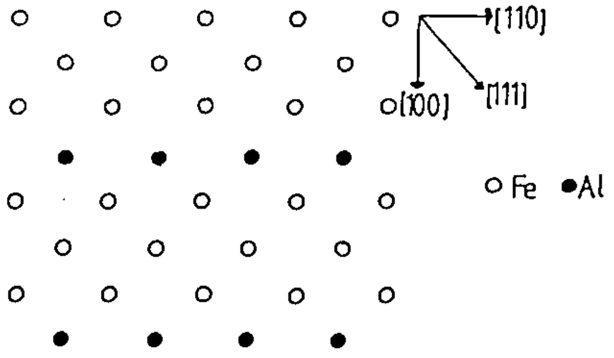

Figure 3.17. Schematic representation of the atom positions in Fe_3Al (DO_3 superlattice).

The complexity of the alloy structure may further affect the probability of disordering occurring by replacement collision sequences down mixed-atom rows. For example in the A_3B A15 alloys it is improbable that long chain replacement collision sequences will occur in the mixed-atom <102> directions, as a void exists between each A-B-A sequence. This is shown schematically in Figure 3.16. In the Fe_3Al DO_3 structure Jackson et al (1972) have carried out computer simulated disordering in a static lattice. It was found that replacement collision sequences readily occurred in the <100> and <110> directions with primary displacement energies of $\sim$50 eV. However in these directions the atom chains are composed of like atoms therefore little disordering would result, see Figure 3.17. In the <111>, AAA-B-AAA, direction replacement collision sequences would not propagate, the threshold displacement energy being a factor of three times greater than in the <100> and <110> directions and so primary displacements of energies $\sim$100 eV were defocused. It was suggested that the mixed atom structure of the <111> direction and the factor of two difference in the atomic masses of the constituent atoms greatly increased the complexity of the collision events.

Experimental evaluation of the disordering mechanism is possible by determining ε or the d.p.a. to achieve a certain state of disorder, say 0.1 (Schulson (1979)). In both methods a value of σ_d must be assumed but the second method frequently necessitates an extrapolation according to equation (53) as well. Table 3.5. shows the d.p.a. values required to create a certain amount of disorder and the corresponding ε values evaluated assuming order was not detectable when $S = 0.15$, using the theoretical σ_d quoted in the d.p.a. analysis. On this basis the experimental results can be interpreted in terms of disordering by uncorrelated recombination and replacement collision sequences.

Carpenter and Schulson (1978), (1981), from their work on Zr_3Al and Ni_3Al, suggested that both uncorrelated recombination and short chain replacement collision sequences are likely disordering mechanisms under electron irradiation, however no discussion was made of the relative importance of each mechanism. Although at low temperatures, ε in Ni_3Al under 650 kV irradiation is greater than one, Liu et al (1981) concluded that uncorrelated recombination is the dominant disordering mechanism because there was no orientation dependence of the disordering rate. Butler and Swann (1977) however concluded that the measured disordering rates in <110> Zr_3Al, Ni_3Fe and Ni_3Si are consistent with the creation of replacement collision sequences. In support of this, Cordier et al

Table 3.5. Experimental Evidence of Disordering of Alloys Under Electron Irradiation

Alloy	Technique	Electron Energy MeV	Temperature K	Orientation <uvw>	σ_d Theor. (barns)	Initial S	dose d.pa	Final S	ε	Reference
V_6C_5	S.L.I.	0.033 →0.1	298	<110>		1	∿1	→0		Venables & Lye (1969)
Ni_3Mn $(L1_2)$	S.D.S.	1.2	298	<110>	40	1	0.25	0.6	2	Cordier et al (1973)
				$<3\bar{5}2>$		1	0.25	0.9	1	
				$<3\bar{1}\bar{8}>$		1	0.25	0.8	1	
Zr_3Al $(L1_2)$	S.L.I.	1	300	<110>	44	1	0.25	0.3	3.6	Butler & & Swann (1977)
	S.L.I.	1	135	Low Index Zone	44	1	1	→0	2	Carpenter & Schulson (1978)
			320			1	1	→0	2	
			375			1	1	→0	2	
			575			1	20	1>S>0		
			675			1	18	1>S>0		
			775			1	10	1>S>0		
Mg_3Cd DO_{19}	S.L.I.	1	160	$<\bar{2}4\bar{2}3>$	160	1	1	→0	1	Butler (1978)
			213			1	10	0.2		
			243			1	10	0.4		
			300			1	5	0.95		
Ni_3Fe $L1_2$	S.L.I.	1	300	<110>	50	1	0.2	∿0.2	6	Butler & Swann (1977)
Ni_3Si $(L1_2)$	S.L.I.	1	300	<110>	50	1	0.5	0.3	2	Butler & Swann (1977)

Table 3.5. (continued)

Alloy	Technique	Electron Energy MeV	Temperature K	Orientation <uvw>	σ_d Theor. (barns)	Initial S	dose d.pa	Final S	ε	Reference
Ni_3Al ($L1_2$)	S.L.I.	0.65	190	<111>	25	1	0.7	0.15	2.7	Liu et al (1981)
			210			1	1.0	0.15	2	
			230			1	1.4	0.15	1	
			250			1	2.5	0.2		
			290			1	2.5	0.4		
			310			1	2.5	0.5		
			150	<100>		1	0.9	0.1	2	
			150	<110>		1	0.82	0.1	2	
			150	<111>		1	0.95	0.1	2	
Ni_3Al ($L1_2$)	S.L.I.	1	144	Low Index Zone	50	1	0.3	$S\to 0$	6	Carpenter & Schulson (1981)
			157			1	0.4	$S\to 0$	4.5	
			179			1	0.7	$S\to 0$	3	
			238			1	0.65	$S\to 0$	3	
			248			1	0.65	$S\to 0$	3	
			313			1	0.6	$1>S>0$		
			350			1	2.5	$1>S>0$		
			440			1	3.0	$1>S>0$		
			575			1	4.5	1		
NiAl B2	S.L.I.	0.65	150	<100>		1	7	0.5		Liu et al (1981)
FeAl B2	S.L.I.	0.65	150	<110>		1	1.2	$\to 0$		Liu et al (1981)
FeAl	T.F.S.	1.25	300	<100> & <110>	90	1	0.25	0.75		Kinoshita et al (1982)
		1.0	300		80	1	0.2	0.75		
		0.75	300		70	1	0.21	0.75		
		0.5	300		40	1	0.1	0.9		
		0.35	300		20	1	0.25	0.75		
		0.25	300		5	1	0.1	0.99		

(1973) observed an orientation dependence of disordering in Ni_3Mn under 1.2 MeV electron irradiation, the disordering rate being greatest in the <110> direction. This observation was put forward as evidence of the creation of replacement collision sequences. In the B2 alloy, FeAl, Kinoshita (1982) concluded that uncorrelated recombination is the dominant disordering mechanism over the range of electron energies from 0.25 to 1.25 MeV at 300K.

Kinetics of Disordering

Rearranging equation (53) the rate of disordering under irradiation is given by

$$\frac{ds}{dt} = -K'S \qquad (55)$$

The disordering rate is linearly dependent on the instantaneous degree of order S and at long irradiation times S will tend to zero.

Simultaneous Ordering and Disordering Under Irradiation

The response of an ordered alloy to irradiation depends on the relative magnitudes of the disordering and ordering rates, i.e.

$$\frac{ds}{dt}_{irr} = \frac{ds}{dt}_{ord} + \frac{ds}{dt}_{disord} \qquad (56)$$

The disordering rate is given by equation (55) and the ordering rate is equal to the sum of the thermal ordering rate equation (16) and the irradiation enhanced ordering rate equation (50). This model predicts that at high temperatures the mobility and concentration of the irradiation produced and/or thermal vacancies is high, and so ordering is favoured. At low temperatures the defect mobility is insufficient to resist disordering, which should proceed at a linear rate if equation (55) is obeyed. At some intermediate temperature the ordering and disordering rates will have approximately the same magnitude, and these become equal at some limiting value of S. Fully ordered alloys will partially disorder and disordered alloys will partially order to this pseudo-equilibrium, steady-state value of S.

Liou and Wilkes (1979) applied an almost identical theoretical radiation disorder model, as the one described above, to the Cu_3Au superlattice to determine the resulting long-range order parameter, S, as a function of temperature for a series of dose rates. The results and assumed variables are shown in Figure 3.18. Interstitial ordering under

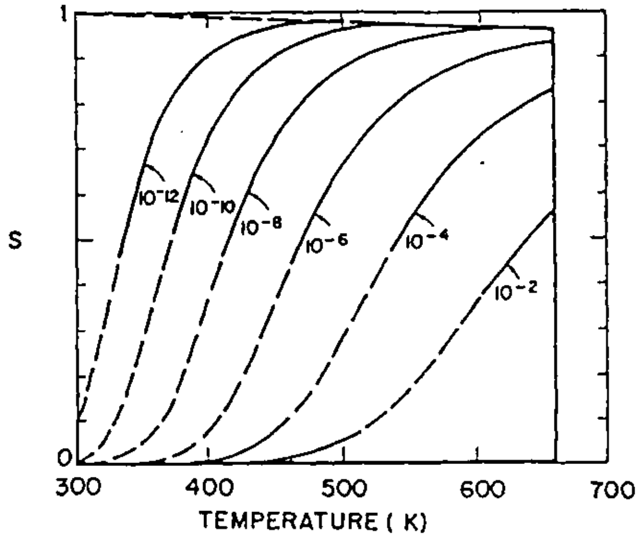

Figure 3.18. The steady state long-range order parameter of Cu_3Au predicted by Liou and Wilkes (1979) for the various irradiation rates indicated in dpas^{-1}. The upper dashed line is the equilibrium value of S in the absence of irradiation. The lower parts of the irradiation curves are dashed to indicate the lower reliability of the model at low S values. (Assumed activation energies are $E_v^F = 1.28$ eV and $E_v^M = 1.4$ eV).

irradiation was neglected on size factor arguments. As predicted, high temperatures favour ordering and low temperatures favour disordering. The temperature regime in which fully ordered alloys disorder and disordered alloys reorder to some steady-state value of S is dependent on the displacement rate. For the Cu_3Au system, below T_c, an increase in the displacement rate increases the disordering component of equation (56) more than the ordering component. Thus, the temperature regime in which a steady-state value of S is observed, is higher, the greater the displacement rate.

Experimental evidence for simultaneous disordering and ordering under electron irradiation has been reported at intermediate temperatures where an equilibrium steady-state value of S is reached. Such effects have been observed in Zr_3Al between 575K and 775K under 1 MeV electron irradiation (Carpenter and Schulson (1978)), in Mg_3Cd between 213K and 300K under 1 MeV electron irradiation (Butler (1978)) and in Ni_3Al between 313K and 575K under 650 kV electron irradiation (Liu et al (1981)).

CHAPTER 4

EXPERIMENTAL PROCEDURE

4.1. Alloy Preparation

Table 4.1. lists the ordered alloys investigated in the present work. All except Mg_3Cd were prepared by melting weighed quantities of the constituent metals in an argon arc furnace using a non-consumable electrode with a water cooled copper hearth. Each ingot was remelted at least three times before final casting into a figure shaped ingot ∿50 g in weight. The alloy Mg_3Cd was kindly provided by Magnesium Electron Limited in the form of a 25 mm diameter sand cast rod. The ingots were sealed in an argon atmosphere in silica tubes and given the corresponding homogenisation treatment shown in Table 4.2.

Electron microprobe analysis showed that the constituents of all the alloys were within ± 2 wt% of the stoichiometric composition as shown in Table 4.1.

4.2. Electron Irradiation

The electron irradiations were carried out in an AEI EM7 high voltage electron microscope operating over a range of accelerating voltages from 200 kV to 1000 kV. The microscope was equipped with double tilt side entry heating and cooling stages. The hot stage (maximum temperature 1000 K) consisted of a miniature coil furnace as shown in Figure 4.1. The cooling stages were of the continuous gas-flow design and employed liquid nitrogen and liquid helium as coolants to attain lowest temperatures of 120 K and 10 K respectively. A diagram of the nitrogen cold stage is shown in Figure 4.2.

4.2.1. Characteristics of the Electron Beam and its Interaction with the Specimen

An accurate knowledge of the current density as a function of position in the beam profile is important for two reasons,

(i) for accurate determination of the electron flux,

(ii) for calculation of the magnitude of the heating effect of the beam.

The total electron current falling onto the screen, which is electrically insulated from the microscope, was measured using an electrometer. Typical beam currents of the order of 0.02μA were measured with an accuracy of ± 5%.

Table 4.1. Alloy Composition

Alloy	Constituent Elements	Weight %	Atomic %
Ni_3Al	Ni	87.49	76.24
	Al	12.51	23.76
Ni_3Fe	Ni	75.93	75.01
	Fe	24.07	24.99
NiAl	Ni	66.85	48.12
	Al	33.15	51.88
FeAl	Fe	69.48	52.33
	Al	30.52	47.67
Mg_3Cd	Mg	37.35	73.35
	Cd	62.65	26.65

Table 4.2. Homogenisation Heat Treatment

Alloy	Temperature (°C)	Time (hrs)
Ni_3Al	1150	36
Ni_3Fe	1050	36
NiAl	1250	36
FeAl	1150	36
Mg_3Cd	400	24

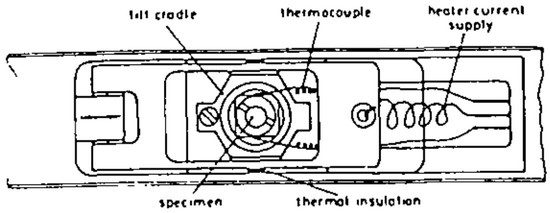

Figure 4.1. Side entry double tilt hot stage. Swann (1978).

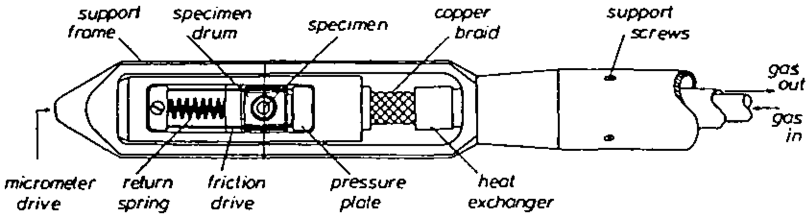

Figure 4.2. Side entry double tilt cold stage. Swann and Lloyd (1974).

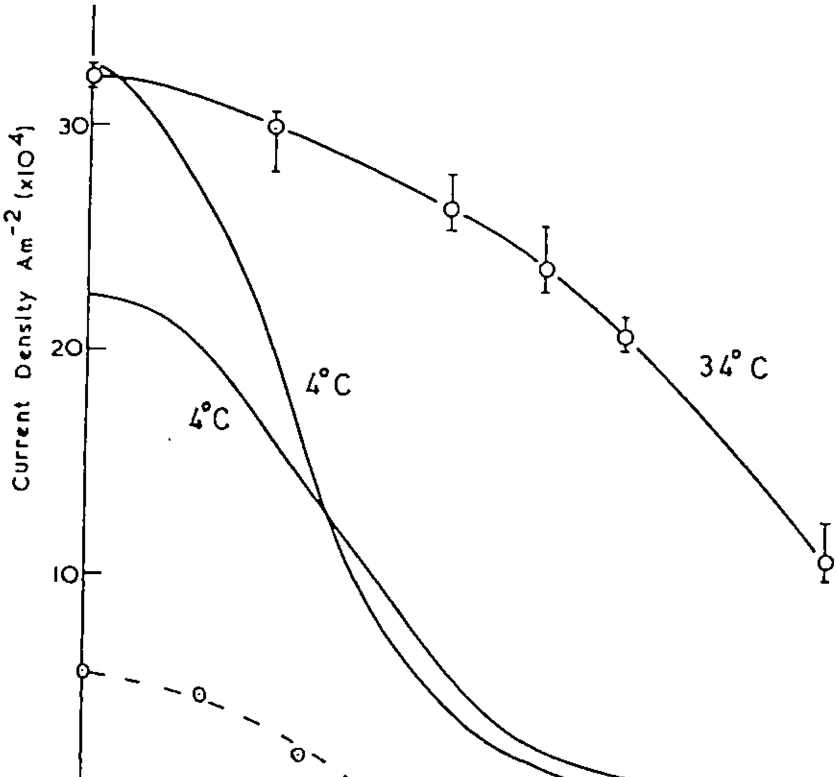

Figure 4.3. 1 MeV beam intensity profiles and the corresponding temperature rise in stainless steel. The dotted line represents the intensity profile of a typical beam current used in the present work.

The focused beam profile was determined by recording the beam photographically, without over exposing the film, and scanning the resultant negative with a microphotodensitometer. Previous investigations (Gale and Hale (1961)) have shown that the intensity distribution is symmetrical about the beam axis and can be represented by the Gaussian relation:

$$I(r) = I_o \exp(- r^2/a^2) \qquad (57)$$

where r is the distance from the beam axis, a is the effective beam radius and I_o the peak intensity. Measurement of the beam profile offers the most accurate control of the temperature rise due to beam heating. The magnitude of this effect has been investigated using both theoretical heat transfer calculations (Gale and Hale (1961)) (Fisher (1970)) and experimental techniques. The experimental techniques include straightforward calorimeter methods (Makin (1971a)) and the use of physical processes which are sensitive to temperature, e.g. the annealing of Frank loops (Kritzinger and Ronander (1974)), order $\rightleftharpoons$ disorder transformations (Laidler et al (1976)) and changes in the critical accelerating voltage (Fukamachi and Kikuchi (1975)). The results of these investigations are remarkably consistent and verify the relationship

$$\Delta T \sim \frac{I_o\ a^2}{K} \rho$$

where ΔT is the temperature rise, I_o is the maximum beam intensity, a is the effective beam radius, ρ is the density and K the thermal conductivity.

Another important consideration in evaluation of the heating effect of the beam is the proximity of the irradiated area to the foil edge. Heat transfer calculations (Garner et al (1975)) indicate that irradiations performed a few beam diameters or less from the foil edge can lead to significant distortions of the temperature rise profile and yield an additional increase as large as 20-50%. Figure 4.3. shows three 1 MeV electron beam profiles and the corresponding temperature rise in stainless steel measured by Makin (1971a) using a calorimeter technique. The dotted line represents the intensity profile of a typical beam current used in the present work. Such low intensity beam currents were attained using a small condenser aperture (∿ 500 μm) and minimum bias settings. Since the irradiations were carried out close to the edge of the foil it was estimated that the maximum beam heating was 5 K for each of the alloys investigated.

4.3. Measurement of Changes in S During Electron Irradiation Using Electron Diffraction

Electron diffraction has been used to monitor changes in the degree of long-range order during electron irradiation because the intensity of a superlattice reflection is directly proportional to S^2 (see Chapter 2.1.2.). Diffraction patterns were recorded sequentially from the irradiated volume and the intensities of the superlattice reflections, I_S, and fundamental reflections, I_F measured. Values of S were determined using the following expression

$$S_{\phi t} = \left[\left(\frac{I_S}{I_F}\right)_{\phi t} \Big/ \left(\frac{I_S}{I_F}\right)_{\phi t = 0} \right]^{1/2} \qquad (58)$$

where ϕ is the irradiation flux and t the irradiation time. Although this technique is experimentally straightforward and allows convenient variation of experimental conditions, it is necessary to be aware of its limitations and factors which can affect the determination of an accurate value of S. These are discussed in the following sections.

4.3.1. Electron Diffraction in the Kinematical Condition

When electron diffraction is used to measure changes in S the specimen should be in a kinematical condition as this is assumed in the structure factor calculations from which the S^2 relationship of the superlattice reflection intensity is derived (Appendix I). The kinematical theory (Makin (1968b)) assumes that, although part of the incident beam is diffracted by each plane of atoms traversed by the wave within the crystal, the amplitude of the incident beam is unaltered. Hence the total amplitude of the diffracted beams must be small and if a wave is scattered, it is scattered only once, i.e. there is no rescattering or interaction between the diffracted and undiffracted beams. The diffracted intensity is calculated by adding together the amplitudes of the waves scattered by the individual atoms, taking due account of their phase differences. The closest useful approximation to this condition experimentally is to:

(i) use thin areas of the specimen where rescattering and multiple diffraction is minimised.

(ii) orientate the specimen a few degrees away from the zone axis, so that only one systematic row of the diffraction pattern is excited.

4.3.2. Electron Diffraction in a Crystalline Specimen Containing a High Density of Defect Loops

The diffraction pattern of a crystalline specimen of moderate thickness consists, in general, of a few strong low order reflections. Upon introducing a high density of lattice defects into the specimen, by, for example, irradiation above the threshold displacement energy, the pattern changes. The (originally) strong low order reflections decrease in intensity whereas the intensities of the (originally) weak, or even invisible, higher order reflections increase. This effect was first reported by Urban (1973) in a low temperature in-situ HVEM study of radiation damage in copper and nickel. Figure 4.4. shows the effect occurring in nickel under 1 MeV irradiation at 120 K.

The intensity redistribution can be explained qualitatively by reference to the weak beam imaging technique of lattice defects, (Cockayne et al (1969)), where the intensity of a weak beam is strongly enhanced in the vicinity of a lattice defect when the strain field is sufficiently high to bend the planes into the Bragg position. If the density of defects is so large that every electron passing through the specimen successively encounters the strain fields of a number of defects, then the intensity of the originally weak beam must increase appreciably. Since the total number of incident electrons is constant then the originally strong beams must become weaker. More recently Wilkens and Rapps (1977) have developed a statistical theory to describe the effect. Since the magnitude of the intensity redistribution increases with increasing defect density and foil thickness, they concluded that it is controlled by the total number of defects encountered by an electron passing through the specimen. The theory has been successfully applied to the evaluation of the dislocation density in cyclically deformed copper (Rapps et al (1978)).

It is clear that if displacement damage leads to the build-up of a sufficiently high density of defect loops, then this intensity redistribution effect will be superimposed on any change in the superlattice intensities due to disordering. Hence the technique used for measuring changes in S will be subject to error. The density of defect loops nucleated under irradiation increases as the temperature decreases (Makin (1970)), and so the intensity redistribution will be greatest in thick foils under low temperature irradiation.

Figure 4.4.

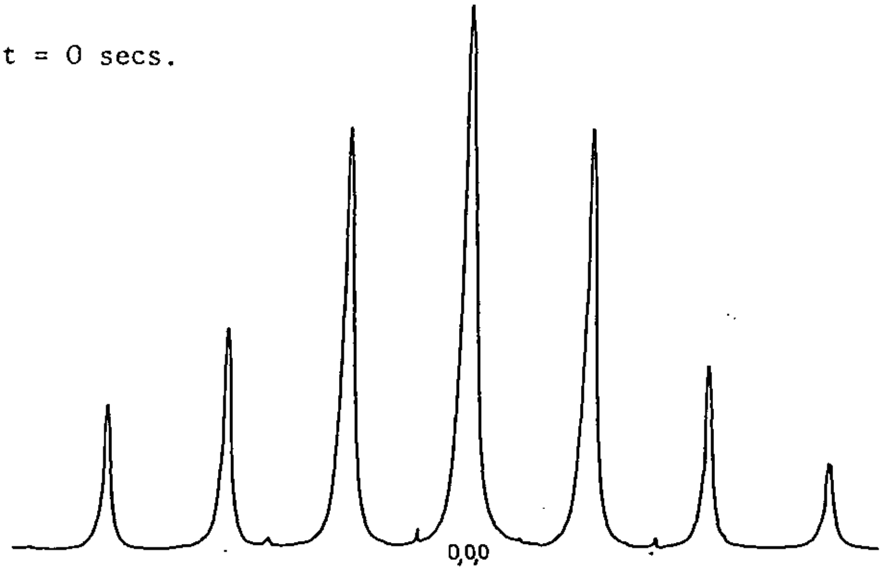

t = 0 secs.

t = 500 secs.

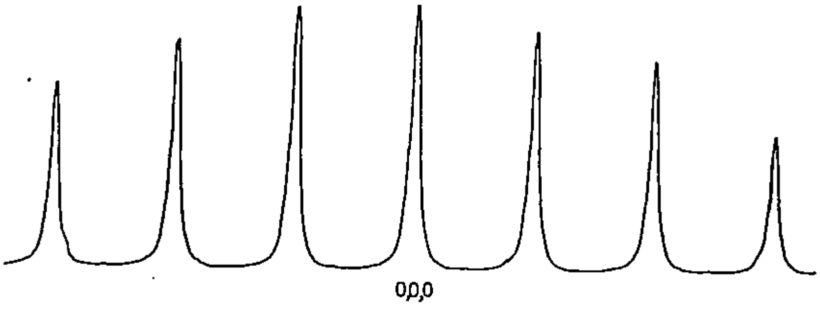

The observed change in the diffracted intensities of the reflections of <100> orientated nickel (foil thickness $\sim$2000 Å) under 1 MeV irradiation at 120K with a flux of 10^{19}e.cm^{-2}sec^{-1}. (t is the irradiation time).

To eliminate the effect it is necessary to prevent the formation of point defect loops. This can be achieved if the irradiations are carried out in thin foils where the foil surfaces act as sinks and prevent aggregation. Using equation (29), which is equal to

$$x = 0.66\lambda \left(\frac{\nu_i}{\sigma_d Z \phi}\right)^{1/4}$$

the variation in the width of defect denuded layer has been calculated as a function of temperature for nickel and magnesium. The results with the assumed values for the parameters are shown in Figure 4.5. At any particular temperature the 'safe' thickness, in which loops do not form, is greater for magnesium than nickel because magnesium has a lower interstitial migration energy. As the temperature is lowered the safe thickness decreases until it is not possible to irradiate only within the denuded layer.

In spite of these limitations it has been found that in practice reproducible measurements of the disordering response can be attained, even at low temperatures, if certain conditions are applied. These are

(i) the irradiations should be carried out in thin foils (< 1000 Å)

(ii) only the lowest ± g superlattice/fundamental ratios should be used to determine values of S.

At the lowest temperatures used in this investigation (∿15 K) it was not possible to prevent some rescattering into the higher order reflections, but this appeared to come from the essentially undiffracted (0,0,0) beam which became slightly weaker as the irradiation proceeded. To monitor the extent of the intensity redistribution a criterion employed was that the fundamental reference intensities should not change by ± 10%. This allowed for intensity changes due to surface contamination and an increase in the background level as the superlattice intensity is diffused over the whole range of 2Θ. (Cullity (1967)). Figure 4.6. shows the disordering response of Ni_3Al irradiated with 1 MeV electrons at room temperature for three different foil thicknesses. At 1000 Å the fundamental reference intensities remain constant (as Figure 4.5. predicts) and so changes in the superlattice intensities can be directly related to changes in S. However, as the foil thickness increases, evidence of rescattering is apparent in the change in the fundamental reference intensities which at a thickness of 3000 Å totally masks the disordering response.

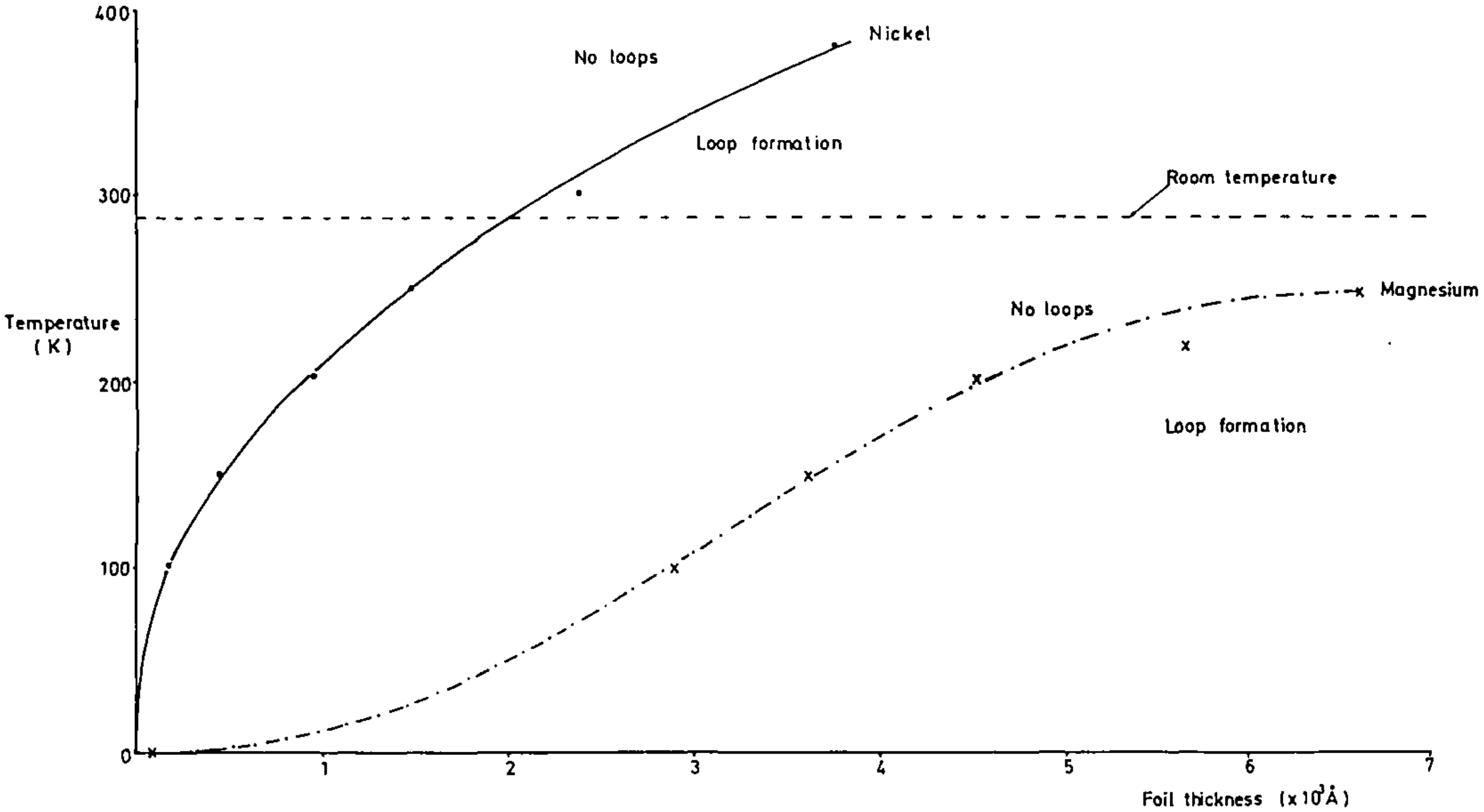

Figure 4.5. Variation in the width of the defect denuded layer as a function of foil thickness and temperature in nickel and magnesium under 1000 kV irradiation. (Assumed parameters:- Z = 100 and ϕ=1 x 10^{19}e.cm^{-2}s^{-1}. For Ni E_i^M = 0.15eV and σ_d = 50 barns. For Mg E_i^M = 0.03 eV and σ_d = 100 barns).

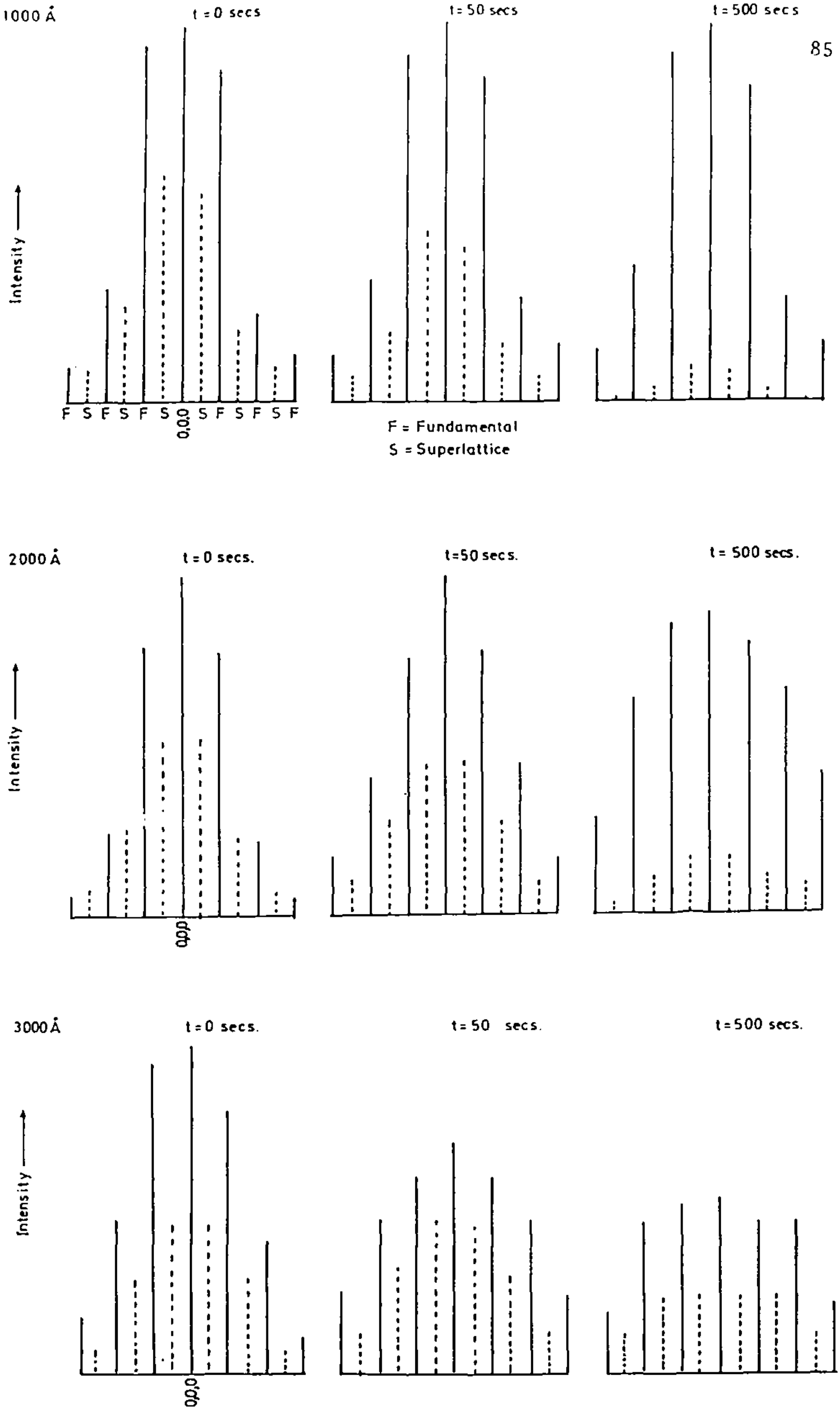

Figure 4.6. Disordering response of <110> Ni_3Al under 1 MeV electron irradiation at 305K as a function of foil thickness.

4.3.3. The Anisotropy of Superlattice Reflection Intensity Change

When using electron diffraction to monitor changes in S it is necessary to be aware of an anisotropy that exists in the change of the superlattice reflection intensities. The presence of this anisotropy, which can be shown to exist by structure factor calculations (see below), can complicate the study of the effect of orientation on the disordering response. However, the anisotropy will only be present when the atomic displacements are unidirectional, i.e. momentum is transferred in the electron - atom collision only in a direction parallel to the incident electron beam, and there are no secondary displacements out of this direction. On this basis, see Chapter 3.1.1. the following analysis represents a limited theoretical approach to displacement damage in ordered materials. This treatment is a development of the work of Mukai (1981).

$L1_2$ AB_3 Alloys

Consider a fully ordered $L1_2$ AB_3 alloy as shown in Figure 4.7. The structure factor F for any hkl reflection can be calculated from equation (3) where

$$F_{hkl} = \sum_{1}^{n} f_n \, e^{2\pi i(hu_n + kv_n + lw_n)}$$

Since there are four atoms in the unit cell

A at (0,0,0)
B at (1/2,1/2,0)
B at (0,1/2,1/2)
B at (1/2,0,1/2)

The structure factor F_{hkl} is equal to

$$F_{hkl} = f_A \, e^{2\pi i(0)} + f_B \, e^{\pi i(h+k)} + f_B \, e^{\pi i(k+l)} + f_B \, e^{\pi i(h+l)}$$

If the crystal is orientated with the [110] direction, a mixed atom row, parallel to the incident electron beam then the structure factors of the superlattice reflections observed in the diffraction pattern are equal to

$$F_{(\bar{1}10)} = F_{(1\bar{1}0)} = f_A - f_B$$

$$F_{(001)} = F_{(00\bar{1})} = f_A - f_B$$

If [110] irradiation causes displacements only in this direction, random rearrangement of the displaced atoms will lead to a site occupancy as shown in Figure 4.8., i.e.

Figure 4.7.

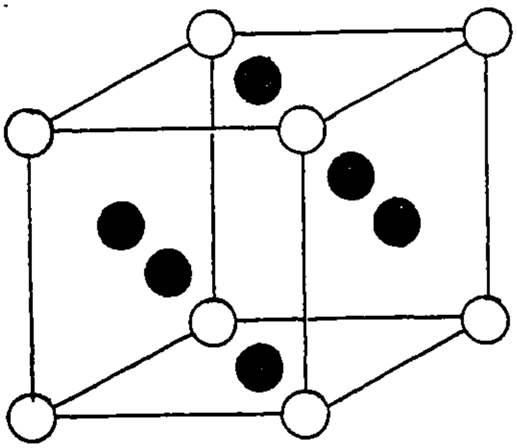

Atomic arrangement in a fully ordered AB_3 alloy with an $L1_2$ superlattice.

Figure 4.8.

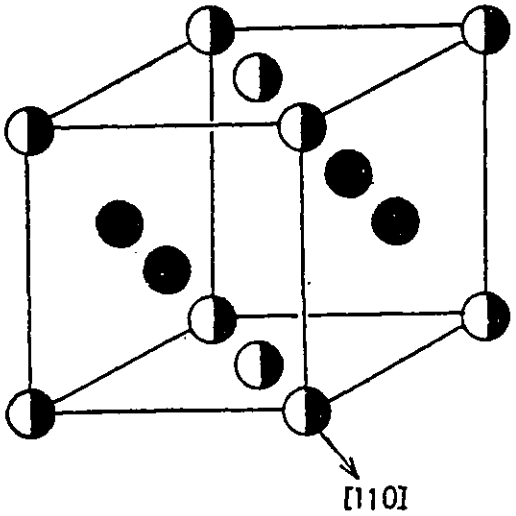

Atomic arrangement in an AB_3 alloy with an $L1_2$ superlattice after unidirectional displacements in the [110] direction.

Figure 4.9.

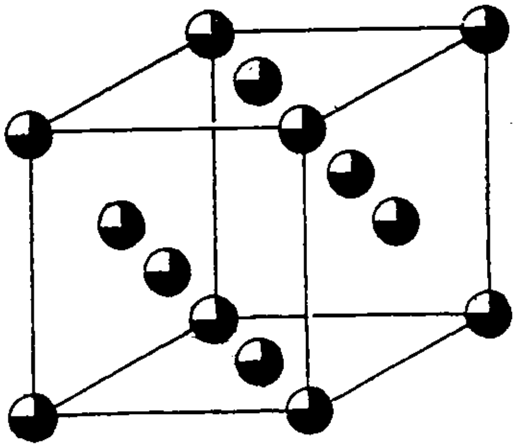

Fully disordered AB_3 alloy with a f.c.c. structure.

1/2(A + B) at (0,0,0)
1/2(A + B) at (1/2,1/2,0)
B at (0,1/2,1/2)
B at (1/2,0,1/2)

The structure factor is now equal to

$$F_{hkl} = 1/2(f_A + f_B)\ e^{2\pi i(0)} + 1/2(f_A + f_B)\ e^{\pi i(h+k)} + f_B\ e^{\pi i(k+l)} + f_B\ e^{\pi i(h+l)}$$

Therefore

$$F_{(\bar{1}10)} = F_{(1\bar{1}0)} = f_A - f_B$$
$$F_{(001)} = F_{(00\bar{1})} = f_A - f_B$$

Although the alloy has been fully disordered in the [110] direction, the structure factors of the superlattice reflections observed in the diffraction pattern have remained unchanged. However, calculations of the structure factors of other superlattice reflections show that these have fallen to zero, i.e. the decrease in the superlattice intensity is anisotropic,
viz:
For beam direction [101]:

$$F_{(\bar{1}01)} = F_{(10\bar{1})} = F_{(010)} = F_{(0\bar{1}0)} = 0$$

For beam direction [011]:

$$F_{(01\bar{1})} = F_{(0\bar{1}1)} = F_{(100)} = F_{(\bar{1}00)} = 0$$

Hence the alloy would still appear fully ordered in the [110] orientation and evidence of disordering would only be found by tilting to another <110> orientation. However, it is experimentally well documented, (Butler and Swann (1977), Carpenter and Schulson (1978)), that the superlattice intensities in the diffraction pattern of a <110> orientated $L1_2$ alloy do decrease in intensity when there is displacement damage in this direction. From the structure factor calculations it is evident that there must be secondary displacements at 60° to the incident beam direction along the <011> and <101> mixed atom rows. The subsequent arrangement of atoms is shown in Figure 4.9.; the alloy is now fully disordered. Therefore

$$F_{(\bar{1}10)} = F_{(1\bar{1}0)} = 0$$
$$F_{(001)} = F_{(00\bar{1})} = 0$$

For irradiation in the <100> direction, which is a like atom row, similar arguments can be used to show that order will only be destroyed if displacements occur at 45° to the incident beam direction along a <110> mixed atom row. Therefore, whether irradiation is carried out along mixed or like-atom rows, any change in the observed superlattice intensities corresponds to displacements at 60° and 45° respectively to the incident beam direction.

The Effect of Domain Size

In the fully ordered state the AB_3 $L1_2$ alloy has a structure in which the A atoms occupy the corner sites and the B atoms the face-centred sites (see Figure 4.7). Three other equivalent unit cells can be formed which are characterised by the displacement of A atoms to B sites by a shift of 1/2[110], 1/2[101] and 1/2[011] as shown in Figure 4.10 . The effect of having a range of site occupancies, i.e. a small antiphase domain size within the irradiated area, has no effect on the anisotropy of the superlattice intensity change. Again this can be shown by structure factor calculations. For example, in the fully ordered state the structure factor of a 1/2[101] antiphase domain is equal to

$$F_{hkl} = f_B\, e^{2\pi i(0)} + f_B\, e^{\pi i(h+k)} + f_A\, e^{\pi i(h+l)} + f_B\, e^{\pi i(k+l)}$$

If the crystal is orientated with the [110] direction parallel to the electron beam then the structure factors of the superlattice reflections observed in the diffraction pattern are equal to

$$F_{(\bar{1}10)} = F_{(1\bar{1}0)} = f_B - f_A$$

$$F_{(001)} = F_{(00\bar{1})} = f_B - f_A$$

If [110] irradiation causes displacements only in this direction, random rearrangement of the displaced atoms will lead to a site occupancy as shown in Figure 4.11. The structure factor is now equal to

$$F_{hkl} = f_B\, e^{2\pi i(0)} + f_B\, e^{\pi i(h+k)} + 1/2(f_A+f_B)e^{\pi i(k+l)} + 1/2(f_A + f_B)\, e^{\pi i(h+l)}$$

Therefore

$$F_{(\bar{1}10)} = F_{(1\bar{1}0)} = f_B - f_A$$

$$F_{(001)} = F_{(00\bar{1})} = f_B - f_A$$

i.e. the structure factors are unchanged.

Figure 4.10.

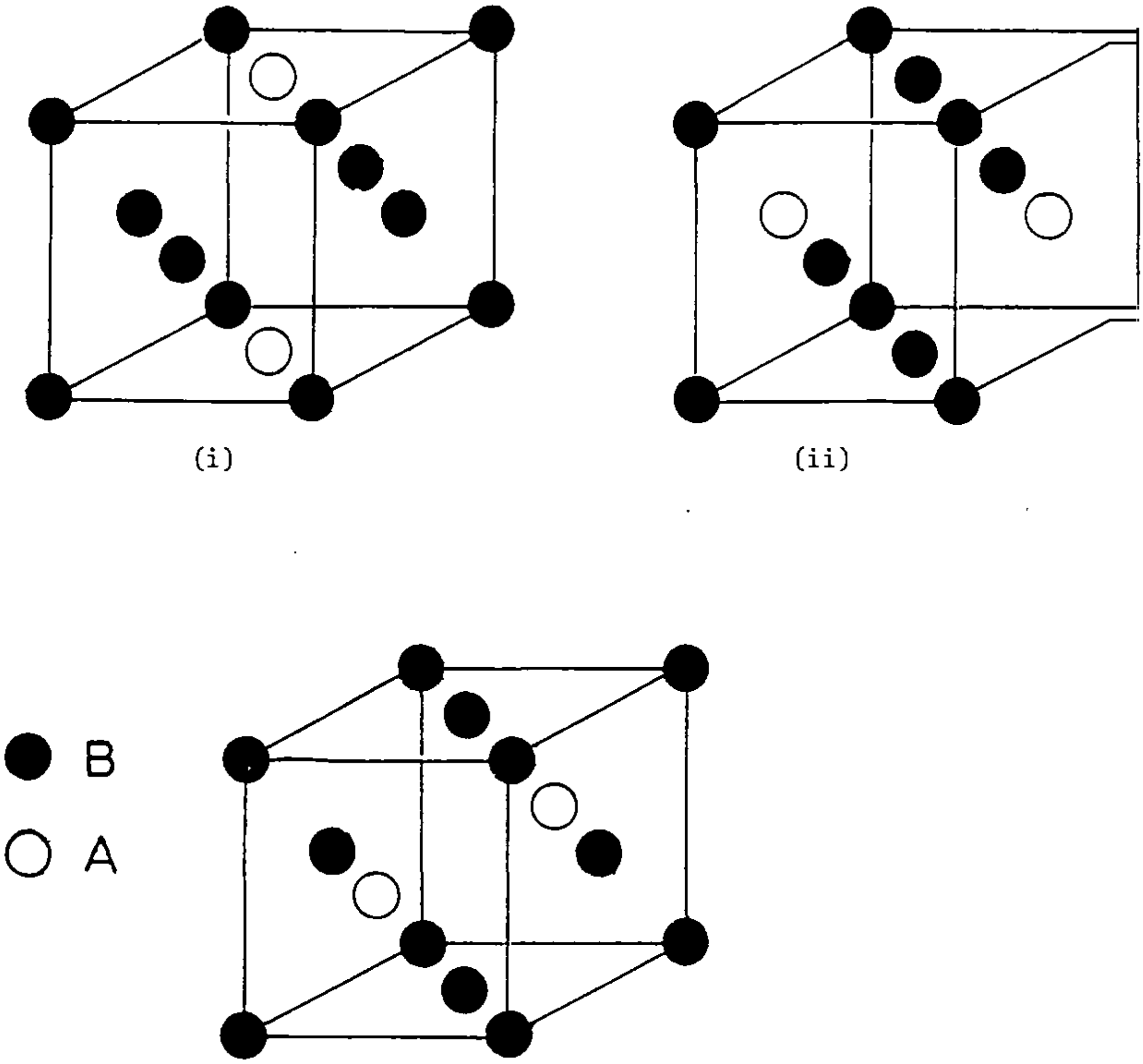

(i)

(ii)

(iii)

Three equivalent unit cells of the $L1_2$ structure characterised by the displacement of A atoms to B sites by a shift of (i) 1/2[110], (ii) 1/2[101] and (iii) 1/2[011].

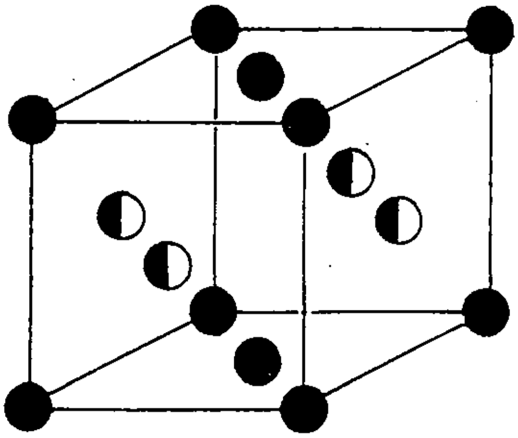

Figure 4.11. Atomic arrangement of the structure shown in Figure 4.10(ii) after unidirectional displacements in the [110] direction.

Disordering will only be observed if displacements occur at 60° to the incident beam direction. This is also true for the 1/2[110] and 1/2[011] antiphase domains and so domain size will have no effect on the anisotropy of superlattice intensity change.

B2 AB Alloys

There are no superlattice reflections present in the electron diffraction pattern of a B2 crystal orientated with the [111] mixed atom row direction parallel to the electron beam. Therefore, it is not possible to consider the superlattice intensity change from unidirectional displacements only in this direction. However, it is clear that whenever disordering is observed from a [100] or [110] irradiation displacements must have occurred in the <111> direction.

DO_{19} AB_3 Alloys

Within the limited regime of unidirectional displacements there is also anisotropy in the superlattice of the DO_{19} AB_3 alloys. The structure factor calculations are given in Appendix III.

4.3.4. Photography and Measurement of the Diffracted Electron Intensity

The electron diffraction patterns were recorded on Kodak 4489 photographic film and developed in ID 11 for 4 minutes at 20°C. In order to quantify changes in the diffracted electron intensity and hence the degree of order, S, the photographic emulsion was calibrated in terms of its optical density (D) against exposure (E). The photographic emulsion consists of a suspension of silver halide grains in gelatin. When these are exposed to radiation a latent image is formed which on development is reduced to a visible image of black metallic silver. The optical density of the image on the negative is defined as

$$D = \log \emptyset/\emptyset_o \qquad (59)$$

where $\emptyset_o$ is the intensity of the incident and $\emptyset$ the intensity of the transmitted radiation. The exposure is the product of the exposure time and the intensity of the radiation at the surface layer. Figure 4.13. shows the density/exposure relationship under 1000 kV and 200 kV electron irradiation. The response can be represented by the equation

$$D = D_s(1 - e^{-(naE)}) \qquad (60)$$

where D_s is the saturation density, n is the number of grains hit by an electron, a the area of the developed grain. For small values of E the expression reduces to

$$D = D_s \, naE = kE \qquad (61)$$

where k is a constant. Thus there is a linear relationship between D and E, because D is proportional to the number of developed grains per unit area and the latter is proportional to the number of electrons per unit area. This linearity holds for most combinations of emulsion and developer up to a density of between 1.0 and 2.0. After this the slope of the response diminishes as the number of grains that can be exposed is reduced and the density approaches saturation. In the present work all the measurements were made below a density of 1.5.

Figure 4.12. shows the variation in the relative speed of the film as a function of electron energy (Alderson(1974)). The speed is a measure of the exposure required to produce a given density, i.e. the greater the speed the lower the required exposure. Such a variation exists because the higher energy electrons pass through the emulsion without losing much of their energy. However, in the present practical situation the speed of the film is independent of electron energy between 200 kV and 1000 kV. This is because the higher energy electrons increase the intensity of the backscattered electrons and X-rays emitted from the emulsion support and the steel backing plate of the film holder, which also expose the emulsion. Figure 4.13. shows that the density/exposure relationship of equation (60) is valid up to $D \sim 1.5$ for the complete range of electron energies used in the present work.

The diffracted electron intensity was measured using a Joyce-Loebl double beam automatic recording microdensitometer. A schematic diagram is shown in Figure 4.14. Light from a source is divided into two narrow beams by passing through an arrangement of slits and lenses. The reference beam passes through a manually adjustable density wedge and allows a background level to be set. The second beam passes through the film negative and is incident on a photomultiplier. The out-of-balance photomultiplier current drives the measuring wedge until the intensity difference between the reference and the measured beam is zero. The measuring wedge has a pen attached to it, allowing the intensity to be recorded directly. Figure 4.15. shows a typical series of diffraction patterns taken of <0001> Mg_3Cd under 400 kV electron irradiation and the corresponding microdensitometer traces.

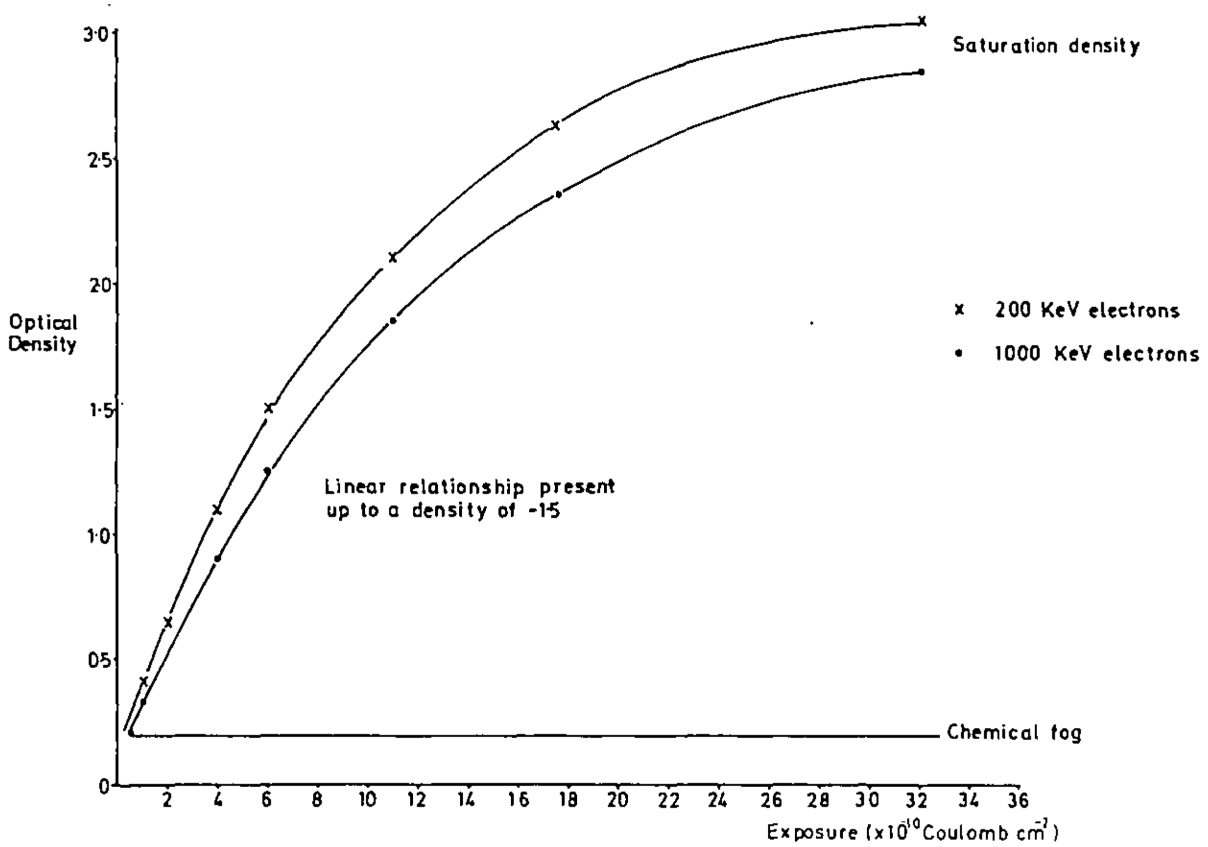

Figure 4.13. Variation of density with exposure of Kodak 4489 film to 200 keV and 1000 keV electron irradiation.

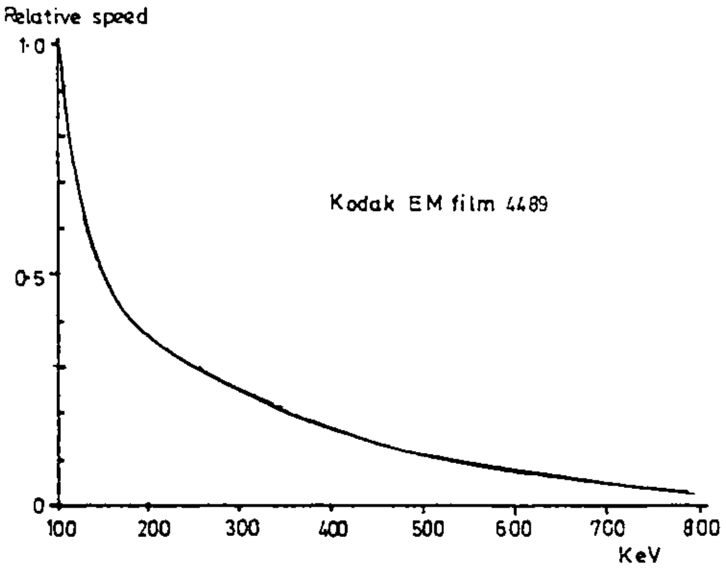

Figure 4.12. Variation of relative speed with electron energy in the range 100 - 800 keV.

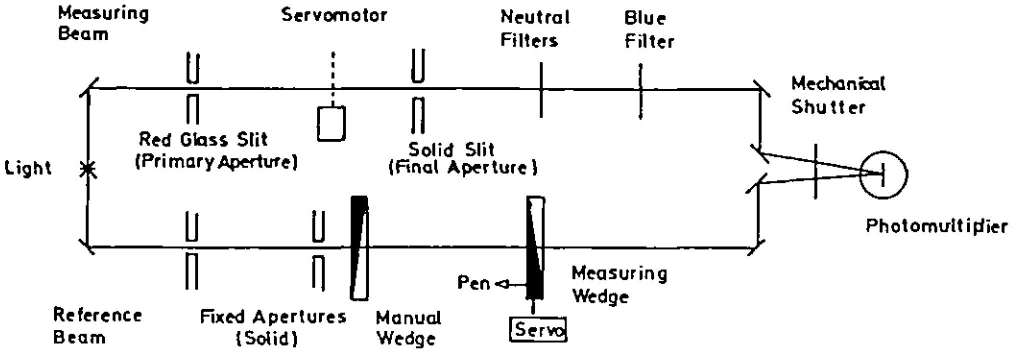

Figure 4.14. Schematic representation of a microphotodensitometer.

The intensity of each diffracted beam was measured in terms of the area under the microdensitometer trace above background level. The errors in the area measurement resulted in errors in S of ∿ 5% at S ≃ 1 increasing to ∿ 20% for S ≃ 0.2.

4.4. Electron Microscopy Specimen Preparation

The ingots of each alloy were cut into ∿ 0.5 mm thick slices using a diamond saw slitting wheel and given heat treatments shown in Table 4.3. to develop a fully ordered structure. Discs 3 mm in diameter were then spark machined from the slices. These were then polished down further to a thickness of ∿ 0.1 mm using 1200 grade SiC paper to prevent deformation and cracking. Thin foils were prepared by using a Struers commercial jet polishing machine with the electrolytes and approximate conditions shown in Table 4.4.

4.5. Evaluation of the Vacancy Migration Energy in Mg_3Cd

Analysis of the disordering response of ordered alloys under irradiation frequently requires assumptions to be made of the defect migration energies. The activation energy for vacancy migration in Mg_3Cd has been evaluated from an X-ray diffraction study of thermal ordering and a transmission electron microscopy study of antiphase domain growth. A preliminary investigation was also made of point defect loop growth in the HVEM under 1000 kV irradiation.

4.5.1. X-ray Diffraction Study of Ordering in Mg_3Cd

The kinetics of thermal ordering in Mg_3Cd have been investigated using X-ray diffraction at temperatures between 298K and 352K, in order to estimate the activation energy for ordering and vacancy migration. X-ray diffraction has been used to monitor changes in S since the intensity of a superlattice reflection is directly proportional to S^2 (see Chapter 2.1.2.).

Disc specimens 25 mm in diameter and 5 mm in thickness were cut from the bar provided by Magnesium Electron. The alloy was prepared by the sand-casting technique and consequently has a grain size > 150 μm which was too large to generate signals of reproducible intensity from which S could be calculated. Attempts to create a small equiaxed grain size were unsuccessful and an inhomogeneous texture was produced from which the intensity measurements were irreproducible. Therefore, the intensity measurements were carried out in-situ using a small furnace in the diffractometer. The ratio of the intensities of the $(10\bar{1}0)$ superlattice (I_S) and (0002) fundamental (I_F) reflections was measured periodically until it reached a constant value of $(I_{S_{max}}/I_{F_{max}})$. $(I_{S_{max}}/I_{F_{max}})$ was assumed to represent the intensity ratio when S is equal to unity. Davies and Stoloff (1964) have shown that the equilibrium degree of order below 373K is unity. S was determined from the relation

$$S = \left(\frac{I_S/I_F}{I_{S_{max}}/I_{F_{max}}}\right)^{\frac{1}{2}} \qquad (61)$$

The specimens were examined in a Philips X-ray diffractometer (PW 1049) using a CuK_α radiation source. A proportional counter with a graphite monochromator was employed to measure the diffracted intensity. To minimise the experimental errors the specimens were stored in liquid nitrogen, after quenching from 583K, to reduce the possibility of a change in the degree of order. The copper block containing the furnace element was held at the annealing temperature before the specimen was clamped into position, thus the specimen reached the annealing temperature within 1 minute. After a steady-state ratio had been reached at each of the annealing temperatures, the temperature was raised to 370K and the intensities were monitored further until they remained constant. The steady-state ratio at the higher temperature was assumed to represent S equal to unity and this was used in equation (61). This procedure ensured that errors were not introduced by assuming non-equilibrium intensities represented S equal to unity and was most important at the lower temperatures of 298K and 315K.

4.5.2. Determination of the Activation Energy for Domain Coarsening from the Kinetics of Antiphase Domain Growth

The activation energy for domain coarsening in Mg_3Cd has been determined by measuring the rate of domain growth at 363K, 393K and 408K. The specimens were quenched from 583K and aged at the above temperatures for periods ranging from 30 to 1500 minutes. Electropolished thin foils were prepared by the procedure outlined in Section 4.4. The foils were examined in a Philips EM 301 electron microscope operating at 100 kV.

The APB energy in Mg_3Cd is isotropic (Blackburn (1967)) i.e. there is no tendency for the domain boundaries to lie on preferred planes. Therefore, the mean domain size was calculated from a linear intercept method, which determines the mean distance between APB on randomly orientated straight lines. Several hundred domain boundary intersections were counted to evaluate each experimental point.

Table 4.3. Heat Treatment to Develop a Fully Ordered Structure

Alloy	Temperature (°C)	Time (hrs)
Ni_3Al	900	10
Ni_3Fe	470	500
NiAl	900	10
FeAl	800	24
Mg_3Cd	80	10

Table 4.4. Electropolishing Conditions

Alloy	Electrolyte	Voltage (V)	Temperature (°C)
Ni_3Al	)	22	-50
Ni_3Fe	)20 vol.%	15	-50
NiAl	)Perchloric acid	15	-60
FeAl	)in methanol	12	-50
Mg_3Cd	10 vol.% nitric acid in methanol	15	-40

Figure 4.15.

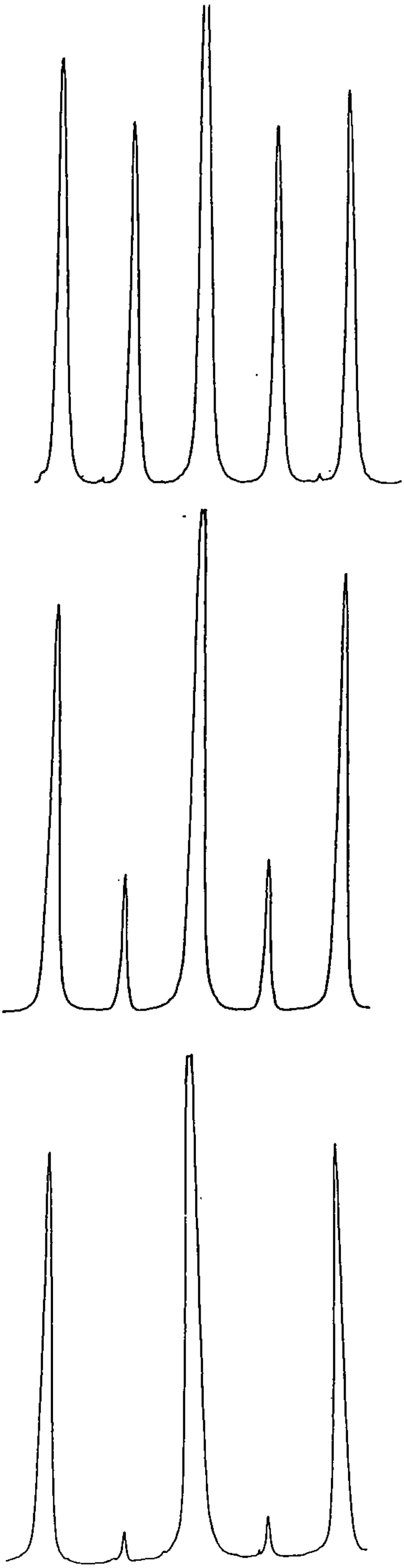

0 secs, S = 1.0

200 secs, S = 0.6

500 secs, S = 0.2

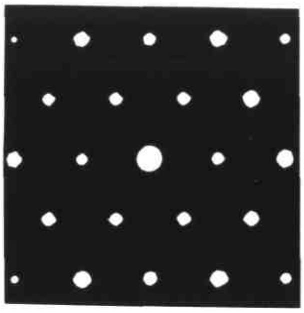

<0001> Mg_3Cd

0 secs, s = 1.0

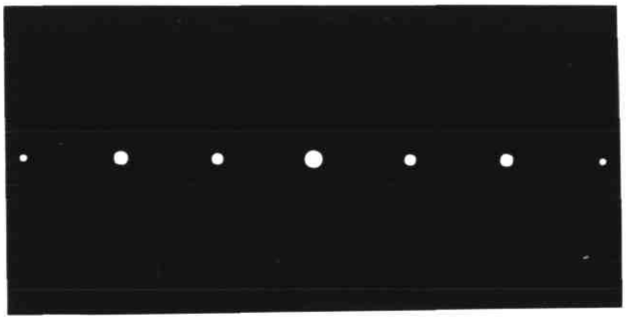

200 secs, s = 0.6

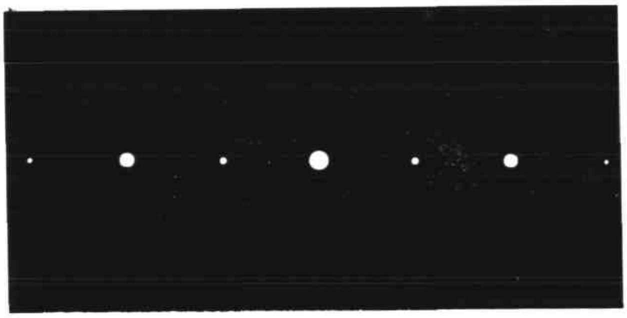

500 secs, s = 0.2

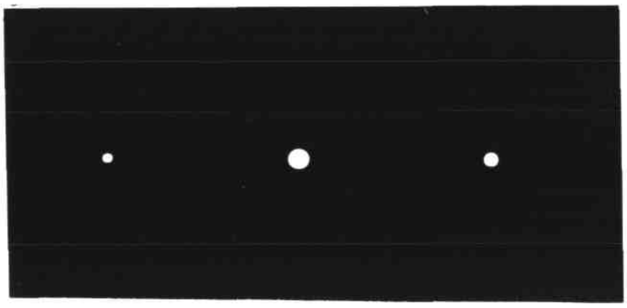

Figure 4.15. Decrease in the superlattice reflection intensities as Mg_3Cd disorders under 400 kV irradiation at 118K. (Incident flux = 1.6×10^{23} $cm^{-2}s^{-1}$)

CHAPTER 5

EXPERIMENTAL RESULTS

The results of this investigation conveniently fall into three categories corresponding to the three different types of crystal structure, i.e. DO_{19}, $L1_2$ and B2. The results for each crystal structure are presented in separate sections which are almost identical in format.

5.1. The Response of Fully Ordered Mg_3Cd (DO_{19} structure) to Electron Irradiation

5.1.1. Effect of Temperature and Accelerating Voltage

The response of fully ordered Mg_3Cd to electron irradiation has been investigated using 400 kV, 700 kV and 1000 kV irradiation at temperatures between 15K and 330K. All the irradiations were carried out with the specimens close to the <110> orientation along a systematic row of the diffraction pattern. The incident flux was $\sim 1.5 \times 10^{19}$ electrons cm^{-2} sec^{-1} for all temperatures above 200K and below this it was lowered to 5×10^{18} electrons cm^{-2} sec^{-1}. Figure 5.1. shows the decrease in S plotted against electron dose (= flux x time) as a function of temperature under 1000 kV electron irradiation. Extended irradiation at 330K and temperatures above caused little change in S. However, as the temperature was lowered the disordering rate increased rapidly. Between 305K and 158K the alloy did not disorder completely and a steady-state value of S was attained. At 118K and temperatures below the alloy became fully disordered. The maximum rate of disordering was observed at 15K.

Figure 5.2. shows the results of Figure 5.1. plotted according to the simple expression for disordering, ($S = S_0 \exp(-K't)$ equation (53)) as ln S versus dose. The linearity implied by this equation is only strictly obeyed at 15K and the disordering cross-section, $\varepsilon\sigma d$, for this temperature has been determined from the slope of the plot. At temperatures above 118K linearity is not adhered to and the alloy only partially disorders to some steady-state value of S. These results can be understood in terms of the theory of Chapter 3.2. which predicts that the alloy will only partially disorder when defects have sufficient mobility to restore order to the lattice. The ln S versus dose plots are not linear because of the reordering component of the response.

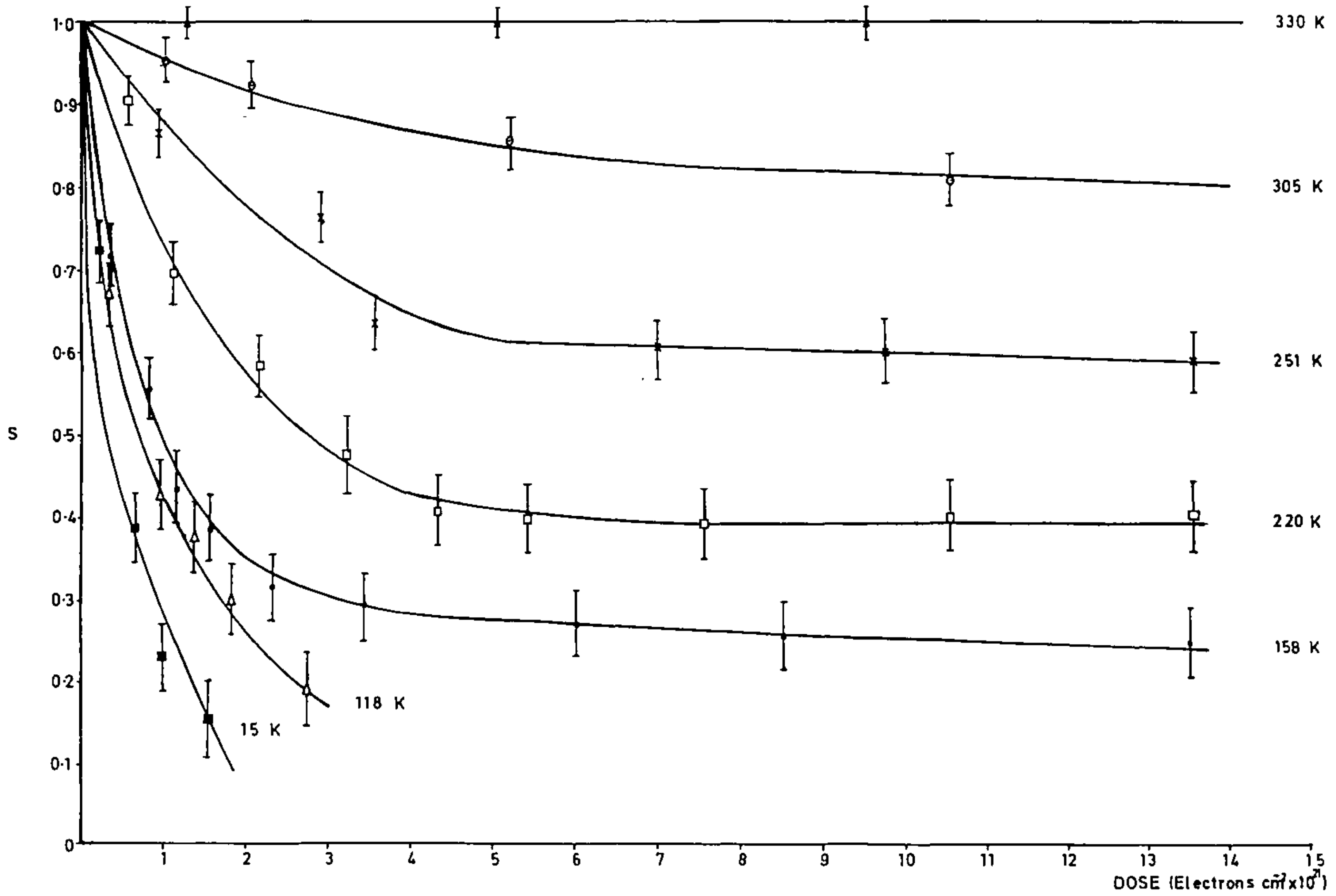

Figure 5.1. The disordering response to 1000 kV electron irradiation of <0001> Mg_3Cd as a function of temperature.

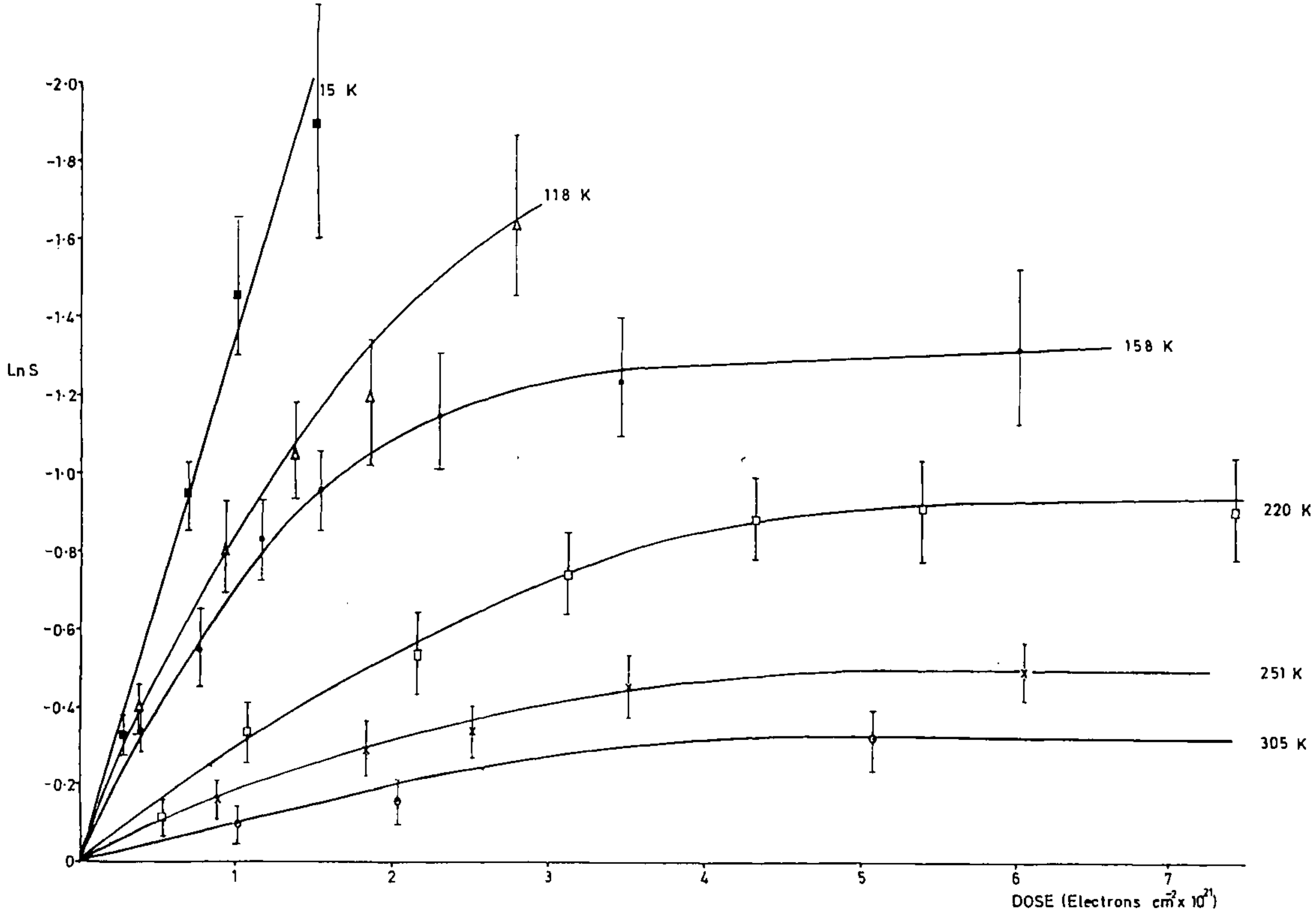

Figure 5.2. The disordering response to 1000 kV electrons irradiation of <0001> Mg_3Cd as a function of temperature plotted as lnS versus electron dose.

Therefore at temperatures above ∿100K the disordering cross-section has been evaluated from the slope of the tangent taken to the initial linear portion of the graph where $S \sim 1$ and the reordering components are very small. The results which are shown in Table 5.1. suggest that the increase in the disordering rate with decreasing temperature is accompanied by an increase in the disordering cross-section. These results do not agree with the simple theory which predicts,

(i) that the temperature dependence of disordering should be explainable only in terms of the decreasing resistance by progressively less mobile defects, and

(ii) that the disordering component of equation (56) is temperature independent, such that the instantaneous ds/dt at $S \sim 1$ is constant.

Table 5.1. Variation in the Experimentally Determined Disordering Cross-Section with Temperature of <0001> Mg_3Cd under 1000 kV Electron Irradiation

Temperature (K)	Disordering cross-section (barns)
305	100
251	234
220	284
158	770
118	850
15	1210

Although the absolute values of $\varepsilon\sigma_d$ determined from the non-linear plots are subject to more error than those from the linear plots, the magnitude of the increase in the disordering rate with decreasing temperature is large enough to show a clear trend which cannot be explained by experimental error. The results imply that in addition to the reordering by progressively less mobile defects being responsible for the temperature dependence of disordering, there is also some temperature dependence of the disordering component of equation (56) which results in an increase in $\varepsilon\sigma_d$ with decreasing temperature.

The response of fully ordered Mg_3Cd to 400 kV and 700 kV electron irradiation at temperatures between 15K and 330K is shown in Figures 5.3. and 5.4. as S versus dose. The response of the alloy was found to be almost identical to that under 1000 kV irradiation in that a steady-state value of S was observed at temperatures between $\sim$150K and 305K, and above $\sim$330K the alloy would not disorder. From ln S versus dose plots of these results the disordering cross-sections were evaluated. The variation in the disordering cross-section with temperature and accelerating voltage is shown in Figure 5.5. The disordering cross-section increases with decreasing temperature for each of the accelerating voltages employed, the increase being slightly greater for the higher energy electrons. At any particular temperature below $\sim$330K the disordering cross-section is greater the higher the electron energy, i.e. the rate of disordering increases with increasing electron energy. Thus with reference to Figures 5.1., 5.3., and 5.4. it can be seen that the steady-state value of S observed at any particular temperature below $\sim$330K decreases with increasing electron energy.

The threshold energy for disordering was found to be between 150 kV and 200 kV at 15K, which is consistent with the displacement of Cd atoms in secondary collisions with the lighter, higher energy Mg primary knock-ons (see Chapter 6.1.).

5.1.2. Effect of Orientation

The orientation dependence of disordering was briefly examined in Mg_3Cd under 400 kV electron irradiation at 158K. The experimentally determined disordering cross-sections are listed in Table 5.2. As predicted in Chapter 3.2. no significant orientation effect was observed.

Table 5.2. Effect of Orientation on the Experimentally Determined Disordering Cross-section in Mg_3Cd under 400 kV Electron Irradiation at 158K

Orientation (uvw)	Disordering cross-section (barns)
<$\bar{2}4\bar{2}3$>	189
<0001>	165
<$10\bar{1}1$>	178

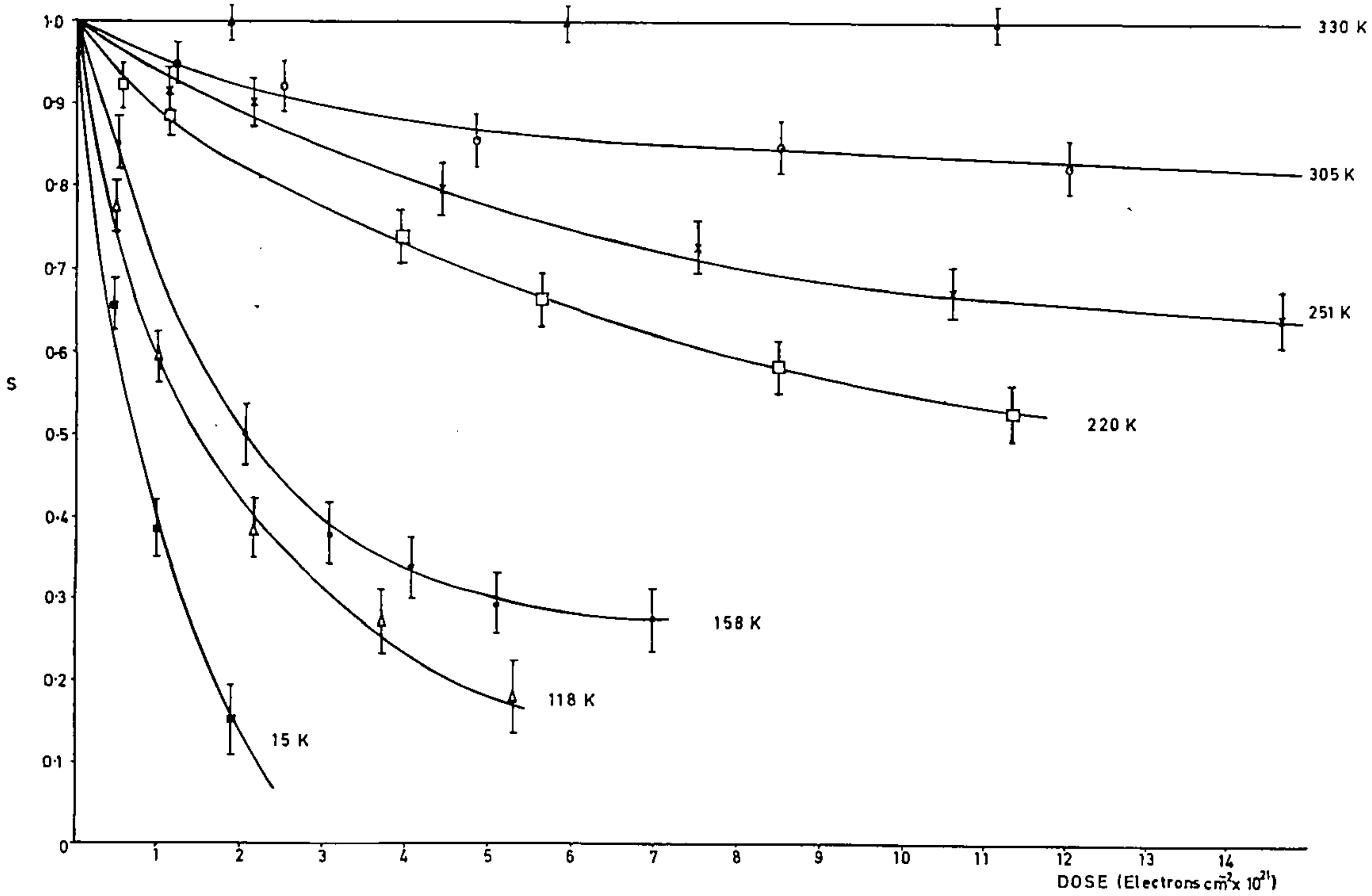

Figure 5.3. The disordering response of <0001> Mg_3Cd to 700 kV electron irradiation as a function of temperature.

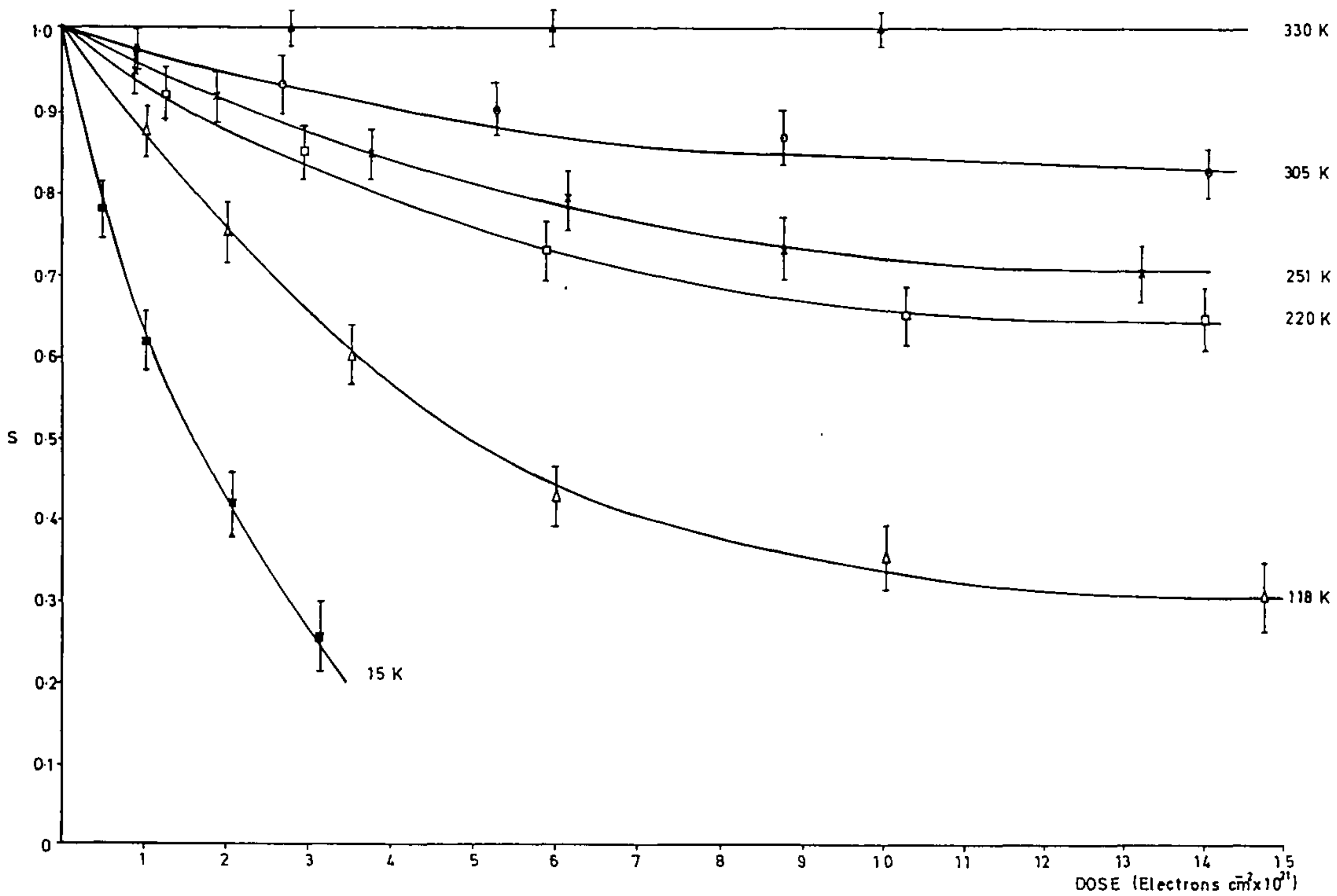

Figure 5.4. The disordering response of <0001> Mg_3Cd to 400 kV electron irradiation as a function of temperature.

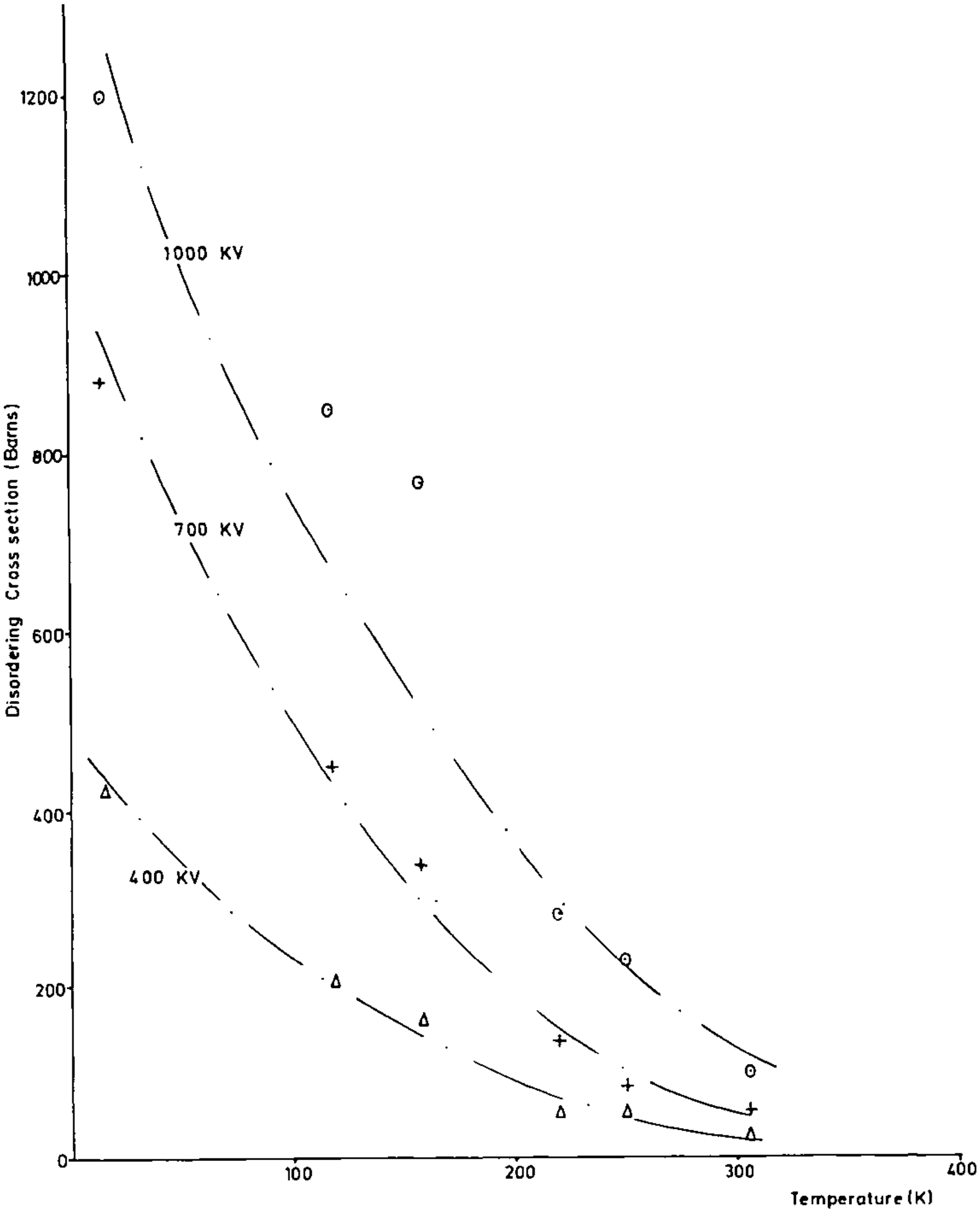

Figure 5.5. The experimentally determined disordering cross-section of <0001> Mg_3Cd as a function of accelerating voltage and temperature.

5.2. Evaluation of the Activation Energy for Vacancy Migration in Mg_3Cd

5.2.1. X-ray Diffraction Study of Ordering in Mg_3Cd

The change in the degree of long-range order upon isothermal ordering was measured using X-ray diffraction. Figure 5.6. shows the increase in the $(10\bar{1}0)$ superlattice reflection intensity with ageing time at 298K. The (0002) fundamental reference intensity remained constant throughout this treatment. The variation in S upon isothermal ordering at a range of temperatures between 298K and 352K is shown in Figure 5.7. It can be seen from this figure that after quenching from 583K into iced brine and then up-quenching to the transformation temperature it was not possible to retain the alloy in the disordered state. The ordering transformation was measured from a well defined degree of long-range order varying from $\sim$ 0.4 at 298K to $\sim$ 0.65 at 352K. Figure 5.8. shows a dark field micrograph of a specimen quenched from 583K into iced brine and up-quenched to 298K. A well defined domain network of ordered nuclei $\sim$ 100Å in diameter can be observed.

Analysis of the Results

The activation energy for ordering could not be determined from an 'Arrhenius' analysis of the experimental results because measurement of the ordering rates began with a different initial value of S at each temperature. The Arrhenius equation assumes that the transformation rate is dependent on a thermally activated rate exponent and so the activation energy can be determined from the logarithm of the transformation time against the absolute temperature. However, in the present work the initial value of S varies with temperature and so there are inherent errors in the transformation time values which invalidate such an analysis. An alternative method of estimating the ordering energy is to compare the experimental results to those predicted by a theoretical ordering model, assuming different values of the physical parameters to attain the best fit. Such an analysis has been carried out with the results of the present work. The simple kinetic analysis of Dienes (1955) predicts the rate of ordering in an AB_3 alloy is given by equation (16) which can be written as:

$$\frac{ds}{dt} = 0.19(1-S)^2\ A_v\nu_o\ \exp(-E_v{}^F/k_bT)\exp\left(-\ \frac{E_{vd}{}^M(1+CS^2)}{k_bT}\ \right)$$

$$x\ \left[1 - \left\{\left(\exp - \frac{V_o(S + S^3/3)}{k_bT}\right)\left[\frac{(1 + S)^2 + 1.3S}{(1 - S)^2}\right]\right\}\right]$$

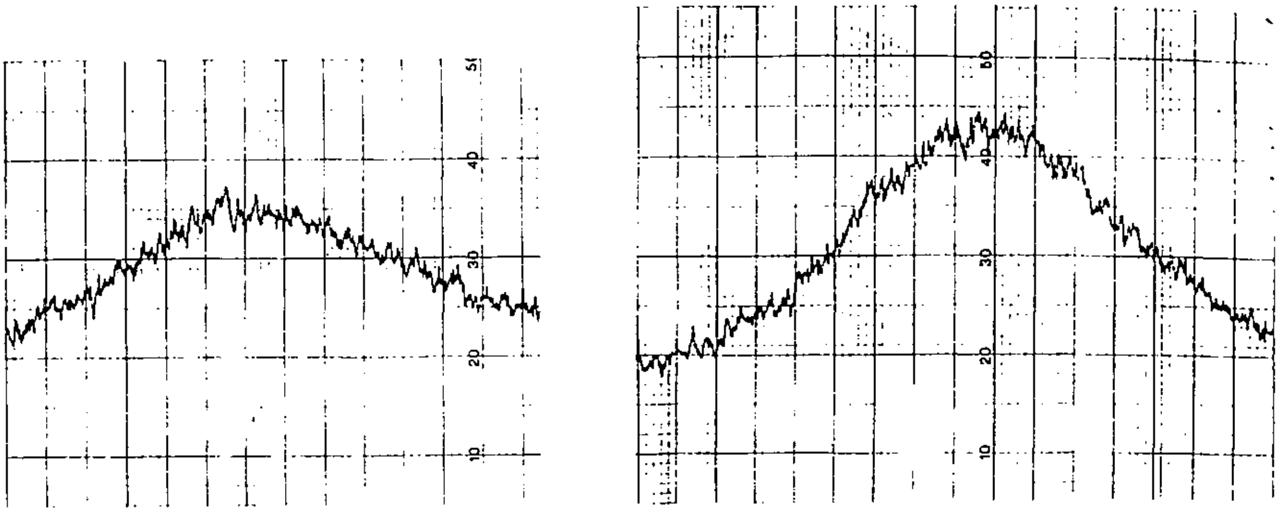

t = 2 mins.
S = 0.4

t = 104 mins.
S = 0.5

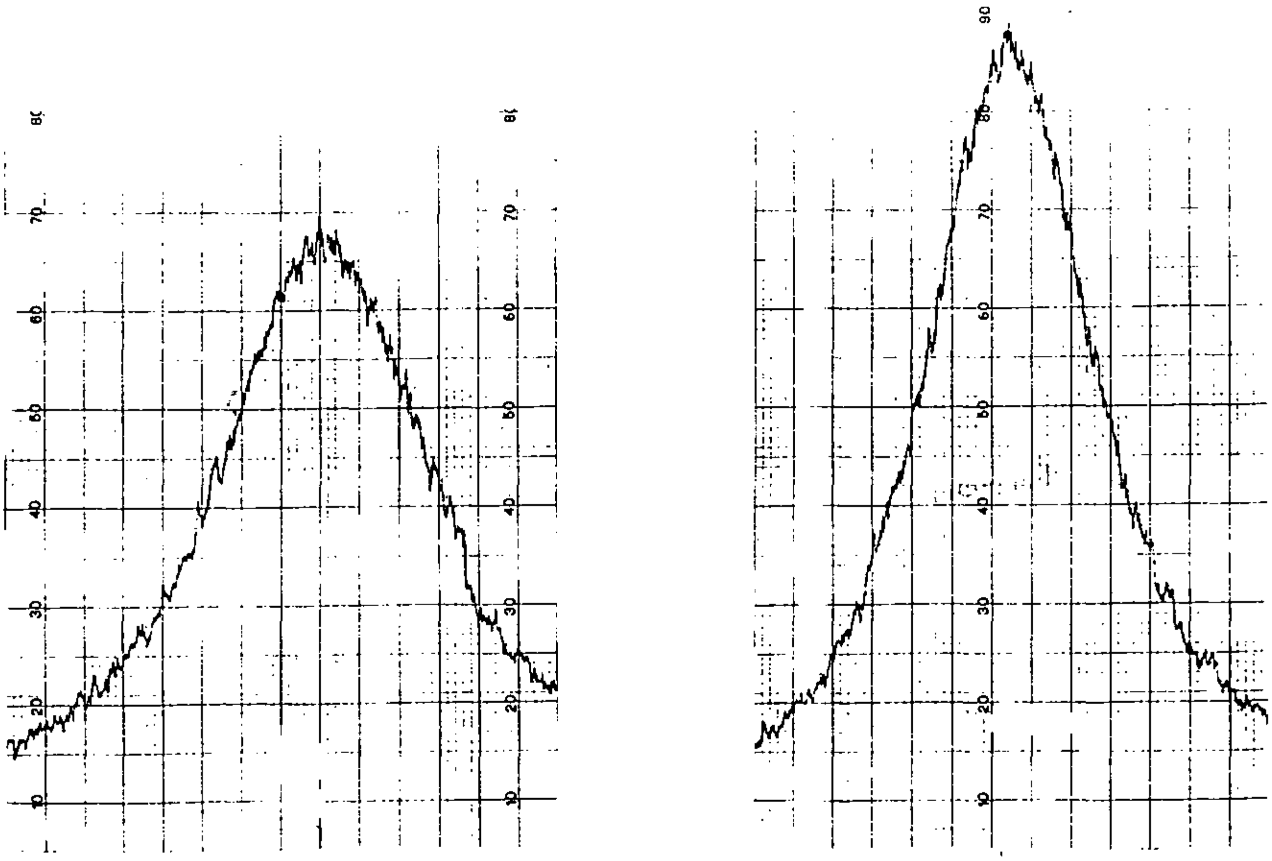

Figure 5.6. Increase in the (10$\bar{1}$0) superlattice reflection intensity with ageing time, t, at 298K after quenching from 583K into iced brine.

t = 1200 mins.
S = 0.72

t = 4000 mins.
S = 0.85.

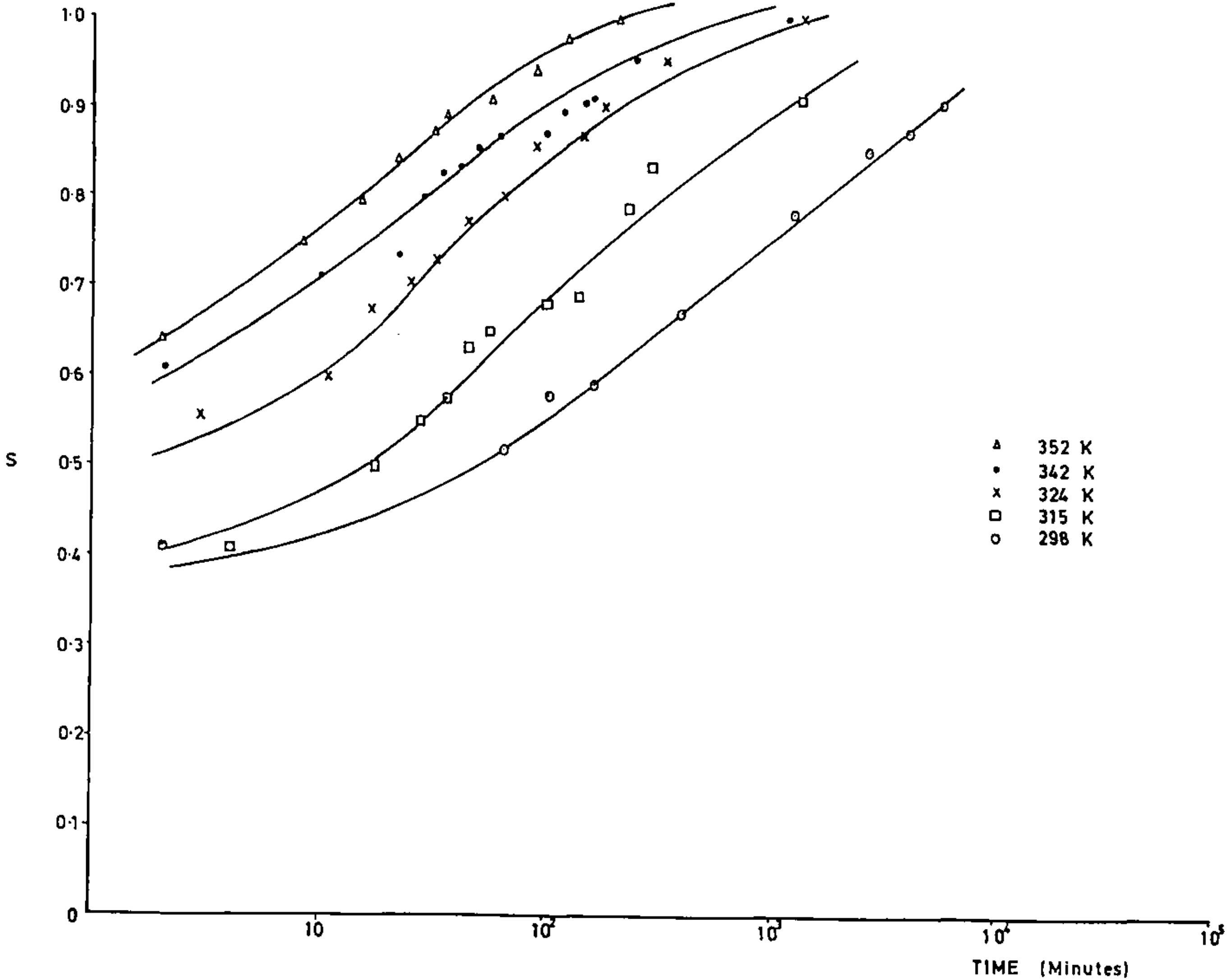

Figure 5.7. Variation in the degree of long-range order of Mg_3Cd on isothermal ordering after quenching from 583K into iced brine.

Figure 5.8.

Dark field electron micrograph ($g = 0001$) of Mg_3Cd quenched from 583K showing a fine network of ordered nuclei.

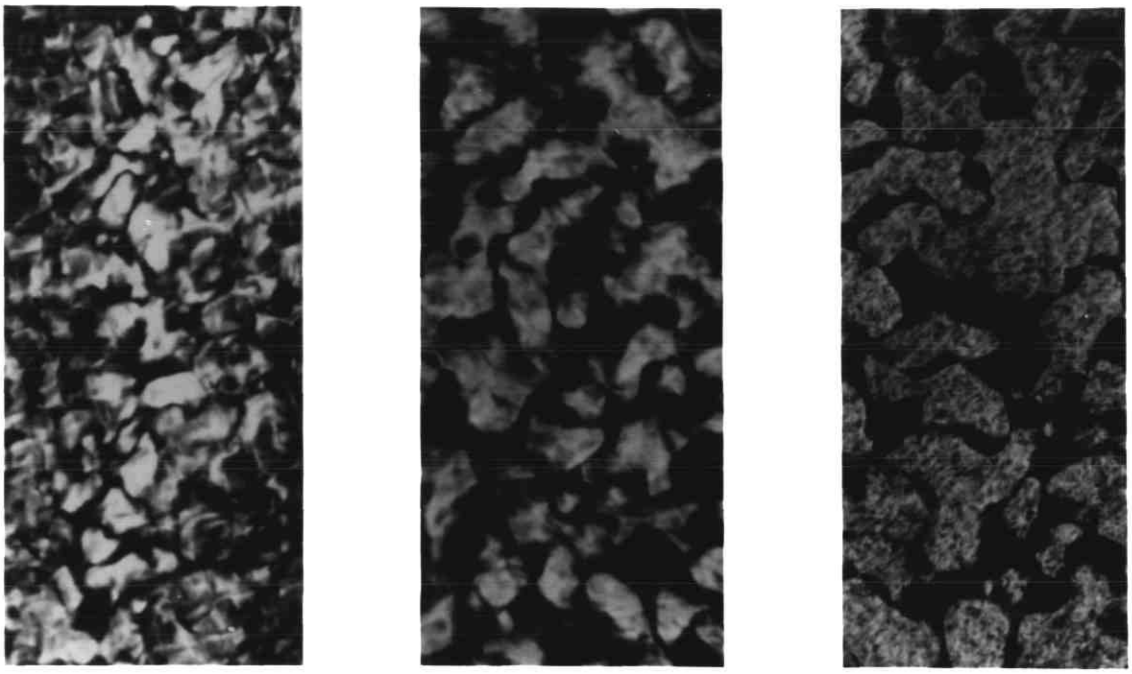

180 mins. 420 mins. 1050 mins.

Figure 5.10.
Dark field electron micrographs ($g = 0001$) of Mg_3Cd showing the increase in antiphase domain size with annealing time at 363K.

0·12 µm

It has been assumed that the activation energy for ordering E is equal to the sum of the vacancy formation and migration energies, E_v^F and E_v^M respectively and that any variation in S occurs mainly in the migration energy term (see Chapter 2.1.5.). It has also been assumed that V_o is related to T_c by equation (7) and that the average vibrational frequency ν is equal to $A_v\nu_o$, where ν_o is the natural vibration frequency of an atom and A_V is an entropy term. ($A_V = \exp S_V^M/k_b$ where S_V^M is the migration entropy). The above equation was evaluated assuming the parameters in Table 5.3. to attain the best fit between the theoretical and experimental ordering rates at all the temperatures considered. The result of this analysis is shown in Figure 5.9.

Table 5.3. Parameters used in Fitting Mg_3Cd Thermal Ordering Data

vacancy formation energy	E_V^F	0.42eV
vacancy migration energy	$E_{vd}(1 + CS^2)$	$0.5\ (1 + 0.25S^2)$eV
ordering energy	V_o	0.18eV
critical temperature	T_c	426K
atomic vibrational frequency	ν_o	$10^{13}s^{-1}$
migration entropy term	A_V	1

T_c is known and all the other parameters are reasonable. Note that the fit shown in Figure 5.9. is excellent but could only be made with the inclusion of a dependence of the vacancy migration energy on S. This analysis thus indicates that the activation energy for self diffusion (= $E_v^F + E_v^M$) is $\sim$ 0.92 eV in the disordered state and $\sim$ 1.05 eV in the ordered state.

This result is in good agreement with that of Tukhfatullin et al (1968) who determined the activation energy for ordering in Mg_3Cd. Electrical resistivity measurements were made at temperatures between 323K and 473K to monitor the rate of ordering inside large ordered domains when the initial degree of order was close to the equilibrium value. An Arrhenius analysis was applied to the results and an activation energy for ordering of 0.92 eV was determined. The result is also in reasonable agreement with the activation energy for creep of 1.2 eV in the disordered state, measured by Stoloff and Davies (1966). The results of the present investigation are higher than those quoted by Smithells (1976) of 0.56 eV in the disordered state and 0.71 eV in the ordered state, however, the original source of these values is not known.

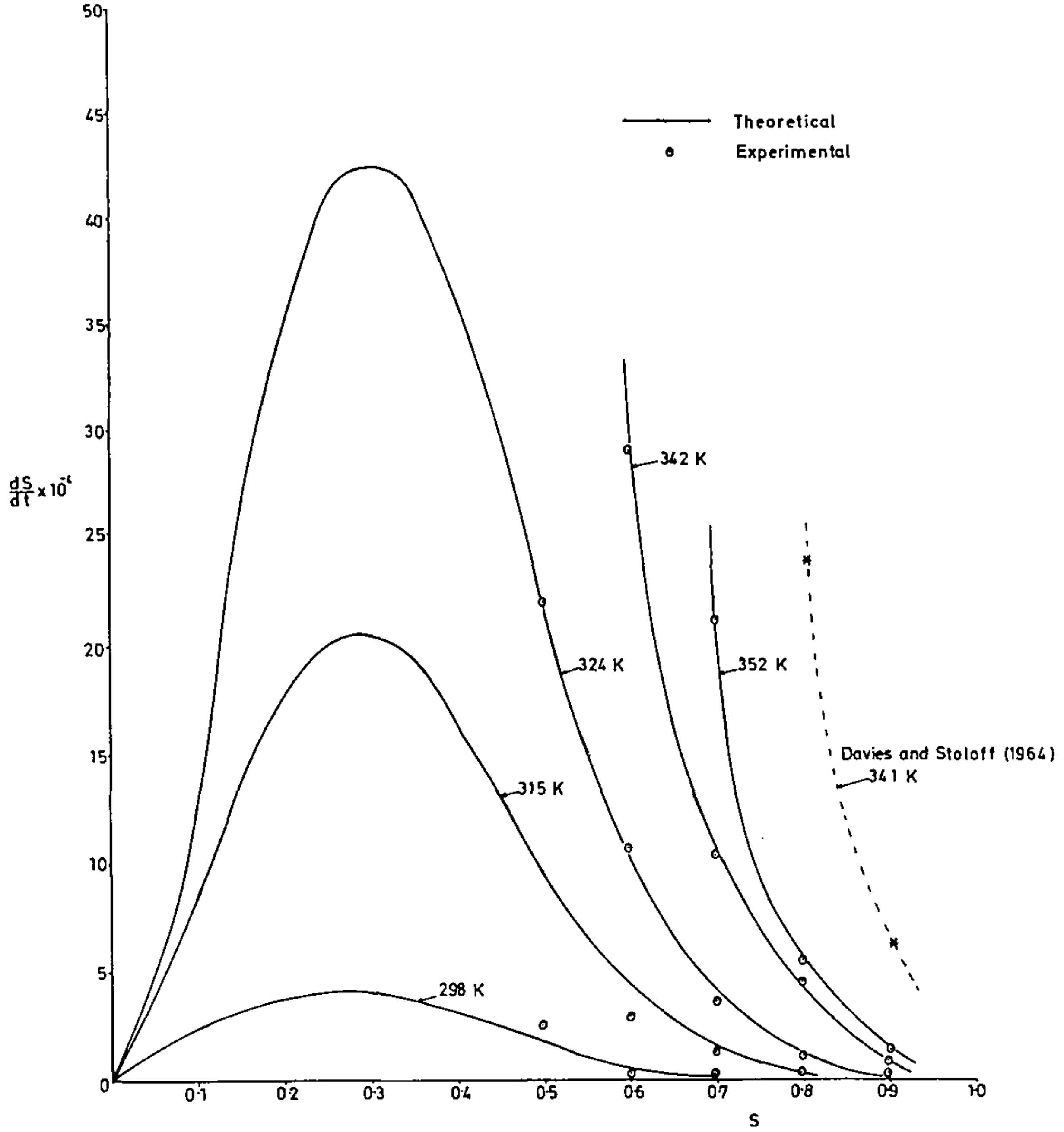

Figure 5.9. Comparison of the experimentally determined and theoretical variation of ds/dt with S as a function of temperature.

Figure 5.9. also shows the rate of ordering at 341K determined from the data of Davies and Stoloff (1964) of S versus time. These results suggest a faster rate of ordering than was observed at 342K in the present work. However, all the measurements of Davies and Stoloff were carried out at room temperature where, as has been shown in the present work, significant ordering can occur; this could account for the discrepancy in the two results.

5.2.2. Determination of the Activation Energy for Domain Coarsening from a Study of the Kinetics of Antiphase Domain Growth

Antiphase domain growth kinetics have been investigated to determine the activation energy for domain coarsening. This was carried out to verify that the activation energy for ordering determined from the X-ray study was reasonable. Figure 5.10. shows the increase in domain size with increasing ageing time at 363K. The results for three temperatures are presented graphically in Figure 5.11. and are consistent with the relationship

$$D^2 \alpha t$$

It should be noted that the domain size versus time graphs do not extrapolate to zero domain size at t = 0 because it was not possible to suppress the formation of ordered nuclei on quenching. Therefore the relationship between D and t is that of equation (22) which is of the form

$$D^2 - D_o^2 = k't$$

where k is proportional to $\exp(-Q/k_bT)$ and Q is the activation energy for domain coarsening. If D_o is equal to zero then the activation energy can be determined by plotting the natural logarithm of the time to attain a given domain size versus the reciprocal of the absolute temperature. However, in the present work Q must be evaluated from the slope of the plot of the logarithm of the gradients of the D^2 versus t plots versus the reciprocal temperatures; this analysis is equivalent to employing equation (22). The result of this analysis is shown in Figure 5.12; where the activation energy determined from the slope of the graph is 0.95 eV. Although only three temperatures were used to evaluate this energy it is in excellent agreement with the results of the X-ray experiments which estimate the activation energy for self diffusion to be 0.92 eV in the disordered alloy and 1.05 eV in the ordered alloy.

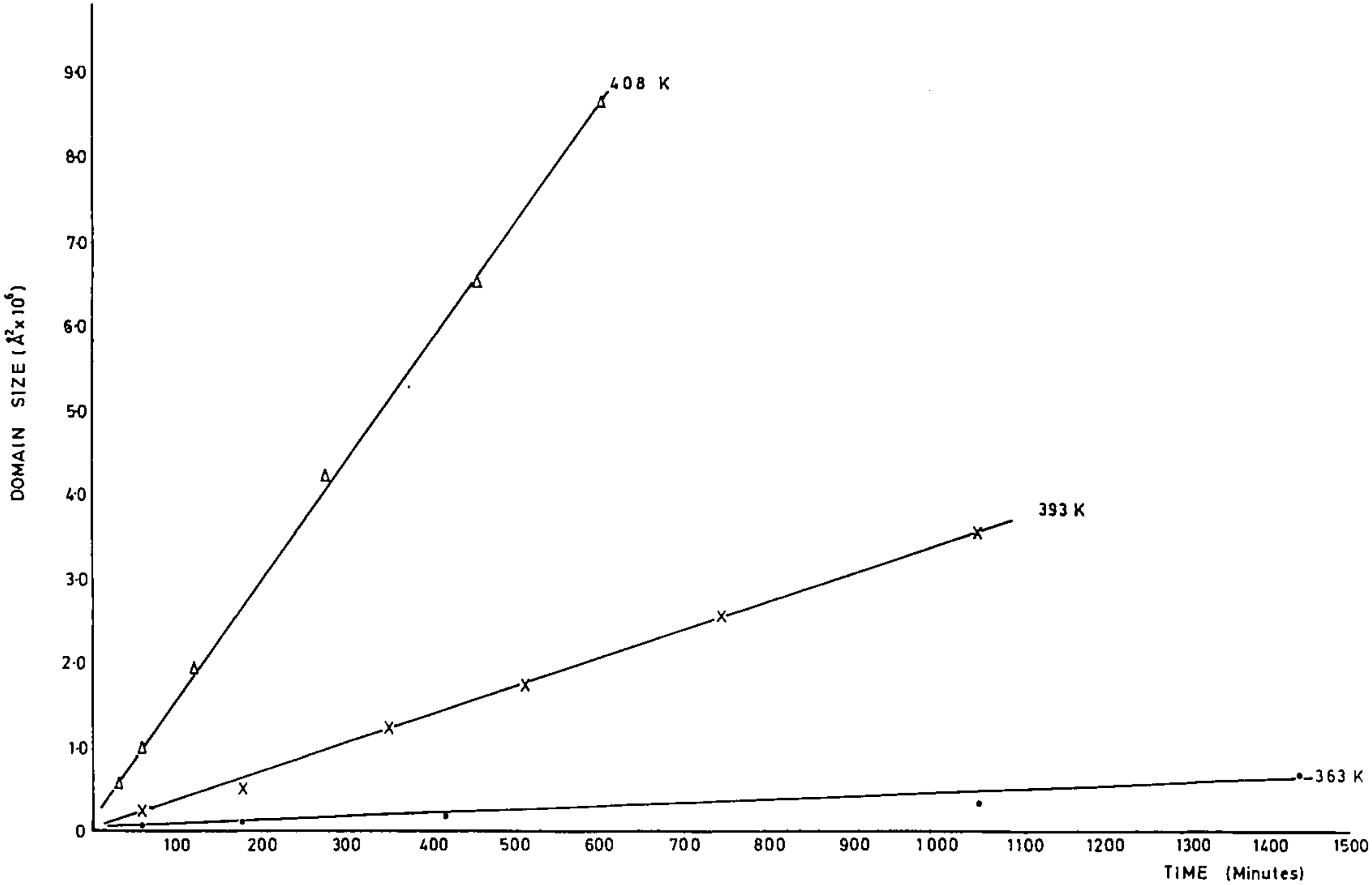

Figure 5.11. Variation in the rate of antiphase domain growth in Mg_3Cd as a function of temperature.

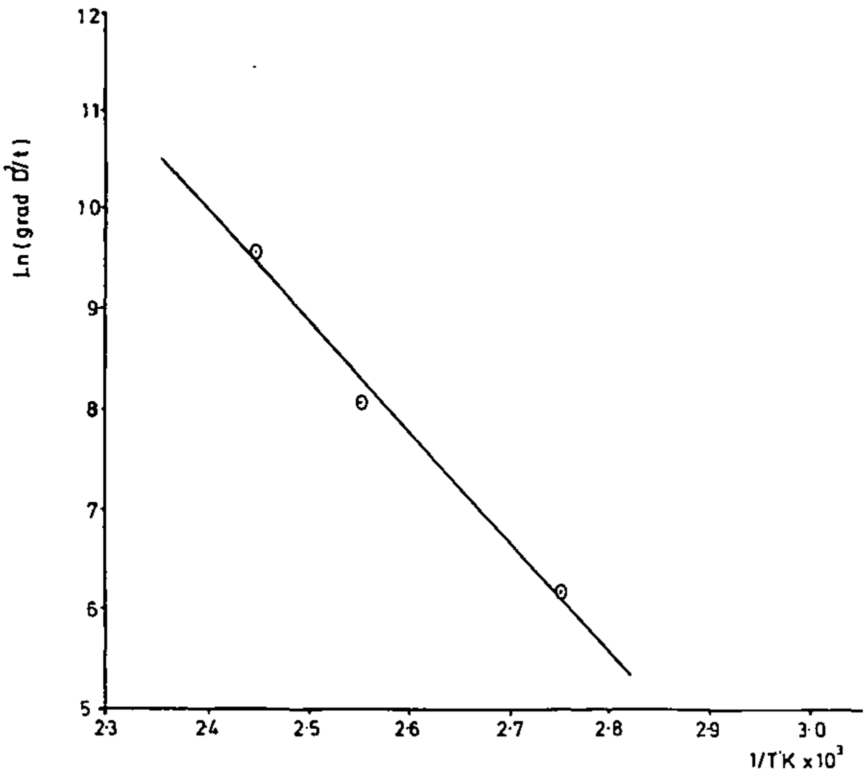

Figure 5.12. Logarithm of the gradient of the Mg_3Cd D^2 versus t plots figure 5.11. versus the reciprocal ageing temperature.

This result is significantly higher than that of 0.58 eV for the activation energy of self diffusion determined by Butler and Swann (1975) who observed the growth of ordered domains in-situ in the HVEM at 393K and 413K. However, it was pointed out that kinetic results from in-situ experiments should always be interpreted with caution as the electron beam may have sufficient energy to displace atoms and thus (i) produce excess vacancies which by enhancing diffusivities can increase the rate of ordering and the migration of the APB's and (ii) disorder the alloy. The first of these effects may be expected to increase the rate constant k and the second effect may reduce both the activation energy for diffusion and the magnitude of the exponent n. The above investigation was carried out under 500 kV electron irradiation which in reference to section 5.1.1. is well above the threshold displacement energy. At 393K and 413K disordering will be resisted by mobile defects, however if the irradiation produced vacancy concentration, (v), is greater than the thermal vacancy concentration, (v_o), then the activation energy determined from the kinetics of domain growth as a function of temperature will be only that of the defect migration energy. A comparison of the thermal and irradiation produced vacancy concentrations can be made if certain experimental parameters are assumed. Assuming a displacement rate K of 1×10^{-3} d.p.a.s^{-1}, a fixed neutral sink density of 10^{10} cm^{-2}, the number of sites around a defect from which spontaneous recombination can occur, Z, is equal to 100 and the vacancy migration energy is 0.6 eV; mutual recombination is the dominant defect loss mechanism and the concentration of irradiation produced vacancies is given by equation (40) which is equal to

$$v = (K/Z\nu_v)^{\frac{1}{2}}$$

where ν_v is the vacancy jump frequency and is given by equation (36) which is equal to $A_v \nu_o \exp^{-E_v^M/kT}$. Assuming A_v is unity and ν_o is 10^{13} s^{-1}, v is equal to $\sim 7 \times 10^{-6}$ and $\sim 5 \times 10^{-6}$ at 393K and 413K respectively. The concentration of thermal vacancies is equal to

$$\nu_o = \exp\,(-\,E_v^F/k_bT)$$

If a vacancy formation energy of 0.42 eV is assumed ν_o is equal to 4×10^{-6} and 7×10^{-6} at 393K and 413K respectively. The thermal and irradiation produced vacancy concentrations are approximately equal and so it is quite possible that the activation energy determined from in-situ domain growth experiments corresponds only to the vacancy migration energy. Such a conclusion is a reasonable explanation of the discrepancy in the two sets of experimental results.

5.2.3. A Study of Point Defect Loop Growth in Mg_3Cd Under 1000 kV Electron Irradiation

A preliminary study has been made of the formation and growth of point defect loops in Mg_3Cd under 1000 kV electron irradiation at temperatures between 316K and 342K. The object of the work was to assess the feasibility of determining the activation energy of vacancy motion from the temperature dependence of the linear growth rate of interstitial loops.

At 316K defect clusters could be clearly observed within 30 seconds of irradiation with a flux of $1.5 \times 10^{18} e.cm^{-2}s^{-1}$ and these could be resolved as loops after a further 500 seconds. The cluster density was found to be constant after ∿ 200 seconds of irradiation. The temperature dependence of the growth rate was monitored by allowing the loops nucleated at 316K to grow and then increasing the temperature in steps of ∿ 10K. Figure (5.13) shows the loops growing under irradiation at 316K and 324K. Although the loops did not have a regular shape it was assumed that they were approximately circular and so the growth rate was determined from measurements of the maximum length. Analysis of the results at 316K showed that there was a large variation in the growth rates of the individual loops and n in the relation $d \alpha t^n$ (where d is the loop diameter and t the irradiation time) varied from 0.5 to 1.1. At 324K the growth rate of the loops decreased and n varied from 0.2 to 0.6. Under irradiation at 333K the larger loops stopped growing and the smaller loops shrank and disappeared completely within 500 seconds. Increasing the temperature to 342K caused all the loops to disappear.

Although the vacancy/interstitial nature of the loops was not established, for the purpose of a discussion it will be assumed that they were interstitial (Makin (1971b)). The variation in the growth rate of individual loops at any particular temperature can be explained using the model of Yoo and Stiegler (1977). This model takes into account the proximity of the loops to the foil surfaces and the resulting variation in vacancy concentration which leads to a range of loop growth rates (see Chapter 3.1.6.) However, the decrease in loop growth rate with increasing temperature suggests that there is an increase in the vacancy concentration which inhibits further growth.

316K

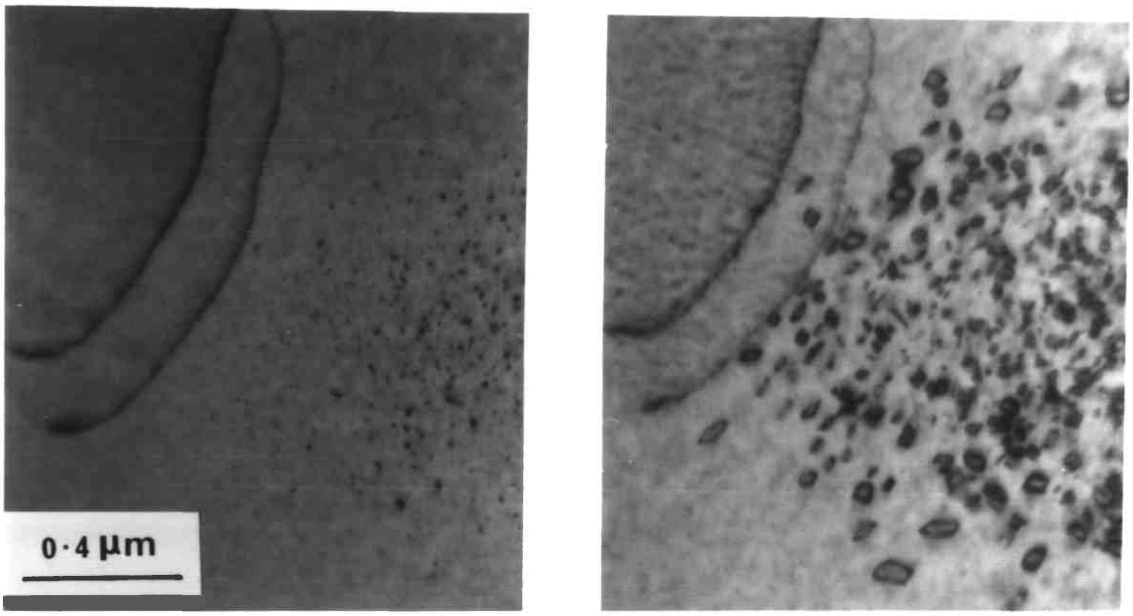

100 secs

1500 secs

324K

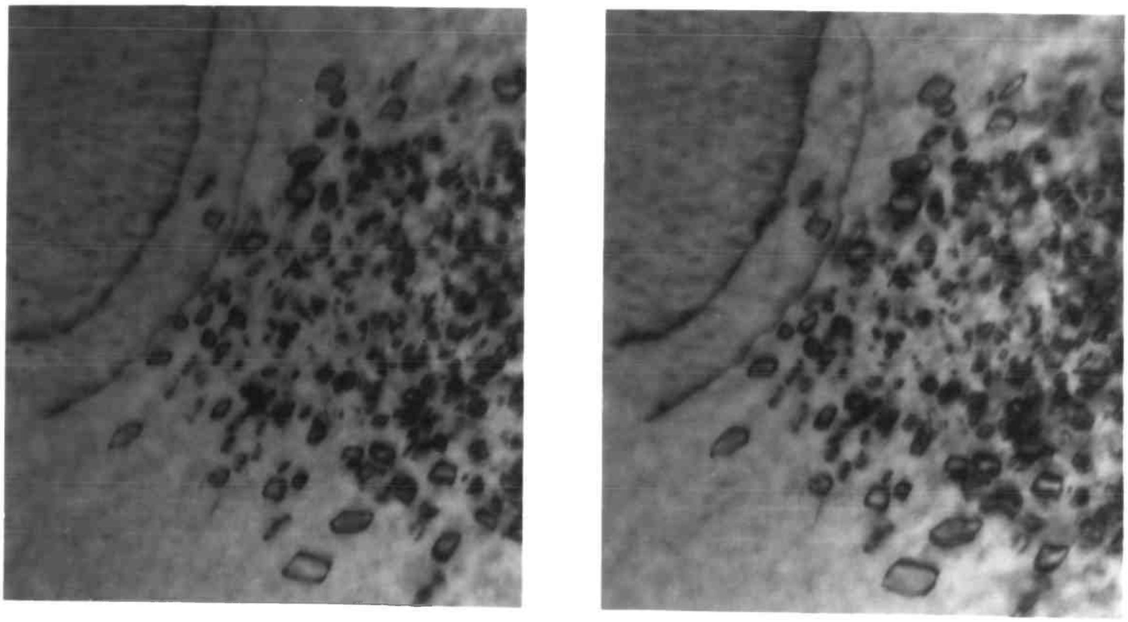

400 secs

1000 secs

Figure 5.13. Growth of point defect loops in Mg_3Cd under 1000 kV irradiation at 316K and 324K.
(flux = 1.5×10^{22} $em^{-2}s^{-1}$)

A possible explanation of this effect is that the alloy was found to be susceptible to oxide formation after electropolishing and that the surface deteriorated on exposure to the electron beam (Dahmen 1977). If oxidation takes place by the outward diffusion of the metal ions, then excess vacancies will be injected into the foil which could retard the growth of the existing loops. Hossain and Brown (1977a) have reported similar effects occurring in magnesium. Also at these temperatures the thermal equilibrium concentration may be comparable with the irradiation concentration which could again lead to a reduction in the rate of loop growth. From these preliminary observations it is apparent that analysis of the damage experiments to determine vacancy migration energies is not straightforward and the results may be complicated by oxidation effects. For these reasons it was decided not to continue with this experimental approach.

An interesting microstructural feature was observed when a specimen consisting of large antiphase domains was irradiated at 325K under 1000 kV irradiation with a flux of 2 x 10^{23}e.$cm^{-2}sec^{-1}$. It can be seen in Figure 5.14 that most of the loops were nucleated at the antiphase boundaries. This effect has also been observed in Cu_3Au by Mukai and Mitchell (1982). They proposed that the wrong bonds at the antiphase boundary interface become trapping sites for the interstitial atoms. A wrong Mg-Cd bond, for example, may attract a Mg atom to form a partly correct like-atom bond in the form of the Mg atom plus the Mg-Cd dumb-bell interstitial. An alternative explanation of the observation is that in the disordered region of the antiphase boundary the activation energy for vacancy migration is lower than in the perfect ordered crystal. This results in an increase in the local interstitial concentration and preferential nucleation at the antiphase boundary.

Figure 5.14. Formation of point defect loops on antiphase boundaries in Mg_3Cd under 1000 kV irradiation at 325 K with a flux of 2×10^{23} $em^{-2}sec^{-1}$.

5.3. The Response of Fully Ordered Ni_3Al and Ni_3Fe ($L1_2$ Structure) to Electron Irradiation

5.3.1. Effect of Temperature and Accelerating Voltage

5.3.1. (i) Ni_3Al

The response of fully ordered Ni_3Al to electron irradiation has been investigated using a range of electron energies from 400 keV to 1000 keV at temperatures between 15K and 540K. All the irradiations were carried out with the specimens close to the <110> orientation along a systematic row of the diffraction pattern. For temperatures above 300K the incident flux was 1.5×10^{19} electrons $cm^{-2}sec^{-1}$; below this the flux used was 5×10^{18} electrons $cm^{-2}sec^{-1}$. Figure 5.15 shows the decrease in the long range order parameter S against electron dose, (= flux x time), as a function of temperature under 1000 kV electron irradiation. Irradiation at 466K and temperatures above, caused little change in S even after extended times. As the temperature was reduced the disordering rate increased rapidly. Between 466K and 305K the alloy would not disorder completely and a steady-state value of S was attained. Below 305K the alloy became fully disordered and the initial disordering rate continued to increase as the temperature was decreased. This effect of temperature on the disordering rate can be seen qualitatively in figure 5.16, which shows a series of diffraction patterns taken under 1000 kV irradiation at 305K and 10K.

The response of the alloy at temperatures between ∿ 300K and ∿ 500K can be interpreted in terms of the theoretical ideas contained in Chapter 3.2, which lead to the prediction that the alloy will only partially disorder when defects have sufficient mobility to restore order to the lattice. However, at temperatures where defects are ineffective in restoring order to the lattice, the theory predicts that the alloy will fully disorder and that the disordering rate will be temperature independent. The results of the present work do not support this as below 300K the alloy becomes fully disordered and the disordering rate continues to increase as the temperature is decreased. Figure 5.17 shows the results of Figure 5.15 plotted according to the simple expression for disordering ($S = S_0 \exp(-K't)$ equation (53)) as ln S versus dose. The linearity implied by this equation is obeyed up to ∿ 250K and the disordering cross-section has been determined for each temperature from the slope of the plots. However, at 305K and temperatures above the plots are not linear and the alloy only partially disorders to some steady-state value of S. Therefore for these higher temperatures the disordering cross-section has been evaluated from the slope of the tangent taken to the initial linear portion of the graph where $S \sim 1$ and the reordering components are very small. The increase in the disordering cross-section with decreasing temperature under 1000 kV irradiation is shown in Table 5.4. The disordering rate is temperature dependent even when defects do not have sufficient mobility to restore order to the lattice.

Table 5.4. Variation in the Experimentally Determined Disordering Cross-section with Temperature of <110> Ni_3Al under 1000 kV Irradiation

Temperature (K)	Disordering Cross-Section (barns)
383	68
305	108
248	235
203	268
118	355
15	550

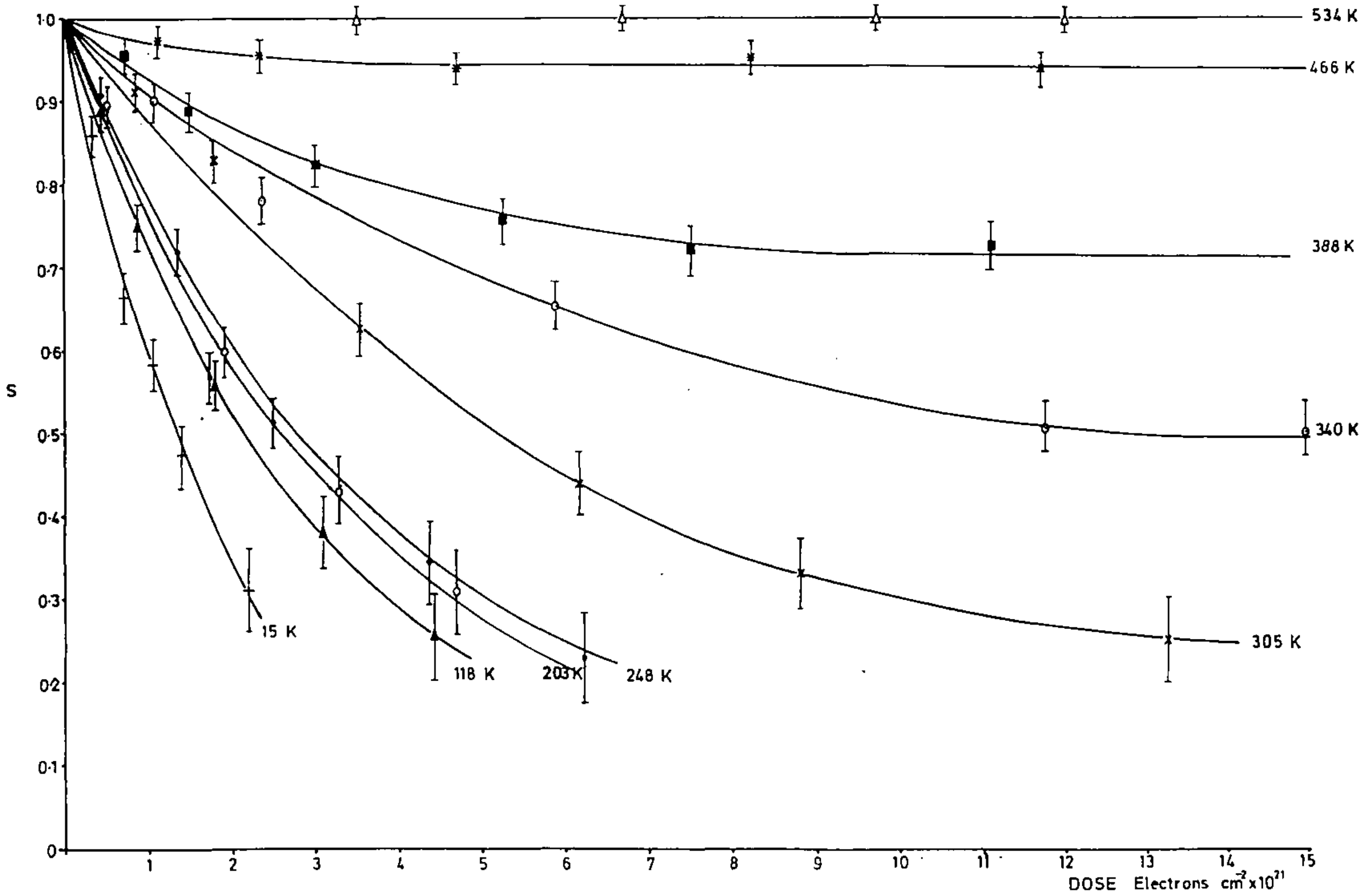

Figure 5.15. The disordering response to 1000 kV electron irradiation of <110> Ni_3Al as a function of temperature.

305K

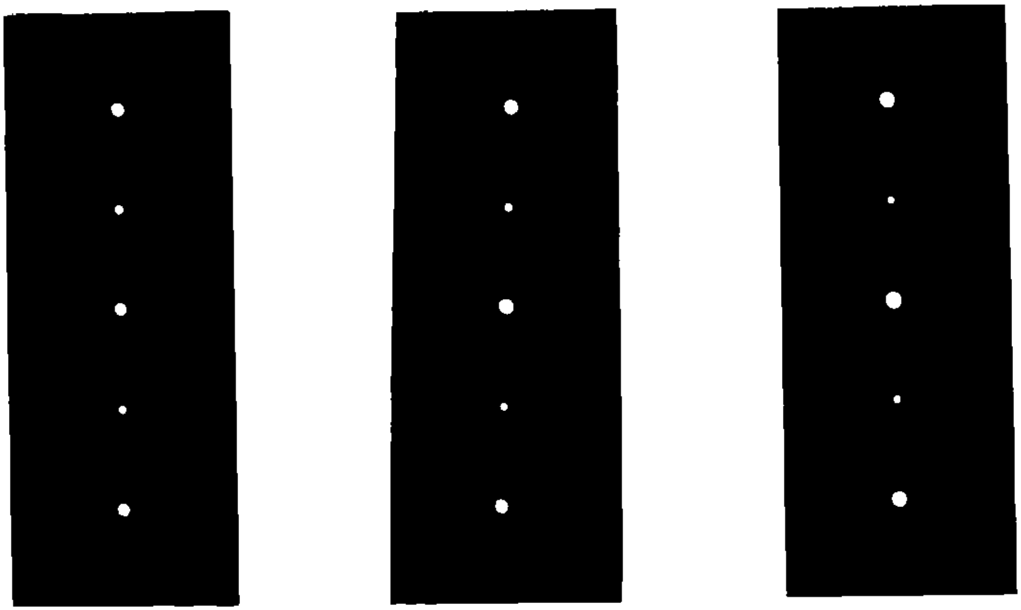

0 secs
s = 1.0

50 secs
s = 0.98

250 secs
s = 0.9

10K

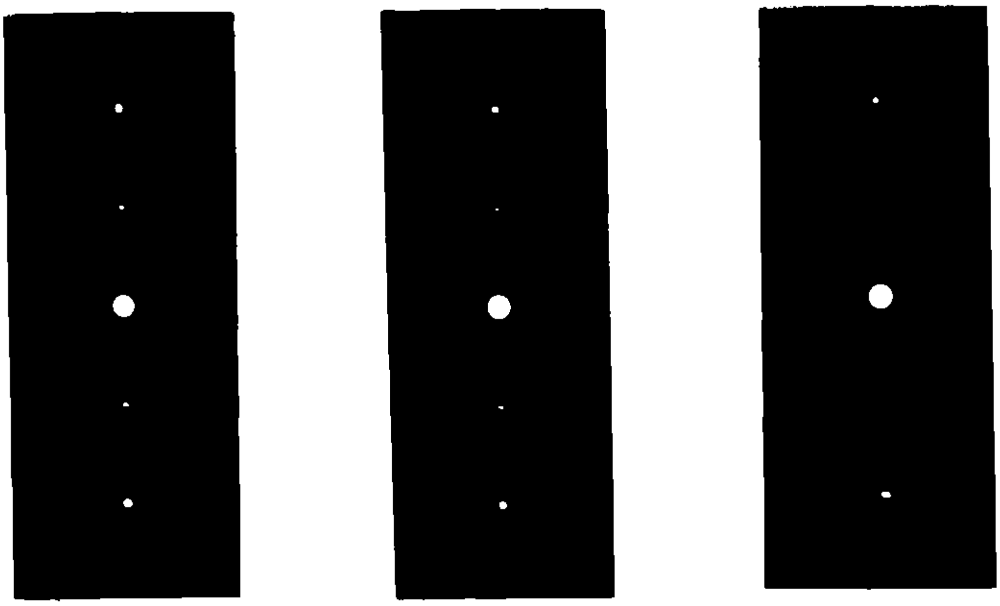

0 secs
s = 1.0

50 secs
s = 0.86

250 secs
s = 0.4

Figure 5.16.

Comparison of the rate of decrease of superlattice reflection intensities as <110> Ni_3Al disorders under 1000 kV irradiation at 305K and 10K. (Incident flux = 7×10^{22} cm^{-2}s^{-1})

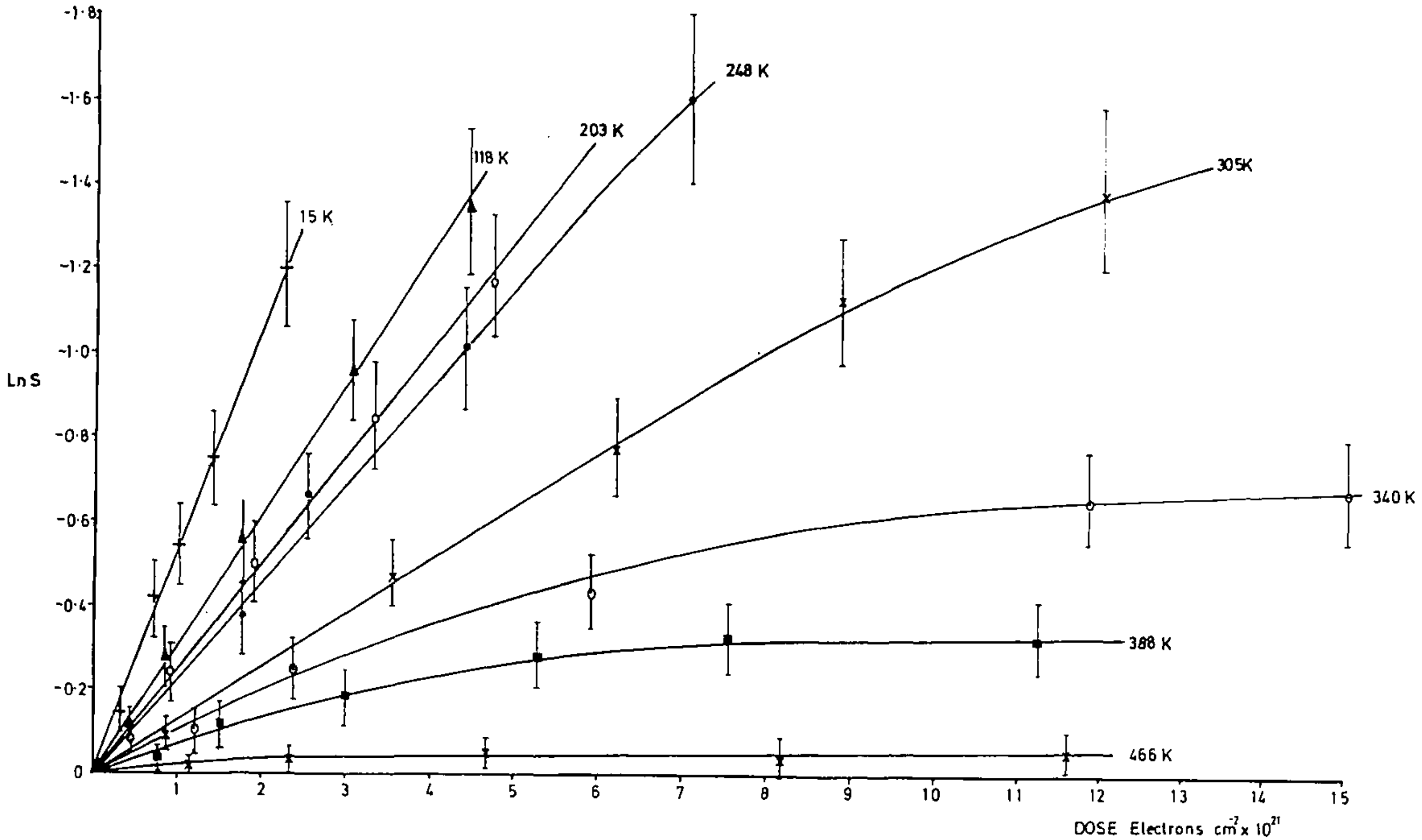

Figure 5.17. The disordering response of <110> Ni_3Al under 1000 kV electron irradiation plotted as lnS versus dose.

The effect of accelerating voltage on the disordering response of <110> Ni$_3$Al has been investigated at temperatures between 15K and 305K where the ln S versus dose plots are linear, i.e. the re-ordering component of the response is small, (see Chapter 3. 2). The disordering response under 800 kV, 600 kV, 500 kV and 450 kV irradiation is shown, for temperatures in the range 15K to 305K, in Figures 5.18, 5.19, 5.20, and 5.21 respectively plotted as S against dose. For each of the accelerating voltages employed the alloy became fully disordered at temperatures below ∿ 250K, and in conflict with the simple theory, the disordering rate increased as the temperature was decreased. At any particular temperature the disordering rate was greater the higher the electron energy. The disordering rate as a function of electron energy at 15K is shown in Figure 5.22 plotted as ln S versus dose. The disordering cross-section has been evaluated as a function of electron energy and temperature from ln S versus dose plots. The results are shown in Figure 5.23. The disordering cross-section increases as the temperature decreases for all the electron energies employed, but the increase is greater for the higher energy electrons.

The threshold energy for disordering is estimated to be between 400 kV and 450 kV as disordering was not observed under 400 kV irradiation at 15K.

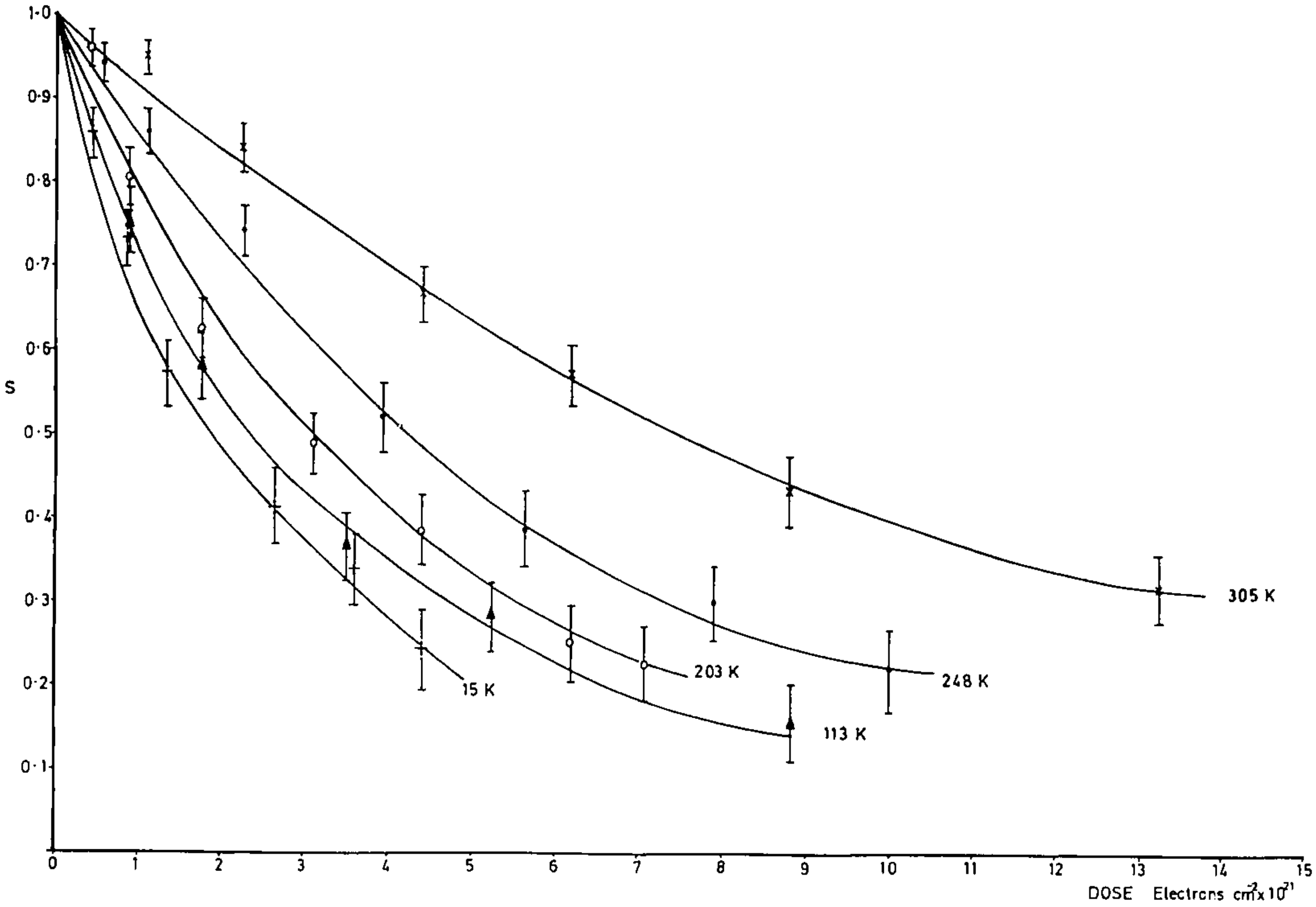

Figure 5.18. The disordering response of <110> Ni_3Al under 800 kV electron irradiation as a function of temperature.

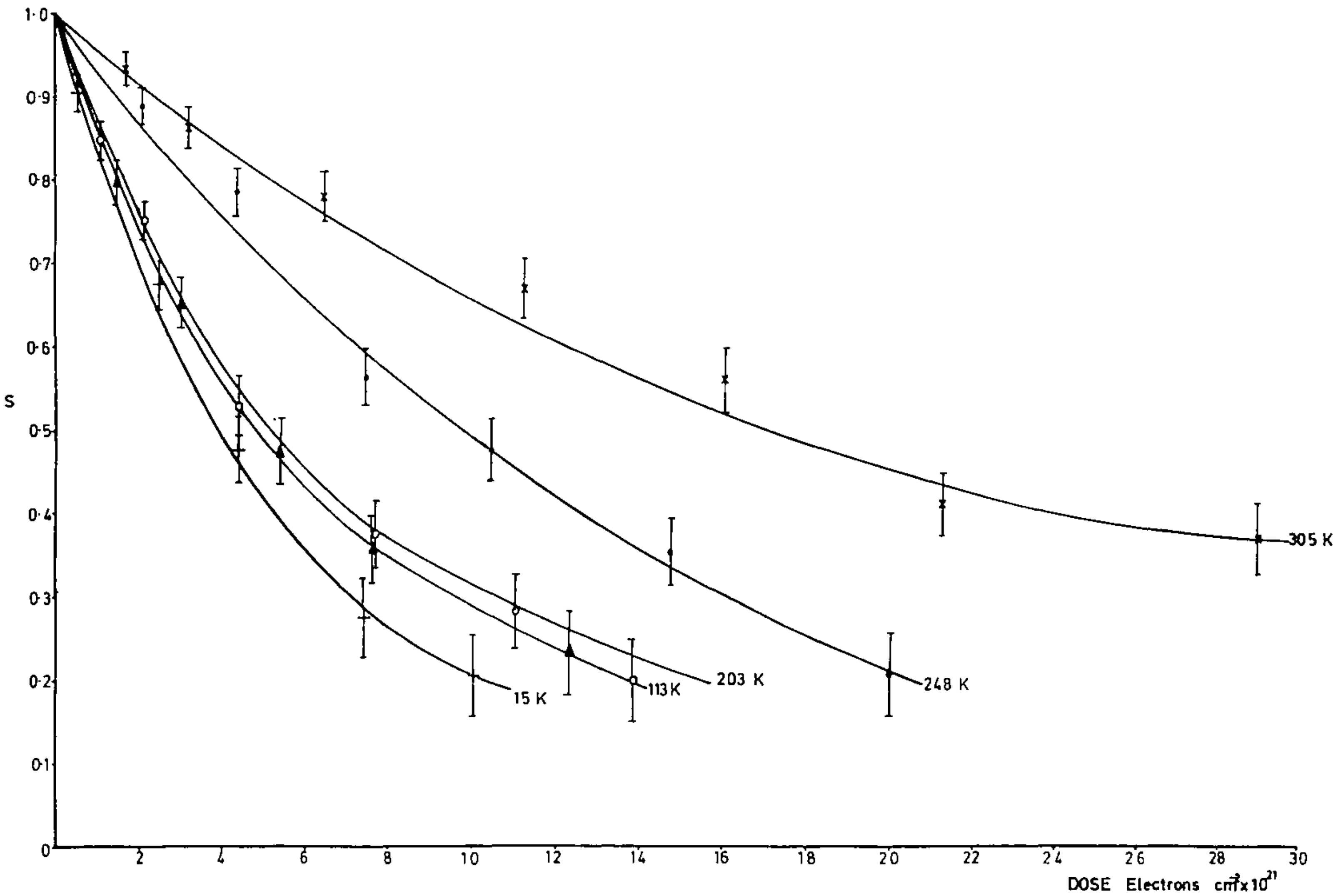

Figure 5.19. The disordering response of <110> Ni_3Al under 600 kV electron irradiation as a function of temperature.

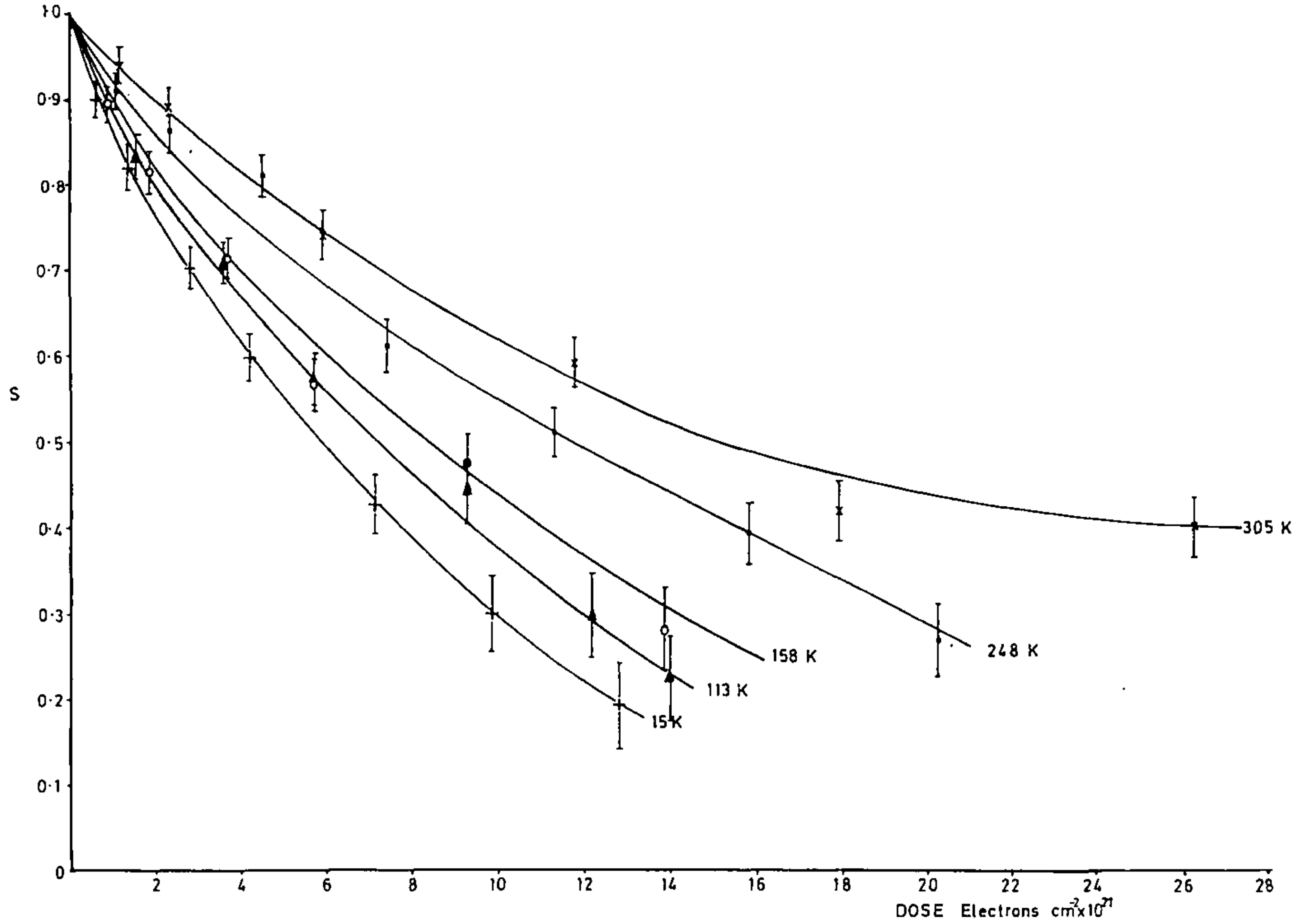

Figure 5.20. The disordering response of <110> Ni_3Al under 500 kV electron irradiation as a function of temperature.

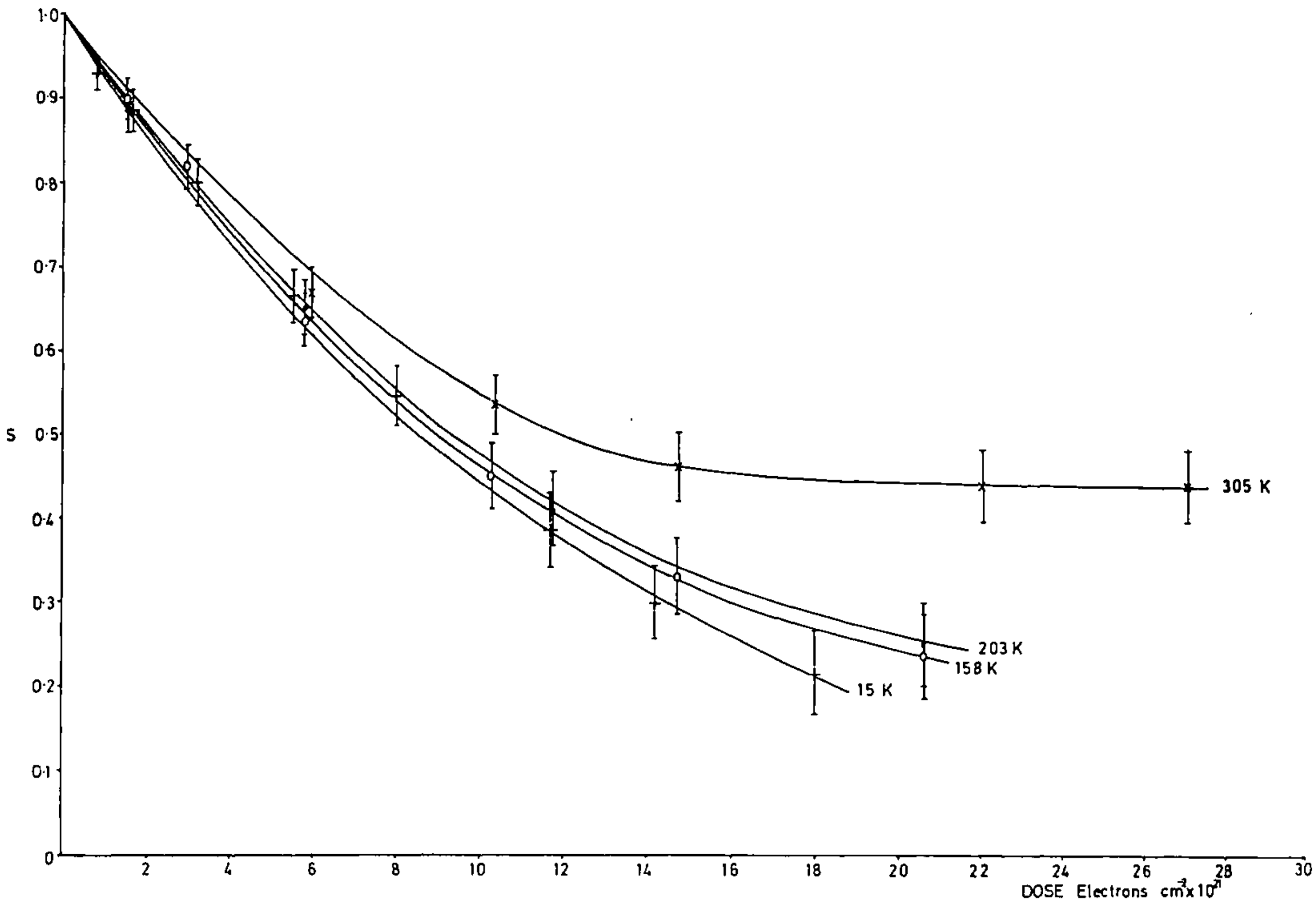

Figure 5.21. The disordering response of <110> Ni_3Al under 450 kV electron irradiation as a function of temperature.

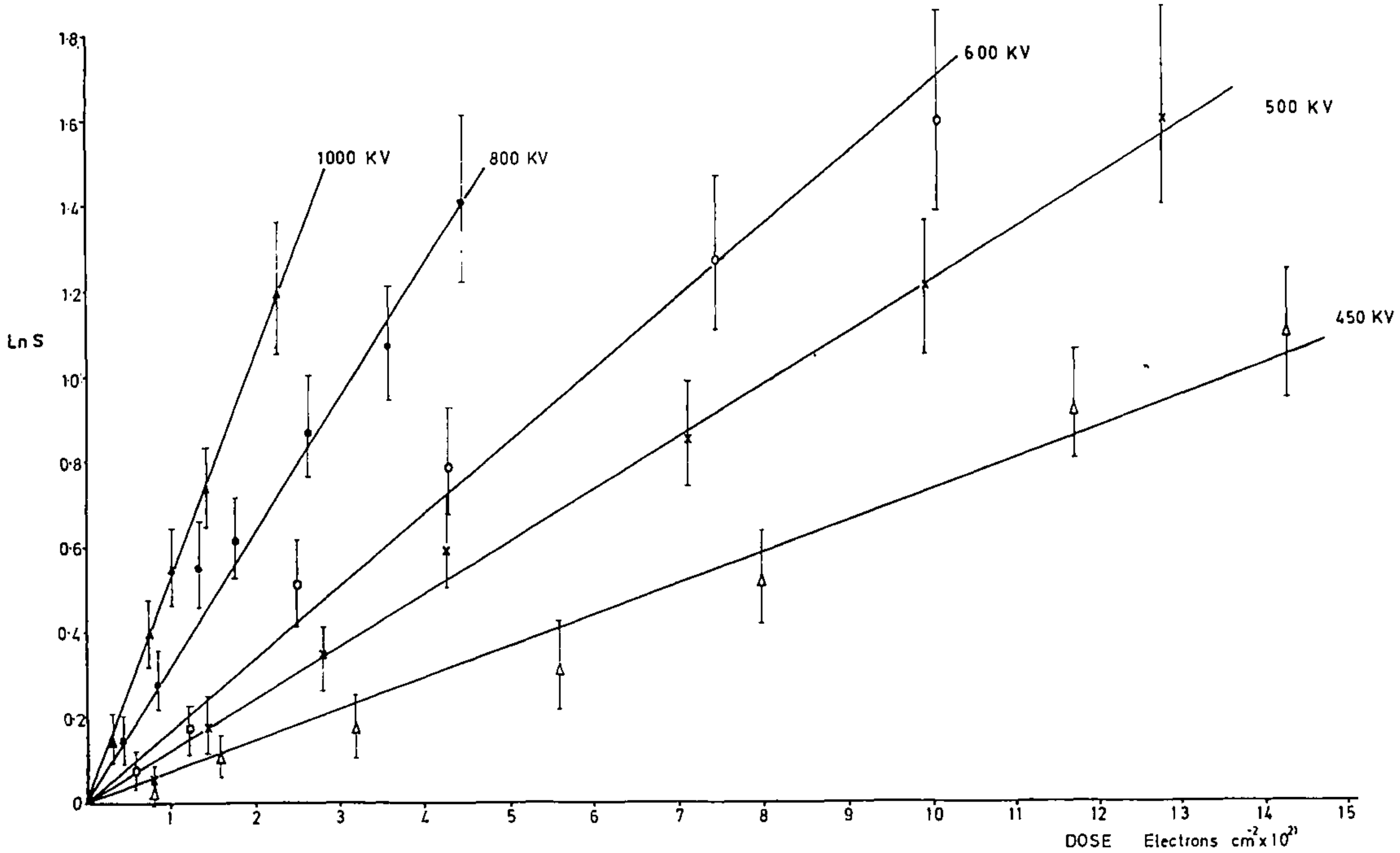

Figure 5.22. The disordering response of <110> Ni_3Al at 15K as a function of accelerating voltage plotted as lnS versus dose.

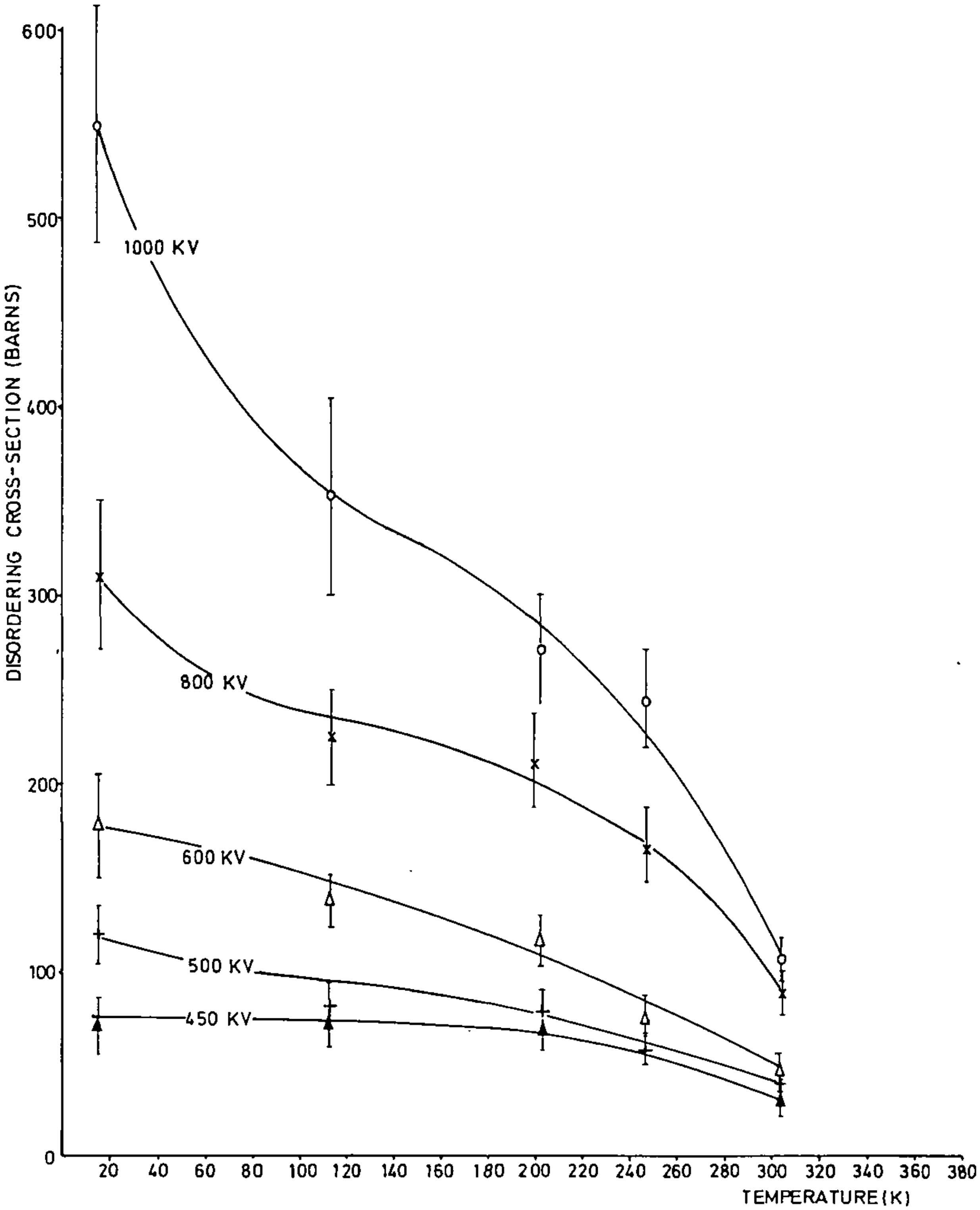

Figure 5.23. The experimentally determined disordering cross-section of <110> Ni_3Al as a function of temperature and accelerating voltage.

5.3.1. (ii) Ni_3Fe

The response of fully ordered Ni_3Fe to electron irradiation has been investigated as a function of temperature from 154K to 408K and accelerating voltage from 350 kV to 1000 kV. All the irradiations were carried out with the specimens close to the <110> orientation along a systematic row of the diffraction pattern. For temperatures above 300K the incident flux was 1 x 10^{19} electrons $cm^{-2}sec^{-1}$; below this the flux was reduced to 5 x 10^{18} electrons $cm^{-2}sec^{-1}$. Figure 5.24 shows the response under 1000 kV irradiation as a function of temperature plotted as S versus dose. At all temperatures S could only be monitored to a minimum value of ∿ 0.3 because the atomic scattering factors of Ni and Fe are very similar and so the intensities of the superlattice reflections are weak even when the alloy is fully ordered (see Chapter 2.1.2.). Evidence of this can be seen in Figure 5.25 which shows a series of diffraction patterns taken at 305K under 600 kV irradiation. Figure 5.26 shows the results of Figure 5.24 plotted according to equation (53) as ln S versus dose. The response is similar to that of Ni_3Al in that the linearity implied by this equation is obeyed at temperatures below ∿ 305K and above this the alloy disorders to a steady state value of S. The disordering rate appears to increase as the temperature is decreased but further measurements below 154K were not possible because of the increased experimental errors involved with rapid disordering when the superlattice reflections are very weak.

The disordering rate was also measured under 600 kV and 400 kV irradiation at 305K, 248K and 154K. The results are shown for each temperature together with the 1000 kV results in Figures 5.27 and 5.28., 5.29, plotted as ln S versus dose. At each temperature the disordering rate is greater for the higher energy electrons. From the slope of these plots the disordering cross-section has been evaluated as a function of temperature and accelerating voltage. The results are listed in Table 5.5. and show that there is a temperature dependence of the disordering cross-section, as observed in Mg_3Cd and Ni_3Al.

The threshold energy for disordering is estimated to be between 350 kV and 400 kV as the alloy would not disorder under 350 kV irradiation at 15K.

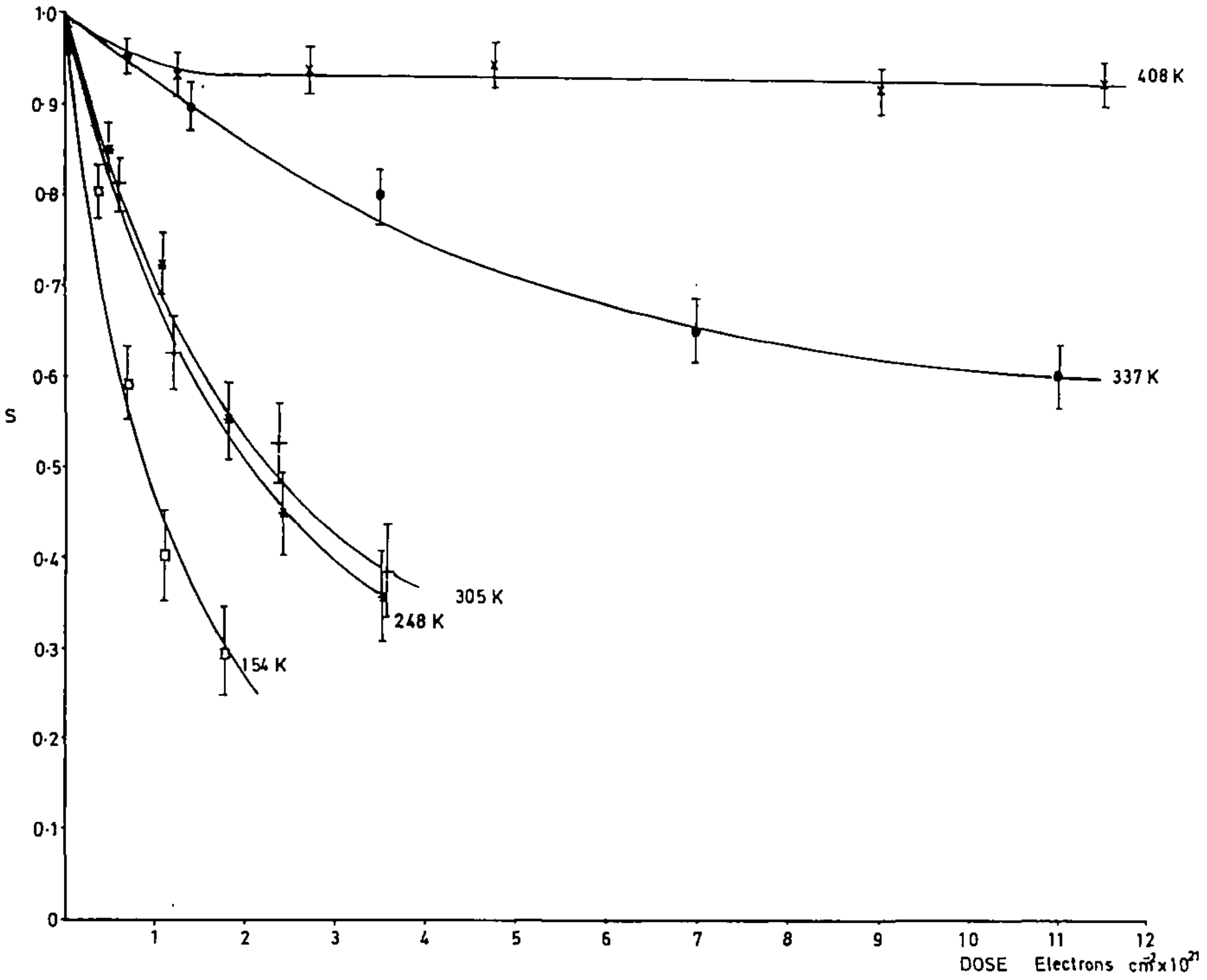

Figure 5.24. The disordering response of <110> Ni_3Fe under 1000 kV electron irradiation as a function of temperature.

0 secs, s = 1.0

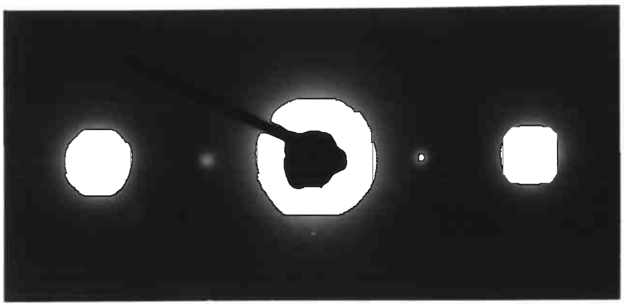

200 secs, s = 0.8

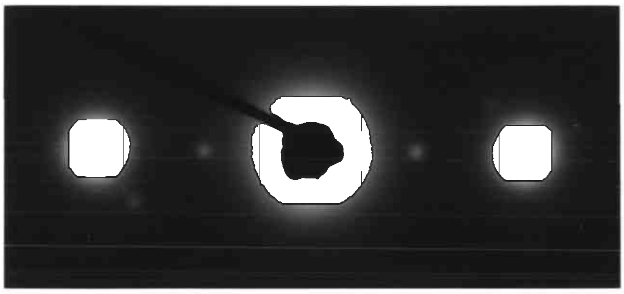

500 secs, s = 0.55

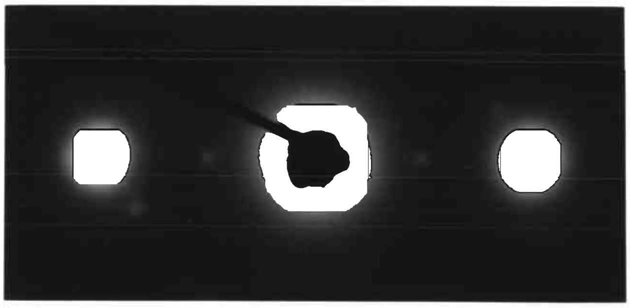

Figure 5.25. Decrease in the superlattice reflection intensities as <110> Ni_3Fe disorders under 600 kV irradiation at 298K. (Incident flux = 1.2×10^{23} $em^{-2}s^{-1}$)

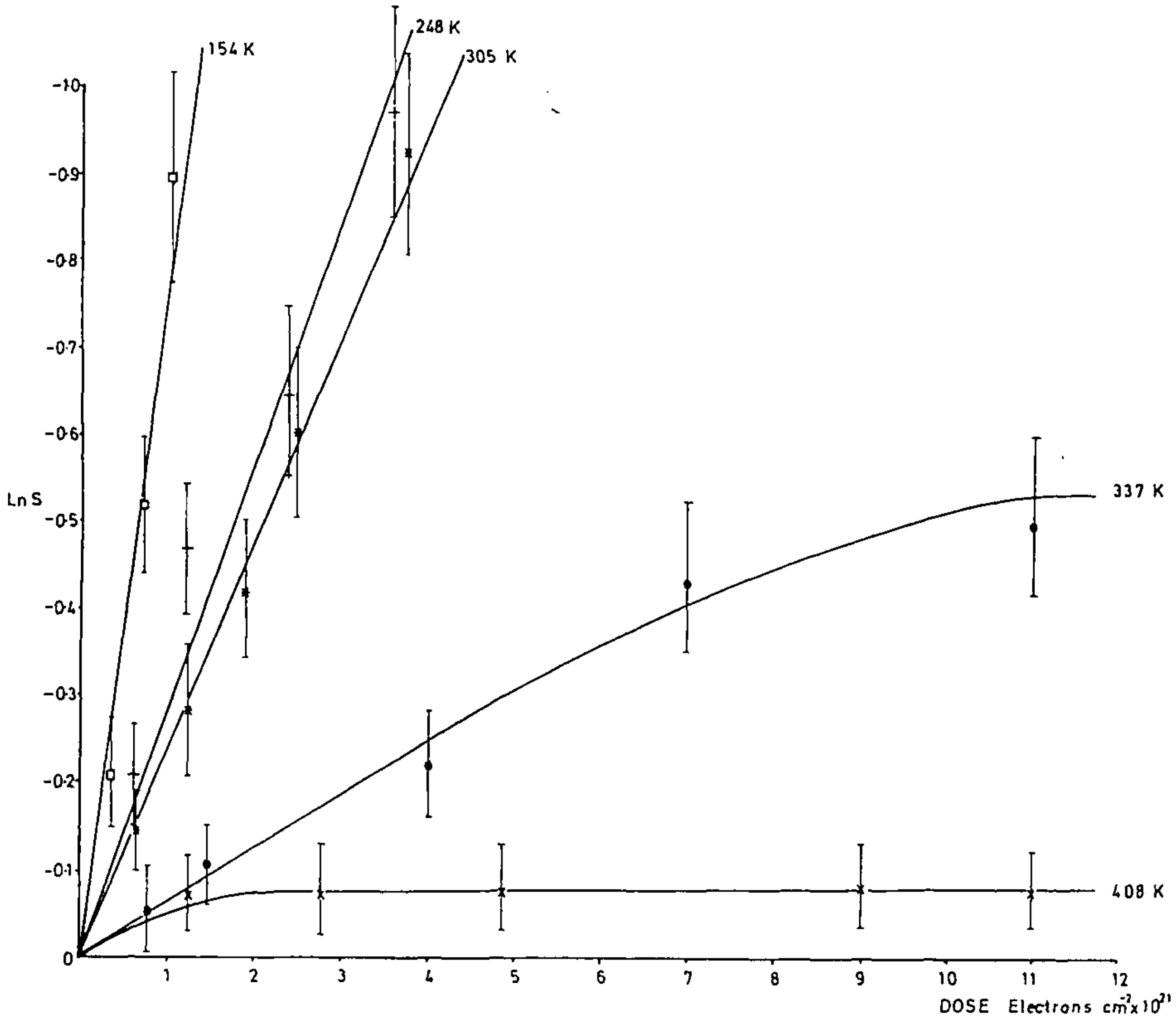

Figure 5. 26. The disordering response of <110> Ni_3Fe under 1000 kV electron irradiation as a function of temperature plotted as lnS versus dose.

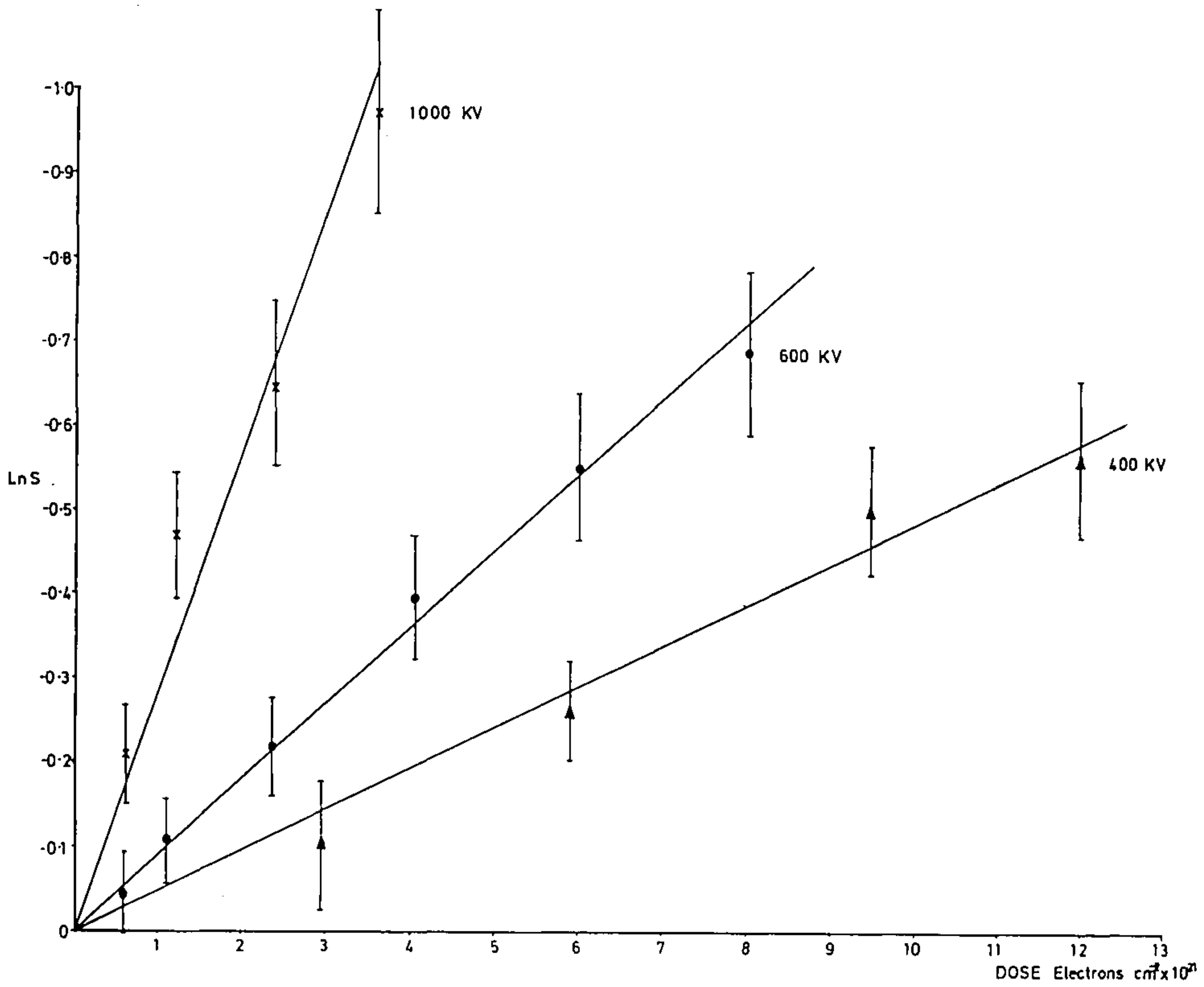

Figure 5.27. The disordering response of <110> Ni$_3$Fe at 305K as a function of accelerating voltage plotted as ln$\bar{S}$ versus dose.

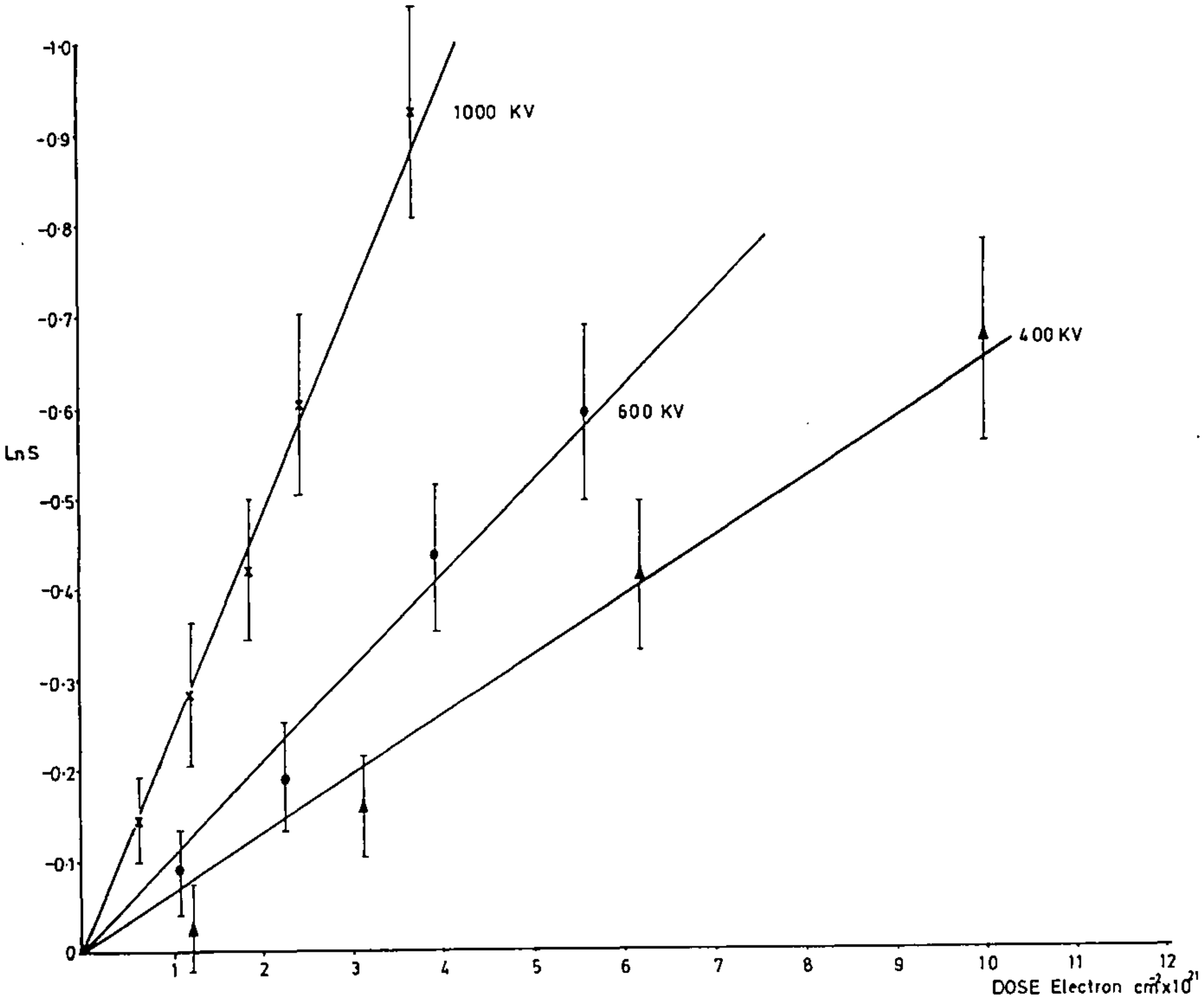

Figure 5.28. The disordering response of <110> Ni_3Fe at 248K as a function of accelerating voltage plotted as lnS versus dose.

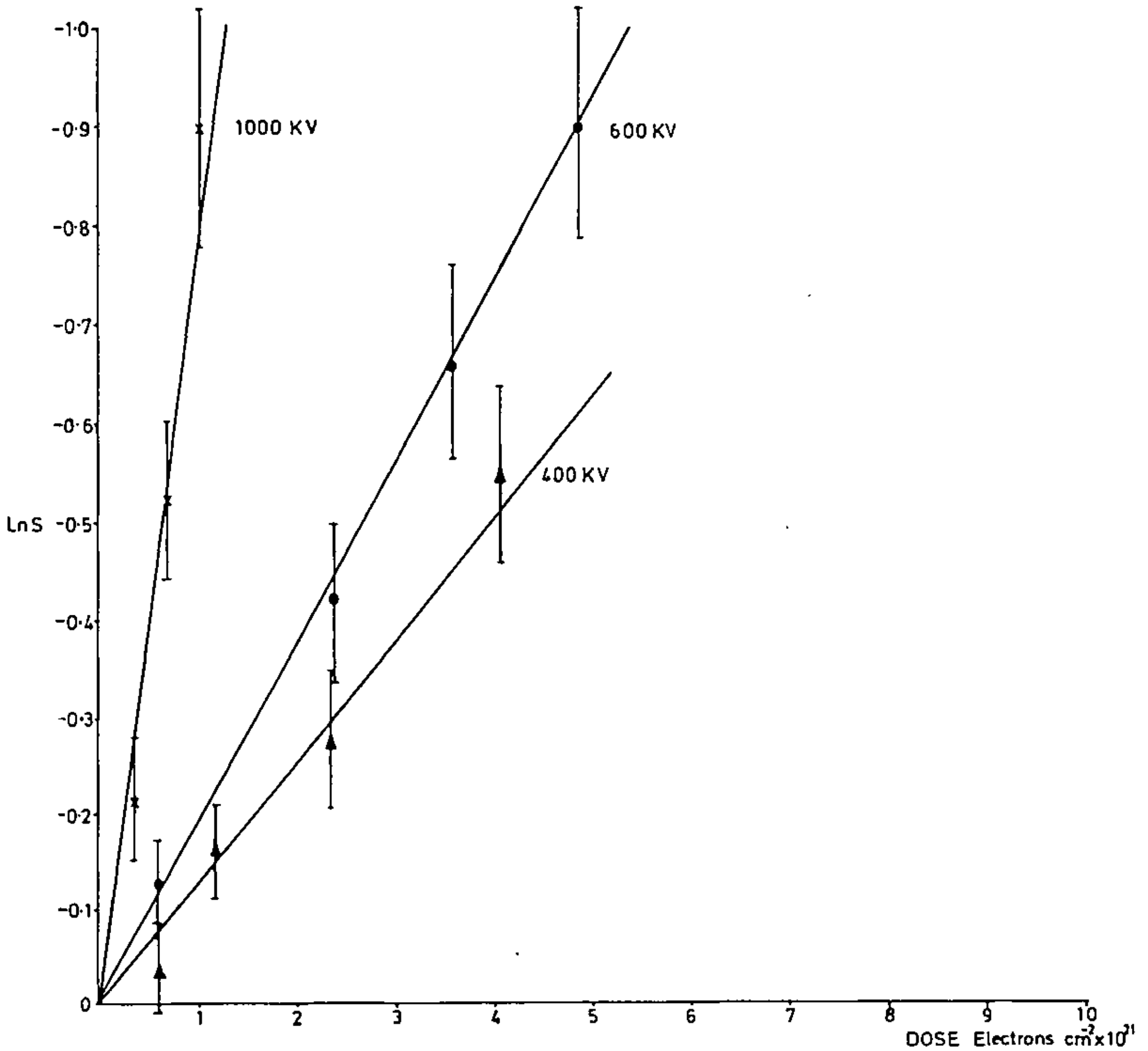

Figure 5.29. The disordering response of <110> Ni_3Fe at 154K as a function of accelerating voltage plotted as ln S versus dose.

Table 5.5. Variation in the Experimentally Determined Disordering Cross-section as a Function of Accelerating Voltage and Temperature of <110> Ni_3Fe

Accelerating Voltage (kV)	Temperature (K)	Disordering Cross-section (barns)
1000	305	285
600	305	97
400	303	49
1000	248	305
600	248	120
400	248	68
1000	154	650
600	154	199
400	154	115

5.3.2. Effect of Orientation

The orientation dependence of disordering was briefly examined in fully ordered Ni_3Al. The results are listed in Table 5.6. As predicted in Chapter 3.2. no significant orientation effect was observed.

Table 5.6. Effect of Orientation on the Experimentally Determined Disordering Cross-section of Ni_3Al Under Electron Irradiation

Orientation <uvw>	Temperature (K)	Accelerating Voltage (kV)	Disordering Cross-section (barns)
100	305	500	40
110	305	500	44
111	305	500	37
100	305	1000	100
110	305	1000	108
100	15	600	176
110	15	600	182
100	15	1000	498
110	15	1000	550

5.4. The Response of Fully Ordered NiAl and FeAl (B2 Structure) to Electron Irradiation

5.4.1. NiAl

5.4.1. (i) Effect of Temperature and Accelerating Voltage

The response of fully ordered NiAl to 600 kV and 1000 kV electron irradiation has been investigated at temperatures between 305K and 15K. The irradiations were carried out with the specimens close to the <100> orientation with an incident flux of $\sim 1 \times 10^{19}$ electrons $cm^{-2}sec^{-1}$. The results, plotted as S versus dose, are shown in Figures 5.30 and 5.31 for 1000 kV and 600 kV respectively for the range of temperatures. Although the rate of disordering increases with decreasing temperature, the alloy does not completely disorder under either 1000 kV or 600 kV irradiation even after extended irradiation at 15K. With reference to the theory of Chapter 3.2. such a response suggests that defects are mobile enough at 15K to restore order to the lattice which implies that the activation energy for defect migration is very small. Figure 5.32. shows the results of Figure 5.30. plotted according to equation (53) as ln S versus dose. The plots are not linear at any of the temperatures; however, a disordering cross-section has been estimated from the slope of a tangent taken to the early part of the response. These values are clearly subject to more uncertainty than those evaluated from the linear plots of ln S versus dose and their physical significance may be questionable as the reordering component of the response is high even at the lowest temperatures. This point will be returned to in the discussion. With these provisos however, disordering cross-sections evaluated from both the 1000 kV and 600 kV results are tabulated below in Table 5.7. and show that the disordering cross-section increases with decreasing temperature.

It is clear that the alloy NiAl has a significantly higher resistance to disordering compared with the other alloys examined. The threshold energy for disordering was found to be between 350 kV and 400 kV at 15K, so the reasons for the difference would not appear to lie in NiAl having a much higher displacement energy.

5.4.1. (ii) Effect of Orientation

The orientation dependence of disordering has been examined in fully ordered NiAl under 1000 kV irradiation at 158K. The results are shown in Figure 5.33. plotted as S versus dose. No significant

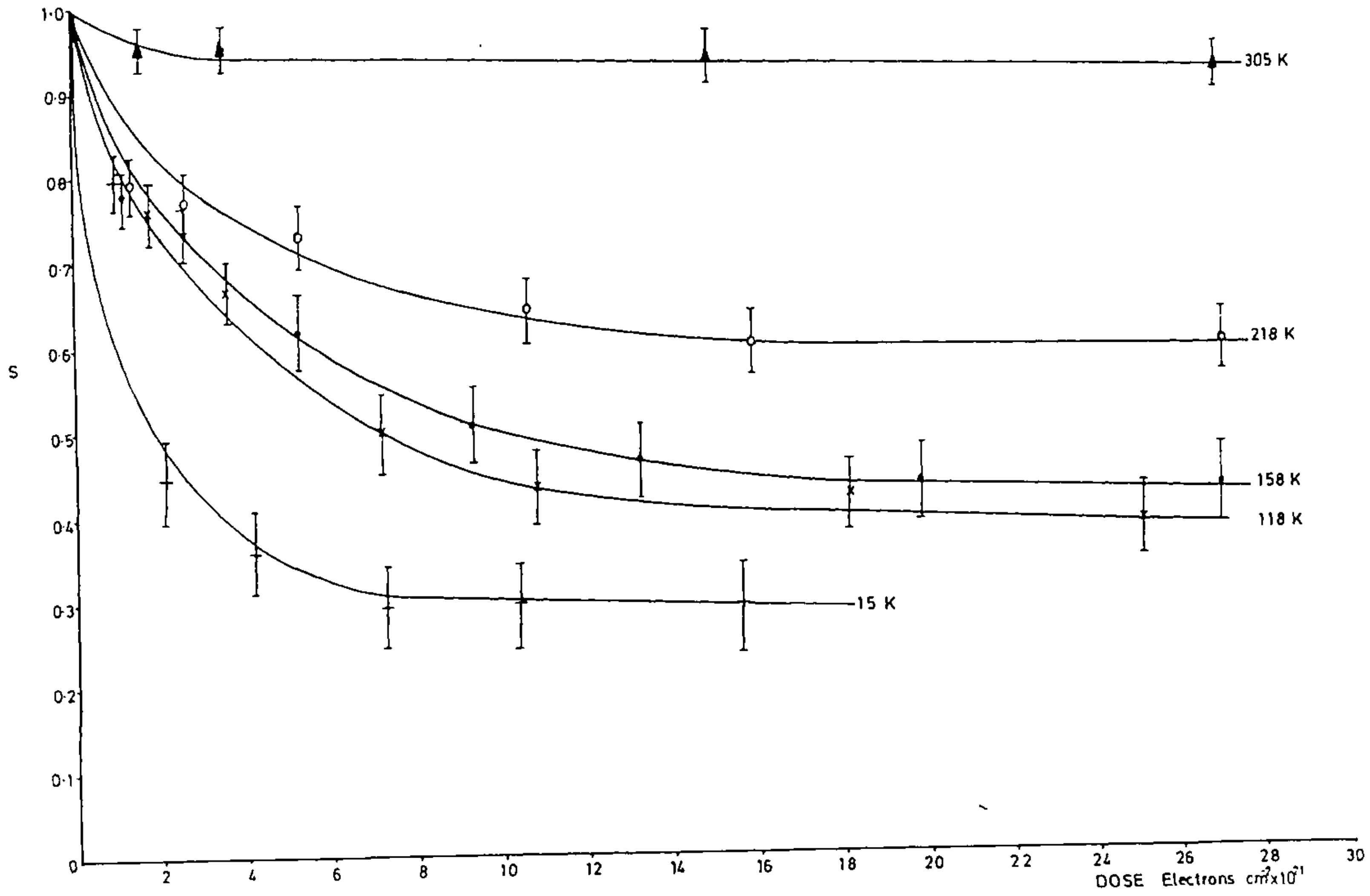

Figure 5.30. The disordering response to 100 kV electron irradiation of <100> NiAl as a function of temperature.

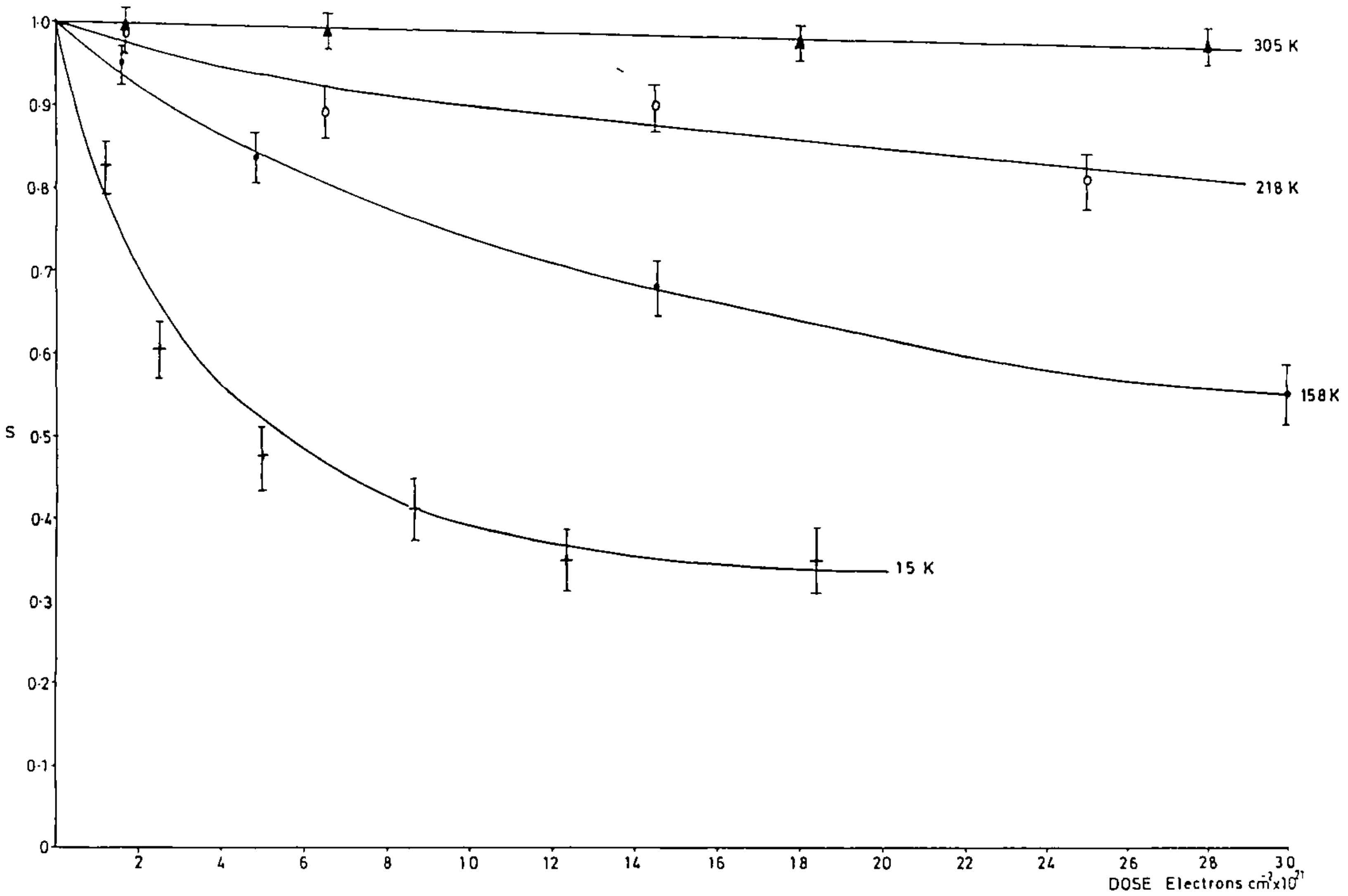

Figure 5.31. The disordering response of <100> NiAl to 600 kV electron irradiation as a function of temperature.

orientation effect is apparent.

Table 5.7. Variation in the Experimentally Determined Disordering Cross-section of <100> NiAl under 1000 kV and 600 kV Irradiation

Temperature (K)	Experimentally determined disordering cross-section (barns)	
	1000 kV irradiation	600 kV irradiation
305	20	10
218	73	20
158	106	42
118	117	-
15	330	170

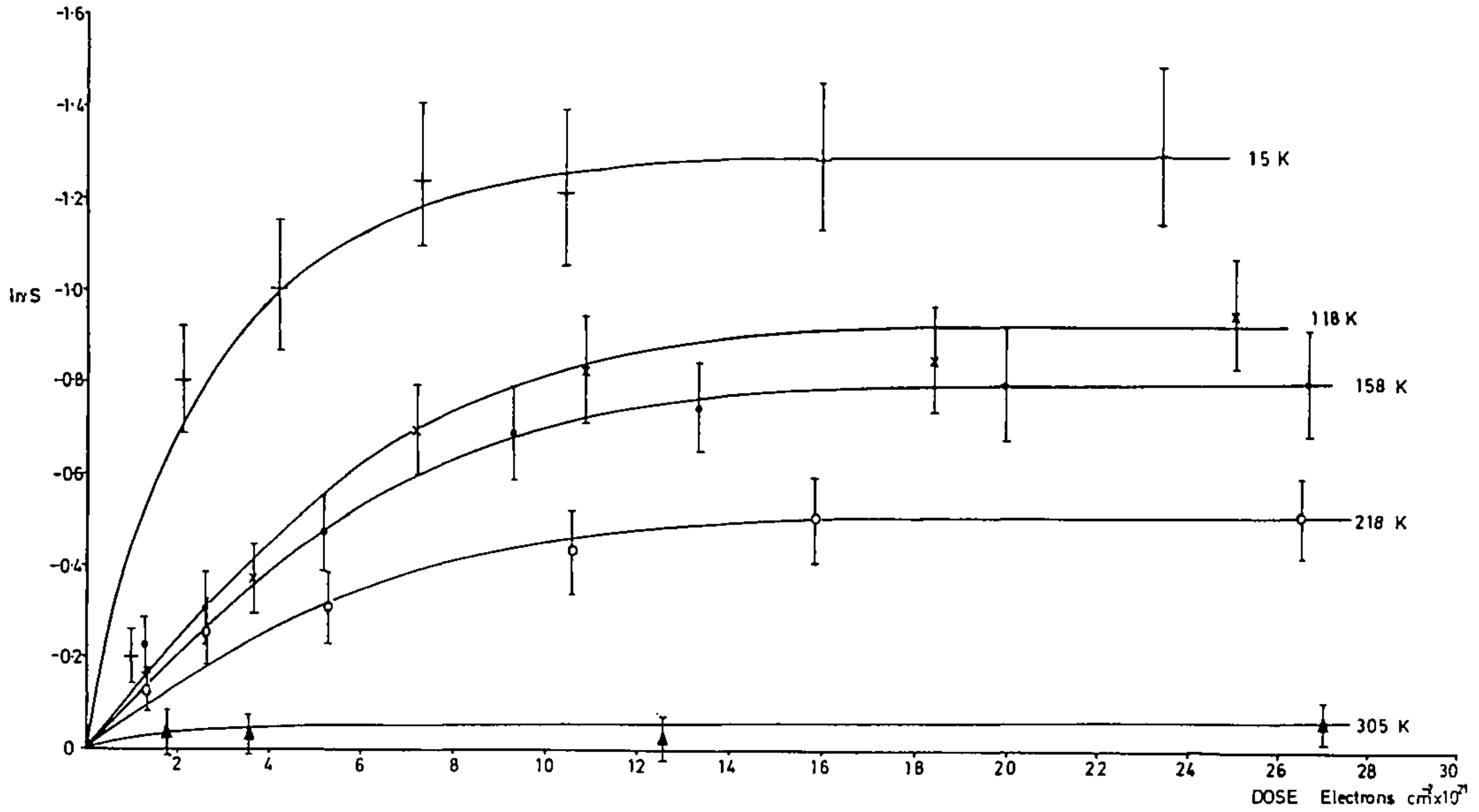

Figure 5.32. The disordering response of <100> NiAl under 1000 kV electron irradiation as a function of temperature plotted as lnS versus dose.

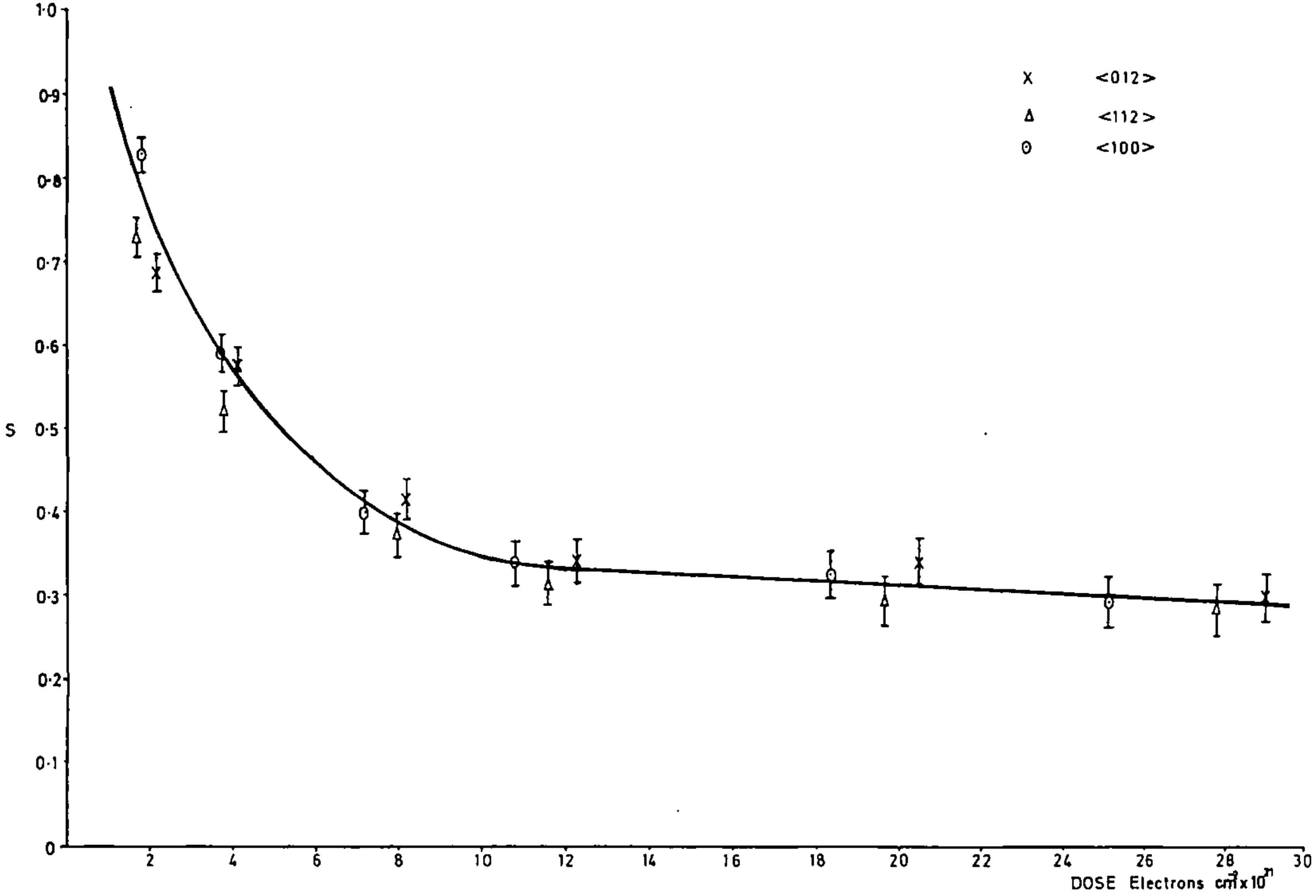

Figure 5.33. The orientation dependence of disordering in NiAl under 1000 kV electron irradiation at 158K.

5.4.2. Effect of 1000 kV Irradiation on <100> FeAl as a Function of Temperature

The response of fully ordered FeAl to electron irradiation has been briefly examined to investigate whether the resistance of NiAl to disordering is characteristic of alloys with the B2 structure. FeAl was chosen because, like NiAl, it is fully ordered up to its melting point. The irradiations were carried out with specimens close to the <100> orientation with an incident flux of 5 x 10^{18} electrons $cm^{-2}sec^{-1}$. The results of 1000 kV irradiation at 305K, 158K and 118K are shown in Figure 5.3.4. plotted as ln S versus dose. Unlike NiAl the alloy readily disordered at these temperatures and the disordering rate increased with decreasing temperature. Accurate evaluation of the disordering rate in FeAl is difficult using the electron diffraction technique because the alloy has a high interstitial migration energy of 1.35 eV (see Table 2.1.) which leads to the formation of a high density of defect loops, even in thin specimens (< 1000 Å), at relatively high temperatures (∿ 300K), see Chapter 4.3.2. However, the experimental observations suggest that the disordering cross-section is temperature dependent in a manner similar to the $L1_2$ alloys. The estimated disordering cross-sections for each temperature are listed in Table 5.8.

The threshold energy for disordering was observed to be between 350 kV and 400 kV at 15K.

Table 5.8. Estimated Disordering Cross-section of <100> FeAl under 1000 kV Irradiation

Temperature (K)	Disordering cross-section (barns)
305	109
150	270
118	350

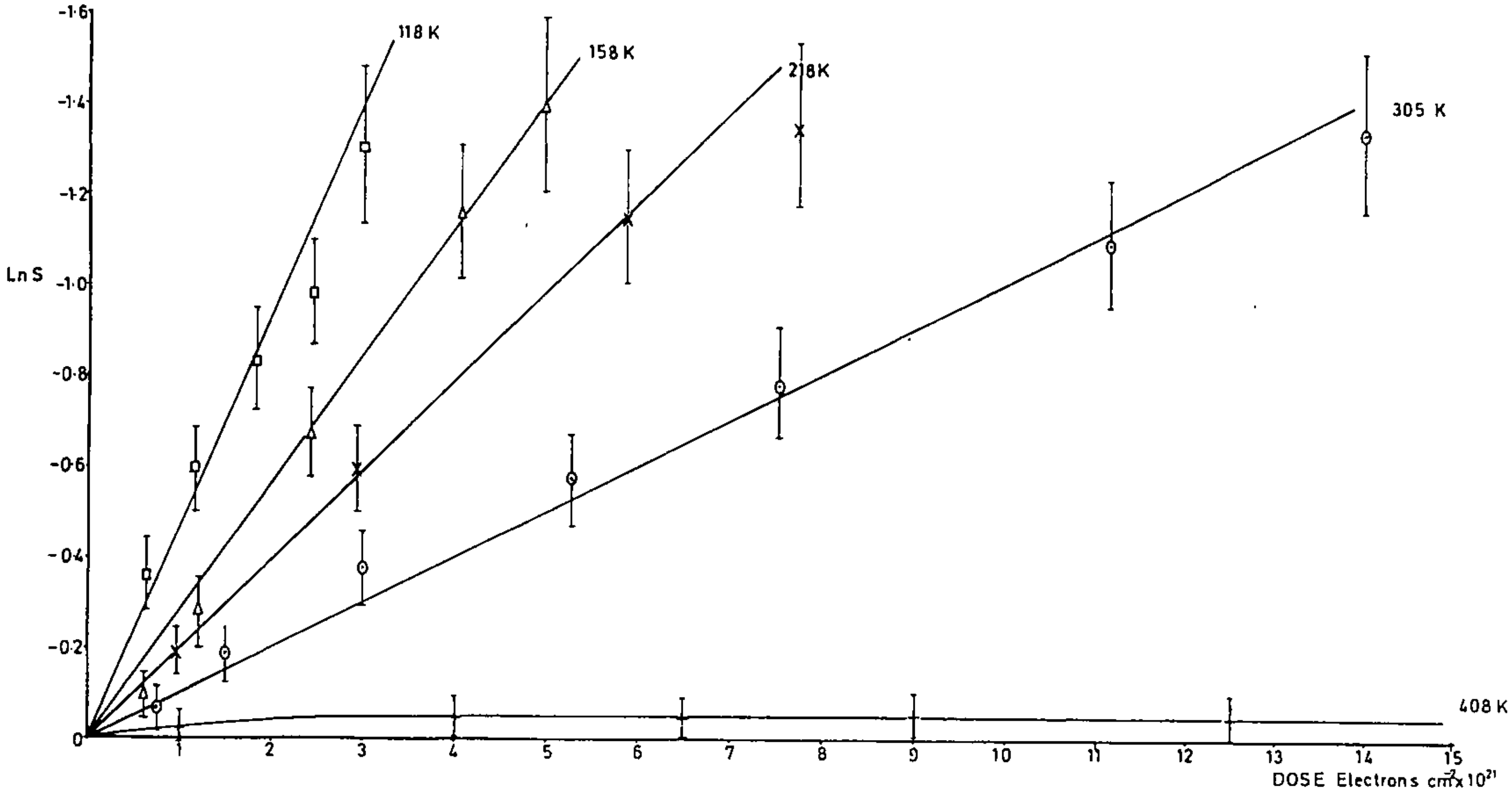

Figure 5.34. The disordering response of <100> FeAl to 1000 kV electron irradiation as a function of temperature plotted as lnS versus dose.

CHAPTER 6

Discussion

Although there are some marked differences in the response to electron irradiation of the ordered alloys investigated in the present work, there is a common pattern which can be identified as a function of the irradiation temperature. At elevated temperatures the alloys do not disorder, at intermediate temperatures the ordering and disordering forces balance to give a steady-state value of S, and at low temperatures the alloys disorder completely. However, the experimental results show that the increase in the degree of disorder and disordering rate with decreasing temperature cannot be explained only in terms of existing theoretical ideas (Chapter 3.2.); as there is also some temperature dependent component to the disordering cross-section.

The first part of the discussion is concerned with an analysis of the temperature dependence of the disordering cross-section and identification of the relevant disordering mechanisms. In the second part of the discussion the theoretical models outlined in Chapter 3.2. are fitted to the experimental results when there is a balance between disordering and reordering.

6.1. Temperature Dependence of the Disordering Cross-section

An increase in the disordering cross-section with decreasing temperature was most apparent in the $L1_2$ alloys, when irradiated with electrons of energies up to 1000 keV, because below ∿ 300K the alloys became fully disordered, i.e. the ln S versus dose plots were linear (for example see Figures 5.17 and 5.26) and the corresponding disordering cross-sections were readily determined. In Mg_3Cd and NiAl under electron irradiation there was evidence of reordering at temperatures as low as ∿ 150K and 15K respectively (e.g. see Figures 5.2. and 5.32) and so analysis of the disordering response of these alloys was slightly more complex. However, an increase in the disordering cross-section with decreasing temperature was identified in both of these alloy systems as shown in Figure 5.5. and Table 5.7.

The temperature dependence of the disordering cross-section can be explained by a decrease in the threshold displacement energy with decreasing temperature. Figure 6.1. shows the experimentally determined variation in $\varepsilon\sigma_d$ with accelerating voltage for <110> orientated Ni_3Al

Figure 6.1. (i) 305K

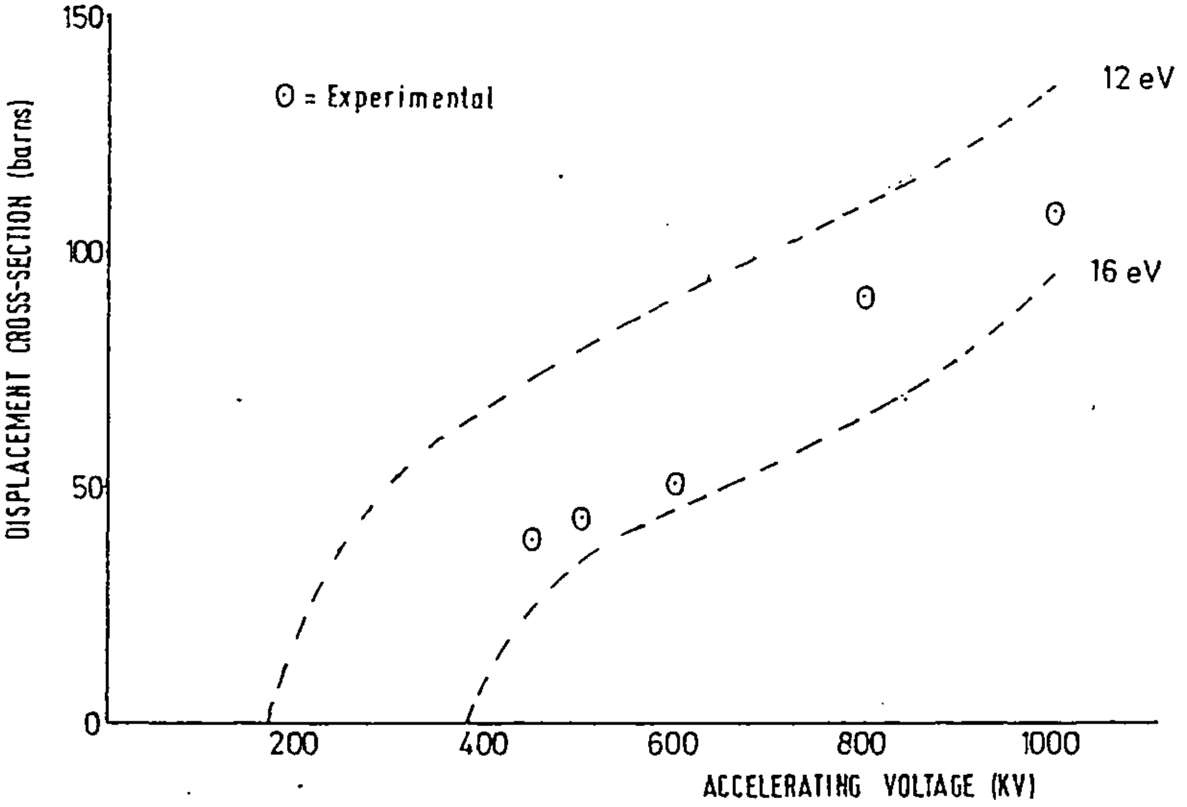

(ii) 203K

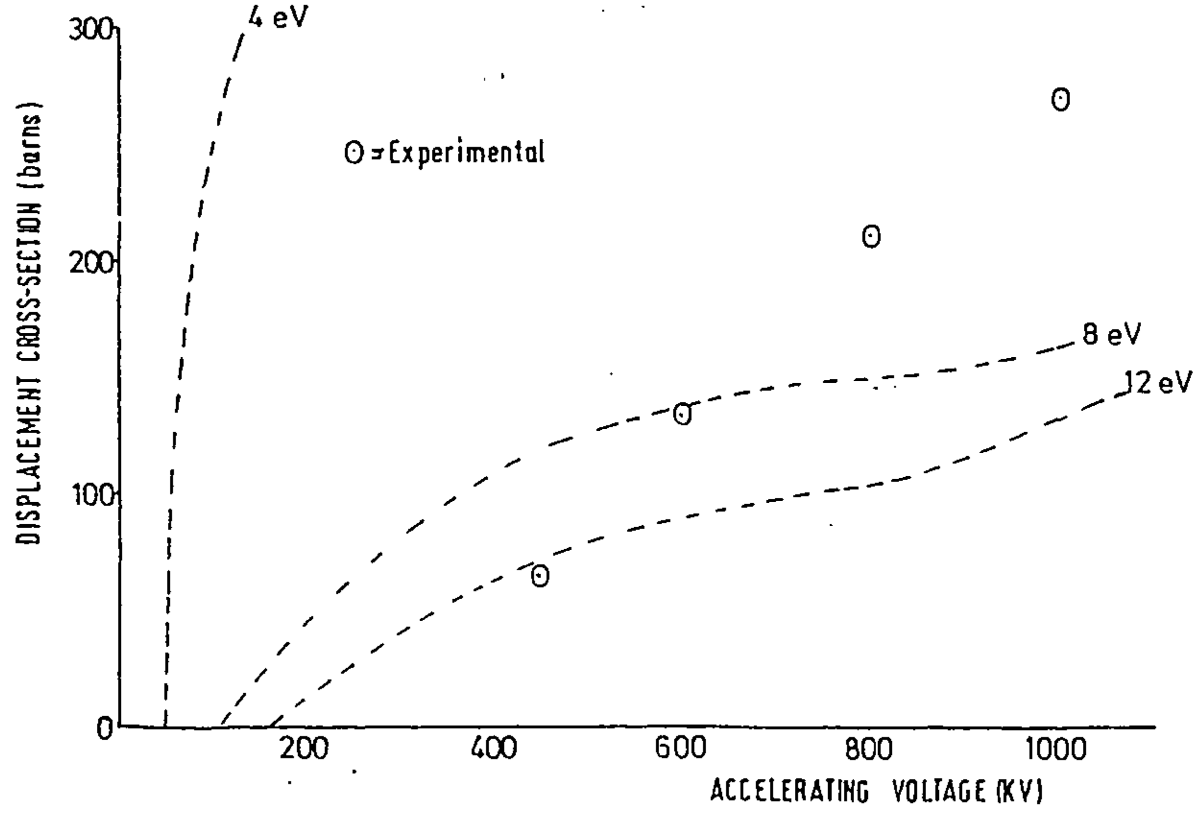

ʘ Experimentally determined variation in the disordering cross-section for <110> Ni_3Al as a function of accelerating voltage at (i) 305K (ii) 203K and (iii) 15K. (Theoretical weighted mean displacement cross-section assuming the single displacement energy indicated.)

Figure 6.1. (iii) 15K

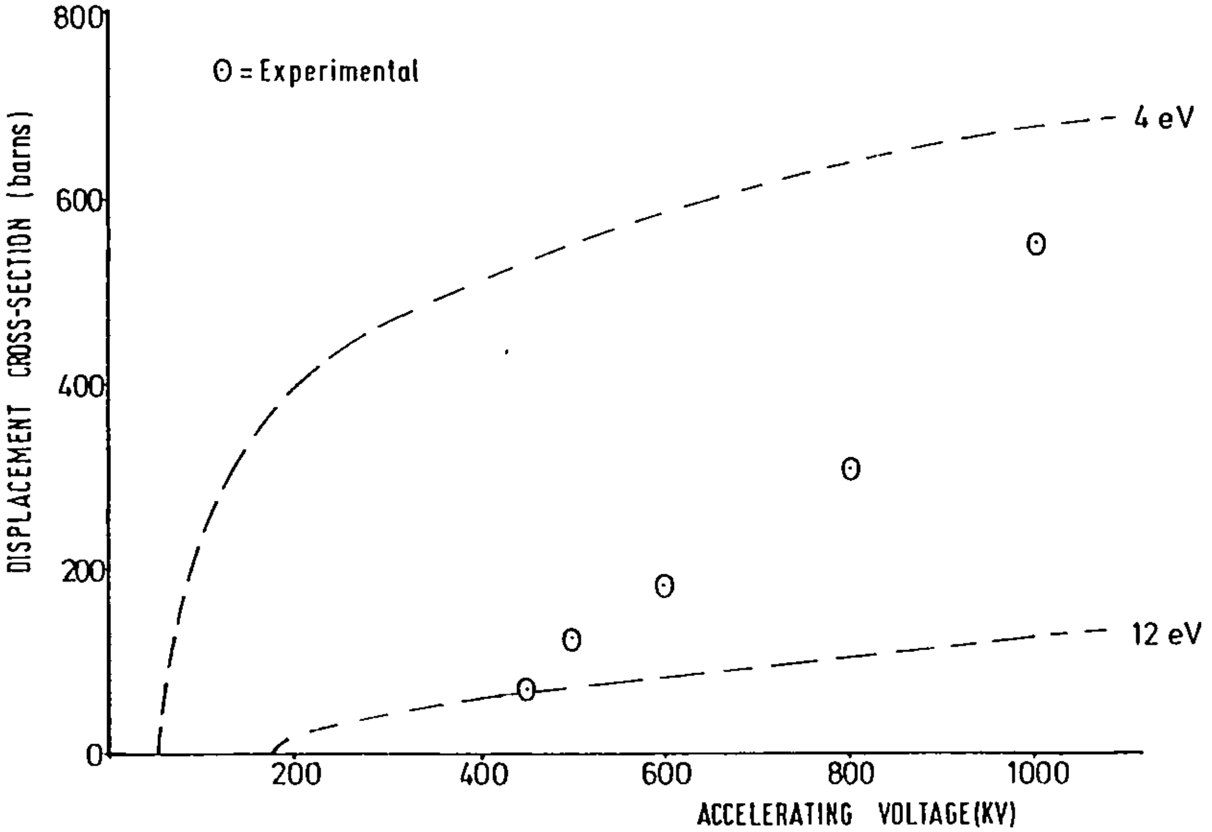

at 305K, 203K and 15K. The dotted lines represent the variation in the theoretical weighted-mean displacement cross-section assuming the single displacement energy indicated. It can be seen that at 305K the variation in $\varepsilon\sigma_d$ is in accord with a threshold displacement energy of between 16eV and 12eV. However, as the temperature is lowered it is not possible to fit the variation of $\varepsilon\sigma_d$ to a single displacement energy and at 15K the disordering cross-section under 1000 kV irradiation corresponds to a threshold displacement energy of ∿4 eV which is considerably lower than that of pure nickel (see Table 3.2.). A similar situation exists in the variation of $\varepsilon\sigma_d$ as a function of temperature and accelerating voltage in Ni_3Fe, Mg_3Cd and NiAl. Figure 6.2. shows the variation of $\varepsilon\sigma_d$ of <110> Ni_3Fe with accelerating voltage for 305K and 154K again it can be seen that the variation at each temperature cannot be fitted to a single threshold displacement energy. In Mg_3Cd the disordering cross-section measured at the lower temperatures (< 150K) corresponds to a threshold displacement energy of less than 4eV which seems unrealistically small. Thus, it is concluded that a decrease in the threshold displacement energy with decreasing temperature does not adequately explain the present experimental observations. Moreover there is no experimental evidence to support such a temperature dependence of the threshold displacement energy. The recent investigations into the temperature dependence of the <110> displacement energy in Cu have shown that, for this material E_d increases with decreasing temperature, see Figure 3.4. Therefore, the results have been analysed via the disordering parameter ε by assuming isotropic threshold displacement energies. The temperature dependence of the disordering cross-section in the $L1_2$ alloys is first discussed.

6.1.1. Threshold Displacement Energy Assumptions

Analysis of the experimental results in terms of damage rate calculations and by determination of the disordering parameter ε requires accurate knowledge of the threshold displacement energy, E_d. There is no data available for the ordered alloys studied and so isotropic values have been assumed for each of the atomic components of the alloys. The assumed values are based on those reported in the literature, (Table 3.2.), for the pure elements and are consistent with the disordering thresholds measured at 15K. The disordering threshold corresponds to the minimum energy that is required to displace both the atomic species in a binary alloy, because if only one type of atom is displaced

Figure 6.2. (i)

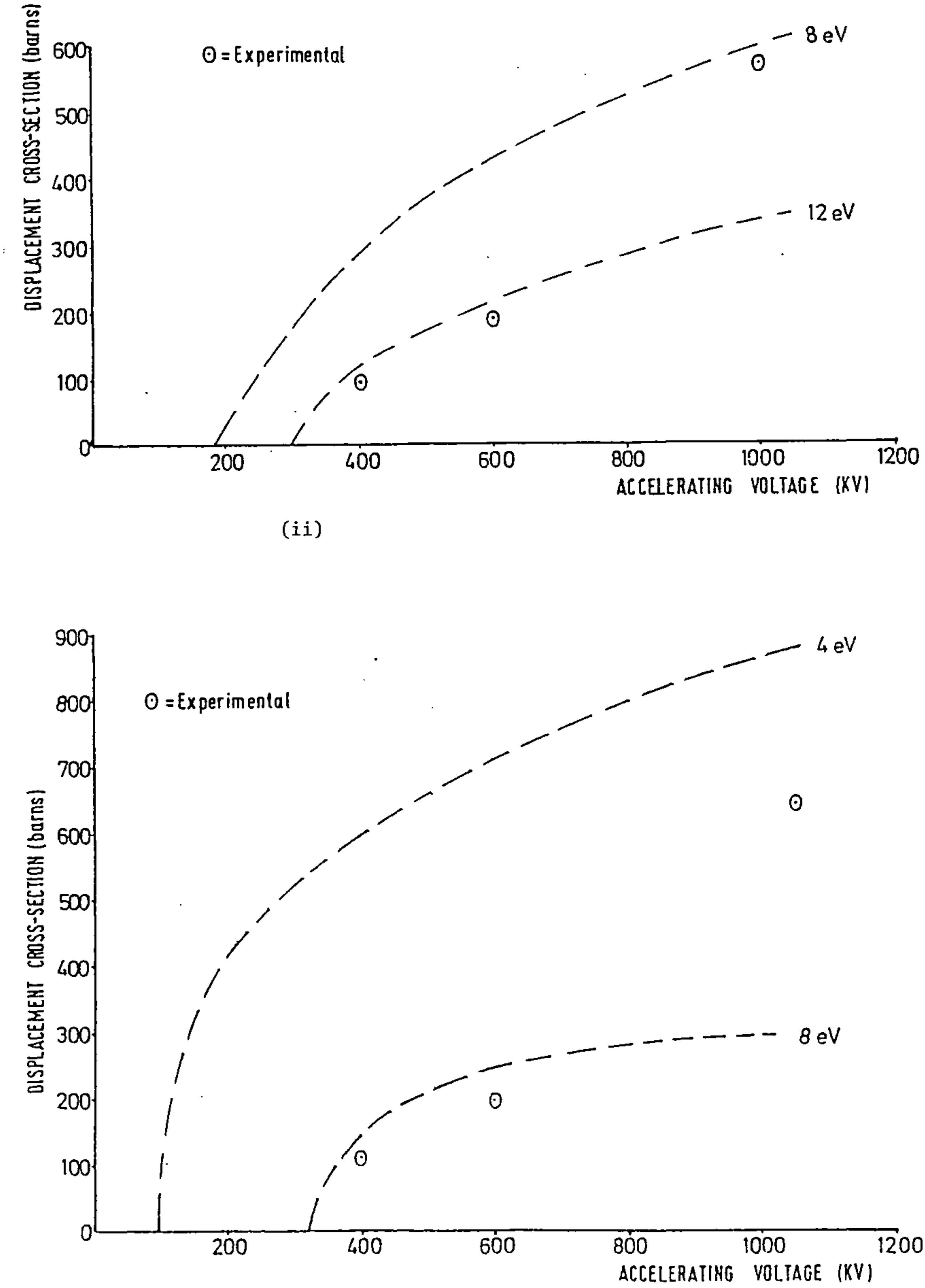

Θ Experimentally determined variation in the disordering cross-section of <110> Ni$_3$Fe as a function of accelerating voltage at (i) 305K and (ii) 154K. (Theoretical weighted mean displacement cross-section assuming the single displacement energy indicated.)

there would be no wrong sites for it to occupy, i.e. disordering would not occur.

The disordering threshold alone cannot be used to evaluate the threshold displacement energies because the damage can be a complex superposition of primary and secondary events involving both types of atom. For example, in Mg_3Cd disordering occurred readily under 200 kV electron irradiation but not under 150 kV irradiation. Since the energy transferred to a Cd atom in a primary electron-atom collision is less than 5 eV it is much more probable that the Cd atoms are displaced in secondary collisions with the lighter, and hence more energetic, Mg atoms. Also as the superlattice reflection intensity change monitored using the electron diffraction technique is anisotropic, (Chapter 4.3.3.) the disordering threshold measured using this technique will reflect the upper limit of the estimated displacement energy.

Taking these limitations into consideration, Table 6.1. lists the measured disordering thresholds, the maximum energy transferred in a primary electron-atom collision (equation (23)), the maximum energy transferred in a secondary unlike atom collision and the assumed threshold displacement energies.

6.1.2. $L1_2$ Alloys

Analysis of the temperature dependence of the disordering cross-section via the parameter ε requires accurate knowledge of the displacement cross-section σ_d. Weighted mean theoretical displacement cross-sections have been determined for Ni_3Al and Ni_3Fe using the displacement energies assumed in Table 6.1. The cross-sections which include secondary displacements are shown in Tables 6.2a and 6.2b respectively.

The disordering parameter ε has been determined as a function of accelerating voltage and temperature for <110> Ni_3Al, using the experimental results of Chapter 5.3.1. and the theoretical cross-sections in Table 6.2a. The results of this analysis are shown in Figure 6.3. At 305K ε is approximately equal to 2 and is independent of accelerating voltage. As the temperature is lowered ε increases and below ∿200K the increase is greater for the higher accelerating voltages.

Table 6.1. Assumed Threshold Displacement Energies for the Ordered Alloys Investigated in the Present Work

Alloy	Experimentally Determined Disordering Threshold Electron Energy Range (keV)	Energy transferred in a primary electron-atom collision (eV)		Maximum Energy transferred in a secondary unlike atom collision (E = Energy of pko) (eV)	Assumed Threshold Displacement Energy (eV)	
		Ni	Al		Ni	Al
Ni$_3$Al	400	21	45	0.85E	22	16
	450	24	53			
		Ni	Fe		Ni	Fe
Ni$_3$Fe	350	18	18	0.99E	18	20
	400	21	21			
		Fe	Al		Fe	Al
FeAl	350	18	38	0.85E	22	16
	400	21	45			
		Ni	Al		Ni	Al
NiAl	350	18	38	0.85E	22	16
	400	21	45			
		Mg	Cd		Mg	Cd
Mg$_3$Cd	150	15	3	0.59E	10	10
	200	22	5			

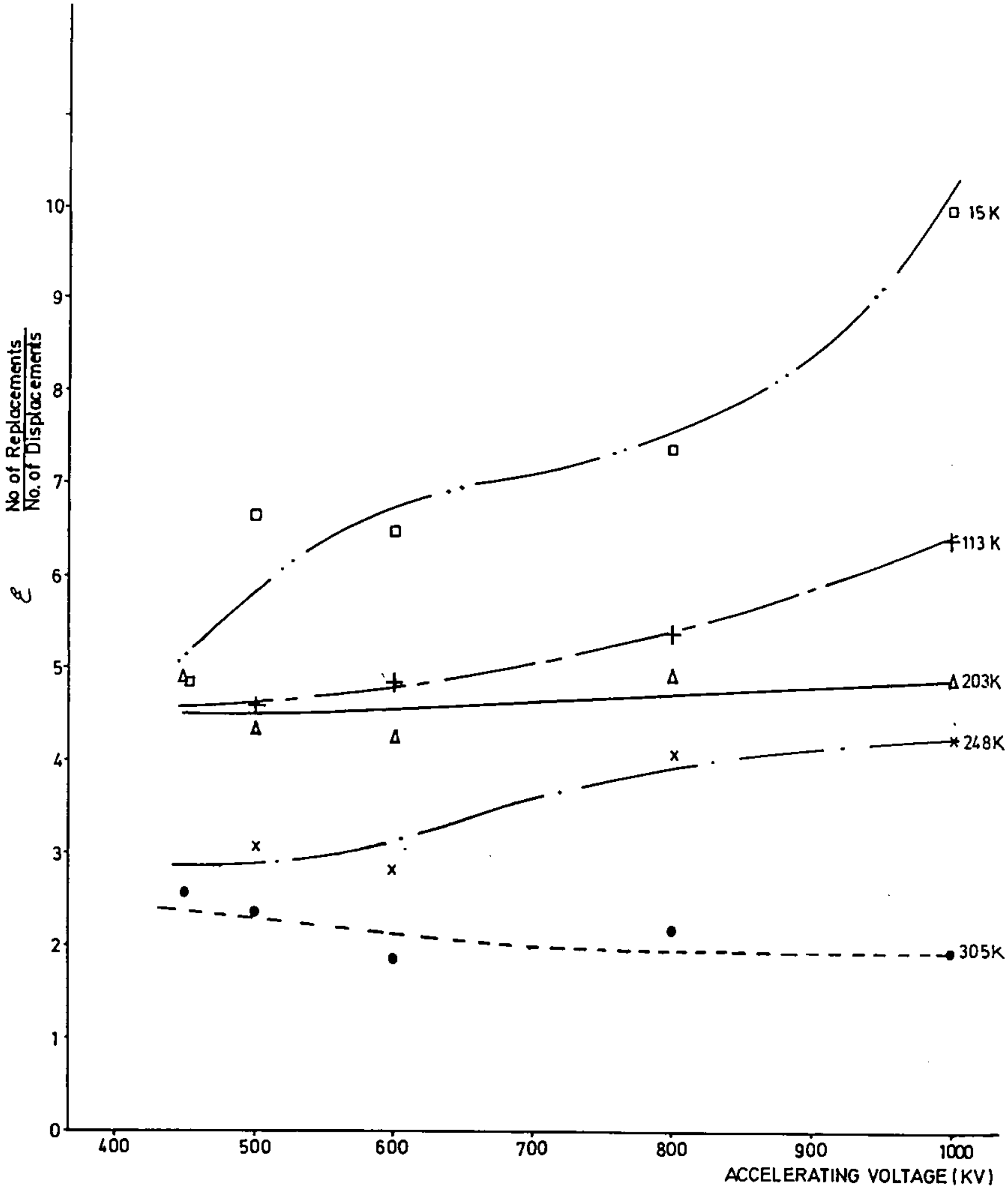

Figure 6.3. Variation in the disordering parameter ε for <110> Ni_3Al as a function of temperature and accelerating voltage.

Table 6.2a: Theoretical Displacement Cross-section of Ni_3Al as a Function of Accelerating Voltage

Accelerating Voltage (kV)	σ_d Theor. (barns)
1000	55
800	42
600	28
500	18
450	14

Table 6.2b: Theoretical Displacement Cross-section of Ni_3Fe as a Function of Accelerating Voltage

Accelerating Voltage (kV)	σ_d Theor. (barns)
1000	45
600	32
400	23

Table 6.3. shows the results of a similar analysis of the disordering response of <110> Ni_3Fe using the theoretical cross-sections in Table 6.2b. ε increases as the temperature decreases for each of the accelerating voltages, at any of the three temperatures ε is greater for the higher energy electrons.

Table 6.3. Variation in ε for <110> Ni_3Fe as a Function of Temperature and Accelerating Voltage

Temperature K	Accelerating Voltage 1000 kV	 600 kV	 400 kV
305	6.3	3	2.1
248	6.6	3.8	3.0
154	14.4	6.2	5.0

The actual values determined for ε depend crucially on the assumed values of σ_d and it is conceivable that these values could be in error by a factor of ~ 2. Therefore in an attempt to eliminate the uncertainty in σ_d a second approach has been taken to the analysis of the results. Assuming σ_d is independent of temperature, the ratio of the experimentally determined cross-section, $\varepsilon\sigma_d$, at two temperatures gives a direct measure of any change in the magnitude of ε. For Ni_3Al and Ni_3Fe ratios of the experimentally determined cross-sections have been taken with respect to $\varepsilon\sigma_{d\ 305K}$. The results of this analysis are shown in Tables 6.4a and 6.4b for Ni_3Al and Ni_3Fe respectively.

Table 6.4a. Variation in the Ratio $\varepsilon\sigma_{dT}/\varepsilon\sigma_{d305K}$ of <110> Ni_3Al as a Function of Accelerating Voltage

Ratio	Accelerating Voltage				
$\varepsilon\sigma_{dT}/\varepsilon\sigma_{d305K}$	1000 kV	800 kV	600 kV	500 kV	450 kV
$\varepsilon\sigma_{d305K}/\varepsilon\sigma_{d305K}$	1	1	1	1	1
$\varepsilon\sigma_{d248K}/\varepsilon\sigma_{d305K}$	2.2	1.8	1.5	1.3	-
$\varepsilon\sigma_{d203K}/\varepsilon\sigma_{d305K}$	2.5	2.4	2.4	1.8	1.1
$\varepsilon\sigma_{d118K}/\varepsilon\sigma_{d305K}$	3.2	2.5	2.7	1.9	2
$\varepsilon\sigma_{d15K}/\varepsilon\sigma_{d305K}$	5.1	3.4	3.7	2.7	2

Table 6.4b. Variation in the Ratio $\varepsilon\sigma_{dT}/\varepsilon\sigma_{d305K}$ in <110> Ni_3Fe as a Function of Accelerating Voltage

Ratio	Accelerating Voltage		
	1000 kV	600 kV	400 kV
$\varepsilon\sigma_{d305K}/\varepsilon\sigma_{d305K}$	1	1	1
$\varepsilon\sigma_{d248K}/\varepsilon\sigma_{d305K}$	1.1	1.3	1.5
$\varepsilon\sigma_{d154K}/\varepsilon\sigma_{d305K}$	2.3	1.7	2.4

It is clear from Tables 6.4a and 6.4b that there is an increase in ε with decreasing temperature for all the accelerating voltages. Between 305K and ∿ 150K ε increases by a factor of 2 in both Ni_3Al and Ni_3Fe and the increase does not vary appreciably with accelerating voltage. In Ni_3Al below ∿ 200K the increase is slightly greater for the higher energy electrons.

6.1.3. Summary

The preceding analysis of the results in terms of the disordering parameter, ε, is consistent with disordering by the propagation of replacement collision sequences down mixed-atom rows. The temperature dependence of the disordering cross-section results from an increase in the replacement collision sequence length with decreasing temperature.

This mechanistic hypothesis is discussed and defended in the following sections with respect to the present experimental results and those of previous investigations.

6.1.4. Effect of Temperature on Replacement Collision Sequence Length

The decrease in replacement collision sequence length with increasing temperature can be explained by the increased attenuation of the collision sequences by lattice vibrations. The lattice vibrations cause the atoms to be displaced away from the collision axis leading to a decrease in the efficiency of energy transfer and also to an increase in the amount of energy absorbed by the atoms surrounding the collision axis. The relative magnitudes of these effects have been evaluated for a <110> collision sequence in nickel using the theoretical model of Nelson et al (1962), (see Section 3.1.5(ii)). The energy loss equations are listed in Appendix II. A Debye temperature of 380K was assumed as this is close to that of the alloys Ni_3Al and Ni_3Fe (Table 2.1). The true Debye temperature of nickel is 450K.

Born-Mayer lattice potential constants were calculated using Brinkman's empirical equations also listed in Appendix II. The relative magnitudes of the energy losses ΔE_1 and ΔE_2 are shown in Figure 6.4., where ΔE_1 is the loss of energy to the rings of atoms surrounding the collision axis and ΔE_2 is the energy loss due to scattering out of the line of the collision axis. These energy losses are shown in Figure 6.4. for three temperatures, 305K, 158K and 19K as a function of E/E_F where E is the energy of the p.k.o. and E_F is the critical

Figure 6.4. (i)

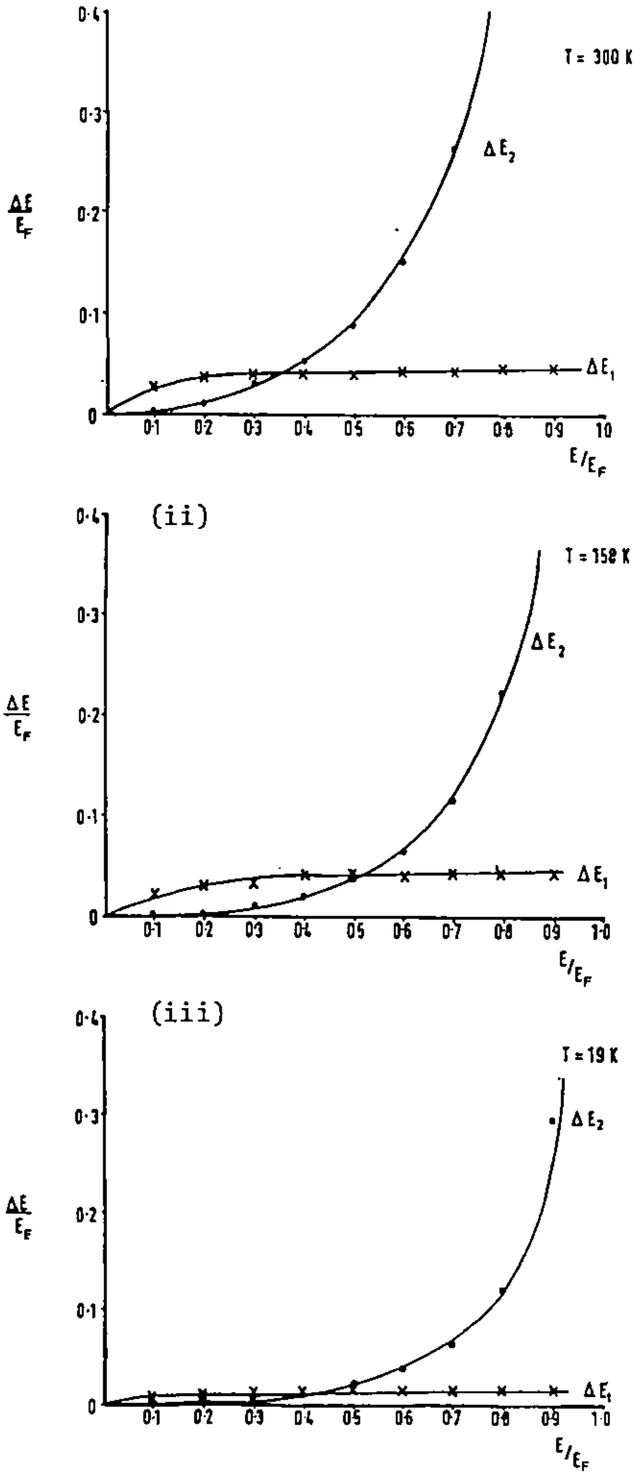

The relative magnitudes of the energy losses in a <110> focused collision sequence in nickel at (i) 300K (ii) 158K and (iii) 19K. E is the energy of the p.k.o. and E_F is the critical focusing energy. ΔE_1 is the energy loss to the rings of atoms surrounding the collision axis and ΔE_2 is the energy loss due to scattering out of the line of the collision axis.

focusing energy. For energies just above E_R, (= 0.25 E_F) the minimum energy required to create a replacement collision sequence, the energy loss mechanism ΔE_1 dominates at all temperatures. At higher energies ΔE_2 dominates with its importance as an energy loss mechanism increasing significantly with temperature for energies above 0.5 E_F.

The number of collisions, n(E) made by a sequence starting with an energy E has been calculated from the following equation

$$n(E) = \int_0^E \frac{dE}{\Sigma \Delta E} \qquad (62)$$

The result for a <110> sequence in nickel is shown in Figure 6.5. At 158K and 305K the collision range increases rapidly up to $E_F/4$, at this point the energy losses due to the scattering of the atoms out of the focusing line become important and prevent further significant increase. At 19K this mechanism of energy loss, (ΔE_2), is reduced and thus the range is increased by a factor of 3 compared with that at 305K. A decrease in the range occurs at energies close to E_F due to defocusing below E_F (Sanders and Fluit (1964)). The focusing energy for nickel calculated by the hard sphere model is 35 eV (Table 3.3.). Therefore, at 19K the energy lost per collision is ∿1 eV. The predictions of this simple model regarding the effect of temperature on replacement collision sequence length are in good agreement with the experimental observations of both Ni_3Al and Ni_3Fe.

Looking at the more sophisticated models introduced in Chapter 3.1.5.(ii) which have been applied to Cu, having a similar atomic weight, lattice parameter and Debye temperature to that of nickel, Kirsanov (1980) has shown that the length of a replacement collision sequence starting with a 100 eV p.k.o. is reduced by a factor of 2 between 0 and 300K. Also Tenenbaum (1978), in his more detailed study has shown that for the range of focusing energies below 100 eV the collision sequence length is reduced by a factor of ∿2 from 0K to 293K in both the <110> and <100> directions (see Figure 3.7.). Thus, these models support the conclusion that temperature dependence of the disordering cross-section arises from the attenuation of the replacement collision sequence length due to lattice vibrations.

Experimental evidence for the effect of temperature on the range of replacement collision sequences is limited. However, Merkle and Averback (1976) used transmission electron microscopy to investigate

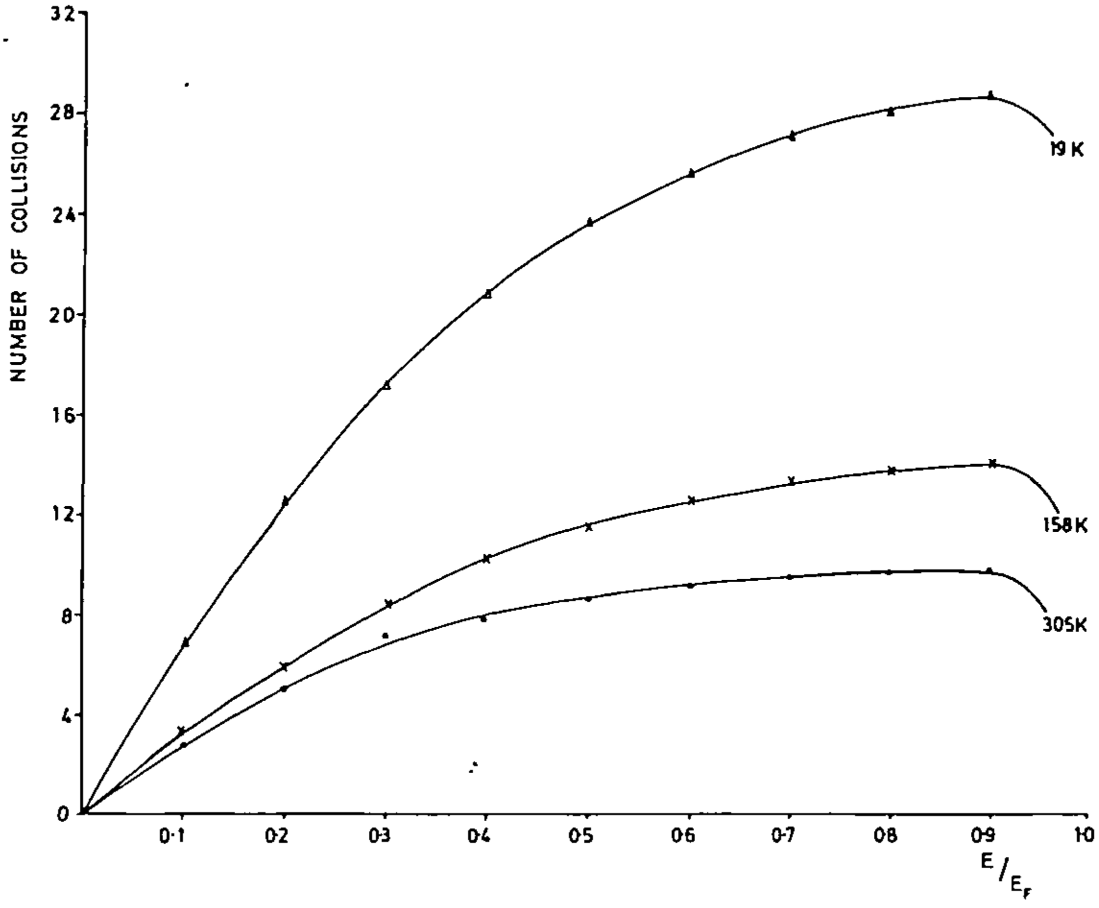

Figure 6.5. The effect of temperature on the number of collisions in a <110> focusing sequence in nickel. (E is the energy of the p.k.o. and E_F is the critical focusing energy.)

collision cascade tracks in Au and Ag at temperatures between 10K and 573K. The collision cascades were produced by self ion bombardment in the 200-600 keV energy range. The authors noted an interesting feature in that it was possible to observe the cascades splitting into subcascades more easily at temperatures between 300K and 573K than between 10K and 300K. A possible explanation for this observation is that, in addition to the increased rate of annealing with increasing temperature, the increased lattice vibrations localise the low energy subcascade branches of the high energy cascade and so aid the observed division. This mechanism is shown schematically in Figure 6.6.

6.1.5. Effect of Accelerating Voltage on R.C.S. Length

The dependence of disordering rate on accelerating voltage is also in accord with disordering by a replacement collision sequence mechanism. The magnitude of ε is greater for the higher energy electrons, when it is not limited by lattice vibrations, because the energy of the p.k.o. directly determines the length of the collision sequence. The creation of a replacement collision sequence is a low energy phenomenon and it is generally accepted, (see Chapter 3.1.5.(ii)), that the critical focusing energy is less than $\sim$100 eV. The maximum energy transferred in a primary electron-atom collision to the Ni, Al and Fe atoms, for the range of electron energies used in the present work is listed in Table 6.5. With the exception of the primary displaced Al atoms at the higher electron energies, all the other primary displacements are below the critical focusing energy and thus are able to create collision sequences. It is clear therefore that if the high energy Al atoms are involved in secondary atom-atom displacements the resulting lower energy displacements will also be able to create collision sequences.

Table 6.5. The Maximum Energy Transferred in a Primary Electron-Atom Collision

Electron Energy (eV)	Maximum Primary knock-on energy (eV) Ni	Fe	Al
1000	74	78	161
800	53	56	116
600	36	38	77
500	28	29	61
450	24	25	53
400	21	22	45

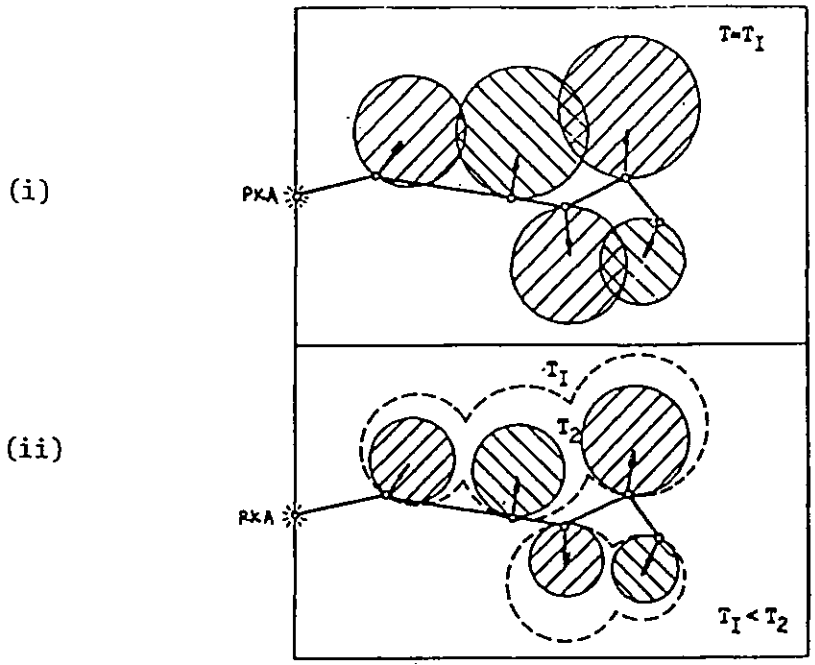

Figure 6.6. Schematic diagram showing subcascade formation at two temperatures, T, where $T_1 < T_2$. (i) The subcascades overlap at low irradiation temperatures (ii) As temperature increases splitting occurs into separate visible subcascades.

The above explanation of the results does not take into account the anisotropy in the superlattice intensity change, i.e. that disordering observed using electron diffraction in a [110] orientated $L1_2$ alloy represents displacements occurring in the [101] and [011] mixed atom rows at 60° to the incident beam direction. (see Chapter 4.3.3.). With reference to Table 3.1. for the nickel lattice it can be seen that recoil events are relatively unimportant in the incident beam direction. Under 1000 kV irradiation the recoils readily occur at 60° from the incident beam direction and even just above the threshold energy the p.k.o. atoms recoil at angles up to 30°. However, when an atom is scattered at an angle Θ to the electron beam its energy is reduced by the factor $\cos^2\Theta$ (Equation (25)). Table 6.6a lists the energies of the atoms from a primary electron-atom collision recoiling at an angle of 60° to the incident electron beam.

Table 6.6a. Energy of p.k.o. Recoil at 60° to Incident Electron Beam

Electron Energy (eV)	Energy of 60° recoil (eV) Ni	Fe	Al
1000	19	20	40
800	13	14	29
600	9	10	19
500	7	7	15
450	6	6	13
400	5	6	11

The theoretical model of Nelson et al (1962) estimates that the replacement energy, E_R, below which an atom cannot initiate a replacement collision sequence is $0.25E_F$. Assuming E_F is 100 eV, E_R is equal to 25 eV which is in reasonable agreement with the work of Tenenbaum (1978) where E_R is 15-20 eV. If the replacement energy of Ni_3Al and Ni_3Fe is also of a similar magnitude, one would only expect to observe disordering by replacement collision sequences, using the electron diffraction technique, at the higher accelerating voltages (> 700 kV). However, in this investigation there is evidence of disordering by the propagation of replacement collision sequences under 450 kV irradiation in Ni_3Al, (Figure 6.3.), and under 400 kV irradiation in Ni_3Fe (Table 6.3.). A possible explanation for this disparity is that replacement collision sequences are initiated even when there is a large angle between the displaced atom and the close packed direction.

It has been shown by computer simulation (Vineyard (1963) and Tenenbaum (1978)) that replacement collision sequences can be initiated by atoms that make an angle of up to 30° with the <110> directions and up to 20° with the <100> directions. Thus a knock-on atom in an arbitrary direction is probably 'absorbed' along a close packed direction. Table 6.6b presents the energies of atoms from a primary electron-atom collision recoiling at an angle of 30° to the incident electron beam. It is clear that even the atoms displaced by the lower energy electrons will have sufficient energy to create a replacement collision sequence.

Table 6.6b. Energy of p.k.o. Recoil at 30° to Incident Electron Beam.

Electron Energy (eV)	Energy of 30° Recoil (eV) Ni	Fe	Al
1000	56	59	121
800	40	42	87
600	27	29	58
500	21	22	46
450	18	19	40
400	16	17	34

From a comparison of the ε values (= ratio of the number of replacements to displacements of Ni_3Al (Figure 6.3.) and Ni_3Fe (Table 6.3.) at particular temperatures between 305K and 150K, it can be seen that whereas ε, in Ni_3Fe, is significantly higher than in Ni_3Al under 1000 kV irradiation; for the lower energy electrons ($\leq$ 600 kV) the ε values are very similar being only slightly higher in Ni_3Fe. There are two factors which could account for such an observation:-

(i) Mass difference effects, and

(ii) Defocusing of the primary knock-ons when they are above E_F.

This result is consistent with the attenuation of the collision sequence length in Ni_3Al being caused by the difference in the masses of the nickel and aluminium with the magnitude of the energy loss increasing as the primary knock-on energy increases.

The theoretical collision models outlined in Chapter 3.1.5. have been used to simulate the energy losses due to lattice vibrations in crystals composed of identical atoms. The energy lost per collision is predicted to be of the order of a few eV and to increase with increasing temperature. However, in ordered alloys there is an additional factor which can attenuate the replacement collision sequence, this is the efficiency of energy transfer between atoms of different mass.

From classical mechanics the maximum energy that can be transferred ($E_{s\ max}$) in a head-on collision between two atoms of masses M_1 and M_2 is given by equation (27) which is equal to

$$E_{s\ max} = \frac{4M_1M_2\ E_1}{(M_1 + M_2)^2}$$

where E_1 is the energy of the incident atom. Thus for a Ni-Fe collision, where $M_1 \approx M_2$, the energy transfer in a head on collision is ~ 100% efficient. However, for a Ni-Al collision the energy transfer is only ∿85% efficient. Since the additional energy loss due to the difference in the masses of the atoms is a percentage of the incident atom energy, the energy losses are greater for the higher energy knock-ons and so the mass-difference effects are more apparent for the irradiations with the higher energy electrons. For example, consider a primary nickel displacement with an energy of 80 eV initiating a replacement collision sequence down a mixed-atom, Ni-Al, row. If energy is lost due only to mass difference effects then there will be twelve collisions in the sequence before the energy of the moving atom falls to less than 10 eV. If the primary knock-on energy is 40 eV, then there will be eight collisions in the sequence before the energy falls below 10 eV. Thus, although the high energy primary knock-on has twice the energy of the low energy knock-on the collision sequence length is only increased by a factor of 1.5.

The second factor which could explain the experimental observations is that when the primary knock-ons have an energy greater than the critical focusing energy, E_F, then energy must be lost before a replacement collision sequence can be propagated. Thus, at these 'high' energies the primary knock-ons are less efficient at creating collision sequences than those which are just below E_F. This effect may be occurring in Ni_3Al under 1000 kV irradiation as the primary aluminium displacements have an energy greater than 100 eV whereas in Ni_3Fe, both the nickel and iron primary displacements are less than 100 eV.

6.1.6. Effect of Debye Temperature, Θ_D

The displacement amplitude of an atom away from the focusing axis is directly related to the Debye temperature, Θ_D, of the lattice, such that at any particular temperature the displacement amplitude of a material with a high Θ_D will be lower than that of a material with a low Θ_D. Thus, for materials with similar lattice potentials, at any particular temperature, replacement collision sequences are more easily propagated in those with the greater Θ_D's. The energy loss calculations due to lattice vibrations have been carried out for a <110> focusing sequence in lead, which has a Debye temperature of 88K. Using the collision model of Nelson et al (1962) in Appendix II. The effect of temperature on the length of the replacement collision sequence is shown in Figure 6.7. In contrast to the nickel results (Figure 6.5.) it can be seen that on increasing the temperature from 19K to 305K the replacement collision sequence length is reduced by a factor $\sim$ 13. (The actual number of collisions in a focusing sequence at any particular temperature depends upon assumptions concerning the lattice potential. The lattice potential was calculated from Brinkman's empirical equations, Appendix II.)

It is significant that between $\sim$ 300K and $\sim$ 150K ε increases by a factor of $\sim$ 2 for both Ni_3Al and Ni_3Fe over the range of accelerating voltages investigated, i.e. the energy losses due to lattice vibrations are approximately the same in each of the alloys. This is consistent with the predictions of the theoretical models since the alloys have almost identical Debye temperatures (see Table 2.1.).

6.1.7. Mg_3Cd

Analysis of the disordering response of <0001> Mg_3Cd to electron irradiation has shown that there is a temperature dependent component to the disordering cross-section, $\varepsilon\sigma_d$, such that it increases with decreasing temperature for all the accelerating voltages employed. (see Figure 5.5.). In order to analyse this temperature dependence via the disordering parameter ε weighted mean displacement cross-sections have been determined using assumed threshold displacement energies of 10 eV for both Mg and Cd. The theoretical cross-sections which include secondary displacements are listed in Table 6.7.
The variation in ε as a function of accelerating voltage and temperature is shown in Table 6.8.

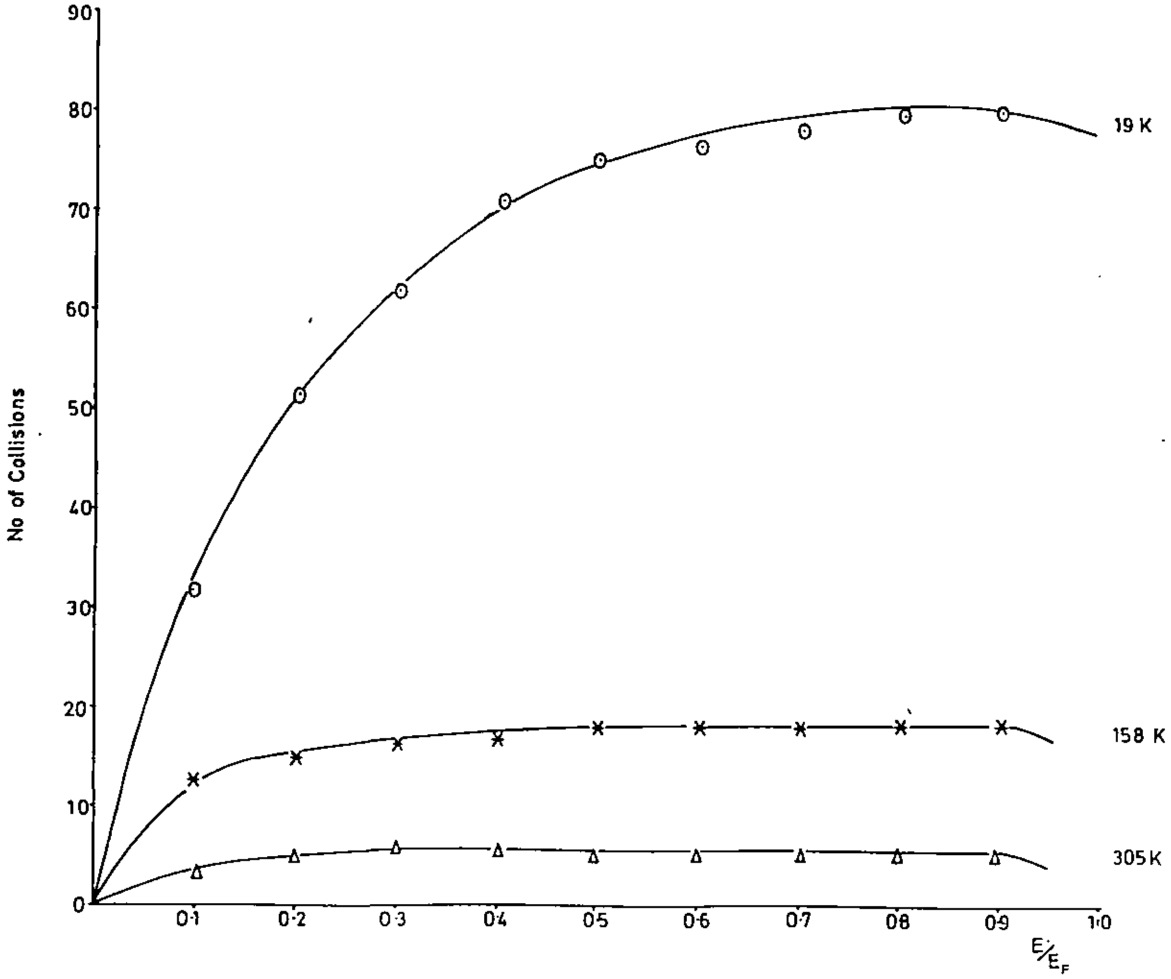

Figure 6.7. The effect of temperature on the number of collisions in a <110> focusing sequence in lead. (E is the energy of the p.k.o. and E_F is the critical focusing energy.)

Table 6.7. Theoretical Displacement Cross-Section of Mg_3Cd as a Function of Accelerating Voltage

Accelerating Voltage (kV)	σ_d Theor. (barns)
1000	164
700	135
400	79

Table 6.8. Variation in ε for <0001> Mg_3Cd with Temperature and Accelerating Voltage

Temperature (K)	Accelerating Voltage (kV)		
	1000	700	400
305	0.6	0.4	0.4
251	1.4	0.6	0.7
220	1.7	1.0	0.8
158	4.7	2.9	2.1
118	5.2	3.3	2.6
15	7.3	6.5	5.4

At temperatures greater than ∿ 200K where there is a high reordering component of the response, $\varepsilon \lesssim 1$ for all accelerating voltages. However, for temperatures less than 200K $\varepsilon > 1$ and increases with decreasing temperature to a maximum of 7 for 1000 kV irradiation at 15K. The increase is slightly less for the lower accelerating voltages.

At temperatures less than ∿ 200K these results are consistent with disordering by the propagation of replacement collision sequences down mixed-atom rows, with the increase in disordering rate with decreasing temperature resulting from an increase in the replacement collision sequence length. Above ∿ 200K the results suggest that replacement collision sequences do not propagate and that uncorrelated recombination is the dominant disordering mechanism.

One possible explanation of the latter effect is that Mg_3Cd has a low Debye temperature. However, a much more likely explanation is that there is a high reordering component above 200K which significantly reduces the measured disordering rate, and, hence $\varepsilon\sigma_d$, even when S is close to unity.

In Appendix III it is shown that for disordering by unidirectional displacements in the DO_{19} superlattice, there is anisotropy in the superlattice reflection intensity change. Thus, for disordering to be observed when the alloy is irradiated in the <0001> orientation displacements must have occurred in directions non-parallel to this. It is predicted that replacement collision sequences will propagate most easily in the close packed directions of the basal plane which are composed of alternating rows of like and mixed atoms. When the irradiation is incident in the <0001> direction, the most likely mechanism by which disordering can occur by the propagation of replacement collision sequences in the basal plane is via secondary displacements in the <$10\bar{1}3$> and <$02\bar{2}3$> directions which are at 36° and 59° respectively to the incident beam. Table 6.9. lists the maximum energy transferred in a primary electron-atom collision as a function of accelerating voltage.

Table 6.9. The Maximum Energy Transferred in a Primary Electron-Atom Collision

Accelerating Voltage (kV)	Maximum Primary Knock-on Energy (eV)	
	Mg	Cd
1000	178	39
700	107	23
400	50	11

The low atomic weight Mg p.k.o. atoms have approximately four times the energy of the primary Cd displacements, hence the Mg atoms are more likely to be responsible for secondary displacements out of the incident beam direction.

Although there is a large difference in the energies of the primary displacements under 1000 kV and 400 kV irradiation, there is not a large difference in the replacement collision sequence length at temperatures approaching absolute zero where energy losses due to lattice vibrations are at a minimum. Possible explanations of this observation are mass difference effects and defocusing when the primary knock-on is above the critical focusing energy (see Section 6.1.5.).

6.1.8. B2 Alloys

6.1.8.(i) NiAl

The results of the investigation into the disordering response of <100> NiAl to electron irradiation have shown that the alloy is resistant to disordering under 600 kV and 1000 kV irradiation at temperatures as low as 15K (see Figures 5.30. and 5.31.). However, the initial disordering rate was observed to increase significantly with decreasing temperature and from this the variation in the disordering cross-section, $\varepsilon\sigma_d$, was estimated (Table 5.7.).

To analyse the temperature dependence of the disordering cross-section, via the parameter ε, weighted mean theoretical displacement cross-sections have been determined using the threshold displacement energies assumed in Table 6.1. Cross-sections of 57 barns and 34 barns have been assumed for 1000 kV and 600 kV irradiation respectively and the resulting ε values are shown in Table 6.10.

Table 6.10. Variation in ε for <100> NiAl as a Function of Accelerating Voltage and Temperature

Temperature (K)	Accelerating Voltage (kV)	
	1000	600
305	0.4	0.3
218	1.3	0.6
158	1.9	1.2
118	2.0	-
15	5.8	5

It can be seen that for both accelerating voltages ε increases from less than unity at 305K to $\sim$ 5 at 15K. It is not possible to be certain that the values of ε which are less than unity represent disordering by a mechanism of uncorrelated recombination as all the values are subject to errors resulting from a high reordering component observed at all the temperatures. However, the magnitude of the experimentally determined disordering cross-section at 15K, where reordering is at a minimum, does support disordering by a replacement collision sequence mechanism.

6.1.8. (ii) FeAl

The preliminary investigation into the disordering response of <100> FeAl to electron irradiation has shown that, unlike NiAl, it disorders readily at temperatures below 300K. The increase in the disordering rate with decreasing temperature is consistent with disordering by a replacement collision sequence mechanism, see Table 5.8.

6.1.9. Orientation Effects

In the present experimental investigation into the disordering response of ordered alloys to electron irradiation, electron diffraction was used to monitor changes in S. It has been shown (Chapter 4.3.3.) that there is anisotropy in the superlattice reflection intensity change, such that disordering is not observed when displacements occur only in the incident beam direction. Thus, using this technique one would not expect to monitor the effects of orientation on the disordering response as displacements must have occurred in directions non-parallel to the electron beam. This situation was confirmed experimentally for Ni_3Al, Mg_3Cd and NiAl. However, since the analysis of the experimental results for all the alloy systems investigated in the present work is consistent with disordering occurring by replacement collision sequences down mixed atom rows in directions which are not parallel to the electron beam, no matter what experimental technique is used to monitor changes in S, no effect of orientation should be observed. This point is discussed more fully in Section 6.1.11. with respect to previous investigations where disordering by a replacement collision sequence mechanism has been refuted because of the lack of an orientation dependence of disordering.

6.1.10. Recombination Volume Effects

There is another factor which could also account for an increase in the disordering rate with decreasing temperature which is a decrease in the recombination volume with decreasing temperature, i.e. an increase in the degree of uncorrelated recombination. Experimental evidence in Cu, Al and their dilute alloys (Lennartz et al (1977), Theis and Wollenberger (1980)) indicates that Z increases from $\sim 10^2$ at 300K to $\sim 10^3$ at 50K, i.e. there is a temperature dependence of the recombination volume but it is such that the recombination volume becomes larger as the temperature is decreased. Thus, if uncorrelated recombination was the dominant disordering mechanism and a similar temperature dependence of the recombination volume existed, a slight decrease in the disordering rate would be expected with decreasing temperature. However, this is the opposite effect to that which is observed experimentally and thus it is reasonable to conclude that a temperature dependent recombination volume cannot adequately explain the results.

6.1.11. Previous Investigations

The effect of temperature on the disordering rate/cross-section, when reordering is not observed, has been systematically studied for very few alloy systems. Carpenter and Schulson (1981) and Liu et al (1981) investigated the disordering response of Ni_3Al under 1000 kV and 650 kV irradiation respectively at temperatures from 300K to 150K. They found that below ∿250K the alloy became completely disordered and that the disordering rate increased with decreasing temperature. Evaluation of the disordering parameter ε from their data, assuming order was not detectable when $S = 0.15$ and using the $\sigma_{d\ \text{Theor.}}$ quoted in their d.p.a. analysis (see Table 3.5.) results in an increase in ε from 3 at 248K to 6 at 144K under 1000 kV irradiation and from 1 at 240K and 3 at 190K under 650kV irradiation. The magnitude of the increase in ε is in very good agreement with the results of the present work (see Figure 6.3.) and is consistent with disordering by the propagation of replacement collision sequences whose length increases with decreasing temperature. Although Carpenter and Schulson proposed that the temperature dependence of the disordering cross-section could be explained by a replacement collision sequence mechanism, no firm conclusion was reached because in the experimental procedure no attempt was made to hold the orientation constant. Similarly Liu et al refuted the replacement collision sequence mechanism because of the lack of an orientation dependence of the disordering rate. However, it has been discussed in Chapters 3.1. and 6.1.9. that for energies just above the threshold recoils are relatively unimportant in the incident beam direction and so replacement collision sequences are readily propagated in other close packed directions, i.e. the lack of an orientation dependence of the disordering rate is consistent with a replacement collision sequence mechanism of disordering. Furthermore, in the above experimental work the disordering response was not investigated at temperatures below 140K. Since the disordering cross-section is greatest at temperatures approaching absolute zero, for all accelerating voltages, it is understandable that disordering by a replacement collision sequence mechanism was not concluded.

The effect of temperature on the disordering response of Zr_3Al has also been studied by Carpenter and Schulson (1978) who observed that under 1000 kV irradiation the alloy became completely disordered below 375K and that the disordering rate was independent of temperature between 375K and 130K. Throughout this temperature range the disordering parameter ε was found to be equal to ~ 2. That an increase in the replacement collision sequence length was not observed with decreasing temperature, in this temperature range, could be explained by the large mass-difference between the constituent atoms or possible Debye temperature effects (see 6.1.6.). However, an alternative explanation is that at low temperatures there are errors in the experimental determination of S due to the formation of a high density of defect loops. Defect aggregation studies of electron irradiated Zr_3Al indicate that the interstitial migration energy is probably quite high. (Howe and Rainville (1977)).

The formation of a high density of defect loops in FeAl at $\sim$300K prevented accurate determination of the disordering response. However, it was apparent that the alloy disordered completely at 305K and that the disordering rate increased with decreasing temperature. Kinoshita et al (1982) investigated the disordering response of FeAl with a range of accelerating voltages from 250 kV to 1000kV at temperatures from 600K to 50K. The thickness fringe method was used to monitor changes in S, see Chapter 3.2.2. It was found that the disordering rate, for changes in S from unity to 0.75, showed a sudden increase below 373K and was fairly constant above and below this stage (with ε equal to ~ 1 for $T < 373K$). This slight temperature dependence of disordering was related to mobile interstitials escaping correlated recombination. It is interesting to note that the threshold energy for disordering using this technique was found to be 250 kV whereas using the electron diffraction technique, in the present work, it was found to be between 350 kV and 400 kV.

6.2. Analysis of the Results where a Balance Exists Between Disordering and Reordering Under Electron Irradiation

6.2.1. Ni_3Al

The temperature regime in which the disordering and reordering components of equation (56) are of equal magnitude and a pseudo-equilibrium or steady-state value of S is observed has been identified in Ni_3Al to be between ∿300K and ∿500K (see Figure 5.15) when it is irradiated with a damage rate of 10^{-3} d.p.a. sec^{-1}. The simple theory (equation (50)) predicts that in this temperature regime the thermal or irradiation produced defects have sufficient mobility to restore order to the lattice after atomic displacement.

The temperature below which defects become immobile can be determined by calculating the temperature at which no jump is made in the duration time of the experiment, t_e. The jump frequencies of a vacancy and an interstitial are given by equations (36) and (37) respectively, which can be written in a general form as

$$\nu_d = A_d \nu_o \exp(-E_d^M / k_b T) \qquad (63)$$

where d can be v or i, ν_o is the natural atomic vibration frequency and A_d an entropy factor. The average time per jump is equal to $1/\nu_d$, therefore for defects to be considered immobile

$$t_e << \frac{1}{(A_d \nu_o \exp -E_d^M / k_b T)} \qquad (64)$$

or

$$T << \frac{E_d{}^M}{k_b \ln (A_d \nu_o t_e)} \qquad (65)$$

The temperatures below which defects can be considered immobile in Ni_3Al have been calculated assuming a vacancy migration energy of 1.65 eV (see Table 2.1.), an interstitial migration energy of 0.15 eV (which is equal to that of pure nickel (Yoo and Stiegler (1977)), entropy factors of unity, ν_o equal to $10^{13} s^{-1}$ and t_e equal to 10^6 seconds.

The results of these calculations are that vacancies can be considered immobile below 440K and interstitials below 40K. This suggests that interstitials are not the defect responsible for the balance observed between disordering and reordering, because reordering is not observed above ∿250K. However, if it is assumed that reordering is due to mobile vacancies the activation energy for vacancy migration must be less than 1.65 eV. In the following analysis, reordering via a vacancy mechanism is assumed and the resulting vacancy migration energy in accord with this assumption determined.

Fitting of the Experimental Data to a Theoretical Model

The theoretical model discussed in Chapter 3.2. predicts the response of an ordered alloy to irradiation by evaluation of the relative magnitudes of the disordering and reordering components of equation (56). Assuming reordering occurs by a vacancy mechanism, the reordering component of the response for an AB_3 alloy can be written as

$$\frac{ds}{dt}_{ord} = 0.19\nu_o A_V(1-S)^2(v+v_o)\exp(-E_V{}^M/k_bT)[1-[(e - \frac{V_o(S+S^3/3)}{k_bT})[\frac{(3S+1)(S+3)}{3(1-S)^2}]]] \quad (66$$

where v_o is the thermal vacancy concentration and v is the irradiation-produced vacancy concentration. To determine the relevant equations for v and to assess the applicability of the model over the temperature range of interest the parameters listed in Table 6.11. have been assumed. The sink density was taken to be fixed and calculated, (assuming the surfaces to be the most important sink) from the equation $\alpha_i = \alpha_v = \pi/f^2$ where f is the foil thickness (Sharp (1969)). The natural atomic vibration frequency is equal to $\nu_o \simeq (h/k_b\Theta_D)^{-1}$ where Θ_D is the Debye temperature and h and k_b are Plancks and Boltzmann's constants respectively. Thus, as Θ_D for Ni_3Al is 390K (Table 2.1.) ν_o is $10^{13}s^{-1}$. The vacancy migration entropy factor A_v was calculated from the pre-exponent of the diffusivity which is equal to $D_o \sim \lambda^2\nu_oA_v$ (Cottrell (1975)). For Ni_3Al D_o has been experimentally determined to be 1 cm^2s^{-1} (Hancock (1971b)) and so A_v is $\sim 10^2$. T_c is known, and all the values tabulated would appear to be reasonable.

Table 6.11. Parameters Assumed in Analysis of Response of Ni_3Al to Electron Irradiation where a Balance Exists Between Disordering and Reordering.

Vacancy migration energy	$E_v{}^M$	1.65 eV
Vacancy formation energy	$E_v{}^F$	1.49 eV
Vacancy, interstitial sink density	α_v, α_i	$10^{11}cm^{-2}$
Vacancy jump distance	λ	$\sim 3 \times 10^{-8}cm$
Vacancy migration entropy factor	A_v	10^2
Natural atomic jump frequency	ν_o	$10^{13}s^{-1}$
Recombination volume	Z	100
Critical temperature	T_c	1658K
Atomic Displacement rate	K	1×10^{-3}d.p.a. s^{-1}

Vacancy Concentration

Firstly, it should be noted that no account has been taken of the thermal concentration of vacancies. It can be seen with reference to Figure 3.9. that this is quite reasonable as in the temperature range of interest, with a damage rate of 10^{-3}d.p.a. s^{-1}, the concentration of irradiation produced vacancies is far in excess of the thermal concentration.

To calculate the irradiation-produced vacancy concentration it is necessary to determine whether mutual recombination or losses to sinks is the dominant defect annealing mechanism. Using the parameters of Table 6.11. in equation (44), it can be calculated that below 960K mutual recombination is dominant. Therefore, the concentration of irradiation produced vacancies is given by equation (40), which is equal to

$$v = (K/Z\nu_v)^{1/2}$$

This equation represents the steady-state vacancy concentration and is only applicable when the build-up time to this condition is much shorter than the duration of the experiment. The temperature above which equation (40) is valid has been calculated using equation (45), assuming a maximum build up time of 100 seconds and the parameters of Table 6.11, this gives a value of 740K. Hence, below this temperature the build-up times are too large compared with the duration of the experiment and so a non steady-state time dependent vacancy concentration, given by equation (46), must be used in the theoretical model.
This is equal to

$$v = \left(\frac{2K\ \alpha_i\ \lambda^2}{Z}\right)^{1/2} t^{1/2}$$

Thus assuming reordering via a vacancy mechanism the theoretical response of Ni_3Al to electron irradiation, ds/dt_{irr}, at temperatures where reordering by thermal vacancies can be neglected is equal to

$$\frac{ds}{dt_{irr}} = -\varepsilon KS + 0.19(1-S)^2 A_v \nu_o \left(\frac{2K\alpha_i\lambda^2}{Z}\right)^{1/2} t^{1/2} \exp -\frac{E_v^M}{k_bT}[1-](e -\frac{V_o(S+S^3/3)}{k_bT}) \left(\frac{(3S+1)(S+3)}{3(1-S)^2}\right)]] \qquad (67)$$

Evaluation of the Vacancy Migration Energy

The steady-state condition when $ds/dt_{irr} = 0$ and $1 > S > 0$ has been observed experimentally in Ni_3Al at three temperatures. The activation energy of the rate constant, E_V^M, has been evaluated for each temperature by assuming equation (56) is equal to zero and fitting into the equation the assumed parameters of Table 6.11 and the experimentally determined parameters, i.e. the steady-state value of S, the time to reach the steady-state condition and ε, the number of replacements per displacement. The results of this analysis are shown in Table 6.12. and are consistent with reordering by a vacancy mechanism with a migration energy of ∿1 eV. Note that the value of E_V^M determined is in good agreement at the three temperatures.

Table 6.12. The Activation Energy for Vacancy Migration which is Consistent with the Experimentally Determined Steady-State Value of S in Ni_3Al under Electron Irradiation

Temperature (K)	Steady-state value of S	Time to steady-state S (secs)	ε	E_V^M (eV)
388	0.8	500	1	1.0
340	0.5	800	1.5	0.95
305	0.25	1000	2	0.95

Zee and Wilkes (1980), (1981), have successfully applied this type of theoretical model to the available irradiation data on Cu_3Au under thermal and fast neutrons. A complete analysis was carried out by integrating equation (56) numerically and fitting the experimental variation of S with time for a range of temperatures using the same diffusion parameters throughout. The point defect parameter critical to the fitting of the model was an activation energy for vacancy motion of 0.84 eV, which is in good agreement with the data available in the literature.

The value of ∿1 eV which is predicted by the theoretical model to be equal to the activation energy for vacancy migration in Ni_3Al is significantly lower than that of 1.65 eV estimated from diffusion data. (see Table 2.1.). A possible explanation for this discrepancy is that thermal diffusion in this alloy does not occur by the random motion of vacancies, but by a higher energy mechanism involving a cycle of correlated jumps. This allows diffusion of both Ni and Al atoms involving disordering during the cycle but no net disorder in the lattice after the cycle has been completed, (see Chapter 2.1.5.). However, under irradiation the alloy becomes disordered and so the vacancy migration can occur randomly, resulting in a decrease in the observed activation energy. If it is assumed that E_V^M varies quadratically with S, (Girifalco (1964)), equation (19) applies which is of the form

$$E_{V_d}^{M} (1 + CS^2)$$

The experimental results suggest that in Ni_3Al

$$E_V^M = 1(1 + 0.65\ S^2)\ eV$$

There is no experimental data available to support any variation of E_V^M with S for Ni_3Al since it is fully ordered up to within a few degrees of its melting point. However, Girifalco (1964) analysed tracer diffusion activation energy data for CuZn (Kuper et al (1956)) and found that for Cu; $E_V^M = 0.59\ (1 + 0.3\ S^2)$ eV and for Zn; $E_V^M = 0.39\ (1 + 0.66\ S^2)$ eV. Similarly the activation energies for vacancy formation and migration in fully ordered Cu_3Au have been estimated to be 0.94 eV and 1.07 eV respectively (Benci and Gasparrini (1966)) and the activation energy for self diffusion in the disordered state 1.66 eV. (Smithells (1976)). If the increase on ordering takes place mainly in the migration energy term (Girifalco (1964)), then for Cu_3Au

$$E_V^M = 0.72\ (1 + 0.4\ S^2)\ eV$$

Thus, the suggested variation of E_V^M with S in Ni_3Al is in accord with the variation observed in other ordered systems, and so it may be concluded that vacancies are the defect species responsible for reordering under irradiation in this alloy.

Figure 6. 8. shows the experimentally determined variation of the steady-state value of S as a function of temperature for three displacement rates, $\sim 10^{-2}$ d.p.a. sec^{-1} (Carpenter and Schulson (1981)) $\sim 10^{-3}$ d.p.a. sec^{-1} (present work) and $\sim 10^{-4}$ d.p.a. sec^{-1} (Liu et al (1981)). As predicted by the theoretical model (see Chapter 3.2.2.) increasing the displacement rate results in an increase in the temperature at which a particular steady-state value of S is observed.

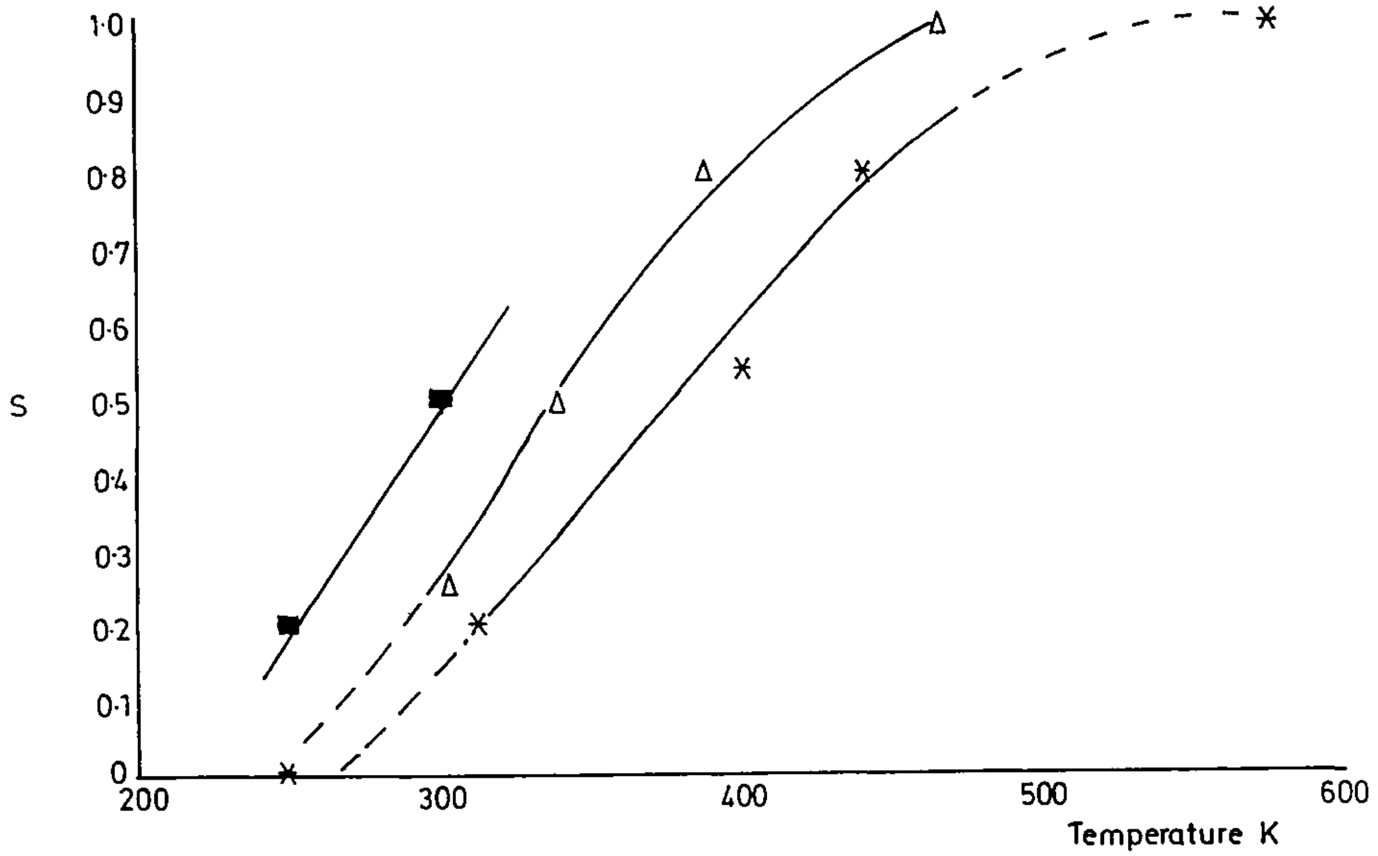

Figure 6.8. Experimentally determined variation in the steady-state value of S in Ni_3Al as a function of temperature and displacement rate.

✱ ∿ 10^{-2} d.p.a. s^{-1} (Carpenter and Schulson (1981)).

Δ ∿ 10^{-3} s.p.a. s^{-1} (present investigation).

■ ∿ 10^{-4} d.p.a. s^{-1} (Liu et al (1981)).

6.2.2. Ni_3Fe

The experimental results of Ni_3Fe which indicate that there is a steady-state value of S under electron irradiation have been treated in an identical manner to those of Ni_3Al. The parameters which have been assumed for the analysis are listed in Table 6.13.

All the assumed parameters are reasonable and the vacancy formation and migration energies have been taken as approximately equal to half the energy for self diffusion (see Table 2.1.). Using these parameters in equation (44) it has been calculated that below 565K mutual recombination is the dominant disordering mechanism and so the steady-state irradiation produced vacancy concentration is given by equation (40). However, assuming a maximum build-up time of 100 seconds to the steady-state condition, equation (40) is only valid above 446K. Therefore equation (46) must be used in the model for the non-steady state vacancy concentration. Since the irradiation-produced vacancy concentration is far in excess of the thermal vacancy concentration, at the temperatures of interest, the theoretical response of Ni_3Fe to irradiation is given by equation (67), which was used in the analysis of Ni_3Al.

Table 6.13. Parameters Assumed in Analysis of the Response of Ni_3Fe to Electron Irradiation where a Balance Exists between Disordering and Reordering

Vacancy migration energy	E_v^M	1 eV
Vacancy formation energy	E_v^F	1 eV
Vacancy, interstitial sink density	α_v, α_i	$10^{11} cm^{-2}$
Vacancy jump distance	λ	$3 \times 10^{-8} cm$
Vacancy migration entropy factor	A_v	10^{2}
Natural atomic jump frequency	ν_o	$10^{13} s^{-1}$
Recombination volume	Z	100
Critical temperature	T_c	776K
Atomic displacement rate	K	5×10^{-4} d.p.a. s^{-1}

Evaluation of the Activation Energy for Vacancy Migration

The steady-state analysis is rather limited for this alloy because:
(i) the large increase in ϵ from 400K to 300K significantly reduces the temperature range over which the steady state is observed, and
(ii), it was not possible to record equilibrium values of S between $0 > seq \gtrsim 0.4$. Therefore, of the three temperatures examined 305K, 337K,

and 408K, only at 337K was a true steady state value of S between zero and unity observed. However, for the three temperatures it has been assumed that there is a steady-state condition, i.e. equation (56) = $ds/dt_{irr} = 0$.

The assumed parameters of Table 6.13. and the experimentally determined parameters; the steady state value of S, the time to reach steady state and ε, have been fitted into the equation to determine the activation energy of the rate constant, which is equal to the vacancy migration energy. The results of this analysis are shown in Table 6.14.

Table 6.14. The Activation Energy for Vacancy Migration which is Consistent with the Experimentally Determined Steady-state Value of S in Ni_3Fe under Electron Irradiation

Temperature K	Steady-State S, Seq	time to S eq (secs)	ε	E_v^M eV
408	0.95	100	1	0.95
337	0.6	1000	2	0.92
305	0	$\sim$400	6	0.92

Although the theoretical model has only been fitted to one temperature where there is a true steady-state value of S, the value of 0.92 eV for the vacancy migration energy is in good agreement with the data available in the literature. Suzuki and Yamamoto (1959) for example showed, using creep studies, that the activation energy for self diffusion does not vary significantly with S being 1.99 eV and 2.07 eV in the disordered and ordered states respectively. This result is also supported by the work of Morris et al (1976) who showed that the activation energy for ordering is 2.2 eV and independent of the degree of order. Thus the analysis is consistent with reordering via a vacancy mechanism with C in equation (19) equal to zero.

6.2.3. Mg_3Cd

The temperature regime in which the disordering and reordering components of equation (56) are of approximately equal magnitude, resulting in a steady state value of S, has been identified in Mg_3Cd to be between $\sim$300K and $\sim$150K when irradiated with a damage rate of $\sim 10^{-3}$ d.p.a. sec^{-1} (see Section 5.1.1.). Simple theory predicts that in this regime the thermal or irradiation-produced defects have sufficient mobility to restore order to the lattice. From the results of Chapter 5.2it was determined that the activation energy for self diffusion is ~ 1 eV and it was estimated that the activation energy for vacancy migration is 0.5 eV. Using this value in equation (65) with the same parameters that were assumed for Ni_3Al (6.3.1.), the temperature below which vacancies can be considered immobile is $<<$ 140K. This result is in agreement with the lower temperature limit of the steady-state regime observed in the present work and so an analysis of the results has been made using a theoretical model based on a vacancy reordering mechanism.

Fitting of the Experimental Data to a Theoretical Model

The theoretical model of reordering via a vacancy mechanism predicts (Butler (1979)) that the rate of reordering in an AB_3 alloy is equal to

$$\frac{ds}{dt}_{ord} = 0.19\ A_V \nu_o (1-S)^2 (v+v_o) \exp\left(-\frac{E_v^M}{k_b T}\right) \left[1 - \left[\left(\exp -\frac{V_o (S+S^3/3}{k_b T}\right) \left[\frac{(3S+1)(S+3)}{3(1-S)^2}\right]\right]\right]$$

where v and v_o are the irradiation-produced and thermal vacancy concentrations respectively. To determine the relevant equations for v and to assess the applicability of the model over the temperature range of interest the parameters listed in Table 6.15 have been assumed.

The activation energies come from Chapter 5.2. The vacancy migration entropy factor, A_v, has been taken as unity since the pre-exponent of the diffusivity is less than $10^{-4} cm^2 sec^{-1}$. (Smithells (1976)). The critical temperature is taken from Davies and Stoloff (1964). All other assumed are reasonable.

Table 6.15. Parameters Assumed in Analysis of the Response of Mg_3Cd to Electron Irradiation where a Balance Exists Between Disordering and Reordering

Vacancy migration energy	E_v^M	0.5 eV
Vacancy formation energy	E_v^F	0.42 eV
Vacancy, interstitial sink density	α_v, α_i	$10^{11} cm^{-2}$
Vacancy jump distance	λ	3×10^{-8} cm
Vacancy migration entropy factor	A_v	1
Natural atomic jump frequency	ν_o	$10^{13} s^{-1}$
Recombination volume	Z	100
Critical temperature	T_c	426K
Atomic displacement rate	K	1.6×10^{-3} d.p.a. s^{-1}

Using the parameters of Table 6.15. in equation (44) it has been determined that mutual recombination is the dominant defect loss mechanism below 310K and so the steady-state concentration of vacancies is given by equation (40) which is equal to

$$v = \left(\frac{K}{Z\nu_v}\right)^{1/2}$$

Assuming a maximum build-up time to the steady-state condition of 100 seconds equation (45) predicts that this steady-state vacancy concentration is valid at temperatures above 215K. Thus, since the irradiation produced vacancy concentration is in excess of the thermal concentration at temperatures below 340K, the theoretical response of Mg_3Cd to irradiation at temperatures between 330K and 215K can be written as

$$\frac{ds}{dt}_{irr} = -\varepsilon KS + 0.19(1-S)^2\left[\frac{KA_v\nu_o}{Z}\exp-\frac{E_v^M}{k_bT}\right]^{1/2}\left[1-\left[\left(e-\frac{V_o(S+S^3/3)}{k_bT}\right)\left[\frac{(3S+1)(S+3)}{3(1-S)^2}\right]\right]\right] \tag{67}$$

At temperatures below 215K, the steady-state vacancy concentration is not applicable, the vacancy concentration is time dependent and is given by equation (46). Thus ds/dt_{irr} is equal to

$$\frac{ds}{dt}_{irr} = -\varepsilon KS + 0.19(1-S)^2A_v\nu_o\left(\frac{2K\alpha_i\lambda^2}{Z}\right)^{1/2}t^{1/2}\exp\left(-\frac{E_v^M}{k_bT}\right)\left[1-\left[\left(e-\frac{V_o(S+S^3/3)}{k_bT}\right)\left(\frac{(3S+1)(S+3)}{3(1-S)^2}\right)\right]\right] \tag{67a}$$

Evaluation of the Vacancy Migration Energy

The steady-state condition, when $(ds/dt)_{irr}$ is equal to zero and $1 > S > 0$, has been observed experimentally in Mg_3Cd at four temperatures. The activation energy of the rate constant has been evaluated for 305K, 251K and 220K by fitting into equation (67), when $ds/dt_{irr} = 0$, the assumed parameters of table 6.15. and the experimentally determined values of ε and the steady-state value of S. For 158K, these parameters have been fitted into equation (67a) together with the time to reach the steady-state condition. At 158K ε is significantly higher than at 220K and temperatures above (Table 6.16) and so, when the experiments were being carried out, the incident flux was lowered from 1×10^{19} e cm^{-2}sec^{-1} to 5×10^{18} e.cm^{-2}sec^{-1}. to record the disordering response more accurately. Hence, a displacement rate of 8×10^{-4} d.p.a. sec^{-1} has been fitted into the theoretical equation at 158K. The results of this analysis are shown in Table 6.16.

Table 6.16. The Activation Energy for Vacancy Migration which is Consistent with the Experimentally Determined Steady-state Value of S in Mg_3Cd under Electron Irradiation

Temperature K	Steady-State S	ε	E_v^M (eV)
305	0.85	1	0.57
251	0.6	1.4	0.56
220	0.4	1.7	0.51
158*	0.25	4.4	0.38

*time to steady-state is equal to 800 seconds.

The values of E_v^M predicted by the theoretical model at 305K, 251K and 220K are in good agreement with the results of the X-ray studies of thermal ordering, which estimate that $E_v^M = 0.5\ (1 + 0.25\ S^2)$. Figure 6. 9. shows the rate of change of order as a function of S for three temperatures 305K, 251K and 220K, evaluated using equation (67) and the parameters indicated. However, at 158K the theoretical model predicts that E_v^M should be ∿0.38 eV to maintain a steady state degree of order of 0.25. Such a low vacancy migration energy is not consistent with the results at higher temperatures. A possible explanation for this discrepancy at 158K, where, if it is assumed E_v^M is ∿ 0.5 eV, the theoretical model predicts that the alloy should disorder completely, in that the formation of defect loops in the specimen is increasing the experimental error in low values of S. A second possibility is that at 158K loop formation could be high, increasing the interstitial sink concentration and resulting in an increase in the irradiation produced vacancy concentration. The enhanced diffusivity would then be sufficient to restore a small amount of order to the lattice.

6.2.4. NiAl

The experimental investigation into the disordering response of NiAl under electron irradiation has shown that it is more resistant to disordering than the other alloys investigated in the present work. With a damage rate of 10^{-3} d.p.a. sec^{-1} the alloy remains fully ordered at temperatures above 300K and even after extended irradiation at 15K the alloy is only partially disordered (see Figure 5.30.).

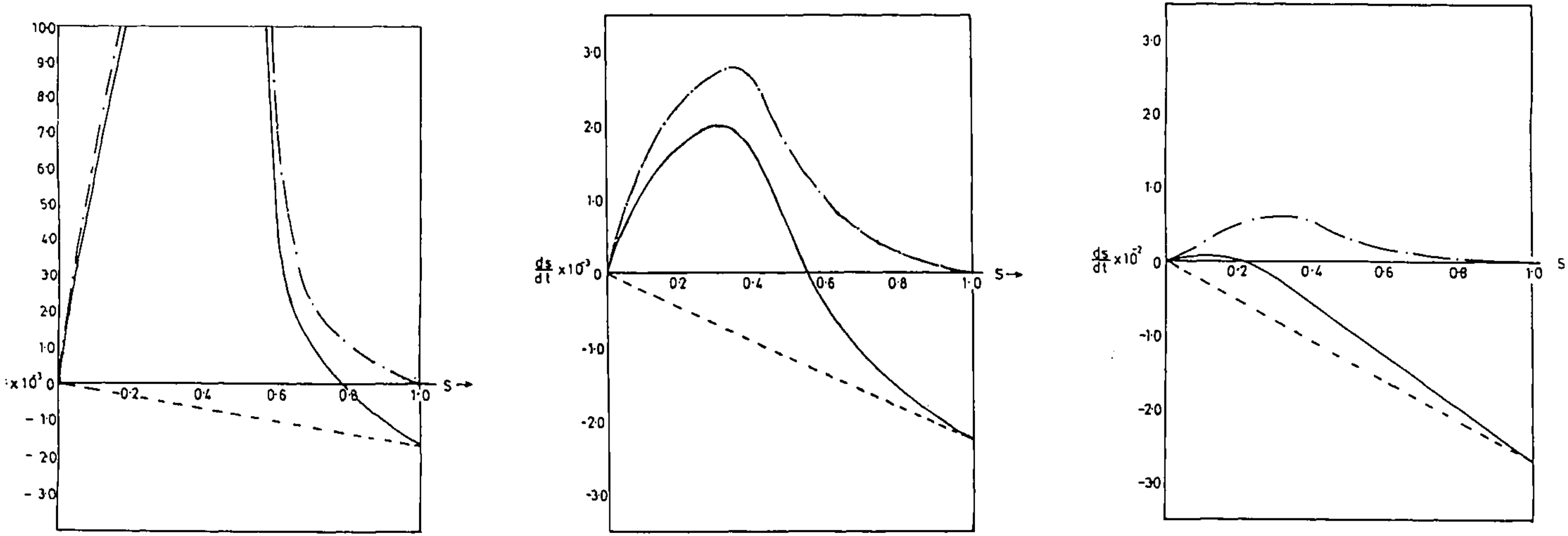

T = 305K
ε = 1

T = 251K
ε = 1.4

T = 220K
ε = 1.7

Figure 6.9. The rate of change of order as a function of S in Mg_3Cd under electron irradiation as a function of temperature. Assuming a displacement rate of 1.6×10^{-3} d.p.a. s^{-1}, $E_V^M = 0.5\ (1 + 0.25S^2)$, $\nu_o = 10^{13}s^{-1}$ and $A_V = 1$.
--- disordering rate; —·—·—·—enhanced ordering rate and —— the sum of the above.

It has been estimated from self-diffusion data (Hancock (1971a)) that the vacancy migration energy is 1.8 eV. This high value is supported by interstitial loop growth studies of Liu and Mitchell (1981). Thus even if E_v^M is a function of S it is unlikely that the enhanced vacancy diffusivity will be high enough to restore order to the lattice at temperatures below 300K. Hence the most obvious explanation for the observed reordering at 15K is via interstitial migration.

If an interstitial mechanism is assumed, the reordering component of Equation (56) which predicts the theoretical response of an AB alloy to irradiation can be written as

$$\frac{ds}{dt}_{ord} = 0.25(1-S)^2 A_i \nu_o \; i \; \exp -\frac{[E_i^M]^o}{k_b T} [1-[\exp(-\frac{V_o(S+S^3/3)}{k_b T})(\frac{1+S}{1-S})^2]] \qquad (68)$$

where i is the irradiation produced vacancy concentration and $[E_i^M]^o$ is the activation energy for an interstitial ordering jump. At the temperatures of interest there is a non steady-state interstitial concentration which is given by Equation (47) and is equal to

$$i = \frac{1}{\nu_i} (\frac{K}{2Z \alpha_i \lambda^2})^{1/2} t^{-1/2}$$

Hence the theoretical response to irradiation of an AB alloy, where reordering occurs by interstitial migration can be written as

$$\frac{ds}{dt}_{irr}, = -\varepsilon KS + 0.25(1-S)^2 (\frac{K}{2Z \alpha_i \lambda^2})^{1/2} t^{-1/2} \exp-[\frac{[E_i^M]^o - E_i^M}{k_b T}][1-[\exp-(\frac{V_o(S+S^3/3)}{k_b T}) (\frac{1+S}{1-S})^2]] \qquad (69)$$

It was discussed in Chapter 3.2. that the interstitial migration energy, E_i^M, is not necessarily the same as the activation energy for an ordering jump, $[E_i^M]^o$. For ordering to occur via an interstitial mechanism, the interstitial atoms must be able to migrate freely over the sublattices. This may involve the formation of a mixed-atom dumbbell configuration whose migration energy is greater than that of a like-atom dumbbell migrating on the sublattice of its own species. To analyse the experimental disordering results of NiAl it is necessary to make some assumptions about the relative magnitudes of the interstitial migration energy and the energy of an interstitial ordering jump.

Liu et al (1981) estimated from defect aggregation studies in NiAl that the interstitial migration energy is ~0.1 eV. If it is assumed that E_i^M is equal to $[E_i^M]^o$ then ds/dt_{irr} is equal to

$$\frac{ds}{dt_{irr}} = -\varepsilon KS + 0.25(1-S)^2\left(\frac{K}{2Z\ \alpha_i\lambda^2}\right)^{1/2} t^{-1/2}\left[1-\left(e-\left(\frac{V_o(S+S^3/3)}{k_bT}\right)\left(\frac{1+S}{1-S}\right)^2\right]\right. \quad (70)$$

Thus for $T \ll T_c$ the reordering component of the response is essentially athermal. To evaluate whether equation (70) is a suitable model for the experimental response, the assumed parameters of Table 6.17, the experimentally determined values of ε and the time to the steady-state condition have been fitted into Equation (70) and assuming ds/dt_{irr} is equal to zero the steady-state value of S as predicted by the model has been determined. This has been compared with the experimentally determined steady-state value of S in Table 6.18.

Table 6.17. Parameters Assumed in the Analysis of the Response of NiAl to Electron Irradiation where a Balance Exists Between Disordering and Reordering.

Displacement rate	K	5×10^{-4} d.p.a. s^{-1}
Recombination volume	Z	100
Critical temperature	T_c	19
Interstitial sink density	α_i	$10^{11}cm^{-2}$
Jump distance	λ	$3 \times 10^{-8}cm$

Table 6.18. Comparison of the Steady-State Value of S with that Predicted by Equation (70)

Temperature	Steady-State S(Experimental)	ε	t to Seq. secs.	Steady-state S predicted by eqn.(70)
305	0.99	1	150	0.7
218	0.6	1.3	1000	0.5
158	0.45	1.9	1000	0.4
118	0.4	2	1000	0.4
15	0.3	5.8	1000	0.2

There is reasonable agreement between the experimentally determined steady-state values of S and those predicted from the evaluation of Equation (70). Although the reordering component of the equation may be considered to be independent of temperature, the increase in ε with decreasing temperature is responsible for the decrease in the steady-state value of S with decreasing temperature.

The agreement between experiment and theory depends on the assumption that $E_i^M = [E_i^M]^o$. If it is assumed that $[E_i^M]^o > E_i^M$, for e.g. $E_i^M = 0.1$ eV and $[E_i^M]^o = 0.2$ eV, and using the same parameters assumed in the previous analysis, the resulting reduction in the reordering component is such that Equation (69) predicts that the alloy will completely disorder at all temperatures below ∿400K. This is clearly not the case experimentally. Hence, although ordering by an interstitial mechanism in which $E_i^M = [E_i^M]^o$ is capable of explaining the observed resistance to disordering of NiAl at temperatures approaching absolute zero, it is not obvious why the energy of an interstitial ordering jump in NiAl should be lower than in the other alloys investigated in the present work. One possible explanation for this might be associated with the high ordering energy of NiAl. It is fully ordered up to its melting point and electron density measurements (Cooper (1963b)) have indicated that there is a degree of covalent bonding between the nickel and aluminium atoms. This could promote spontaneous correlated recombination of the interstitials at vacancy immobile temperatures. However, in FeAl, which is structurally similar to NiAl, there is also evidence of charge transfer (Chaddah and Sahni (1978)) and it is also fully ordered to its melting point, as is Ni_3Al (see Table 2.1.) and yet these alloys readily disorder at vacancy immobile temperatures.

There is one physical property of NiAl which is not found in the other alloys investigated and that is in Al rich, off stoichiometric alloys, the excess Al atoms do not sit on the nickel sites and so vacancies are formed on the nickel sublattice. This property was first established by Bradley and Taylor (1937) who found that the density of NiAl increased with nickel content across the phase field, but the lattice parameter exhibited a maximum near the stoichiometric composition. This unusual defect structure has been explained by the electron theory and Hume-Rothery rules of alloy phases, for background theory see H.Rothery & Coles (1969). Hume-Rothery first observed that in many alloy systems, phases of similar crystal structures are formed at the same ratio of valency electrons to atoms. This ratio can be related to the electron/atom, e/a, concentration when the Fermi surface touches the Brillouin zone boundary, for example in the bcc structure the critical e/a ratio is ∿1.5 which is observed in NiAl (aluminium is trivalent and transition metals are given a valency of zero). Normally when the critical e/a ratio is reached the phase field terminates, but in some compounds, including NiAl, the single phase region may be extended to higher apparent electron concentrations by the formation of a defect structure in which the number of electrons per unit cell does not exceed the critical value. The addition of further aluminium atoms to stoichiometric NiAl would raise e/a above the permitted level if substitution for nickel occurred. Thus the extra aluminium atoms occupy aluminium sites which leads to excess vacancies (over the normal thermal concentration) on nickel sites. An alternative explanation of the defect structure is based on size effects as the larger aluminium atoms will not fit into the nickel sites without causing considerable strain.

Figure 6.10. shows the phase diagrams of NiAl and FeAl, it can be seen that the addition of excess Al atoms to stoichiometric FeAl leads to the formation of the phase $FeAl_2$ whereas NiAl exists with up to ∿60 at% Al.

Recent investigations into the structure of NiAl containing excess vacancies (Jacobi and Engell (1971), Taylor and Doyle (1972) and Yang et al (1978)) have shown that the inflections in the lattice parameter and density curves occur exactly at stoichiometry. Thus it has been concluded that, in alloys containing more than 50 at% Al, nickel vacancies are the only defects present and aluminium atoms do not sit on nickel sites. The concentration of nickel vacancies is shown as a function of at.% Al in Figure 6.11.

X-ray microanalysis of the alloy used in the present investigation showed that the alloy was Al-rich containing ∿ 52 at.% Al. From Figure 6.11. it can be seen that for this composition, ∿8% of the nickel sites are vacant. Thus in 100 atoms; 52 are Al, 44 are Ni and 4 are vacant Ni sites. This is an extremely high concentration of vacancies since, if it is assumed that the vacancy formation energy is 1.39 eV (see Table 2.1.), at 300K the thermal concentration of vacancies will be only 1 vacant site in 10^{24} atoms. A consequence of such a high concentration of vacancies is that, even at temperatures where vacancies can be considered immobile, there will be a high degree of spontaneous recombination. It is conceivable that the high ordering energy of NiAl will promote correlated recombination, which would account for the resistance of the alloy to disordering at temperatures approaching absolute zero. The temperature dependence of the steady-state value of S results from an increase in the replacement collision sequence length with decreasing temperature.

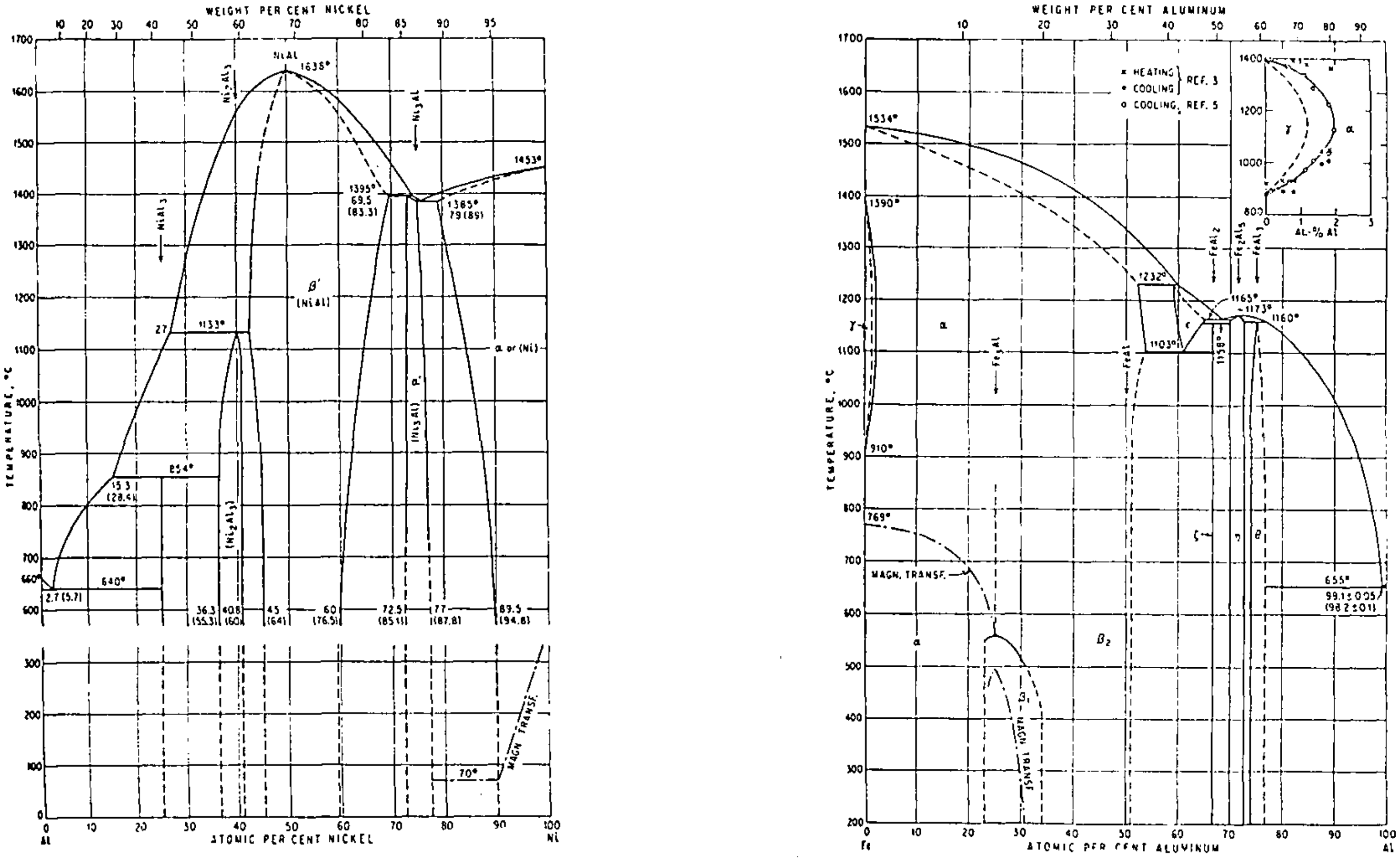

Figure 6.10. (i) (ii)

Binary equilibrium phase diagrams of (i) Ni-Al system and (ii) Fe-Al system.

This alternative explanation of the experimental observations seems more likely than that of a reordering mechanism involving mobile interstitials with $E_i^M = [E_i^M]^o$. Furthermore, no evidence for an interstitial mechanism has been found in the response of any of the other alloys investigated.

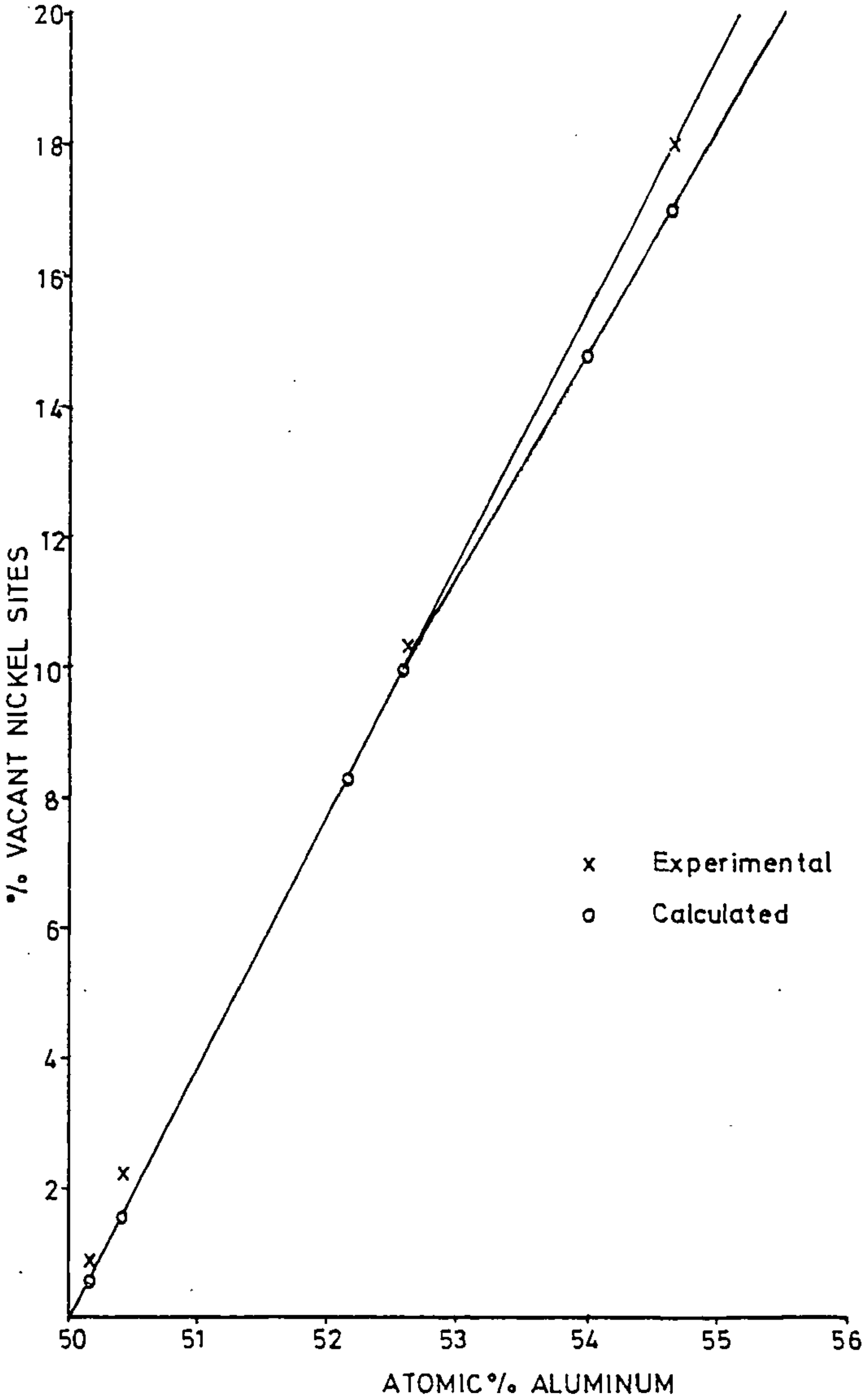

Figure 6.11. Comparison of experimental and calculated concentrations of constitutional vacancies in $Ni_{(1-x)}\ Al_{(1+x)}$. (from Yang et al (1978)).

CHAPTER 7

SUMMARY, CONCLUSIONS AND PROPOSALS FOR FUTURE WORK

7.1. Measurement of Changes in S During Electron Irradiation Using Electron Diffraction

Electron diffraction can be used to monitor reproducibly changes in S during electron irradiation providing the following experimental conditions are upheld. These are:

(i) The irradiations should be conducted in thin areas of the specimen (< 1000Å)

(ii) The specimen should be orientated a few degrees (∿ 5°) from the zone axis, and

(iii) The fundamental reflection intensities should not change by more than ±10% throughout the irradiation.

7.2. The Response of Ordered Alloys to Electron Irradiation

7.2.1. Temperature Dependence of the Disordering Cross-section

The disordering rate of Ni_3Al and Ni_3Fe under electron irradiation has been found to increase with decreasing temperature even when reordering by mobile defects can be neglected. This result has been analysed, via the disordering parameter, ε in terms of a temperature dependent displacement cross-section and is consistent with disordering by the propagation of replacement collision sequences down mixed atom rows. In Mg_3Cd and NiAl the disordering response has a reordering component at temperatures as low as 150K and 15K respectively. However, analysis of the initial disordering rate, when the reordering component of the response is small, has shown that there is a temperature dependent component of the disordering cross-section which is also consistent with disordering by a replacement collision sequence mechanism. At any particular temperature the disordering cross-section of all the alloys studied was found to depend on accelerating voltage but independent of orientation. Thus, it is concluded that:

(i) The principal mechanism of disordering under electron irradiation is the propagation of replacement collision sequences down mixed atom rows, with the temperature dependence arising from an attenuation of the sequence length due to lattice vibrations.

(ii) The disordering cross-section is independent of orientation as replacement collision sequences are readily propagated in close directions which are not parallel to the incident beam direction.

(iii) The disordering cross-section increases with accelerating voltage, as the energy of the primary knock-on atom defines the length of the replacement collision sequence, up to the critical focusing energy, E_F. This effect is most apparent in alloys where there is only a small difference in the masses of the constituent atoms in the alloy, e.g. Ni_3Fe.

7.2.2. Temperature Regime where there is a Balance between Disordering and Reordering

A radiation induced order-disorder transformation model based on reordering via a vacancy mechanism has been successfully applied to the response of Ni_3Al, Ni_3Fe and Mg_3Cd at temperatures where a steady-state value of S is observed. The main results and conclusions are:

(i) Electron irradiation of Ni_3Al with a dose rate of 10^{-3} d.p.a. s^{-1} leads to the formation of a steady-state value of S at temperatures between 300K and 500K. This observation is consistent with reordering by irradiation-produced vacancies which have a migration energy of 1 eV, which is the activation energy for vacancy migration in the disordered state.

(ii) Electron irradiation of Ni_3Fe with a dose rate of 5.10^{-4} d.p.a. s^{-1} leads to the formation of a steady-state value of S at temperatures between ∿300K and 400K. This result is in accord with reordering by irradiation-produced vacancies having a migration energy of 0.95 eV and supports the conclusion that in Ni_3Fe the vacancy migration energy is independent of S.

(iii) The steady-state value of S observed in Mg_3Cd at temperatures between ∿200K and 300K under electron irradiation with a dose rate of 1.5×10^{-3} d.p.a. s^{-1} is consistent with reordering by irradiation-produced vacancies having a migration energy of ∿0.5 eV in the disordered state and ∿0.62 eV in the ordered state.

(iv) NiAl is more resistant to disordering than the other alloys investigated, being only partially disordered after extended irradiation with a damage rate of 10^{-3} d.p.a. s^{-1} at 15K. This behaviour is interpreted in terms of the defect structure of the non-stoichiometric Al-rich NiAl alloy. The concentration of nickel vacancies together with a high ordering energy promotes correlated 'athermal' recombination.

(v) From point (iv) above and the activation energies determined from the other ordered alloys, it is concluded that vacancies, and not interstitials, are the defect species responsible for reordering under electron irradiation.

7.3. Proposals for Future Work

The object of the present investigation was to make a systematic study of the response of ordered alloys to electron irradiation. It was expected that not all aspects of the work could be covered in equal detail, and that areas of research that required further study would be revealed. These areas include a detailed quantitative study of the relative merits of the techniques available for monitoring changes in the degree of long-range order, s, under electron irradiation (Chapter 3.2.2.) and a more complete analysis of the kinetic models available for predicting the variation of s with time as a function of temperature and displacement rate. It is clear that the present approach taken in Chapter 6.2. contains a number of simplifications.

This investigation has concluded that the creation of replacement collision sequences down mixed atoms is the principal mechanism of disordering under electron irradiation at low temperatures, even when there is a significant difference in the masses of the alloys constituent atoms. Therefore, it would be interesting to investigate the disordering response of ordered alloys which have structures in which it is improbable that long-range replacement collision sequences can propagate. For example, in Nb_3Sn and Nb_3Al, which have an A15 structure, the <102> mixed atom row direction is not close-packed and also a void exists between each A-B-A sequence of atoms.

The simple theory (see Chapter 3.1.5.) predicts that replacement collision sequences cannot propagate when a displaced atom has an energy above a critical focusing energy, E_F. Thus, if primary displacements did not undergo secondary atom-atom collisions one would expect that above a certain accelerating voltage the disordering cross-section would decrease. However, it is known that the high energy displacements are involved in secondary atom-atom collisions which result in lower energy displacements which can then create replacement collision sequences.

Theoretical evaluation of the magnitude of the disordering cross-section when the p.k.o. has an energy significantly higher than E_F is complex and so it would be interesting to characterise the effect experimentally. To avoid complications due to mass-difference effects (see Chapter 6.1.5.) an ordered alloy should be chosen where the constituent atoms have approximately equal masses. To undertake such an experiment electron energies of between 1 and 3 MeV would be required and so it is clear that the experimental procedure would not be straightforward.

Further investigation into the orientation dependence of disordering is required. It is conceivable that under irradiation with electrons of energies just above the threshold disordering energy, disordering may occur by uncorrelated recombination or short chain replacement collision sequences in the incident beam direction. However, if this is so, because of the anisotropy in the superlattice reflection intensity change using the electron diffraction technique, disordering will not be apparent. Therefore it is necessary to study this effect using an alternative technique.

To reinforce the conclusion that it is the structural nickel vacancies in aluminium rich, non-stoichiometric, NiAl which are responsible for the resistance of the alloy to disordering, a range of alloys should be prepared with compositions ranging from 46 at.% to 60 at.% Ni and their response to electron irradiation investigated. It is predicted that the stoichiometric and nickel-rich alloys will readily disorder at temperatures less than ∿300K.

Acknowledgements

I would like to thank Dr. Paul Butler and Dr. John Makin for their guidance and advice throughout the course of this project. The financial assistance of the S.E.R.C. and U.K.A.E.A. is gratefully acknowledged.

I am most grateful to my friends in the Department of Metallurgy and Materials Science at Imperial College for their support and encouragement and particularly would like to thank Dr. Harvey Flower for encouragement when I needed it most, Mrs. Gladys Flower for typing the thesis and Mr. Graham Briers for his technical assistance in all aspects of electron microscopy. Also I am indebted to Professor D.W. Pashley for his kindness and the interest he has taken in the work.

Part of this project was undertaken at U.K.A.E.A., Harwell, and I would like to thank the H.V.E.M. group for making me so welcome, especially my good friend Mr. Stan Manthorpe.

My family have helped me immensely during the past four years, but of course my greatest thanks must go to my dearest, long-suffering, husband John.

References

Adam, J., Green, A. and Dugdale, R.A. (1952) Philosophical Magazine, 43, 1216.

Alderson, R.H. (1974) Practical Methods in Electron Microscopy, Vol. 2, 206. Ed. Glauert, A. (North Holland).

Aronin, L.R. (1954) Journal of Applied Physics, 25, 344.

Bauer, W. and Sosin, A. (1964) Journal of Applied Physics, 34, No. 3, 703.

Beavan, L.A., Scanlan, R.M. and Seidman, D.N. (1971) Acta Metallurgica, 19, 1339.

Becker, D.E., Dworschak, F. and Wollenberger, H. (1972) Physica Status Solidi, b 54, 455.

Beeler, J.R. and Beeler, M.F. (1975) Proceedings of the International Conference on Fundamental Aspects of Radiation Damage in Metals, 1, 21. Editors: Robinson, M.T. and Young, F.W. (Gatlinburg, Tenn.)

Benči, S. and Gasparrini, G. (1966) Journal of Physics and Chemistry of Solids, 27, 1035.

Berkowitz, A.E., Jaumot, F.E. and Nix, F.C. (1954) Physical Review, 95, No. 5, 1185.

Bethe, H. (1935) Proceedings of the Royal Society, A150, 552.

Blackburn, M.J. (1967) Transactions of the Metallurgical Society of A.I.M.E. 239, 660.

Born, M. and Mayer, J.E. (1932) Z. Physik, 75, 1.

Bourret, A. (1971) Physica Status Solidi, (a) 4, 813.

Bradley, A.J. and Taylor, A. (1937) Proceedings of Royal Society, 159A, 56.

Bragg, W.L., and Williams, E.J. (1934) Proceedings of the Royal Society, A145, 699.

Brinkman, J.A., Dixon, C.E. and Meechan, C.J. (1954) Acta Metallurgica, 2, 38.

Brown, L.M., Kelly, A. and Mayer, R.M. (1969) Philosophical Magazine, 19, 721.

Brown, N. and Kerman, M. (1956) Journal of Metals, 205, 1353.

Buckley, R.A. and Rajkovic, M. (1979) Spring Conference on Phase transformations series 3, 2, No. 11 (1201-79-Y) Institution of Metallurgists.

Butler, E.P. (1978) Electron Diffraction 1972-1977 (Institute of Phys. Conf. Ser. No. 41, Bristol) Chapter 2, 98.

Butler, E.P. (1979) Radiation Effects, 42. 17.

Butler, E.P. and Swann, P.R. (1975) Scripta Metallurgica, 9, 9.

Butler, E.P. and Swann, P.R. (1977) Proceedings of fifth International Conference on H.V.E.M., Kyoto, Japan, 555.

Calvayrac, Y. and Fayard, M. (1972) Materials Research Bulletin, 7, 891.

Calvayrac, Y. and Fayard, M. (1973) Physica Status Solidi, (a) 17, 407.

Campany, R.G., Loretto, M.H., and Smallman, R.E., (1972) Journal of Microscopy, 98, part 2, 174.

Carpenter, G.J.C. and Schulson, E.M. (1978) Journal of Nuclear Materials, 23, 180.

Carpenter, G.J.C. and Schulson, E.M. (1981) Scripta Metallurgica, 15, 549.

Chaddah, P. and Sahni, V.C. (1978) Philosophical Magazine, B 37, 305.

Chipman, D. and Warren, B.E. (1950) Journal of Applied Physics, 21, 696.

Cockayne, D.J.H., Ray, I.L.F. and Whelan, M.J. (1969) Philosophical Magazine, 20, 1265.

Cooper, M.J. (1963a) Philosophical Magazine, 8, 805.

Cooper, M.J. (1963b) Philosophical Magazine, 8, 811.

Cordier, A., Degeilh, A., Garat, F. and Reynaud, F. (1973) Radiation Effects, 7, 127.

Cottrell, A. (1975) Introduction to Metallurgy, 2nd Edition, 350, (Edward Arnold, Bath).

Cullity, B.D. (1967) Elements of X-ray diffraction, 367,(Addison-Wesley, London.)

Cupschalk, S.G. and Brown, N. (1968) Acta Metallurgica, 16, 657.

Dahmen, U. (1977) Proceedings 35th Annual Conference of E.M.S.A. Boston, Mass. 186.

Davies, R.G. and Stoloff, N.S. (1964) Transactions of the Metallurgical Society of A.I.M.E., 230, 390.

Dederichs, P.H., Lehmann, C., Schober, H.R., Scholz, A., and Zeller, R. (1978) Journal of Nuclear Materials, 69 and 70, 176.

Dienes, G.J. (1955), Acta Metallurgica, 3, 549.

Drijver, J.W. and Van der Woude, F. (1975) Physical Review Letters, 34, No. 16, 1026.

Drosd, R., Kosel, T. and Washburn, J. (1978) Journal of Nuclear Materials, 69 and 70, 804.

Ecker, K.H. (1974) Radiation Effects, 23, 171.

Ehrhart, P. and Schilling, W. (1973) Physical Review, 8, No. 6, 2604.

Elcock, E.W. (1959) Proceedings of the Physical Society of London, 73, 250.

Elich, J.J. Ph. and Roosendaal, H.E. (1970) Physics Letters, 33A, No. 4, 235.

English, A.T. (1966) Transactions of the Metallurgical Society of A.I.M.E. 236, 14.

Erginsoy, C., Vineyard, G.H. and Englert, A. (1964) Physical Review, 133, No. 2A, 595.

Fisher, S.B. (1970) Radiation Effects, 5, 239.

Flinn, P.A. (1960) Transactions of the Metallurgical Society of A.I.M.E., 218, 145.

Fukamachi, M. and Kikuchi, T. (1975) Japanese Journal of Applied Physics, 14, No. 4, 587.

Gale, B. and Hale, K.F. (1961) British Journal of Applied Physics, 12, 115.

Garner, F.A. and Thomas, L.E. and Gelles, D.S. (1975) Proceedings of A.S.T.M. Symposium on Experimental Methods for Charged Particle Irradiations, Gatlinburg, TN, 51.

Gibson, J.B., Goland, A.N., Milgram, M. and Vineyard, G.H. (1961) Physical Review, 120, 1229.

Gilbert, J. and Hermann, H. (1973) Radiation Effects 20, 37.

Gififalco, L.A. (1964) Journal of the Physics and Chemistry of Solids, 24, 323.

Gittus, J. (1978) Irradiation Effects in Crystalline Solids, 21, (Applied Science Publishers Ltd. London).

Gordon, P. and El-Bassyouni, T.A. (1965) Transactions of the Metallurgical Society of A.I.ME. 233, 391.

Greenholz, M., Kidron, A. and Shimony, U. (1972) Journal of Materials Science, 7, 1285.

Guttman, L. (1956) Solid State Physics, 3, 146.

Hancóck, G.F. and McDonnell, B.R. (1971a) Physica Status Solidi, a4, 143.

Hancock, G.F. and McDonnell, B.R. (1971b) Physica Status Solidi, a7, 535.

Hertel, B., Diehl, J., Gotthardt, R. and Sultze, H. (1974) Applications of Ion beams to metals, 507. Edited by Picraux, S.T. Eernisse, E.P. and Vook, F.L. (Plenum Press, New York).

Hossain, M.K. and Brown, L.M. (1977a) Acta Metallurgica, 25, 257.

Hossain, M.K. and Brown, L.M. (1977b) Radiation Effects, 31, 203.

Howe, L.M. and Rainville, H. (1977) Journal of Nuclear Materials, 63, 215.

Hume-Rothery, W. and Coles, B.R. (1969) Atomic Theory for Students of Metallurgy, 125, (The Institute of Metals, London).

Iseler, G., Dawson, H., Mehner, A. and Kauffman, J. (1967) Physical Review, 146, 468.

Jackson, R.O., Leighly, H.P. and Edwards, D.R. (1972) Philosophical Magazine, 25, 1169.

Jacobi, H. and Engell, H.J. (1971) Acta Metallurgica, 19, 701.

Karim, A.S.A., Whitehead, M.E., Loretto, M.H. and Smallman, R.E. (1978) Acta Metallurgica, 26, 975.

Kinchin, G.H. and Pease, R.S. (1955) Reports on Progress in Physics, 18., 1.

King, W.E., Merkle, K.L. and Meshii, M. (1980) Electron Microscopy, 4, 212.

Kinoshita, C., Mukai, T. and Kitajima, S. (1977) Acta Crystallography, A33, 605.

Kinoshita, C., Mukai, T. and Kitajima, S. (1982), Proceedings of Yamada Conference on Point Defects in Metals, (to be published).

Kiritani, M., Yoshida, N., Takata, H. and Maehara, Y. (1975) Journal of the Physical Society of Japan, 38, No. 6, 1677.

Kirk, M.A., Blewitt, T.H. and Scott, T.L. (1977) Physical Review, 15, No. 6, 2914.

Kirsanov, V.V. (1980) Radiation Effects, 46, 167.

Klug, H.P. and Alexander, L.E. (1954) X-ray diffraction procedures, 207, (J. Wiley and Sons, New York).

Koczak, M.J., Herman, H. and Damask, A.C. (1971) Acta Metallurgica, 19, 303.

Koneva, N.A., Kozlov, E.V., Korotayev, A.D., Popov, L. Ye., Perov, G.A., Yesipenko, V.F. and Teplyakova, L.N. (1973) Fiz. Metal Metalloved 35, No. 5, 1075.

Kritzinger, S. and Ronander, E. (1974) Eighth International Congress on Electron Microscopy, Canberra, 1, 190.

Krivoglaz, M.A. and Smirnov, A.A. (1964) The theory of order-disorder in Alloys, (Macdonald, London).

Kuper, A.B., Lazarus, D., Manning, J.R. and Tomizuka, C.T. (1956) Physical Review, 104, 1536.

Laidler, J.J., Garner, F.A. and Thomas, L.E. (1976) Radiation Damage in Metallurgy, editors Peterson, N.L. and Harkness, S.D., 194, published by A.S.M.

Lehmann, C. and Sigmund, P. (1966) Physica Status Solidi, 16, 507.

Lennartz, R., Dworshak, F. and Wollenberger (1977) Journal of Physics, F: Metal Physics, 7, No. 10, 2011.

Liebfried, G. (1959) Journal of Applied Physics, 30, No. 9, 1388.

Liou, K.Y. and Wilkes, P. (1979) Journal of Nuclear Materials, 87, 317.

Liu, H.C., Kinoshita, C. and Mitchell, T.E. (1981) Phase Stability During Irradiation Proceedings of a Symposium on Nuclear Metallurgy, Pennsylvania, ed. Holland, J.R. et al. 343, (The Metallurgical Society of A.I.M.E.).

Lomer, J. and Pepper, M. (1967) Philosophical Magazine, 16, 1119.

Lück, G. and Sizmann, R. (1964) Physica Status Solidi, 5, 683.

Makin, M.J. (1968a) Philosophical Magazine, 18, 637.

Makin, M.J. (1968b) Metallography, 1, 109.

Makin, M.J. (1970) Philosophical Magazine, 20, 1133.

Makin, M.J. (1971a) U.K.A.E.A. Harwell, AERE-R6957.

Makin, M.J. (1971b) Jern Kont. Ann. 155, 509.

Marcinkowski, M.J. (1963) Electron Microscopy and Strength of Crystals, ed. Thomas, G. and Washburn, J. 333. (Interscience Publishers, John Wiley and Sons, New York).

Marcinkowski, M.J. and Poliak, R.M. (1963) Philosophical Magazine, 8, 1023.

Maury, F., Biget, M., Vajda, P., Lucasson, A., Lucasson, P. (1976) Physical Review, B14, 5303.

Merkle, K.L. and Averback, R.S. (1976) Fundamental Aspects Radiation Damage in Metals, Proceedings International Conference, Gatlinburg, Tenn. 127. Ed. Robinson, M.T. and Young, F.W.

McKinley, W.A. and Feshbach, H. (1948) Physical Review, 74, 1759.

Mikkola, D.E. and Rundman, K.B. (1972) Scripta Metallurgica, 6, 1095.

Morris, D.G., Brown, G.T., Piller, R.C. and Smallman, R.E. (1976) Acta Metallurgica, 24, 21.

Mukai, T. (1981) Private Communication.

Mukai, T. and Mitchell, T.E. (1982) Philosophical Magazine, 45. No. 5, 741.

Muto, T. and Takagi, Y. (1955) Solid State Physics, 1, 193.

Nelson, R.S., Thompson, M.W. and Montgomery, H. (1962) Philosophical Magazine, 7, No. 8, 1385.

Nelson, R.S. and Von Jan, R. (1968) Canadian Journal of Physics, 46, 739.

Normanton, A.S., Bloomfield, P.E. and Sale, F.R. (1975) Metal Science, 9, 510.

Oen, O.S. (1973) U.S.A. Report O.R.N.L.-4897.

Peierls, R. (1936) Proceedings of the Royal Society, A154, 207.

Penisson, J.M. and Bourret, A. (1975) Fourth International Congress on H.V.E.M., Toulouse, 205.

Polenok, V.S. (1973) Physics of Metals and Metallography, 36, No. 1, 188.

Poquette, G.E. and Mikkola, D.E. (1969) Transactions of the Metallurgical Society of A.I.M.E., 245, 743.

Rand, W.H. and Oblock, J.M. (1973) Proceedings 31st Annual Meeting of E.M.S.A., 174.

Rapps, P., Katerbau, K.H., Mughrabi, H. Urban, K. and Wilkens, M. (1978) Physica Status Solidi, (a)47, 479.

Rhines, F.N. and Newkirk, J.B. (1953) Transactions of the American Society of Metals, 45, 1029.

Riviere, J.P., Zonon, H. and Grilhe, J. (1974) Acta Metallurgica, 22, 929.

Riviere, J.P. and Grilhe, J. (1975) Scripta Metallurgica, 9, 967.

Rogers, J.A., Flower, H.M. and Rawlings, R.D. (1975) Metal Science, 9, 32.

Sakauchi, T., Sonada, Y. and Suzuki, T. (1979) Scripta Metallurgica, 13, 657.

Sanders, J.B. and Fluit, J.M. (1964) Physica, 30, 129.

Schulson, E.M. (1979) Journal of Nuclear Materials, 83, 239.

Seitz, F. (1956) Solid State Physics, 2, 305.

Sharp, J.V. (1969) UKAEA - Harwell, AERE R-6297.

Shimomura, Y., Noya, E., Kuwabara, S. and Kino, T. (1977) Proceedings of the 5th International Conference on HVEM, Kyoto, 511.

Silsbee, R.H. (1957) Journal of Applied Physics, 28, 1246.

Smithells, C.J. (1976) Metals Reference Book, 5th ed. 891-896, (Butterworths, London).

Stobbs, W.M. (1973) Philosophical Magazine, 27, 257.

Stoeckinger, G.R. and Neumann, J.P. (1970) Journal of Applied Crystallography, 3, 32.

Stoloff, N.S. and Davies, R.G. (1966) Progress in Materials Science, 13, 3.

Suzuki, T. and Yamamoto, M. (1959) Journal of the Physical Society of Japan, 14, No. 4, 463.

Swann, P.R. (1978) Proceedings of 9th International Congress on Electron Microscopy, Toronto, 3, 319.

Swann, P.R. and Lloyd, A.E. (1974) Proceedings of 32nd Annual Meeting of E.M.S.A. St. Louis, 450.

Sweedler, A.R. and Cox, D.E. Physical Review, B, 12, No. 1, 147.

Tanner, L.E. (1972) Acta Metallurgica, 20, 1197.

Taunt, R.J. and Ralph, B. (1974) Philosophical Magazine, 30, 1379.

Taylor, A. and Doyle, N.J. (1972) Journal of Applied Crystallography, 5, 201.

Taylor, A. and Jones, R.M. (1958) Journal of Physics and Chemistry of Solids, 6, 16.

Tenenbaum, A. (1978) Philosophical Magazine, A 37, No. 6, 731.

Tenenbaum, A. and Doan, N.V. (1977) Philosophical Magazine, A 35, No. 2, 379.

Theis, U. and Wollenberger, H. (1980) Journal of Nuclear Materials, 88, 121.

Thomas, G.J. and Venables, J.A. (1973) Philosophical Magazine, A 28, No. 6, 1171.

Thompson, M.W. (1969) Defects and Radiation Damage in Metals, 198 (Cambridge University Press, Cambridge).

Tomokioyo, Y., Kuroda, K., Matsuhata, H. and Eguchi, T. (1980) Proceedings of 6th International Conference on HVEM, (Antwerp, Belgium) 4, 108.

Tukhfatullin, A.A., Makogon, M.B. and Yakovlev, R.F. (1968) Physics of Metals and Metallography, 26, No. 2, 219.

Urban, K. (1973) Journal of Microscopy, 97, 121.

Urban, K. (1975) Proceedings of the International Conference on Fundamental Aspects of Radiation Damage in Metals, Gatlinburg, Tenn. 675. Editors: Robinson, M.T. and Young, F.W.

Urban, K. and Seeger, A. (1974) Philosophical Magazine, A 30, 1395.

Urban, K. and Wilkens, M. (1971) Physica Status Solidi, (a) 6, 173.

Vajda, P. (1977) Review of Modern Physics, 49, No. 3, 481.

Van Tendeloo, G., Van Landuyt, J. and Amelinckx, S. (1979) Radiation Effects, 41, 179.

Venables, J.D. and Lye, R.G. (1969) Philosophical Magazine, A 19, 565.

Vineyard, G.H. (1956) Physical Review, 102, No. 4, 981.

Vineyard, G.H. (1963) Journal of the Physical Society of Japan, 18, 144.

Vineyard, G.H. and Erginsoy, C. (1962) Proceedings of Conference on Lattice Defects in Kyoto, Japan.

Wasilewski, R.J. (1966) Transactions of the Metallurgical Society of A.I.M.E., 236, 455.

Wehner, G.K. (1956) Physical Review, 102, 690.

Welber, B., Webeler, R. and Trumbore, F. (1953) Acta Metallurgica, 1, 374.

West, G.W. (1964) Philosophical Magazine, A 9, 979.

Wilkens, M. and Rapps, P. (1977) Physica Status Solidi, (a) 44, 173.

Wolfenden, A. (1972) Radiation Effects, 14, 225.

Wollenberger, H. (1978) Journal of Nuclear Materials, 69 and 70, 362.

Yang, W.J., Lin, F. and Dodd, R.A. (1978) Scripta Metallurgica, 12, 237.

Yoo, M.H. and Stiegler, J.O. (1977) Philosophical Magazine, 36, No. 6, 1305.

Yoshida, N. and Urban, K. (1980) Physics Letters, 75A, No. 3, 231.

Young, F.W. (1978) Journal of Nuclear Materials, 69 and 70, 310.

Zee, R.H. and Wilkes, P. (1980) Philosophical Magazine, 42, 463.

Zee, R.H. and Wilkes, P. (1981) Journal of Nuclear Materials, 97, 179.

APPENDIX I

Superlattice Reflection Intensity of a Partially Ordered AB B2 Alloy

In a partially ordered AB B2 alloy, of the total number of A atoms, P_A^α atoms of A will sit on α 'ordered' sites and $(1-P_A^\alpha)$ atoms of A will sit on β 'disordered sites. Similarly of the total number of B atoms. P_A^α atoms of B will sit on β sites and $(1-P_A^\alpha)$ β will sit on α sites. Thus the structure factor is equal to

$$F_{hkl} = P_A^\alpha f_A + (1-P_A^\alpha)f_B + \{[P_A^\alpha f_B + (1-P_A^\alpha)f_A][e^{\pi i(h+k+l)}]\}$$

When $h+k+l = 2n$

$$F_{hkl} = f_A+f_B$$

i.e. $\underline{F_{fund} = f_A+f_B}$

when $h+k+l = 2n+1$

$$F_{hkl} = 2P_A^\alpha f_A - f_A + f_B - 2P_A^\alpha f_B$$

$$= \frac{(P_A^\alpha f_A - 1/2f_A + 1/2f_B - P_A^\alpha f_B)}{(1 - 1/2)}$$

$$= \frac{(f_A - f_B)(P_A^\alpha - 1/2)}{(1 - 1/2)}$$

Since from equation (2)

$$S = \frac{P_A^\alpha - 1/2}{1 - 1/2}$$

$$\underline{\underline{F_{super} = (f_A - f_B)\ S}}$$

APPENDIX II

The Born-Mayer (1932) lattice potential, $V(r)$ is of the form

$$V(r) = Ae^{-r/b}$$

where r is the separation of the atomic nuclei and A and b are constants. Brinkman suggested empirical formulae for the Born-Mayer constants, these are

$$A = 2.58 \times 10^{-5} \, (Z_1 Z_2)^{11/4} \text{ eV}$$

$$b = 1.5 \, a_o / (Z_1 Z_2)^{1/6} \qquad \text{Å}$$

where Z is the atomic number and a_o is the Bohr radius of the hydrogen atom (= 0.53 Å).

Equations derived by Nelson et al (1962) to calculate the energy losses in a <110> collision sequence in a fcc lattice.

ΔE_1, energy lost to rings of atoms surrounding the collision axis

$$\frac{\Delta E_1}{E_F^{110}} = 2[\exp\{-\frac{D^{110}}{2b}(\frac{2c-1}{D^{110}})\} - \exp\{-\frac{D^{110}}{2b}\}] \exp(3\bar{x}_n^{\,2}/b^2)$$

where $c = D^{110}(3/4 + \{b/D^{110}\}^2 \log\{E_F^{110}/E\}^2)^{1/2}$

D^{110} is the (110) interplanar spacing, b is a born mayer constant, E_F^{110} is the <110> focusing energy and $\bar{x}_n^{\,2}$ is the Debye-Waller factor (equation (33)).

ΔE_2, scattering of energy out of the focusing line by misalignment of the atoms caused by lattice vibration

(i) For $T < \Theta_D$

$$\frac{\Delta E_2}{E_F^{110}} = \frac{32\,\bar{x}_n^{\,2}}{(D^{110})^2 L(1+L)}\left[1 - \frac{2}{1+L}(0.139 - 0.047\,\frac{1-L}{1+L})\right]\frac{E}{E_F^{110}}$$

(ii) For $T > \Theta_D$

$$\frac{\Delta E_2}{E_F^{110}} = \frac{32\,\bar{x}^2}{(D^{110})^2 L(1+L)}\left[1 - \{\frac{\pi}{6\sqrt{2}}\}^{1/3}\frac{1}{1-L}\log\frac{2}{1+L}\right]\frac{E}{E_F^{110}}$$

where $L = \frac{2b}{D^{110}}\log\frac{E_F^{110}}{E}$

APPENDIX III

The Anisotropy of Superlattice Reflection Intensity Change in DO_{19} AB Alloys

Consider a fully ordered DO_{19} AB_3 alloy as shown in Figure (i). The structure factor F for any hkl reflection can be calculated from equation (3) where

$$F_{hkl} = \sum_{1}^{n} f_n \, e^{2\pi i \, (hu_n + kv_n + lw_n)}$$

Since there are eight atoms in the unit cell.

A at (0,0,0)
A at (1/3,2/3,1/2)
B at (1/2,0,0)
B at (0,1/2,0)
B at (1/2,1/2,0)
B at (1/2,1/6,1/2)
B at (5/6,1/6,1/2)
B at (5/6,2/3,1/2)

The structure factor F_{hkl} is equal to

$$\begin{aligned} F_{hkl} = {} & f_A \, [1 + e^{2\pi i \, (h/3 + 2k/3 + L/2)}] \\ & + f_B \, [e^{\pi ih} + e^{\pi ik} + e^{\pi i(h+k)} \\ & + e^{2\pi i \, (h/3 + k/6 + L/2)} \\ & + e^{2\pi i \, (5h/6 + k/6 + L/2)} \\ & + e^{2\pi i \, (5h/6 + 2k/3 + L/2)} \,] \end{aligned}$$

If the crystal is orientated with the [100] ($\equiv [2\bar{1}\bar{1}0]$) orientation, a mixed atom row, parallel to the incident electron beam then the structure factors of the [010] and $[0\bar{1}0]$ superlattice reflections observed in the diffraction are equal to

$$F_{(010)} = F_{(0\bar{1}0)} = f_A - f_B.$$

If [100] irradiation causes displacements only in this direction random rearrangement of the displaced atoms will lead to a site occupancy as shown in Figure (ii), i.e.

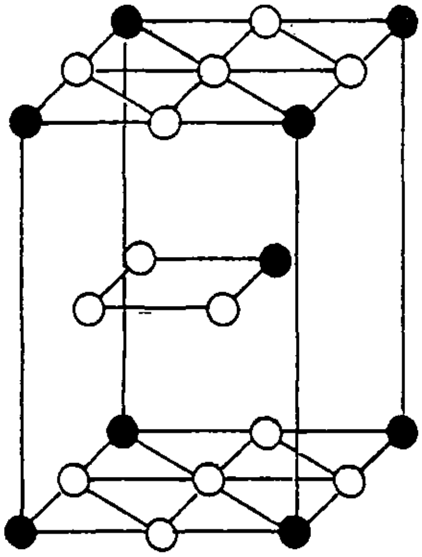

Figure (i) Fully ordered AB_3 alloy with DO_{19} structure

● A

O B

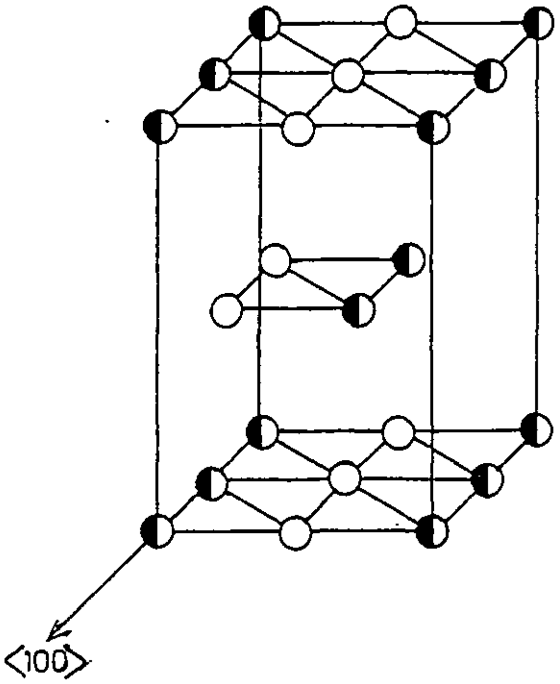

Figure (ii) Atomic arrangement in an AB_3 alloy with a DO_{19} structure after unidirectional displacements in the [100] direction.

1/2(A + B) at (0,0,0)
1/2(A + B) at (1/3,2/3,1/2)
1/2(A + B) at (1/2,0,0)
B at (0,1/2,0)
B at (1/2,1/2,0)
B at (1/3,1/6,1/2)
B at (5/6,1/6,1/2)
1/2(A + B) at (5/6,2/3,1/2)

The structure factor is now equal to

$$\begin{aligned} F_{hkl} = {} & 1/2(f_A + f_B)[1 + e^{2\pi i(h/3 + 2k/3 + L/2)} \\ & + e^{2\pi i(5/6h + 2/3k + L/2)} \\ & + e^{2\pi i(h/2)}] + f_B\ [e^{\pi ik} + e^{\pi i(h + k)} \\ & + e^{2\pi i(5/6h + k/6 + L/2)} \\ & + e^{2\pi i(h/3 + k/6 + L/2)}] \end{aligned}$$

Therefore

$$\begin{aligned} F_{(010)} = F_{(0\bar{1}0)} & = (f_A - f_B)[1 + e^{4\pi i/3}] \\ & = (f_A - f_B) \end{aligned}$$

i.e. Although the alloy has been fully disordered in the [100] direction, the structure factors of the (010) and (0$\bar{1}$0) superlattice reflections observed in the diffraction pattern have remained unchanged. For these reflections to decrease in intensity secondary displacements must occur in directions other than the incident beam direction.